The Extended Nijboer-Zernike Diffraction Theory and its Applications

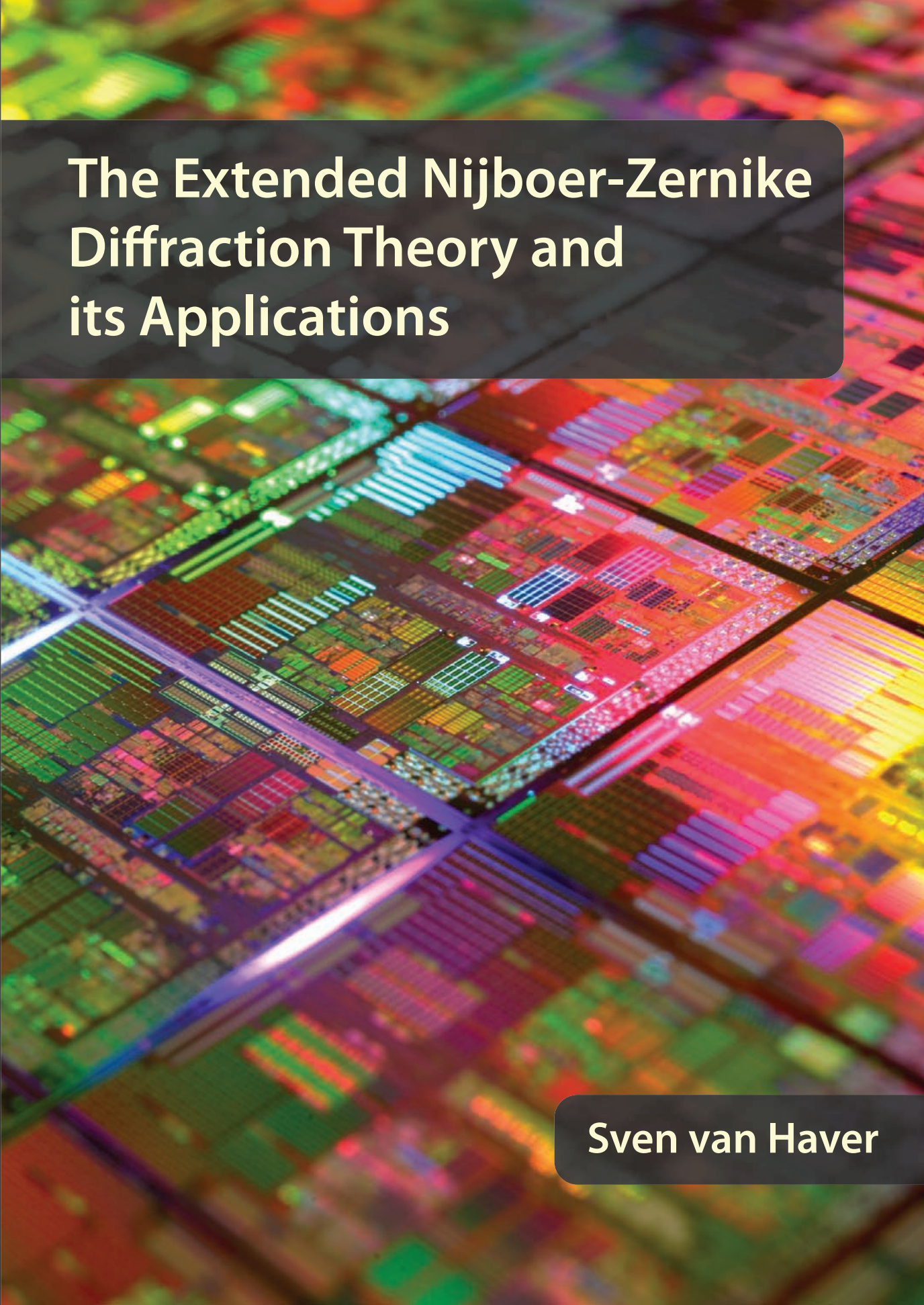

Sven van Haver

THE EXTENDED NIJBOER-ZERNIKE DIFFRACTION THEORY AND ITS APPLICATIONS

Proefschrift

ter verkrijging van de graad van doctor
aan de Technische Universiteit Delft,
op gezag van de Rector Magnificus prof. ir. K.C.A.M. Luyben,
voorzitter van het College voor Promoties,
in het openbaar te verdedigen op vrijdag 5 februari 2010 om 12.30 uur

door

Sven VAN HAVER

natuurkundig ingenieur
geboren te Leidschendam

Dit proefschrift is goedgekeurd door de promotoren:
Prof.dr.ir. J.J.M. Braat
Prof.dr. H.P. Urbach

Copromotor:
Dr.ir. S.F. Pereira

Samenstelling promotiecommissie:

Rector Magnificus,	voorzitter
Prof.dr.ir. J.J.M. Braat,	Technische Universiteit Delft, promotor
Prof.dr. H.P. Urbach,	Technische Universiteit Delft, promotor
Dr.ir. S.F. Pereira,	Technische Universiteit Delft, copromotor
Prof.dr. T.D. Visser,	Technische Universiteit Delft
Prof.dr. F. Wyrowski,	Friedrich Schiller University Jena
Dr. A. Erdmann,	Friedrich Alexander University Erlangen-Nuremberg
Dr. W. Vollrath,	KLA-Tencor MIE GmbH
Prof.dr.ir. P.M. van den Berg,	Technische Universiteit Delft, reservelid

This research was supported by NanoNed, a national nanotechnology program coordinated by the Dutch Ministry of Economic Affairs.

Cover:
Photograph of a lithographic wafer containing 45 nm technology Quad Core processors produced by Advanced Micro Devices, Inc. (AMD).

ISBN: 978-90-78314-12-7

A free electronic version of this thesis can be downloaded from:
`http://www.library.tudelft.nl/dissertations`

How quick are we to learn, that is, to imitate what others have done or thought before. And how slow to understand, that is, to see the deeper connections. Slowest of all, however, are we in inventing new connections or even in applying old ideas in a new field.

- Frits Zernike, Nobel Lecture, December 11th, 1953 -

Summary

The Extended Nijboer-Zernike diffraction theory and its applications

In present-day society, we encounter optical systems on a daily basis. Most people have a DVD player capable of playing content stored on an optical disc, Big Brother is watching us nearly everywhere using surveillance cameras and we consider it to be normal to take photographs with our mobile phone. Also, in less visible areas, such as ultrafast fiber-based data transfer, we rely on optical technology. Although these applications might be considered advanced by the general public, they mostly do not reflect the state of perfection that is currently needed by the scientific and high-tech community. When we speak of advanced optical systems in this context we refer to highly corrected optical systems or optical systems having extreme optical properties. For example, in astronomy, huge optical telescopes are used to produce images of faint astronomical objects located deep in space and also in microscopy, high quality optics are applied to visualize the smallest possible details in a sample such as a living cell. However, by far the most cutting edge optical technology is applied in the semiconductor industry. A process called optical lithography is used to transfer geometrical patterns, that are part of a chip design, into a layer of photosensitive material. Using chemical technology these patterns are developed into metallic and insulating structures and, repeating lithographic pattern transfer and chemical development several times in succession, it is possible to produce a working electronic circuit or chip at the nanometer scale.

The above mentioned applications of optical technology have in common that they require extremely accurate optical components. This is because the objects that they try to visualize or image are so small and faint that even the smallest aberration effects can completely conceal the features of interest. One might think that reducing the aberrations to a low level simplifies the task of simulating these systems. Unfortunately, this is not true. In fact, at this level of perfection, various optical phenomena, that would otherwise have negligible effect in comparison to the imperfections of the optical system, become significant. Therefore, existing optical methods should be extended to properly include these effects in order to allow a sensible analysis of the performance of optical systems in this regime. In addition, also the errors introduced by approximations used in image simulation models become significant and this makes it favorable to apply those methods with the smallest number of incorporated approximations. Although there has been, in recent years, a large research effort by the optical community to extend existing optical methods to correctly describe this class of systems, the results so far have not been totally satisfactory.

As an alternative, we present in this thesis a novel optical model that we believe is superior in the accurate description and simulation of image formation. The formation of an image by an aberrated optical system is accurately described by the corresponding diffraction integral. However, until recently, this integral could only be evaluated numerically to obtain the three-dimensional image structure. This changed in 2002 with the introduction of the Extended Nijboer-Zernike (ENZ) theory. This theoretical framework, extensively described in this thesis, provides a generally valid analytic solution to the diffraction integral. Based on this result we have constructed a novel imaging model that includes all relevant physical effects and applies very few approximations. The resulting ENZ imaging method proposed in this thesis is, therefore, well suited to accurately describe image formation by advanced optical imaging systems.

The second important contribution presented in this thesis pertains to the quality assessment of optical systems. It is shown that it is possible to determine the quality of an optical system by evaluating the image it produces from a point object. This is possible because the analytic results provided by the ENZ theory allow us to devise an expression for the intensity image of a point object. Matching the measurement data with this expression enables complete characterization of the optical system under study without the need of additional complicated optical set-ups.

Altogether, we present in this thesis a comprehensive ENZ formalism that can be used to accurately simulate image formation by a large variety of imaging systems. The most important feature of ENZ imaging is its high accuracy that follows from the semi-analytic nature of the ENZ theory and the few approximations applied in the ENZ imaging model. Additionally it is shown that the aberrations of an optical system can be obtained from intensity measurements alone, introducing an appealing alternative to interferometric methods that are commonly applied for this purpose. Finally, both applications of the ENZ theory are illustrated by a number of practical examples, clearly showing the large potential of the ENZ formalism in the field of advanced optical imaging systems.

Sven van Haver, Delft, November 2009.

Samenvatting

De Extended Nijboer-Zernike diffractietheorie en haar toepassingen

In de huidige maatschappij komt men dagelijks in aanraking met optische systemen. Zo heeft bijna iedereen een apparaat om optische media zoals CD's en DVD's af te spelen, worden we constant in de gaten gehouden door Big Brother met behulp van bewakingscamera's en vinden we het zo langzamerhand normaal om foto's te nemen met onze mobiele telefoon. Ook in minder zichtbare gebieden speelt optische technologie een belangrijke rol, zo worden bijvoorbeeld de belangrijke dataverbindingen van het internet gevormd door optische glasvezelkabels. Alhoewel veel mensen de bovengenoemde toepassingen als geavanceerd beschouwen, weerspiegelen ze bij lange na niet de geavanceerde optische technologie die momenteel wordt ontwikkeld door de wetenschappelijke gemeenschap. Wanneer er in deze context gesproken wordt van geavanceerde optische systemen, dan bedoelt men systemen met extreme optische eigenschappen. Zo worden er bijvoorbeeld in de astronomie enorme optische telescopen gebruikt om objecten diep in het heelal zichtbaar te maken, maar ook in de microscopie worden sterk gecorrigeerde optische elementen gebruikt om de kleinst mogelijke details, in bijvoorbeeld een levende cel, zichtbaar te maken. Echter, veruit de meest geavanceerde optische technologie wordt toegepast in de halfgeleiderindustrie. Door middel van zogenaamde optische lithografie wordt een geometrisch patroon, dat deel uitmaakt van het ontwerp van een chip, afgebeeld in een laag lichtgevoelig materiaal. Vervolgens wordt dit patroon door middel van chemische processen ontwikkeld tot metallische en isolerende structuren. Door optische lithografie en de bijbehorende chemische ontwikkeling verscheidene malen achtereenvolgens toe te passen, is het mogelijk om elektronische circuits op te bouwen die bijvoorbeeld dienst kunnen doen als processor in een computer.

De bovengenoemde toepassingen van optische technologie hebben gemeen dat zij optische elementen vereisen van zeer hoge kwaliteit. Zouden deze systemen namelijk een niet verwaarloosbare hoeveelheid aberraties bevatten, dan resulteert dit in een dusdanige vervorming van hun afbeelding, dat de objecten waarin men geïnteresseerd is niet te onderscheiden zijn. Nu kan men denken dat het simuleren van vrijwel aberratievrije optische systemen relatief makkelijk is, maar helaas, niets is minder waar. Wanneer we namelijk een dergelijk extreem goed gecorrigeerd systeem beschouwen, hebben bepaalde optische effecten, die normaal gesproken verwaarloosd kunnen worden ten opzichte van aberratie-invloeden, opeens wel een significante invloed op de afbeelding. Om deze klasse van optische systemen dus op een zinnige manier te analyseren, hebben we een optisch model nodig dat deze

effecten op een correcte manier in rekening brengt. Daar komt nog bij dat de onnauwkeurigheid, geïntroduceerd door veel gebruikte benaderingen in optische modellen, ook een steeds grotere relatieve invloed krijgt op de beschrijving van het optisch systeem. De trend is dan ook dat steeds vaker die modellen worden toegepast die gebruik maken van het kleinste aantal benaderingen. Hoewel er in de afgelopen jaren veel werk is verzet door de optische gemeenschap om bestaande modellen dusdanig uit te breiden dat ze afbeelding door geavanceerde optische systemen kunnen beschrijven met de gewenste nauwkeurigheid, zijn de resultaten tot nog toe niet geheel bevredigend.

Als alternatief voor bestaande optische modellen wordt er in dit proefschrift een methode gepresenteerd, die in onze ogen superieur is in het nauwkeurig beschrijven van geavanceerde afbeeldingssystemen. Feitelijk wordt het construeren van een afbeelding door een optisch systeem nauwkeurig beschreven door de diffractie-integraal. Echter, tot voor kort kon deze integraal alleen numeriek worden geëvalueerd. Dit veranderde in 2002 met de introductie van de Extended Nijboer-Zernike (ENZ) theorie. Deze theorie, die uitgebreid wordt beschreven in dit proefschrift, verschaft een algemeen geldige analytische oplossing voor de diffractie-integraal. Door gebruik te maken van dit resultaat, hebben wij een afbeeldingsmodel geconstrueerd dat alle relevante optische effecten in rekening brengt en ook nog eens gebruik maakt van zeer weinig benaderingen. De resulterende ENZ afbeeldingsmethode, zoals gepresenteerd in dit proefschrift, is dan ook zeer geschikt voor het beschrijven van zeer geavanceerde optische afbeeldingssystemen.

De tweede belangrijke bijdrage van dit proefschrift is een methode om de kwaliteit van een optisch systeem te bepalen. We laten zien dat het mogelijk is om de aberratiefunctie van een optisch systeem te reconstrueren door middel van analyse van zijn puntbronafbeelding. Deze methode is gebaseerd op de analytische uitdrukking voor de afbeelding van een puntbron die volgt uit de ENZ theorie. Door deze uitdrukking gelijk te stellen aan een experimenteel gemeten afbeelding, is het mogelijk om de aberratiefunctie, of optische kwaliteit, te bepalen zonder dat daar een complexe meetopstelling voor nodig is.

Alles bij elkaar geeft dit proefschrift een zeer uitgebreide beschrijving van de ENZ afbeeldingsmethode die het mogelijk maakt om de afbeeldingsfunctionaliteit van een grote verscheidenheid aan optische systemen nauwkeurig te simuleren. Hierbij is de hoge nauwkeurigheid van de ENZ afbeeldingsmethode de belangrijkste eigenschap, die volgt uit de analytische ENZ oplossing voor de diffractie-integraal en de beperkte toepassing van benaderingen. Verder wordt er een methode geïntroduceerd die de kwaliteit van een optisch systeem zeer nauwkeurig kan bepalen aan de hand van intensiteitsmetingen in de afbeeldingsruimte. Dit verschaft een aantrekkelijk alternatief voor de interferometrische methoden die gebruikelijk worden toegepast om de optische kwaliteit van een systeem te bepalen. Tenslotte bevat dit proefschrift een aantal voorbeelden waarin deze beide toepassingen centraal staan. Dit illustreert het grote potentieel, en vooral ook de verscheidenheid aan toepassingsmogelijkheden, van de ENZ theorie op het gebied van geavanceerde optische systemen.

Sven van Haver, Delft, november 2009.

Contents

Chapter 1

Introduction

Figure 1.1: *The Nimrud lens, found at an archaeological excavation at Nimrud's palace in the 19th century [1]. It is a piece of carved rock crystal that is believed to be the first known evidence of man using lenses to enhance its own perception.*

Evidence of man using optical components to enhance its own perception date back to well before the Christian era. Archaeological finds have indicated that as early as 700 BC pieces of polished crystal were used as rudimentary lenses by the Assyrians living in Mesopotamia (see Figure 1.1). Knowing this, it might come as an surprise that, although the understanding of light and the quality of optical components was largely advanced in the following centuries, it lasted until the end of the 16 th century before the first optical systems emerged that consisted of several optical components. Dutch and Italian lens makers were the first to find that, by combining several lenses, far more interesting optical properties could be obtained and this resulted in the construction of the first optical microscopes and telescopes. These inventions gave a big boost to science as it was now possible to study objects that before were either too small or too far away to be resolved. Ever since, optical systems have been of large interest to the scientific community both as a research topic as well as common tools to assist other fields of research. Nevertheless it would last until the 20th century until somewhat advanced optical systems were introduced into the daily lives of people.

1.1 Advanced optical systems

In present-day society, we encounter optical systems on a daily basis. Most people have a DVD player capable of playing content stored on an optical disc, Big Brother is watching us nearly everywhere using surveillance cameras and we consider it to be normal to take photographs with our mobile phone. Also, in less visible areas, such as ultrafast fiber-based data transfer, we rely on optical technology. Although these applications might be considered advanced by the general public, they mostly do not reflect the state of perfection that is currently needed by the scientific and high-tech community. When we speak of advanced optical systems in this context we refer to highly corrected optical systems or optical systems having extreme optical properties.

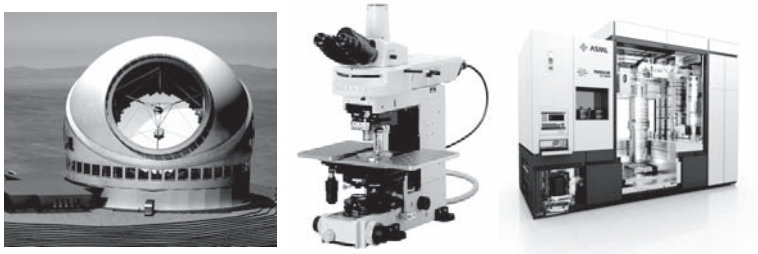

Figure 1.2: *Examples of advanced optical systems. From left to right: a proposed* 30 m *primary mirror earth-based telescope, an immersion microscope and a lithographic wafer stepper for the semiconductor industry. Images are taken from [2–4].*

For example, in astronomy, advanced optical systems are used as telescopes to look deep into space (see Figure 1.2). As one looks further into the universe, the astronomical objects become fainter and smaller in angular size. In order to still resolve these objects, image deterioration introduced by aberrations present in the optical system should be smaller then the object studied and this imposes extreme specifications on the optical components used. Furthermore the faintness of astronomical objects makes it a big challenge to collect a sufficient number of photons on the detector so that an image can be formed. The number of photons is largely determined by the size of the primary mirror of the telescope and this makes enlarging this mirror the primary approach of increasing the sensitivity. The most advanced telescopes in operation today have mirror diameters as large as 10 m and studies are being done to build telescopes having mirrors as large as 50 m in diameter [5]. However, producing mirrors of this magnitude, with a required accuracy that is far better then diffraction-limited, is an extreme technological challenge.

Another optical field in which high quality optics are essential is microscopy. In microscopy one tries to image the smallest possible detail by generating an enlarged image of the object using a collection of lenses. The largest feasible magnification, using a so-called compound microscope (see Figure 1.2), is of the

order of 2500×. To reach such large magnification values, methods such as oil immersion should be applied, maintaining extreme imaging quality.

By far the most cutting edge optical technology is applied in the semiconductor industry. A process called optical lithography is used to transfer geometrical patterns (mask objects), that are part of a chip design, into a layer of photosensitive material (resist) that is deposited on top of a piece of silicon (wafer). Using chemical technology these patterns are developed into metallic and insulating features and, repeating lithographic pattern transfer and chemical development several times in succession, it is possible to produce in this way a working electronic circuit. In this sense optical lithography is very similar to the development of a photograph from a negative produced with an analog camera. The main difference is that in optical lithography one produces a copy of the mask object that is four times reduced in size whereas in photography the image is generally enlarged. The scientific challenge in optical lithography is to print the smallest possible details onto the silicon wafer as this will generally result in the fastest chips and allows for the integration of more applications onto a single chip. Currently the lithographic industry is producing chips having feature sizes of the order of 32 nm using light with a wavelength of 193 nm. This means that details are imaged that are six times smaller than the wavelength. This by itself is already an amazing achievement, but add up the fact that in order to be economically viable both the throughput and reproducibility of these systems should be really high, and one can understand that lithographic wafer steppers are truly amazing machines reflecting the most advanced state-of-the-art in optical system design, manufacture and modeling (a wafer stepper is depicted in Figure 1.2).

1.2 Design and analysis of optical systems

In the early days of optical system design the discovery of a good optical system was largely a matter of trial and error. This gradually changed in the 19 th century with the introduction of various optical models that enabled a mathematical description and analysis of optical system designs. By far the most applied model for this purpose is geometrical optics, in which light traveling through an optical system is represented by rays. Even though physical optics models, that correctly incorporate the wave nature of light, are available since the mid 19 th century, their application remained very limited due to the lack of sufficient computational power to apply them. Even today, geometrical optics remains a powerful tool that is still widely used in optical system design. Only in the case that diffraction effects are significant and the use of a physical optics model is indispensable, we apply powerful computers to perform the computationally expensive analysis of optical systems using wave optics.

Nowadays all advanced optical systems are designed according to advanced optical models and thoroughly tested in simulation before they are actually built. The main advantage of this is, of course, that it is much faster and cheaper than a trial and error based approach. One should keep in mind though that a model based design approach will only be successful if the applied model is an accurate representation of the actual system. The same holds for the accuracy of simulations

in which, for example, the resist image produced by a lithographic wafer stepper is computed. In recent years, there has been a large renewed interest in these optical models that are used to describe advanced optical systems. This is because questions have been raised whether or not the established models remain applicable to the advanced applications of today, in which subwavelength features are imaged and even the smallest design and simulation errors have disastrous implications. Indeed, we believe that some assumptions and approximations commonly applied in optical modeling are questionable for this class of systems. The main response of the optical community to overcome the issues related to this, has been application-specific corrections afterwards applied to the inaccurate simulation results. This is no surprise as the actual optical models are often hidden deep somewhere in a software package used to perform the optical simulation task. Nonetheless, it would be favorable to correct simulation errors at the source by removing applied approximations or by constructing new methods in which these approximations are not used. In this thesis, we will follow the latter approach and introduce a new optical model, the so-called Extended Nijboer-Zernike (ENZ) theory, with the intention to apply it with as few approximations as possible and construct a modeling framework capable of treating present and future advanced optical systems.

This new model also allows us to deal with another important issue related to high quality optical systems, namely, that a measurement approach is required that can actually determine this quality. Traditionally, optical metrology techniques are applied for this purpose, but this technique has the downside that it requires a complex optical setup and that it can generally not be applied in situ. It would be ideal to have a method that can determine the quality of an optical system to a high enough accuracy, solely based on intensity measurements in the focal region. In fact, we will show in this thesis that this is indeed feasible by applying the ENZ theory.

1.3 The Extended Nijboer-Zernike (ENZ) theory

The Extended Nijboer-Zernike theory of diffraction has been introduced in 2002 as an extension of the Nijboer-Zernike diffraction theory. The theory basically provides a semi-analytic solution to the Debye diffraction integral, which is an integral relation between the field distribution in the exit pupil of an optical system and its corresponding field distribution in the focal region. In other words, having available the electric field in the exit pupil of an optical imaging system, the Debye integral can be used to compute the image that will be produced from it. Before the introduction of the ENZ theory, this integral, which was already introduced by Debye (see Figure 1.3) in 1909 [6], could only be evaluated numerically. The solution provided by the ENZ theory is based on an expansion of the pupil distribution in terms of Zernike circle polynomials named after the Dutch physicist Zernike (see Figure 1.3). Janssen proved in his 2002 publication [7] that every Zernike polynomial used in the expansion of the pupil gives rise to a fixed contribution to the field in image space and that this contribution can be written as a power-Bessel series. In the accompanying paper [8] by Braat, Janssen and

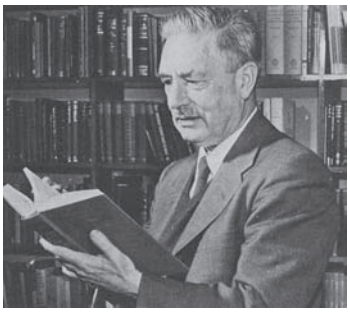


Figure 1.3: *Peter Debye and Frits Zernike, both Nobel laureates for chemistry* (1936) *and physics* (1953)*, respectively, made essential theoretical contributions to enable the development of the ENZ theory. Images are taken from [10, 11].*

Dirksen, it was subsequently shown that, based on the former results, the point-spread function (PSF) of a generally aberrated optical systems can be computed. These results were initially limited to point-sources at infinity imaged by scalar optical systems having a low numerical aperture (NA). The extension to imaging of a point-object by a high-NA optical system, including vector analysis, was given soon after these first two papers [9]. We will show in this thesis that recent developments of the ENZ theory, now allow us to image more general objects using optical systems of high NA requiring a full vectorial imaging analysis.

As already mentioned before, the ENZ theory also provides interesting possibilities with respect to the characterization of an optical system. Because of the semi-analytic relation between the pupil and the focal region it is, in principle, also possible to reconstruct the pupil from a given distribution in image space. One should keep in mind that, as we have in general only access to the intensity in image space, the reconstruction of the field distribution in the pupil from this intensity data is a non-linear operation. Nonetheless, it was already shown in [12–14] that this approach is feasible for scalar systems and we will show in this thesis that it can be generalized to optical systems requiring a vectorial treatment.

1.4 Scope of the thesis

As already mentioned in the title, this thesis treats the Extended Nijboer-Zernike (ENZ) diffraction theory and its applications. In Chapter 2, we will first expand on computational imaging theory in general. This will provide us with an overview of the various computational imaging approaches available and enables us to devise an alternative computational imaging method in which the ENZ diffraction theory can be efficiently applied. Additionally, this chapter will also include a treatment of extended illumination sources and the possible presence of a layered configuration in image space. Such a layered configuration, which can have a significant influence on the image, is for example encountered in lithography where an image is formed in a thin layer of photoresist deposited on top of a substrate. Finally, this chapter will discuss the PSF in general and its role in determining the optical system

quality according to the Strehl ratio.

Chapter 3 is fully dedicated to the formulation of the ENZ theory. Starting from the initial results by Zernike and Nijboer, we present both the scalar and vectorial versions of the ENZ theory. In Section 3.4 of this chapter, the ENZ theory is applied in an imaging scheme to allow image computations of extended objects. Furthermore, ENZ-based imaging in a stratified focal region is discussed in Section 3.5. Another interesting extension of the ENZ formalism is presented in Section 3.6. There, it is shown that optical systems with a variable NA or an annularly shaped pupil can also be efficiently described using the ENZ formalism. The final subject treated in this chapter is an ENZ-based description of electromagnetic quantities in the focal region. As the vectorial ENZ theory provides expressions for both the electric and magnetic field in focus, it is also possible to express electromagnetic quantities like the Poynting vector and optical momentum in terms of the basic ENZ results.

After a thorough discussion of the ENZ capabilities to compute the field in image space, we focus in Chapter 4 on the inverse problem. First we will show that the intensity in the focal region can be written in terms of the ENZ basic functions. Subsequently, this expression is used to construct a linear system of equations that, upon solving, yields the Zernike coefficients describing the optical system under consideration. Again we will show that this approach is applicable to both high- and low-NA systems. The standard ENZ aberration retrieval scheme is limited to rather small aberrations. However, in Section 4.3, it will be shown that the range of aberration magnitudes for which the ENZ inversion scheme yields accurate results can be largely extended by applying a so-called predictor-corrector procedure. Further extensions presented in this chapter include a framework to analyze birefringence present in an optical systems and the possibility to do aberration retrieval for optical systems that are strictly speaking outside the Debye regime. Finally, this chapter also provides an ENZ-based analysis of the Strehl ratio in Section 4.6, with extra attention to the non-trivial definition of Strehl ratio at high NA.

In Chapter 5 we have reached the point that we can apply the ENZ theory in a variety of applications. The first section deals with the computation of the PSF for general optical systems. In the next section, we apply the ENZ theory to visualize and study electromagnetic quantities in a focal spot. Sections 5.3 and 5.4 deal with the extended imaging capabilities of the ENZ formalism both in uniform as well as in stratified space and, finally, in Section 5.5, the ENZ inversion scheme is applied to characterize optical systems based on their through-focus intensity distribution.

The thesis is concluded in Chapter 6 with a summary of the main results and some discussion of the ENZ theory in relation to other methods. Here we will also stress the advantages of the ENZ approach, expand on the applications that we think could benefit from the ENZ theory and finally provide recommendations for further research.

The results on the ENZ theory presented in this thesis are largely obtained by a small group of researchers working at the Delft University of Technology and at Philips Research in Eindhoven. The development of the ENZ theory was initiated

in 2002 by A.J.E.M Janssen, J.J.M Braat and P. Dirksen and they were somewhat later joined by A.S van de Nes. In those early years their work was mainly focused on the scalar and vectorial ENZ theory and its application in aberration retrieval of low-NA optical systems (Sections 3.2, 3.3 and 4.1). As of 2005, the current author of this thesis, started to work on the subject. Although most ENZ developments are to be considered a team effort, his main contributions can be found in the generalization of ENZ theory to enable aberration retrieval of high-NA optical systems (Section 4.2), the construction of an ENZ-based imaging model and method (Sections 2.2 and 3.4), the development of ENZ theory for stratified image regions (Section 3.5), the improved version of the predictor-corrector procedure given in Section 4.3 and all the implementation and accuracy analysis of ENZ-based simulation tools that were used to generate the examples presented in Chapter 5.

Chapter 2

Computational imaging theory

Up until the 1950's the majority of optical imaging systems has been designed and analyzed in the context of geometrical optics. Although in this model the wave nature of light is not taken into account and light is represented as just a collection of rays, it was sufficient to describe imaging by most optical systems that were available at that time. However, present day optical imaging systems are often designed to image complex features in the order of the wavelength and in this regime light diffraction effects occurring at the aperture edges of the optical system can no longer be neglected. To account for these diffraction effects the geometrical optics model should be supplemented by a physical optics model in which the wave nature of light has been correctly incorporated.

When an imaging model is constructed based on wave optics, a choice should be made whether the model operates in the spatial or in the frequency domain. Frequency domain methods determine the plane-wave angular spectrum coming from the object after which imaging is done by applying a low-pass filter and summing all remaining plane wave contributions coherently. The first frequency based methods originate from the Abbe microscope imaging theory. This model, introduced in 1873, describes coherent image formation of elementary periodic structures. Using the basic principles introduced by Abbe, the frequency approach was further developed in the 1940-1950's, with important contributions by Hopkins including the incorporation of general periodic objects, aberrations of the imaging system and a finite extent of the illumination source. This resulted in the so-called Hopkins imaging model which was the first widely used imaging method based on wave optics that presented a complete alternative to geometrical optics.

Alternatively, one can also devise an imaging model based on wave optics that operates in the spatial domain. In this case, the image is constructed by a convolution of the object function with the point response function of the imaging system. The impulse response function or point-spread function (PSF) used by this model is obtained through evaluation of a diffraction integral. However, until recently, general analytic solutions of such a diffraction integral were not available

and, therefore, the convolution method had to rely on numerical integration. As a result this method was never as widely used as the Hopkins method.

All imaging models discussed so far assume light to be a scalar quantity. However, for optical imaging systems operating at a high numerical aperture (NA), vector effects become significant. To accurately describe imaging by these systems one should include the state of polarization in the formalism and apply vector diffraction theory. This will result in advanced versions of the models introduced above. In addition to this we have recently introduced an alternative advanced imaging model that is based on the vectorial version of the Extended Nijboer-Zernike (ENZ) diffraction theory. This model, which will be thoroughly discussed in this thesis, exploits a semi-analytic solution of the Debye diffraction integral provided by ENZ theory.

The remainder of this chapter is organized as follows. In Section 2.1 the imaging models briefly introduced above are discussed in somewhat more detail. This is followed in Section 2.2 by the introduction and detailed description of a new imaging model based on the ENZ theory. In Sections 2.3 and 2.4 we discuss the complications that arise when light sources of finite extent are considered and when image space is not uniform but consists of several layers with different optical properties. Then, in Section 2.5, we will give some extra attention to the special object formed by a point-source in the object plane as these objects will play an important role in the remainder of this thesis.

2.1 Imaging models

For the optical systems considered in this thesis, all optical phenomena can, in principle, be described using Maxwell's equations. However, directly applying Maxwell's equations is cumbersome and often unnecessary. In many cases, the optical processes at hand can be efficiently described using simplified models. In this section, we present the simplified models that play an important role in describing optical imaging.

2.1.1 Geometrical optics

In the geometrical optics or ray optics description of light propagation, the finiteness of the light's wavelength is neglected. In this case a model can be constructed in which the energy transport is approximated by a "ray" that in each point of space is perpendicular to the light's wavefront. Rays travelling in a uniform medium follow a straight line and, whenever a medium transition is encountered, their direction is changed according to Snell's law of refraction. These concepts give rise to a set of geometrical rules that describe light propagation through an optical system. This geometrical optics model provides a significant simplification of light propagation and, although it fails to account for optical effects such as diffraction and polarization, it works very well in many circumstances.

In the upper part of Figure 2.1 a schematic representation of "perfect" imaging in terms of geometrical optics is given. Light rays coming from a single object point are captured by the optical system and subsequently refracted so that they are

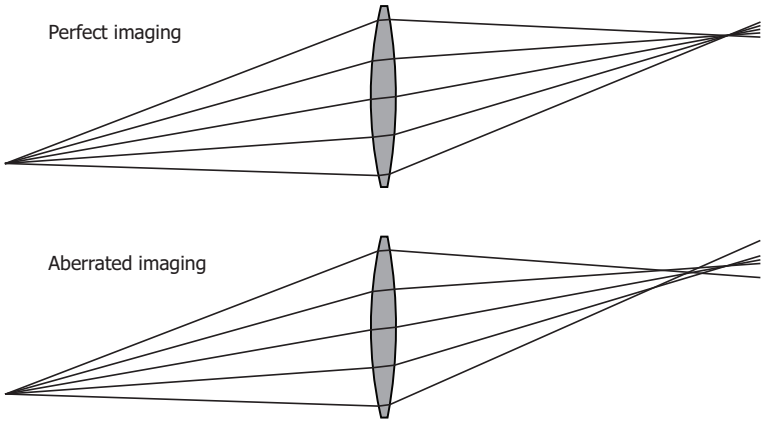

Figure 2.1: *Upper part: schematic representation of perfect imaging using the geometrical optics model. Lower part: imaging in the presence of aberrations.*

recombined in a single point in image space. For a non-ideal, or aberrated system, this is no longer the case. For example, if an optical imaging system suffers from off-axis aberration, it will no longer produce an image point but a spot instead (see lower part of Figure 2.1).

The relatively simple geometrical formulation provided by ray optics has been, and still is, of great importance to the optical community. Especially before the introduction of the computer, the geometrical optics model was the only model capable of providing a systematic analysis of general optical systems. Using the principles of geometrical optics it became possible to design and optimize optical systems in a structured manner. This included the analytical treatment of lens system aberration which had become available through a contribution by Seidel in 1856 [15].

2.1.2 Abbe coherent imaging theory

One of the optical fields in which the ray representation of light is insufficient is microscopy. Before 1866, when Carl Zeiss and Ernst Abbe started their collaboration to devise a microscope imaging theory, microscopes, and the microscope objectives in particular, had been made by trial and error. Although this had resulted in some microscopes with outstanding optical performance, others had less desirable features. Carl Zeiss had been the first to realize that a sound theoretical basis was needed to design microscope systems with consistent performance. He therefore initiated and financed research by Ernst Abbe to devise a microscope imaging theory. Ernst Abbe started out with a geometrical analysis of the problem, but he soon found that this did not lead to satisfactory results. The major breakthrough came in 1873 when Abbe proposed the theory of microscope image formation [16, 17].

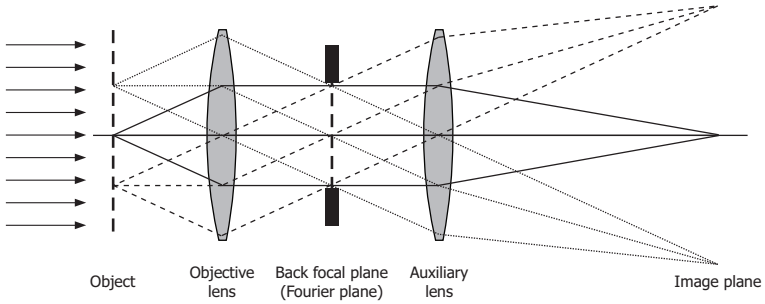

Figure 2.2: *Schematic representation of the Abbe imaging model. Coherent light illuminates a grating-like object. A diffraction image is produced by the objective lens in the back focal, or Fourier, plane. The resolution of the image produced by the auxiliary lens is then determined by the number of diffraction orders accepted by the aperture in the back focal plane.*

The Abbe imaging model, which is schematically depicted in Figure 2.2, assumes that a coherent source illuminates a grating-like structure. This will give rise to diffraction orders that can be observed in the back focal plane of the objective. After countless calculations and experiments, Abbe had realized that it is this diffraction image in the back focal plane of the objective that is decisive for image formation. The resolution of the image is determined by the number of diffraction orders accepted by the objective aperture in the back focal plane. In this way, Abbe was the first to include wave optical phenomena in the description, design and analysis of optical imaging systems.

2.1.3 Hopkins partially coherent imaging theory

Although, the model introduced by Abbe forms the basis of all frequency domain or Fourier based imaging models, its original formulation was of very little practical value to the optical community. This was due to its stringent requirements on both the object, which should be a grating, and the assumed purely coherent illumination. It wasn't until the 1940's that the Fourier based method would be further developed up to a point that it could be applied to general imaging problems. Important contributions were made by Duffieux [18], Maréchal [19] and Hopkins. The latter author, whose name is now commonly used to refer to imaging methods based on Fourier optics, made key contributions to allow imaging with an extended source (partially coherent illumination) [20], including a defocusing of the generally aberrated image [21].

The model that results, known as the Hopkins imaging model, is schematically presented in Fig 2.3. Light coming from a possibly extended source illuminates a periodic object and gives rise to an angular spectrum of diffracted light. Due to the limited extent of the pupil, only part of the spectrum is accepted by the optical system, effectively applying a low-pass filter on the spatial frequency content present in the object. What remains of the angular spectrum is then focused by the imaging lens, effectively applying an inverse Fourier transformation, to construct the image.

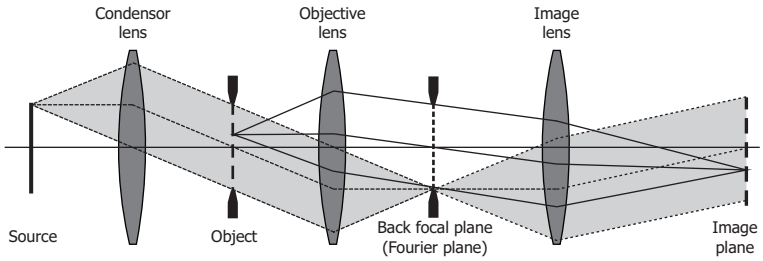

Figure 2.3: *Schematic representation of the Hopkins imaging model. The light originating from a single source-point is transformed into a coherent plane wave incident on the object. The incident illumination gives rise to scattered light coming from the object. The cone of scattered light that contributes to the formation of the image, is limited by the aperture in the back focal plane which, therefore, also determines the maximum obtainable resolution.*

The Hopkins approach has become very popular because of its possibility to employ the Fast Fourier Transform in numerical computations [22]. The fast image calculation does, however, require an inherent periodicity in the object. If this periodicity is not present, it can be artificially introduced by periodically repeating the specific part of the object that has to be imaged. In this case the continuous frequency spectrum of the object is replaced by a discrete comb-like spectrum which introduces certain artifacts in the final image.

2.1.4 Point-spread function (PSF) convolution

The alternative to frequency domain imaging is imaging according to the point-spread convolution method which, similar to geometrical optics, operates in the spatial domain [23]. This approach, schematically displayed in Figure 2.4, involves the calculation of a convolution between the field distribution at the object, that is generated by coherent illumination of the object, and the image of a point source. This basically means that every field point at the object is assumed to generate a PSF in image space, where its relative position, strength and phase are determined by the spatial position, amplitude and phase of this field point, respectively. In this case a coherent image of the object is obtained as a coherent summation over these PSF's. The complete image due to incoherent illumination then follows by repeatedly applying the step described above, for all incoherent points that constitute the light source, and incoherently sum their image contributions.

The method described above requires the point response or point-spread function (PSF) of the imaging system to be known. The first analytical result for the ideal PSF goes back to Airy [24]. Through-focus imaging with an ideal system has been studied by Lommel [25]. Refinements including the influence of aberrations have been studied by Strehl [26], Conrady [27, 28] and Picht [29, 30]. A systematic study of PSF formation in the presence of aberrations has been carried out by Zernike and Nijboer [31, 32], with the use of their circle polynomials on the circular exit pupil as the key contribution. Nevertheless, analytic results for the

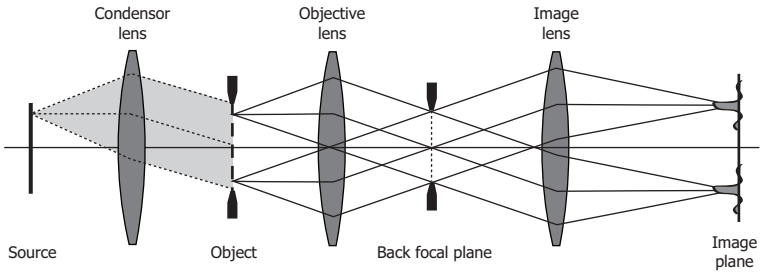

Figure 2.4: *Schematic representation of the point-spread function convolution imaging model. A single point of an incoherent light source gives rise to a coherent illumination of the object. This will generate a field distribution at the object with which a convolution with a point source is performed. The image, due to illumination by a single point in the light-source, is then obtained by coherent summation of all PSF's generated by the individual sample points of the field at the object, taking into account their relative strength and phase.*

PSF of a general system remained unavailable. This meant that the convolution method had to rely on numerical means to obtain the PSF and this, especially in the precomputer age, made the method relatively unattractive.

The quality of the image constructed using the methods described above both depends on the sampling density in the object plane and the accuracy of the PSF used. In general, a fairly dense sampling is required to achieve a reasonable accuracy and this again has a negative effect on the computational efficiency of this method. Altogether, even though the method provides all the desired capabilities and features, it was never as widely used or studied as the Hopkins method as it was generally considered to be too slow in practice to do imaging of general objects.

2.1.5 Advanced imaging models

The models discussed so far are all based on a scalar description of light. Although these models neglect the vectorial nature of light, they are sufficient to describe most imaging phenomena that occur in optical systems operating at a low to modest value for the numerical aperture (NA < 0.60). However, for an accurate description of optical systems that operate at a NA exceeding 0.60, more advanced imaging models are necessary because for these systems vectorial effects such as polarization become important in the formation of the image. For both the Hopkins as well as the PSF convolution method extensions have been devised to include these vector effects. For the Hopkins method the main contributions to include the vector effects were made by made by Flagello [33] and Sheppard [34] and a nice overview on the current state-of-the-art for this method can be found in [35].

To include vector effects in the convolution method one should replace the scalar PSF with its vectorial counterpart. The calculation of the point-spread function at high numerical aperture was initiated by Ignatowsky [36] and fur-

ther developed by Hopkins [37], Wolf [38] and Richards [39]. In the latter two publications, the high-numerical-aperture point-spread function through-focus is presented using a numerical evaluation of the vectorial Debye diffraction integral. This approach has become the standard one to treat point-spread function calculation using so-called vector diffraction.

Instead of the numerical evaluation of a diffraction integral, special functions have been proposed to represent the wave field in the exit pupil that yield a direct analytic solution in the image region, as, for example, Gauss-Laguerre modal expansions [40], multipole functions [41], radial prolate spheroidal functions [42], spherical harmonics [43] and Walsh functions [44]. Most of the special functions quoted above suffer from the fact that they cannot easily cope with the sharp edge that is encountered in optical diffraction problems, namely the circular hard diaphragm that sharply limits the lateral extent of the imaging bundles in an optical system. Only recently, an extension of the method for high-numerical-aperture point-spread calculation according to [38] has become available that deals with this hard aperture efficiently. This method, known as the Extended Nijboer-Zernike (ENZ) theory, provides the user with semi-analytic expressions for the through-focus aberrated point-spread function in both the low-aperture scalar diffraction case [7], [8] and for the vector diffraction case [9]. Although the calculation of the point-spread function is drastically accelerated by the availability of an accurate semi-analytic series expansion instead of a diffraction integral to be numerically evaluated, the direct application of this new tool for convolution calculations to obtain complete images is still too slow in practice. However, in a recent paper, [45], we have proposed an alternative imaging model based on the ENZ theory, that exploits its appealing features in such a way that efficient image calculations are feasible. This novel imaging model is the main topic of the next section.

2.2 Extended Nijboer-Zernike imaging model

The computationally expensive step in the PSF convolution method consists of the convolution of the PSF with the object. Here, we propose a novel method that avoids this step, but still exploits the appealing features of ENZ-based PSF computations. Although the ENZ theory has been developed to compute PSF's of aberrated systems in a systematic way and in doing so enabled the reconstruction of the aberration function from PSF measurements, it is in principle not limited to PSF computations. In fact, ENZ theory provides a means to compute the resulting image from a given exit pupil distribution and this feature is not limited to distributions close to unity that are connected to a PSF. As a result, an arbitrary distribution in the exit pupil, generated by some general object, can be equally well treated using the ENZ formalism as a highly non-uniform exit pupil that originates from heavy aberrations. Recognizing this, we have set out to devise a both accurate and efficient imaging method based on the ENZ theory.

This new method, which we will be referring to as the ENZ imaging model, is schematically depicted in Figure 2.5. It involves the computation of the electric field in the entrance pupil that originates from the coherent illumination of the object. Assuming that the optical system satisfies the Abbe sine condition very

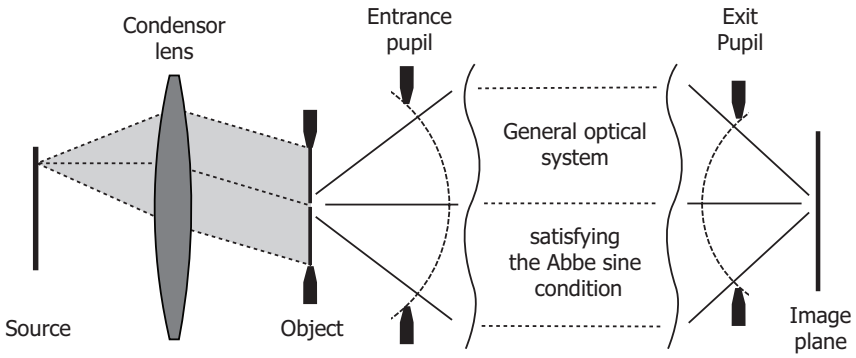

Figure 2.5: *Schematic representation of the ENZ imaging model. A single point in an extended incoherent source gives rise to coherent illumination of the object. Interaction with the object will generate an arbitrary field distribution on the spherical wavefront in the entrance pupil. Next, the field in the entrance pupil is transported to the exit pupil taking into account the transmission function of the optical system. Finally the field in the exit pupil is evaluated using the ENZ theory to generate the image due to a single point of the illumination source.*

well, one can directly obtain the resulting field in the exit pupil, including possible deformations introduced by the optical system. The fields in the exit pupil and in the focal region are related through the Debye-Wolf integrals. In principle, the image can then be obtained by numerical evaluation of this integral using the exit pupil distribution as the input. Of course, such a numerical approach is also far from efficient. However, since it was shown in [45] that the ENZ theory can be applied to efficiently compute images for a given exit pupil, it has become feasible to do efficient general imaging based on the model introduced above.

Before the ENZ theory itself is presented in Chapter 3, we will discuss in this section the theoretical foundations on which the ENZ imaging scheme is based. We will discuss in detail how to accurately obtain the exit pupil distribution of a general optical system using as few approximations as possible. Then, by applying diffraction theory we will obtain an integral relation between the field in the entrance pupil and its corresponding image region. The actual evaluation of these integrals is presented in Chapter 3.

2.2.1 Entrance pupil distribution

Outside the paraxial optics regime, we are interested in the diffraction effects caused by the presence of the sharp diaphragm rim. For reasons of simplicity, we suppose that the diffraction at the diaphragm in the interior of the optical system can still be analyzed using the paraxial concept of entrance and exit pupil. To this aim, we analyze the incident wavefront in object space that intersects the optical axis at the location of the paraxial entrance pupil. Suppose that we have an object being illuminated by a plane wave. At the position of the object, interaction will take place between the incident plane wave and the object, giving rise to scattered

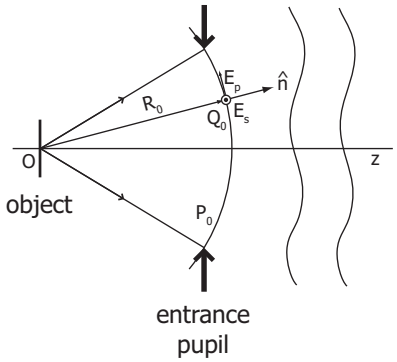

Figure 2.6: *Schematic representation of the geometry under consideration. O is the origin, R_0 is the radius of the entrance pupil sphere P_0, $\hat{n}$ is the normal to the pupil surface and Q_0 is a general point in the entrance pupil where we locally define the orthogonal linear p- and s-polarization states.*

and diffracted light propagating away from the object. Part of this light will be captured by the entrance pupil of the optical system and refocused to construct an image.

Now let us consider an optical system for which the distance, R_0, between the object and the entrance pupil of the optical system, is much larger than the transverse dimensions of the object being imaged. In this case, one can consider the electric field vector, in the point Q on the spherical surface P_0, to be perpendicular to the normal, $\hat{n}$, of this spherical surface. However, it is common for the radius of the entrance pupil to be of the same order of magnitude as R_0, and therefore the entrance pupil can not be considered a flat surface, but is a spherical surface, P_0, with its origin at O (see Figure 2.6). In order to compute an image according to the ENZ imaging model the electric field on the surface P_0 should be known. This field can be obtained in many different ways, for example, using efficient approximate models such as Kirchoff diffraction. However, we will treat this problem using rigorous electromagnetic solvers to ensure that we can always reach the highest possible accuracy. Nevertheless, direct rigorous computation of the field in the entrance pupil is almost never possible due to the simple fact that the computational domain should then include both the object and the pupil at the same time. For almost all practical systems this would impose far too large memory requirements and computation times. In fact, the problem is often split in two, where one first rigorously computes the near field at the object (this is a common problem that can be easily solved with a variety of electromagnetic solvers), and subsequently propagates the radiative components of this field towards the entrance pupil. In principle, the second step could be performed using a Fourier transformation of the field in a plane close to the object and perpendicular to the optical axis. However, for this approach to be accurate, a fairly large surface should be available on which the field is known. This means that also the computational domain for which the near-field is determined should be large and this of course has its computational implications especially when a relatively small

isolated object is considered. An alternative option is to use the Stratton-Chu formulation [46], which relates the field anywhere to the field on the boundaries of a domain enclosing the object. The advantage of this approach is that for small objects it is sufficient to obtain the field in a small computational domain, while the field outside this domain can still be determined with a high accuracy.

2.2.2 Field transfer from entrance to exit pupil

Assuming that we have available the Cartesian field components on the entrance pupil sphere, we describe in this section the transfer of the entrance pupil field to the resulting field distribution in the exit pupil. We suppose that the resulting wavefront in the exit pupil is related to the wavefront in the entrance pupil in the following way:

(a) its average curvature is given by the distance from exit pupil to image plane to assure focusing in the paraxial image plane

(b) its deviation from sphericity is given by the initial deviation in the entrance pupil plus all possible deviations caused by the aberrations of the optical system (and by birefringence effects if these are important)

(c) its amplitude distribution is given by that in the entrance pupil plus the deviations introduced by the optical system (in our case determined by the Abbe sine condition).

We now take a general point $Q_0(\rho, \theta)$ on the entrance pupil sphere P_0, where ρ and θ are polar coordinates with ρ normalized with respect to the lateral half diameter of the entrance pupil. In a very good approximation, the electric field vector of the light arriving at a point $Q_0(\rho, \theta)$ will be perpendicular to the normal $\hat{n}$ of the spherical surface and it is thus possible to locally represent the field at Q_0 by a linear combination of two orthogonal polarization states perpendicular to $\hat{n}$. Here, we will adhere to s- (perpendicular) and p- (parallel) states of linear polarization as they can be conveniently mapped between the entrance and exit pupil of an aplanatic imaging system. In our case, this mapping is uniquely defined as we are considering optical systems that satisfy the Abbe sine condition very well.

We now introduce a new coordinate base in $Q_0(\rho, \theta)$ according to

$$\hat{\mathbf{k}}_\mathbf{0} = \sin\alpha_0 \cos\theta\, \hat{\mathbf{x}} + \sin\alpha_0 \sin\theta\, \hat{\mathbf{y}} + \cos\alpha_0\, \hat{\mathbf{z}}, \tag{2.1}$$

$$\hat{\mathbf{p}}_\mathbf{0} = \cos\alpha_0 \cos\theta\, \hat{\mathbf{x}} + \cos\alpha_0 \sin\theta\, \hat{\mathbf{y}} - \sin\alpha_0\, \hat{\mathbf{z}}, \tag{2.2}$$

$$\hat{\mathbf{s}}_\mathbf{0} = -\sin\theta\, \hat{\mathbf{x}} + \cos\theta\, \hat{\mathbf{y}}, \tag{2.3}$$

where $\alpha_0 = \arcsin(\frac{\rho}{R_0})$ and the right-handed unit vector bases $(\hat{\mathbf{p}}_\mathbf{0}, \hat{\mathbf{s}}_\mathbf{0}, \hat{\mathbf{k}}_\mathbf{0})$ and $(\hat{\mathbf{x}}, \hat{\mathbf{y}}, \hat{\mathbf{z}})$ are depicted in Figure 2.7. We suppose that we have available the Cartesian electric field components at a general point Q_0, for example, by means of rigorous electromagnetic computation. From the components E_x and E_y, we can find E_z by applying the orthogonality of field components with respect to the propagation unit vector $\hat{\mathbf{k}}_\mathbf{0}$ yielding

$$E_{0,z} = -(E_{0,x}\cos\theta + E_{0,y}\sin\theta)\tan\alpha_0. \tag{2.4}$$

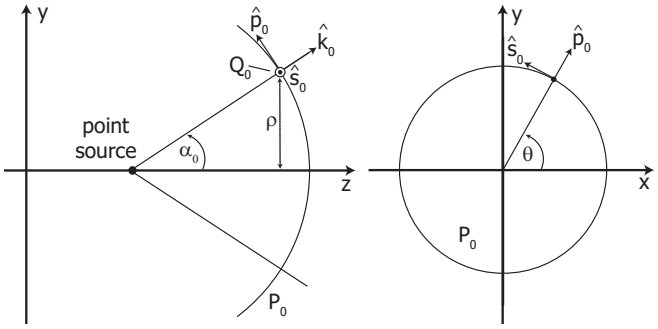

Figure 2.7: *Definition of the local coordinate basis for a general point Q_0 on the entrance pupil sphere with an axial cross-section (left-hand graph) and a cross-section perpendicular to the z-axis, viewed in the negative z-direction (right-hand graph).*

The field components on the new basis are then given by

$$E_{0,p}(\rho,\theta) = \mathbf{E_0}(\rho,\theta)\cdot\hat{\mathbf{p}}_\mathbf{0} = \frac{E_{0,x}\cos\theta + E_{0,y}\sin\theta}{\cos\alpha_0}, \tag{2.5}$$

$$E_{0,s}(\rho,\theta) = \mathbf{E_0}(\rho,\theta)\cdot\hat{\mathbf{s}}_\mathbf{0} = -E_{0,x}\sin\theta + E_{0,y}\cos\theta. \tag{2.6}$$

Note that the component in the direction of $\hat{\mathbf{k}}$, $E_{0,k}$, is by definition equal to zero. Next, we have to relate the field at a general point Q_1 in the exit pupil to the incident field in the corresponding point Q_0 on the entrance pupil sphere P_0. The field in the entrance pupil equals the far-field produced by diffraction of the incident field at the object. For the transition of the far-field from the entrance pupil to the exit pupil, we need to consider the energy transport between the pupil surfaces. The basic relationship between the energy flow through the entrance and the exit pupil follows from paraxial optics. It provides us with the ratio between elementary areas on the pupil surfaces by means of the square of the paraxial magnification. The exact mapping of an elementary surface area from entrance to exit pupil outside the paraxial domain needs an extra condition; in our case, for large-field imaging systems, the Abbe sine condition has to be satisfied. Following the arguments in [33] and allowing for different refractive indices n_0 and n_1 in object and image space, we have the following relationship between the energy flow through corresponding areas in entrance and exit pupil (in the absence of absorption, reflection and scattering)

$$\epsilon v|E|^2 dS = \text{constant}\ , \quad \text{or,} \quad n_0|E_0|^2 dS_0 = n_1|E_1|^2 dS_1\ , \tag{2.7}$$

where $\epsilon = n^2$ is the relative electric permittivity of the medium, $v = c/n$ is the propagation velocity and dS_0 and dS_1 are the corresponding flow cross-sections on the pupil surfaces. Denoting the distances of entrance and exit pupil from the object and image plane by R_0 and R_1, respectively, and using the expression for the elementary solid angles in object and image space, we find

$$n_0 R_0^2 \frac{dk_{x,0}dk_{y,0}}{k_0 k_{z,0}}\ |E_0|^2 = n_1 R_1^2 \frac{dk_{x,1}dk_{y,1}}{k_1 k_{z,1}}\ |E_1|^2, \tag{2.8}$$

with $k_{x,i}$, $k_{y,i}$ and $k_{z,i}$ being the wave vector components in the object and image space.

Denoting the paraxial magnification by M and writing the Abbe sine-condition according to

$$k_{x,0} = Mk_{x,1}, \qquad k_{y,0} = Mk_{y,1}. \tag{2.9}$$

we obtain, by using $k_0/n_0 = k_1/n_1$

$$\begin{aligned} |E_1| &= \left(\frac{MR_0}{R_1}\right) \sqrt{\frac{n_1}{n_0}} \sqrt{\frac{k_{z,1}}{k_1}\frac{k_0}{k_{z,0}}}\, |E_0| \\ &= \left(\frac{MR_0}{R_1}\right) \sqrt{\frac{n_1}{n_0}}\, \frac{(1-s_0^2\rho^2)^{1/4}}{(1-\frac{n_1^2}{n_0^2}M^2s_0^2\rho^2)^{1/4}}\, |E_0|, \end{aligned} \tag{2.10}$$

where $(1-s_0^2\rho^2)^{1/2}$ and $(1-\frac{n_1^2}{n_0^2}M^2s_0^2\rho^2)^{1/2}$ can be identified as $\cos(\alpha_1)$ and $\cos(\alpha_0)$, respectively, with α_1 the corresponding angle in image space and s_0 the image side geometrical aperture. Finally, we use the paraxial relation between pupil object and image distances $R_1/R_0 = (n_1/n_0)MM_p$ with M_p the pupil magnification and use Newton's paraxial imaging equation in putting $|M_p| = |R_p/f_1|$ with R_p being the distance from the image side focal point to the exit pupil and f_1 the image side focal distance. The field in the exit pupil is then given by

$$|E_1| = \left|\frac{f_1}{R_p}\right| \sqrt{\frac{n_0}{n_1}}\, \frac{(1-s_0^2\rho^2)^{1/4}}{(1-\frac{n_1^2}{n_0^2}M^2s_0^2\rho^2)^{1/4}}\, |E_0| = \left|\frac{f_1}{R_p}\right| \sqrt{\frac{n_0}{n_1}}\, T_R(\rho)|E_0|, \tag{2.11}$$

where the transmission factor

$$T_R(\rho) = \frac{(1-s_0^2\rho^2)^{1/4}}{(1-\frac{n_1^2}{n_0^2}M^2s_0^2\rho^2)^{1/4}} = \frac{\sqrt{\cos(\alpha_1)}}{\sqrt{\cos(\alpha_0)}}\,, \tag{2.12}$$

can be ascribed to the radiometric effect for a system satisfying the Abbe sine-condition in our general case with unequal refractive indices in object and image space. In the more common case with $n_0 = n_1$, we can put $|f_1| = |f_0| = f_L$, the focal distance of the imaging system.

As already mentioned above, we limit ourselves to systems satisfying Abbe's sine condition. In this case a point Q_0 at position (ρ, θ) is mapped directly to a point $Q_1(\rho, \theta)$ on the exit pupil sphere with the property that the normalized radial coordinate ρ and the azimuthal coordinate remain unchanged. In addition to the radiometric effect described by the transmission factor T_R, the light traveling through the imaging system will also experience some deformations introduced by imperfections of the imaging system. Although for most advanced optical systems these aberrations are generally small, we do include them in the formalism. We describe both the amplitude and phase aberrations of the imaging system by its complex transmission function T_I. In fact, in the most general case we should consider T_I^p and T_I^s, being the transmission function for p- and s-polarization components respectively, but here we will adhere to imaging systems that are free

of birefringence, allowing a single transmission function for all field components. The transmission function of the imaging system is given as

$$T_I(\rho,\theta) = A(\rho,\theta)\exp\left[i\Phi(\rho,\theta)\right] \quad , \tag{2.13}$$

where $A(\rho,\theta)$ is the amplitude transmission function and $\Phi(\rho,\theta)$ is the phase aberration. In contrast to basic ENZ theory, where the field $\mathbf{E_0}$ in the entrance pupil is uniform, we are dealing here with a general non-uniform field $\mathbf{E_0}$. We can now write the $E_{1,s}$ and $E_{1,p}$ components as

$$\begin{aligned} E_{1,s}(\rho,\theta) &= \frac{f_1\, T_I\, T_R}{R_p}\sqrt{\frac{n_0}{n_1}}\, E_{0,s}(\rho,\theta) \\ &= \frac{f_1\, T_I\, T_R}{R_p}\sqrt{\frac{n_0}{n_1}}\left(-E_{0,x}(\rho,\theta)\sin\theta + E_{0,y}(\rho,\theta)\cos\theta\right) \quad , \end{aligned} \tag{2.14}$$

$$\begin{aligned} E_{1,p}(\rho,\theta) &= \frac{f_1\, T_I\, T_R}{R_p}\sqrt{\frac{n_0}{n_1}}\, E_{0,p}(\rho,\theta) \\ &= \frac{f_1\, T_I\, T_R}{R_p}\sqrt{\frac{n_0}{n_1}}\,\frac{E_{0,x}(\rho,\theta)\cos\theta + E_{0,y}(\rho,\theta)\sin\theta}{\cos(\alpha_0)} \quad , \end{aligned} \tag{2.15}$$

where we have now omitted the the ρ and θ dependences of T_I and T_R for notational convenience. The x-, y- and z-components are given by

$$E_{1,x}(\rho,\theta) = E_{1,p}(\rho,\theta)\cos(\alpha_1)\cos\theta - E_{1,s}(\rho,\theta)\sin\theta \quad , \tag{2.16}$$

$$E_{1,y}(\rho,\theta) = E_{1,p}(\rho,\theta)\cos(\alpha_1)\sin\theta + E_{1,s}(\rho,\theta)\cos\theta \quad , \tag{2.17}$$

$$E_{1,z}(\rho,\theta) = E_{1,p}(\rho,\theta)\sin(\alpha_1) \quad , \tag{2.18}$$

or by inserting Eqs.(2.14)-(2.15), we get

$$\begin{aligned} E_{1,x}(\rho,\theta) = \frac{f_1 T_I T_R}{R_p}\sqrt{\frac{n_0}{n_1}}\Bigg[&\frac{\cos(\alpha_1)}{\cos(\alpha_0)}\left\{E_{0,x}(\rho,\theta)\cos^2\theta + E_{0,y}(\rho,\theta)\cos\theta\sin\theta\right\} \\ &+\left\{E_{0,x}(\rho,\theta)\sin^2\theta - E_{0,y}(\rho,\theta)\cos\theta\sin\theta\right\}\Bigg], \end{aligned} \tag{2.19}$$

$$\begin{aligned} E_{1,y}(\rho,\theta) = \frac{f_1 T_I T_R}{R_p}\sqrt{\frac{n_0}{n_1}}\Bigg[&\frac{\cos(\alpha_1)}{\cos(\alpha_0)}\left\{E_{0,x}(\rho,\theta)\cos\theta\sin\theta + E_{0,y}(\rho,\theta)\sin^2\theta\right\} \\ &+\left\{-E_{0,x}(\rho,\theta)\cos\theta\sin\theta + E_{0,y}(\rho,\theta)\cos^2\theta\right\}\Bigg], \end{aligned} \tag{2.20}$$

$$E_{1,z}(\rho,\theta) = \frac{f_1 T_I T_R}{R_p}\sqrt{\frac{n_0}{n_1}}\frac{\sin(\alpha_1)}{\cos(\alpha_0)}\left\{E_{0,x}(\rho,\theta)\cos\theta + E_{0,y}(\rho,\theta)\sin\theta\right\}, \tag{2.21}$$

representing the Cartesian electric field components in the exit pupil.

2.2.3 From exit pupil to focal region

Once the electric field in the exit pupil is available, the field in the focal region can be obtained through evaluation of the appropriate diffraction integral.

Diffraction integrals

For optical imaging systems, where we are in general dealing with a converging wavefront centered on the focal point F, it is customary to use the Debye diffraction integral (scalar) or its vectorial counterpart (introduced by Ignatowsky [36] and later rederived by Wolf [38]). These diffraction integrals assume that the aperture imposes a sharp boundary limiting the cone of light propagating towards the focal region, thus neglecting the more smooth boundary conditions following from Maxwell's equations. This approximation yields accurate results when both the distance from pupil to focal point and the numerical aperture are sufficiently large. This can be understood through the argument that the sharp truncation of the incident spherical wave has less and less influence when R_1 increases (see [47] for the residual error of this integral).

The Debye integral thus gives the relation between the exit pupil and the field in the focal region as is schematically depicted in Figure 2.8. For optical systems in which the geometrical aperture, $s_0 = \mathrm{NA}/n_1 = \sin(\alpha_{1,\,\mathrm{max}})$, remains below a value of 0.60, this translation is accurately described by the scalar Debye integral. In normalized cylindrical coordinates (ρ, θ) on the exit pupil sphere and (r, ϕ) in the focal region, this integral takes the form (see, for example, [48] for a derivation)

$$\begin{aligned} U(r,\phi,f) \;\approx\; & \frac{-is_0^2}{\lambda}\exp\left\{\frac{-i2f}{s_0^2}\right\}\exp\left\{i\frac{\pi\lambda r^2}{R_1 s_0^2}\right\}\times \\ & \iint_C \exp\left\{if\rho^2\right\} P_1(\rho,\theta)\exp\left\{-i2\pi r\rho\cos(\theta-\phi)\right\}\rho d\rho d\theta, \end{aligned} \tag{2.22}$$

where the scaled integration area C is equal to the unit circle, λ is the wavelength in the medium in which the image is formed and f is defined in the negative z-direction, equals zero at best focus and is normalized with respect to the axial diffraction unit, $\lambda/(\pi s_0^2)$. It was shown in [48] §2.5.2 that the NA-range for which Eq.(2.22) yields accurate results, can be somewhat extended by applying the appropriate high-NA defocus exponential. However, for NA values beyond 0.80 a complete high-NA vectorial treatment is inevitable. The generalized vectorial counterpart of the scalar Debye integral, as formulated by Wolf, is given in [48] as

$$\begin{aligned} \mathbf{E_2}(r,\phi,f) \;=\; & \frac{-is_0^2}{\lambda}\exp\left(\frac{-if}{u_0}\right)\iint_C \frac{\mathbf{E_s}(\rho,\theta+\pi)}{(1-s_0^2\rho^2)^{1/2}}\times \\ & \exp\left\{\frac{if}{u_0}\left[1-(1-s_0^2\rho^2)^{1/2}\right]\right\}\exp\{i2\pi r\rho\cos(\theta-\phi)\}\rho d\rho d\theta, \end{aligned} \tag{2.23}$$

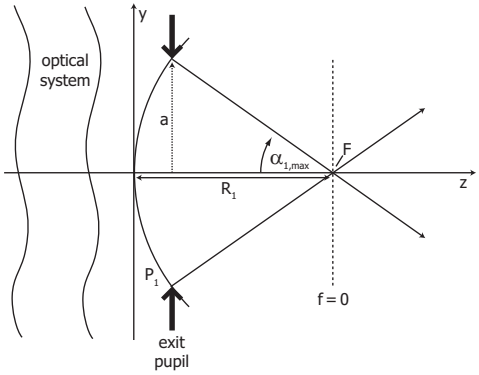

Figure 2.8: *Relevant quantities in determining the field distribution in the focal region from the field in the exit-pupil using the Debye integral. A converging field propagates from the exit-pupil sphere, P_1, towards the focal region with its center in F. The aperture of the imaging pencil (diameter is $2a$) is given by $s_0 = \sin\alpha_{1,max}$ and the distance from the exit pupil sphere, P_1, to the point F is denoted by R_1.*

where in the high-NA case f is related to z according to $f = -2\pi u_0 z/\lambda$, with $u_0 = 1 - \sqrt{1-s_0^2}$. In Eq.(2.23) $\mathbf{E}_s(\rho, \theta + \pi)$ is the exit pupil distribution; note that the phase offset of π is missing in the original formulation by Wolf [38].

Although focusing by the fast majority of imaging systems is well described using the Debye approximation, there do exist situations in which even more advanced models are required. This is for example the case in some micro-optics systems in which the aperture is of the same order of magnitude as the wavelength, or in systems where very high magnification values are applied effectively reducing the NA to values smaller than 0.01. These systems, not fulfilling the Debye requirements, could alternatively be evaluated using the more accurate Rayleigh-type diffraction integrals. However, contrary to the Debye-type integrals, no general analytic solution is known for the Rayleigh integrals thus making it necessary to always evaluate them purely numerical and this is not an option when efficient image computations are concerned. For a comparison between the Debye and Rayleigh-type integrals one can consult [48] §2.4 and [49]. In this thesis we will also further discuss the relation between the Debye and Rayleigh integrals in Chapters 4 and 5 when we consider ENZ aberration retrieval for optical systems outside the Debye regime.

Field in the focal region

We now focus on the high-NA case. We insert Eqs.(2.19)-(2.21) into Eq.(2.23) and this gives an expression that relates the field in the entrance pupil, $\mathbf{E_0}$, to the field, $\mathbf{E_2}$, in the focal region. Unfortunately, a direct analytic solution to this general integral is not available. To obtain the actual field components in the focal region one could resort to numerical integration but, of course, this would disintegrate

the appeal of this method in terms of computational efficiency. This is where the ENZ theory becomes important; in Chapter 3 it will be shown that by representing the pupil distributions as Zernike expansions, the integral can be brought into a tractable form that yields semi-analytic solutions provided by the ENZ theory. In this way, the model proposed in this section, together with the ENZ theory, provides a potentially accurate and efficient means to do computational imaging.

2.3 Illumination

In the description of the ENZ imaging model in Section 2.2 it was assumed that the object is illuminated by a coherent plane wave. Based on this assumption it was shown that the coherent image could be calculated, carrying out the full chain of diffraction at the object, diffraction at the diaphragm or pupils of the imaging system and the wave propagation towards the image region. Of course, in most imaging systems the illumination is more complex. In general, the illumination source will be of finite extent and often generates light that is spatially incoherent. Although this seems to complicate matters significantly, we will show in this section that extended and (partially) incoherent sources can be treated within the same computational framework.

In general, the light-source illuminating the object will be of finite extent. As a result, the coherence properties of the source are important in computing the total field scattered by the object. In the ENZ imaging method we deal with this complication by replacing the actual source with a sampled equivalent source. This so-called Abbe approach is often used in conjunction with a Köhler illumination scheme, in which case every sampling subarea generates a coherent plane wave incident on the object (see Figure 2.9).

Suppose that we can measure the radiance function $L(x, y; \zeta_x, \zeta_y)$ of the effective source (with ζ_x and ζ_y the projection angles of the radiation direction with respect to the x and y axes), so that we are then left with calculating the corresponding electromagnetic field strengths in the object plane. In the following, we limit ourselves to a centered object with very limited extent. With the Köhler illumination arrangement, the axial object collects the forward directed radiation of each source point in the effective source. In this case, we can use the value of the radiance function in this direction, given by $L(x, y; 0, 0)$. The power flow from an elementary source element dS_S towards the object element with size dS_O is given by

$$\begin{aligned} d^2P &= L(x, y; 0, 0)\, dS_S\, d\Omega_O \\ &= L(x, y; 0, 0)\, dS_S\, dS_O \cos(\alpha)/f_C^2 \,, \end{aligned} \tag{2.24}$$

where we have used that the solid angle $d\Omega_O$ subtended by the object is given by its projected surface divided by the square of the focal length f_C of the condensor lens (α is the projection angle). In the case of the sampled source, we suppose a constant behavior of the source over each sampling area and we are then allowed to integrate the elementary power flow using the value of the radiance function at

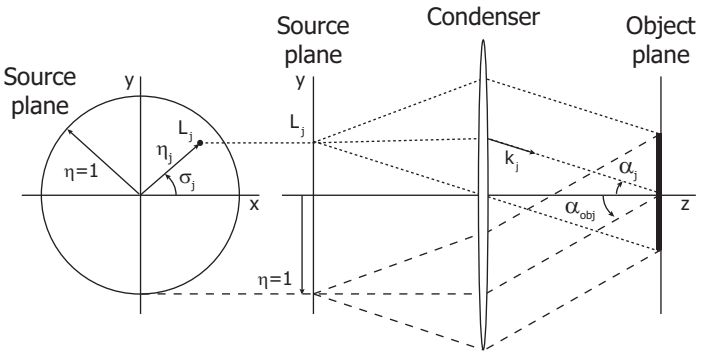

Figure 2.9: *Schematic representation of the Köhler illumination system.*

each sampling point. For a sampled source area with index j we find

$$P_j = L(x_j, y_j; 0, 0)\, S_j\, S_O \cos(\alpha_j)/f_C^2 \;, \tag{2.25}$$

where S_j is the area of the j-th source element. The power contained in the parallel beam that is emitted by the sampling area with index j is given by

$$P_j = \epsilon_0\, c\, n_0\, |\mathbf{E}_O|^2 S_O \cos(\alpha_j) \;. \tag{2.26}$$

From Eqs.(2.25) and (2.26) we obtain for the electric field strength

$$|\mathbf{E}_O| = \sqrt{\frac{L(x_j, y_j; 0, 0)\, S_j}{\epsilon_0\, c\, n_0 f_C^2}} \;. \tag{2.27}$$

In the expression above, we have taken the radiance function in a medium with refractive index n_0, the value in the object space. If the radiance function of the source is only available in vacuum or air, one can apply the relation $L = n_0^2 L_V$ which follows from the conservation law of radiance (L_V is the measured radiance function in vacuum or air).

In what follows, the Cartesian co-ordinates (x_j, y_j) in the effective source will be replaced by reduced coordinates, with the normalized co-ordinates in the entrance pupil of the imaging system as the reference. To this goal, we start with the numerical aperture in the object space, given by $s_{obj} = \sin(\alpha_{obj}) = |n_1 M s_0/n_0|$ with $n_1 s_0$ the numerical aperture in the image space. The angular measure of the source is normalized with respect to s_{obj}, such that the lateral reduced coordinate η of the source is unity if the source completely fills the entrance pupil. The relationship between the Cartesian coordinates (x_j, y_j) of a general source point and its reduced coordinates is given by

$$\begin{aligned} x_j/f_C &= \eta_j \cos(\sigma_j) s_{obj} \;, \\ y_j/f_C &= \eta_j \sin(\sigma_j) s_{obj} \;, \end{aligned} \tag{2.28}$$

where we have used polar coordinates (η, σ) in the reduced domain because of the frequently occurring rotational symmetry in illumination systems. The state of

polarization of the light issued by the light source has not been discussed so far. In the case of an unpolarized source, the source power is equally distributed over two orthogonally polarized states of polarization. In more specific cases, the power has to be distributed over the x-, y- and z-field components of the light according to the measured state of (partial) polarization of the source.

In the Abbe approach, for each source region, we also have at our disposal the average propagation direction that is needed to analyze the diffraction process at the object and the propagation of the diffracted light through the imaging system. A general source point with reduced polar coordinates (η_j, σ_j) gives rise to a fictitious plane wave whose normalized propagation vector is given by

$$\hat{\mathbf{k}}_j = \left(-\eta_j s_{obj} \cos(\sigma_j)\, \hat{\mathbf{x}}, -\eta_j s_{obj} \sin(\sigma_j)\, \hat{\mathbf{y}}, \sqrt{1 - \eta_j^2 s_{obj}^2}\, \hat{\mathbf{z}} \right) . \tag{2.29}$$

We now have available, at the location of the object, the electric field strength and propagation direction of the fictitious wave produced by each sampling area of the source. We can now repeatedly apply the steps described in Section 2.2 to obtain the coherent image contribution generated by each source subarea. The total image for a fully incoherent source is then obtained as the incoherent sum of all the individual contributions.

2.4 Stratified medium in the focal region

So far we have limited our discussion to image formation in homogeneous media. However, in a realistic imaging system it is often the case that the propagating field, between the exit pupil of the lens system and the focal region, is subjected to one or even several transitions between layers of a stratified focal region. Thus, in order to obtain an accurate description of the focused field at the region of interest, one must take into account the effects of these layer transitions. In Figure 2.10 this situation has been schematically depicted. At every layer transition, there is transmission and reflection that depends on the angle of incidence and state of polarization of an incident plane wave. For every angle, transmission and reflection are described by the respective Fresnel coefficients at the given interface and the total effect on the imaging by the system is obtained by integrating over the plane wave components that are present within the angular aperture of the lens system. This approach has been carried out in previous work considering the transition between two media, relevant in microscopy (air/sample or immersion liquid/sample) [50–54], and a general stratified media, with applications in optical lithography [33, 55, 56], optical recording [57–60], and confocal microscopy [61].

For the Hopkins approach, which already deals with a plane wave representation of the focusing field, the implementation of the effects introduced by the layer transitions using Fresnel coefficients is rather straightforward. Implementation of the same procedure for the ENZ imaging model is somewhat more involved but possible and is described below.

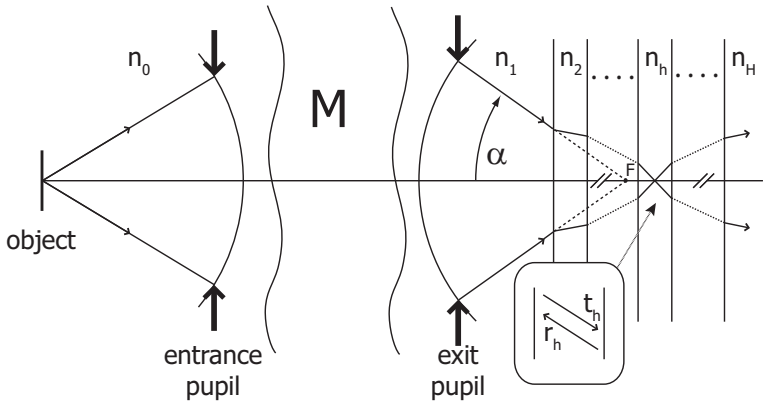

Figure 2.10: *Schematic representation of imaging, by an optical system with magnification M, into a multi-layered image space. The different layers are represented by their effective refractive indices, n_h (possibly complex), where the subscript refers to the h-th layer starting from the exit pupil. t_h and r_h are labels pertaining to the amplitudes of the forward and backward propagating plane wave components, respectively. The point F is the geometrical best focus position in case of a uniform image region and the numerical aperture is* $\mathrm{NA} = n_1 \sin\alpha$ *with* $\sin\alpha = s_0$.

2.4.1 Field in h-th layer of a stratified region

When we introduce a multilayer in the focal region this will give rise to various reflections and refractions at the interfaces between two layers having different optical properties. We will show that the nett effect of all these reflection and refraction effects, taking place in the focal region, can be taken into account by a suitable modification of the exitpupil distribution. Basically this means that we can include all effects introduced by a multilayer by adjusting the expressions for the s- and p-components in the exitpupil, given in Eqs.(2.14) and (2.15), accordingly.

Snell's law applied to the various interfaces of the multilayer yields for the x- and y-components of the unit propagation vector in the h-th layer

$$n_h k_{h,x} = n_1 k_{1,x} \ , \qquad n_h k_{h,y} = n_1 k_{1,y} \ . \tag{2.30}$$

The expressions for the s- and p-field components in the h-th layer are the sum of those pertaining to the forward propagating wave with unit propagation vector $\hat{\mathbf{k}}_{\mathbf{h,t}} = (k_{h,x}, k_{h,y}, k_{h,z})$ and complex transmission factor t_h and those associated with the reflected wave in the h-th layer with unit propagation vector $\hat{\mathbf{k}}_{\mathbf{h,r}} = (-k_{h,x}, -k_{h,y}, -k_{h,z})$ and complex reflection coefficient r_h. The reflected wave originates from a forward propagating wave with unit propagation vector $\hat{\mathbf{k}}_{\mathbf{h}} = (-k_{h,x}, -k_{h,y}, +k_{h,z})$; in the far field, its polar coordinates are given by $(\rho, \theta + \pi)$. We have to define the sign convention for the reflection coefficient r in the case of s- and p-polarization. Like in most textbooks, we choose the s-direction for the reflected wave in the same direction as for the incident wave; the p-direction of the

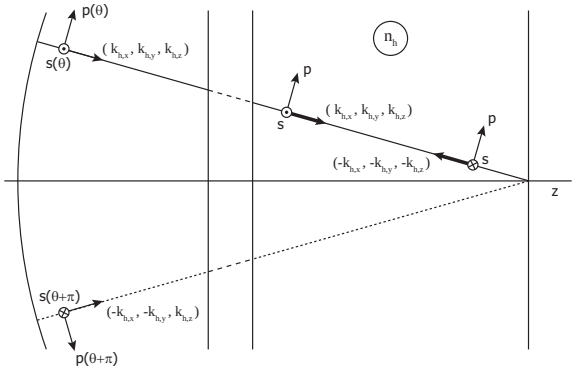

Figure 2.11: *Definition of the s- and p-polarization directions in an azimuthal plane defined by the angles θ and $\theta+\pi$. The transmitted propagation wave vector in the thin layer with refractive index n_h (azimuthal coordinate θ) is derived from an effective wave vector in image space with unit vector $\hat{\mathbf{k}}_{\mathbf{h,t}} = (k_{h,x}, k_{h,y}, k_{h,z})$. The s- and p-components of the oppositely directed reflected wave with unit wave vector $\hat{\mathbf{k}}_{\mathbf{h,r}} = -\hat{\mathbf{k}}_{\mathbf{h,t}}$ are obtained from the diametrically opposed direction of incidence with unit wave vector $(-k_{h,x}, -k_{h,y}, k_{h,z})$ and azimuth $\theta + \pi$. The p-directions of the transmitted and reflected waves are parallel, their s-components have opposite directions.*

reflected wave is chosen opposite to the p-direction of the incident wave. With this convention, we find the following expressions for the s- and p-field components in the h-th layer

$$\begin{aligned} E_{h,s}(\rho,\theta) &= \frac{f_1 T_I T_R}{R_p}\sqrt{\frac{n_0}{n_1}}\ \{t_{h,s}(\rho)E_{0,s}(\rho,\theta) - r_{h,s}(\rho)E_{0,s}(\rho,\theta+\pi)\} \\ &= \frac{f_1 T_I T_R}{R_p}\sqrt{\frac{n_0}{n_1}}\ \{t_{h,s}(\rho)\left[-E_{0,x}(\rho,\theta)\sin\theta + E_{0,y}(\rho,\theta)\cos\theta\right] \\ &\quad -r_{h,s}(\rho)\left[E_{0,x}(\rho,\theta+\pi)\sin\theta - E_{0,y}(\rho,\theta+\pi)\cos\theta\right]\} \quad , \end{aligned} \tag{2.31}$$

$$\begin{aligned} E_{h,p}\ (\rho,\theta) &= \frac{f_1 T_I T_R}{R_p}\sqrt{\frac{n_0}{n_1}}\ \{t_{h,p}(\rho)E_{0,p}(\rho,\theta) + r_{h,p}(\rho)E_{0,p}(\rho,\theta+\pi)\} \\ &= \frac{f_1 T_I T_R}{R_p\cos(\alpha_0)}\sqrt{\frac{n_0}{n_1}}\ \{t_{h,p}(\rho)\left[E_{0,x}(\rho,\theta)\cos\theta\ + E_{0,y}(\rho,\theta)\sin\theta\right] \\ &\quad -r_{h,p}(\rho)\left[E_{0,x}(\rho,\theta+\pi)\cos\theta + E_{0,y}(\rho,\theta+\pi)\sin\theta\right]\} \ , \end{aligned} \tag{2.32}$$

The minus sign in front of $r_{h,s}$ in Eq.(2.31) follows from the opposite sign convention for s-polarization of the transmitted wave and the reflected wave, see Figure 2.11. At this point we recall some of the abbreviations introduced earlier for frequently occurring goniometric quantities and define some additional abbreviations

that are convenient in the analysis provided below. We write

$$\begin{aligned} \sin(\alpha_1) = s_0\rho\ , \quad \cos(\alpha_1) = (1 - s_0^2\rho^2)^{1/2}\ , \\ s_{0,M} = \frac{n_1 M s_0}{n_0}\ , \quad \sin(\alpha_0) = s_{0,M}\rho\ , \quad \cos(\alpha_0) = \left(1 - s_{0,M}^2\rho^2\right)^{1/2}\ , \\ s_{0,h} = \frac{n_1 s_0}{n_h}\ , \quad \sin(\alpha_h) = s_{0,h}\rho\ , \quad \cos(\alpha_h) = \left(1 - s_{0,h}^2\rho^2\right)^{1/2}\ . \end{aligned} \tag{2.33}$$

Now, similar to Eqs.(2.16)-(2.18), the Cartesian components in the h-th layer are given by

$$E_{h,x}(\rho,\theta) = E_{h,p}(\rho,\theta)\cos(\alpha_h)\cos\theta - E_{h,s}(\rho,\theta)\sin\theta\ , \tag{2.34}$$

$$E_{h,y}(\rho,\theta) = E_{h,p}(\rho,\theta)\cos(\alpha_h)\sin\theta + E_{h,s}(\rho,\theta)\cos\theta\ , \tag{2.35}$$

$$E_{h,z}(\rho,\theta) = E_{h,p}(\rho,\theta)\sin(\alpha_h)\ . \tag{2.36}$$

The substitution of $E_{h,s}$ and $E_{h,p}$ in Eqs.(2.34)-(2.36) yields

$$\begin{aligned} E_{h,x}(\rho,\theta) = \frac{f_1 T_R}{R_p}\sqrt{\frac{n_0}{n_1}}\Bigg[\frac{\cos(\alpha_h)}{\cos(\alpha_0)} \times \\ \Big\{ t_{h,p}(\rho)\ T_I(\rho,\theta)\left[E_{0,x}(\rho,\theta)\cos^2\theta + E_{0,y}(\rho,\theta)\cos\theta\sin\theta\right] \\ - r_{h,p}(\rho)\ T_I(\rho,\theta+\pi)\left[E_{0,x}(\rho,\theta+\pi)\cos^2\theta + E_{0,y}(\rho,\theta+\pi)\cos\theta\sin\theta\right] \Big\} \\ + \Big\{ t_{h,s}(\rho)\ T_I(\rho,\theta)\left[E_{0,x}(\rho,\theta)\sin^2\theta - E_{0,y}(\rho,\theta)\cos\theta\sin\theta\right] \\ + r_{h,s}(\rho)\ T_I(\rho,\theta+\pi)\left[E_{0,x}(\rho,\theta+\pi)\sin^2\theta - E_{0,y}(\rho,\theta+\pi)\cos\theta\sin\theta\right] \Big\}\Bigg]\ , \end{aligned} \tag{2.37}$$

$$\begin{aligned} E_{h,y}(\rho,\theta) = \frac{f_1 T_R}{R_p}\sqrt{\frac{n_0}{n_1}}\Bigg[\frac{\cos(\alpha_h)}{\cos(\alpha_0)} \times \\ \Big\{ t_{h,p}(\rho)\ T_I(\rho,\theta)\left[E_{0,x}(\rho,\theta)\cos\theta\sin\theta + E_{0,y}(\rho,\theta)\sin^2\theta\right] \\ - r_{h,p}(\rho)\ T_I(\rho,\theta+\pi)\left[E_{0,x}(\rho,\theta+\pi)\cos\theta\sin\theta + E_{0,y}(\rho,\theta+\pi)\sin^2\theta\right] \Big\} \\ - \Big\{ t_{h,s}(\rho)\ T_I(\rho,\theta)\left[E_{0,x}(\rho,\theta)\cos\theta\sin\theta - E_{0,y}(\rho,\theta)\cos^2\theta\right] \\ + r_{h,s}(\rho)\ T_I(\rho,\theta+\pi)\left[E_{0,x}(\rho,\theta+\pi)\cos\theta\sin\theta - E_{0,y}(\rho,\theta+\pi)\cos^2\theta\right] \Big\}\Bigg]\ , \end{aligned} \tag{2.38}$$

$$E_{h,z}(\rho,\theta) = \frac{f_1 T_R}{R_p}\sqrt{\frac{n_0}{n_1}}\frac{\sin(\alpha_h)}{\cos(\alpha_0)} \times \left\{ t_{h,p}(\rho)\, T_I(\rho,\theta)\,[E_{0,x}(\rho,\theta)\cos\theta + E_{0,y}(\rho,\theta)\sin\theta] - r_{h,p}(\rho)\, T_I(\rho,\theta+\pi)\,[E_{0,x}(\rho,\theta+\pi)\cos\theta + E_{0,y}(\rho,\theta+\pi)\sin\theta] \right\}. \quad (2.39)$$

The field expressions above should be compared with Eqs.(2.19)-(2.21) that describe the case of a uniform image region. The Eqs.(2.37)-(2.39) can thus be considered as the field distribution of an effective pupil that governs the field distribution in the h-th layer of the focal region. The terms depending on $r_{h,s/p}$ originate from reflections off the layer interfaces and consequently represent electric energy propagating in the negative z-direction. Now in order to obtain the actual field in the h-th layer, Eqs.(2.37)-(2.39) should be inserted into the diffraction integral. However, these expressions can not be directly inserted in the vectorial Debye integral given in Eq.(2.23), as this expression is not equipped to cope with light travelling in the negative z-direction. In this case, the correct expression reads

$$\begin{aligned}\mathbf{E_2}(r,\phi,f) = \frac{-in_1 s_0^2}{\lambda_0}\Bigg[&\exp\left(\frac{-if}{u_{0,h}}\right)\iint_C \frac{\mathbf{E_h^t}(\rho,\theta+\pi)}{(1-s_0^2\rho^2)^{\frac{1}{2}}} \times \\ &\exp\left\{\frac{if}{u_{0,h}}\left[1-(1-s_{0,h}^2\rho^2)^{\frac{1}{2}}\right]\right\}\exp\left\{ i2\pi r\rho\cos(\theta-\phi)\right\}\rho\, d\rho d\theta \\ &+\exp\left(\frac{if}{u_{0,h}}\right)\iint_C \frac{\mathbf{E_h^r}(\rho,\theta)}{(1-s_0^2\rho^2)^{\frac{1}{2}}} \times \\ &\exp\left\{\frac{-if}{u_{0,h}}\left[1-(1-s_{0,h}^2\rho^2)^{\frac{1}{2}}\right]\right\}\exp\left\{ -i2\pi r\rho\cos(\theta-\phi)\right\}\rho\, d\rho d\theta \Bigg],\end{aligned} \quad (2.40)$$

with $u_{0,h} = 1-\sqrt{1-s_{0,h}^2}$. As Eq.(2.40) very much resembles, apart from some minus signs, a sum over two vectorial Debye integrals in the case of a uniform image region, it comes as no surprise that also this integral can be evaluated using the semi-analytic ENZ theory (see Chapter 3, Section 3.5).

2.5 Point-spread function (PSF)

In this section we elaborate on a special kind of image that is formed by a point source located in the object plane. These simple objects play an important role in both the testing of optical imaging systems as well as in computational imaging itself. The image formed by an optical system of such an object is known as the Point Spread Function (PSF).

As already discussed in Section 2.1, the point object is one of the very few objects for which analytic expressions are available to compute its image [24,25,32].

This appealing feature was used to construct a PSF convolution imaging model in which the PSF's serve as the basic building blocks to form the image of a more complicated object. Nevertheless, the method never became really popular, mostly due to the fact that for a general aberrated optical system no solution was available. As stated before, this lack was resolved by the introduction of the ENZ theory in 2002, which made it possible to calculate the PSF of general systems. With the semi-analytic expression for the PSF available, it is in principle possible to construct a far more efficient implementation of the PSF convolution method. But, what might be even more interesting is that, once the analytic image for a general aberrated system is known, it becomes possible to systematically study unknown imaging systems and possibly reconstruct their aberration function. In fact, the ENZ theory was originally developed in order to devise a system characterization methodology based on PSF measurements. This matter is discussed in detail in Chapter 4.

2.5.1 Computing the PSF of an optical system

The physical point source in optics is the dipole. When placed at infinity, it will generate a uniform field distribution in the entrance pupil. To obtain in this case the PSF, one should evaluate Eq.(2.22) with $P_1(\rho, \theta)$ equal to the complex transmission function that describes the amplitude and phase defects of the optical system. On the other hand, when the magnification is finite, the amplitude in the entrance pupil is not uniform due to the azimuthal amplitude dependence of the dipole far-field radiation which depends on the dipole orientation. To correctly simulate the PSF for this configuration, one should take $P_1(\rho, \theta)$ in Eq.(2.22) equal to the general entrance pupil distribution times the complex transmission function. When the PSF is determined using a numerical analysis of Eq.(2.22) there is no real difference in the effort required to compute either the finite or infinite magnification cases. However, for the remainder of this thesis we will assume that the field in the entrance pupil is uniform when we are dealing with the computation of PSF's. In this way, we assure that all non-uniformity in the exit pupil can be attributed to aberrations. This will somewhat simplify our discussion in the coming chapters when we will introduce an analytic formalism to compute PSF's and, based on this, derive a method to reconstruct the aberrational state of an optical system by evaluating its PSF (note that the methods presented in the coming chapters do not rely on this uniformity assumption and are, as long as the non-uniformity in the entrance pupil remains limited and smooth, generally applicable).

2.5.2 The vectorial PSF

In the vectorial regime, the PSF can not be computed using Eq.(2.22). Instead the vectorial version of the Debye integral should be used, which is given in Eq.(2.23). In this integral expression, both the polarization as well as the high-NA defocus

exponential,

$$\exp\left\{\frac{if}{u_0}\left(1-\sqrt{1-s_0^2\rho^2}\right)\right\}=\exp\left\{if\left(\frac{1-\sqrt{1-s_0^2\rho^2}}{1-\sqrt{1-s_0^2}}\right)\right\}, \tag{2.41}$$

are correctly incorporated, and the resulting integral can be used to accurately compute the field in the focal region given the field distribution in the exit pupil. Nevertheless, if we want to compute the PSF of a high-NA system, one other effect should be considered. The distribution of the intensity on the exit pupil sphere of the optical system is, apart from a lateral magnification factor, not a simple one-to-one mapping of the intensity distribution on the entrance pupil. For optical systems that satisfy the Abbe-sine condition very well, a special mapping should be applied that, with respect to the lateral pupil coordinate, leads to an increasing intensity towards the rim of the exit pupil. This so-called radiometric effect, already defined in Eq.(2.12), is of minor importance at low aperture but needs to be incorporated in the high numerical aperture case. Finally, the high-NA PSF is obtained through evaluation of Eq.(2.23) where we have put $E_s(\rho,\theta)$ equal to the transmission function of the optical system times the radiometric effect (note that this again implies that the entrance pupil distribution was assumed to be equal to unity for both polarization states).

2.5.3 Strehl ratio

As mentioned before, PSF related quantities play an important role in the assessment of optical system. For example, the Strehl ratio is a generally accepted number to characterize the quality of an imaging system. The original definition by Strehl for optical system quality is given by the ratio of the central PSF intensity in the diffraction image of an aberrated system and the theoretical maximum intensity in the unaberrated case [26]. It is usually applied to systems with a uniform amplitude transmittance function but can be extended to more general systems [62],[23] where the exit pupil function $P(\rho,\theta)$ is given by

$$P(\rho,\theta)=A(\rho,\theta)\exp\{i\Phi(\rho,\theta)\}, \tag{2.42}$$

with (ρ,θ) the normalized polar coordinates on the exit pupil sphere, A the normalized amplitude transmission function (normally taken equal to unity in the center of the exit pupil) and Φ the phase departure due to the wavefront aberration function W in the exit pupil of the optical system ($\Phi=2\pi W/\lambda$ with λ the wavelength of the light). The Strehl ratio is then given by

$$S=\frac{\left|\frac{1}{\pi}\int_0^{2\pi}\int_0^1 A(\rho,\theta)\exp\{i\Phi(\rho,\theta)\}\rho d\rho d\theta\right|^2}{\left|\frac{1}{\pi}\int_0^{2\pi}\int_0^1 A(\rho,\theta)\rho d\rho d\theta\right|^2}, \tag{2.43}$$

leading to unity in the aberration-free case ($\Phi\equiv 0$) and an optical system, claiming to be diffraction limited, should not produce a Strehl value below 0.80.

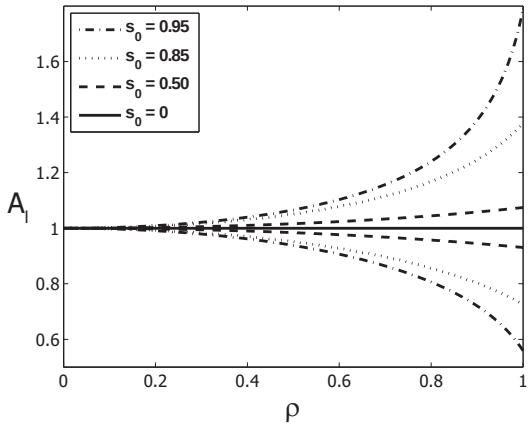

Figure 2.12: *Plot of the function $A_l(\rho,\theta)$, the contribution to the E_x-component in the focal region, as a function of the radial coordinate ρ, see Eq.(2.44), for two cross-sections: $\theta = 0$ with $A_l \leq 1$ and $\theta = \pi/2$ ($A_l \geq 1$). The values of the numerical aperture s_0 are 0.0, 0.50, 0.85 and 0.95, respectively.*

In the low-NA approximation and again under the assumption that the incident beam is uniform, we are allowed to take $A(\rho,\theta)$ equal to unity in Eq.(2.43). However, at high-NA, the amplitude in the exit pupil can no longer be taken uniform due to vector diffraction effects and the radiometric effect. Combination of these contributions leads to an amplitude function given by (see [63])

$$A_l(\rho,\theta) = A_E(\rho,\theta)\left[\frac{1+\sqrt{1-s_0^2\rho^2}-[1-\sqrt{1-s_0^2\rho^2}]\cos 2\theta}{2(1-s_0^2\rho^2)^{1/4}}\right], \qquad (2.44)$$

with $A_E(\rho,\theta)$ the incident field in the entrance pupil. We have added the index l to emphasize that the amplitude function corresponds to an incident beam that is linearly polarized, in this particular case along the x-axis ($\theta = 0$).

In all cases of interest, $A_l(\rho,\theta)$ will be a smooth function but its deviation from unity can become important. This is illustrated in Figure 2.12 where we have plotted the amplitude function $A_l(\rho,\theta)$ of Eq.(2.44) for several values of the numerical aperture s_0 and for two values of the azimuth ($\theta = 0$ and $\pi/2$) where the deviation from unity is maximum. The function A_E in the entrance pupil has been set equal to unity. The curves in Figure 2.12 show that for the high value of s_0=0.95 there is, at the rim of the exit pupil, an apparent amplitude nonuniformity of more than a factor of three. We use the adjective "apparent" to stress that it is the contribution to the E_x-field in the focal region that has been plotted in Figure 2.12, with each point on the exit pupil corresponding to a particular wave vector direction in the focusing field.

Although moderate amplitude variation over the beam cross-section in the exit pupil is commonly believed to be of minor influence on the Strehl ratio, it will be shown in Section 4.6 (or see [63]) that, in combinations with a high-NA value (say $s_0 \geq 0.85$), it does give rise to such a modulation that it is absolutely

necessary to include this effect. There we will also substantiate that the position of maximum intensity of a PSF formed at high-NA no longer coincides with the position predicted using the scalar defocusing term $\exp(if\rho^2)$. In fact the best focus position at high-NA depends on the high-NA defocus exponential given in Eq.(2.41) and on both the amplitude and phase aberrations present in the optical system. Therefore the Strehl ratio at high-NA should be written as [63]

$$S = \frac{\left|\frac{1}{\pi}\int_0^{2\pi}\int_0^1 A_l(\rho,\theta)\exp\{i[\Phi(\rho,\theta)+f\Delta(\rho)]\}\rho d\rho d\theta\right|^2}{\left|\frac{1}{\pi}\int_0^{2\pi}\int_0^1 A_l(\rho,\theta)\rho d\rho d\theta\right|^2}\,, \tag{2.45}$$

where we have introduced the defocus function

$$\Delta(\rho) = \frac{1-\sqrt{1-s_0^2\rho^2}}{1-\sqrt{1-s_0^2}}\,. \tag{2.46}$$

The Strehl ratio at high-NA can be computed using Eq.(2.45) when the value of f, corresponding to best focus, is inserted. A detailed description on how to obtain the optimum value for f, together with an analytic evaluation of Eq.(2.45), is given in Section 4.6.

2.6 Summary and discussion

In this chapter, we have introduced and discussed the optical models that play an important role in advanced optical imaging. Our discussion included methods operating in the spatial as well as the frequency domain and we have reasoned why the Hopkins or frequency domain method is by far the most widely used. Nevertheless, based on our experiences with the ENZ theory, we have set out to devise a new imaging model that operates somewhere in between the Hopkins and PSF convolution model. This new model, which we named the ENZ imaging model, computes the exit pupil field distribution due to a coherently illuminated extended object and subsequently relies on the ENZ theory to generate the resulting image. Furthermore, it was shown that this new approach can deal with extended illumination sources by applying the Abbe approach and that also a stratified configuration in image space does not pose insurmountable difficulties. Another important subject of this chapter involved the so-called PSF of the optical systems. The PSF is the image produced by an optical system when the object consists of a point-source located at the object plane. As the image of such an elementary object is analytically known, it was discussed that this enables a systematic analysis of the imaging quality of a system. In addition, we looked forward to Chapter 4, where we will demonstrate that it is even possible to fully reconstruct the aberrational state of an optical system by evaluation of its PSF.

Chapter 3

Extended Nijboer-Zernike diffraction theory

For a long time, the diffraction integrals presented in the previous chapter did not allow for a generalized analytic treatment. Only in some very specific cases, evaluation of the diffraction integrals was possible without the use of numerical methods. This situation remained unchanged until the 1930-1940's when, by the joint work of Frits Zernike and his PhD-student Bernard Nijboer, diffraction theory was greatly advanced. Based on the famous circle polynomials developed by Zernike [31], Nijboer was able to formulate an efficient representation of the complex field in the exit pupil and corresponding field in the focal plane [32]. Using the Zernike polynomials to represent the wave-front aberration of a focusing beam, Nijboer's work provided a direct representation of the complex amplitude distribution in the image plane.

Since Nijboer's thesis in 1942, the development of the Nijboer-Zernike based scalar diffraction theory related to focused fields has been limited. It was not until 2002 that another significant contribution was made by Janssen [7]. He succeeded in formulating a general expression, in terms of power-Bessel series, to compute the PSF of an aberrated optical system that was described in terms of Zernike coefficients. While Nijboer's results are only valid in case of small aberrations and can only produce accurate values of the PSF at positions close to the geometrical focus, the results by Janssen allow large aberrations and accurately computes the PSF for a substantial volume around the geometrical focus. The mathematical results by Janssen, combined with the physical interpretations provided in [8], basically marked the origination of the Extended Nijboer-Zernike (ENZ) theory of diffraction and accelerated further developments in focused field diffraction theory, including extensions to arbitrary defocus values, vectorial diffraction, annular pupils and more.

In the remainder of this chapter, we present the Extended Nijboer-Zernike (ENZ) theory as a theoretical framework to compute the Point-Spread Function (PSF) of a general optical system and discuss its application in image formation in more complex situations. We will start in Section 3.1 with a summary of the

pioneering work by Zernike and Nijboer related to diffraction theory of focused fields. In Section 3.2 we present the extension of their work which resulted in the scalar ENZ theory. Subsequently, Section 3.3 deals with the vectorial version of the ENZ theory. The later sections of this chapter expand on the more recent developments of the ENZ theory including its use in general imaging (Section 3.4), the treatment of a stratified image region (Section 3.5), its application to optical systems with variable numerical apertures or annular pupils (Section 3.6) and its use in studying electromagnetic quantities in the focal region (Section 3.7). Finally, in Section 3.8, we discuss the maximum attainable accuracy when applying the ENZ formalism and the computational burden that goes with it.

3.1 Nijboer-Zernike diffraction theory

In this section, we summarize the important contributions made by Zernike and Nijboer to scalar diffraction theory in relation to focused fields. Their combined work in this field, as it is written down in Nijboer's thesis [32], is commonly referred to as the Nijboer-Zernike or NZ-theory. The main results of their work are reproduced below, starting with the expansion of the pupil in terms of circle polynomials and finally arriving at an expression for the PSF in terms of Bessel functions.

3.1.1 Zernike representation of the pupil

As already discussed in Section 2.5, a point-source imaged by a perfect optical system gives rise to a uniform distribution in the exit pupil. However, if this optical system is not perfect, or in other words suffers from certain aberrations, its exit pupil distribution will no longer be uniform. This means that, in order to obtain the PSF of a general aberrated system in a manner that is not purely numerical, one should be able to solve the diffraction integral for a general exit pupil distribution. To come to a solution, one requires a convenient and systematic representation of general pupil distributions. Although many different sets of orthogonal functions can be selected to represent the field in the pupil, the most famous and commonly used set of basis functions is formed by the circle polynomials, Z_n^m, introduced by Zernike [31]

$$Z_n^m(\rho,\theta) = R_n^m(\rho).\begin{cases} \cos m\theta \ , \\ \\ \sin m\theta \ , \end{cases} \tag{3.1}$$

where the radial part $R_n^m(\rho)$ is the Zernike polynomial of azimuthal order m and degree n with integers $n, m \geq 0$ such that $n - m \geq 0$ and even. As can be seen from Eq.(3.1), the circle polynomials depend on either a sine or cosine part. Both are necessary to form a complete basis to describe a general pupil distribution.

In the original work by Zernike, the circle polynomials were used to represent a pupil function $P = \exp\{i\Phi\}$ by writing its phase distribution Φ as a series

expansion

$$\Phi(\rho,\theta) = \sum_{n,m} \alpha_n^m Z_n^m(\rho,\theta) \ , \tag{3.2}$$

with α_n^m the corresponding expansion coefficients. Here, it is assumed that P has a uniform amplitude and is completely described by its phase aberrations, assuring that both Φ and α_n^m are real valued. Now, for the remainder of this section we assume that $\Phi(\rho,\theta)$ can be represented using the cosine-based expressions of Eq.(3.1) only. This will somewhat improve the readability of the derivations below. Equivalent expressions related to the sine-based circle polynomials can be easily obtained following the same reasoning as presented below.

An interesting feature of the Zernike circle polynomials presented here is that, once they are inserted in the diffraction integral, they allow an analytic evaluation of this integral. In other words, every Zernike coefficient used to describe the pupil, translates into an analytically known contribution to the PSF. Although, other sets of basis functions with this same feature exist, the Zernike polynomials are special in a sense that they can easily cope with the sharp circular pupil boundaries that are often present in an optical system and that they can be directly related to a specific aberration. Other expansion bases require a large number of expansion coefficients to approximate the sharp pupil boundary and in general lack a direct and clear relation to optical aberrations.

In the next subsection, it will be shown that the pupil representation introduced by Zernike enabled Nijboer to devise an analytic expression for the PSF close to focus for a limited number of small aberrations.

3.1.2 Nijboer-Zernike expression for the PSF

The relation between the Zernike polynomials in the pupil and their contributions to the image was first derived by Nijboer and can be found as follows. We start by inserting the purely phase aberrated pupil, $P(\rho,\theta) = \exp\{i\Phi(\rho,\theta)\}$, into the expression for the normalized complex point-spread function, which can be obtained from Eq.(2.22) by normalizing in such a way that the maximum of $U(r,\phi;f)$ is equal to one for an aberration free system ($P(\rho,\theta) = 1$). In this way, we obtain

$$U(r,\phi;f) = \frac{1}{\pi}\int_0^1 \int_0^{2\pi} \exp(if\rho^2) \exp\{i\Phi(\rho,\theta)\} \exp\{i2\pi r\rho\cos(\theta-\phi)\}\ \rho d\rho d\theta \ . \tag{3.3}$$

Next, the Taylor expansion of $\exp\{i\Phi\}$ is applied to obtain

$$U(r,\phi;f) = \frac{1}{\pi}\sum_{k=0}^{\infty}\frac{i^k}{k!}\int_0^1 \int_0^{2\pi} \exp(if\rho^2)\Phi^k(\rho,\theta) \exp\{i2\pi r\rho\cos(\theta-\phi)\}\ \rho d\rho d\theta \ . \tag{3.4}$$

Following the same approach as Nijboer, we insert the Zernike expansion of the phase aberration and perform the integration over θ using elementary Bessel function operations. Then, by assuming that the phase aberration is small enough so that truncation of the infinite series in Eq.(3.4) after the term $k = 1$ is allowed,

$U(r,\phi;f)$ can, in very good approximation, be written as

$$\begin{aligned} U(r,\phi;f) &\approx 2\int_0^1 \exp(if\rho^2)J_0(2\pi\rho r)\rho d\rho \; + \\ & \quad 2i\sum_{n,m} i^m \alpha_{nm}\cos(m\phi)\int_0^1 \exp(if\rho^2)R_n^m(\rho)J_m(2\pi\rho r)\rho d\rho \;, \end{aligned} \tag{3.5}$$

where J_m is a Bessel function of the first kind and of order m. Further reduction of this integral is possible using the identity

$$\int_0^1 \rho R_n^m(\rho)J_m(2\pi\rho r)d\rho = (-1)^{\frac{n-m}{2}} \; \frac{J_{n+1}(2\pi r)}{2\pi r} \;, \tag{3.6}$$

which is the key result found by Nijboer. Altogether, the complex amplitude distribution of a point source image in the focal plane ($f = 0$) due to an aberrated pupil with the phase function given by Eq.(3.2) can be written as

$$U(r,\phi;f=0) = \frac{J_1(2\pi r)}{\pi r} + {\sum_{n,m}}' i^{n+1}\frac{J_{n+1}(2\pi r)}{2\pi r}\left\{\alpha_n^m \cos m\phi\right\} \;, \tag{3.7}$$

with the prime indicating that $m = n = 0$ should be excluded from the summation. Although Eq.(3.7) is a rather elegant result, it has never been widely used. This is largely due to the fact that its derivation requires the amplitude over the pupil to be uniform and that the permitted wave-front aberration should not, in terms of the phase, exceed a few radians. These two conditions, together with the fact that for $f \neq 0$ the reduction of Eq.(3.5) becomes cumbersome, imply that the analysis has limited value in evaluating practical problems, where in many cases the defocusing ($f \neq 0$) and aberrations are relatively large and the condition of a uniform amplitude is too restrictive.

The limiting requirements discussed above, that prevented a widespread use of the Nijboer-Zernike theory, are largely removed by the introduction of the Extended Nijboer-Zernike (ENZ) theory in 2002. This extension to the work of Zernike and Nijboer is the main topic of the next section.

3.2 Extension of the Nijboer-Zernike theory

In this section, we present a recent extension of the classical Nijboer-Zernike theory that has been developed to overcome the practical limitations discussed at the end of Section 3.1. This will result in a convenient expression to compute the through-focus PSF for general optical system and the hereby created more elaborate theoretical framework is commonly referred to as the Extended Nijboer-Zernike (ENZ) theory.

3.2.1 General pupil representation

In deriving the main results of the Nijboer-Zernike theory, it was assumed that the pupil had a uniform amplitude distribution. As discussed above, this prerequisite

strongly limits the number of practical situation in which the NZ-theory can be applied. When we drop the requirement for the pupil to have a uniform amplitude, we need a new pupil representation that accommodates for a general pupil distribution. We thus have

$$P(\rho,\theta) = A(\rho,\theta)\exp\{i\Phi(\rho,\theta)\} \ , \tag{3.8}$$

where both the amplitude, $A(\rho,\theta)$, and phase aberration, $\Phi(\rho,\theta)$, are real valued. In order to conveniently represent such a pupil, we introduce

$$Z_n^m(\rho,\theta) = R_n^{|m|}(\rho)\exp\{im\theta\} \ , \tag{3.9}$$

with $R_n^{|m|}(\rho)$ the Zernike polynomial of azimuthal order $|m|$ and degree n with integers $n, |m| \geq 0$ such that $n-|m| \geq 0$ and even. Using them as an expansion basis, one gets the following series expansion for the pupil

$$P(\rho,\theta) = A(\rho,\theta)\exp\{i\Phi(\rho,\theta)\} = \sum_{n,m} \beta_n^m Z_n^m(\rho,\theta) \ , \tag{3.10}$$

where the β_n^m are the corresponding, in general complex valued, expansion coefficients. We may point out here that this Zernike expansion involves the complex exponential $\exp(im\theta)$, integer m, instead of the real trigonometric functions $cos(m\theta)$, $sin(m\theta)$, integer $m > 0$. This is because the formulas that result when using complex exponentials are more concise and convenient. Now that we expand the full aberration, complex valued β_n^m coefficients enter the scene naturally and there is no reason to insist on real expansion functions. It has to be said that, while the α_n^m in Eq.(3.2) can be directly related to the strength of a specific aberration, this is in general not the case for the β_n^m in Eq.(3.10). In order to obtain the aberration coefficients α_n^m from the more general β_n^m coefficients, and vice-versa, one needs to perform an additional transformation step.

3.2.2 Analytic expressions for the point-spread function

When we insert the Zernike series representation of Eq.(3.10) for $P(\rho,\theta)$ into the diffraction integral and perform the integration over θ, we get for the point-spread function $U(r,\phi;f)$ the expression

$$U(r,\phi;f) = 2\sum_{n,m} \beta_n^m \ i^{|m|} \ V_n^{|m|}\exp\{im\phi\} \quad , \tag{3.11}$$

where

$$V_n^m = \int_0^1 \rho\exp(if\rho^2)R_n^{|m|}(\rho)J_m(2\pi\rho r)d\rho \tag{3.12}$$

for integers n, m, where $n \geq 0$ and $n-|m| \geq 0$ and even.

The crucial contribution made by Janssen in [7], was the derivation of a Bessel-series representation for the integral at the right of Eq.(3.12). It reads

$$V_n^m = \varepsilon_m \exp(if)\sum_{l=1}^{\infty}(-2if)^{l-1}\sum_{j=0}^{p} v_{lj}\frac{J_{|m|+l+2j}(v)}{lv^l} \tag{3.13}$$

with $\varepsilon_m = -1$ for odd $m < 0$ and $\varepsilon_m = 1$ otherwise. The coefficients v_{lj} occurring in Eq.(3.13) are given by

$$v_{lj} = (-1)^p(|m| + l + 2j)\binom{|m| + j + l - 1}{l - 1}\binom{j + l - 1}{l - 1}\binom{l - 1}{p - j}\Big/\binom{q + l + j}{l} \quad , \tag{3.14}$$

with $l = 1, 2, \ldots$ and $j = 0, \ldots, p$. In Eqs.(3.13) and (3.14) we have set

$$v = 2\pi r \quad , \qquad p = \frac{n - |m|}{2} \quad , \qquad q = \frac{n + |m|}{2} \quad . \tag{3.15}$$

Note that Eq.(3.13) still contains an infinite sum over l, but it is shown in [8] that sufficient accuracy is attained when the series is truncated for $l \geq 3f$. Moreover, in the literature (see for example [64]), a slightly different version of the solution to the diffraction integral is used. For completeness, we have included this alternative but equivalent expression in Appendix A.1.

Using Eq.(3.13) we can thus compute the PSF of an optical system having an exit pupil defined by a set of β-coefficients according to Eq.(3.10). In the case of a perfect optical system, the pupil distribution $P(\rho, \theta)$ will be uniform, resulting in a single non-zero β-coefficient, $\beta_0^0 = 1$. Inserting this single coefficient into the expression for the PSF, we obtain $U(r, \phi; f) = V_0^0(r; f)$. This means that, the aberration-free PSF is, as expected, circularly symmetric and that its shape in the radial direction is given by the function V_0^0. In Figure 3.1, we show the through-focus PSF that we obtain in this case, which is identical to the famous Airy pattern [24] in the plane $f = 0$.

In the non-perfect or aberrated case, $P(\rho, \theta)$ will no longer be uniform and, in general, will become complex valued. Nevertheless, $P(\rho, \theta)$ will remain a smooth function and this implies that we require only a modest amount of additional Zernike coefficients to describe the pupil. Then, according to Eq.(3.11), the corresponding PSF is constructed as a sum over the aberration-free contribution, V_0^0, and additional contributions, V_n^m, pertaining to the other non-zero β-coefficients describing the pupil. To illustrate this simple relation between the expansion of the pupil and its PSF we have included in Figure 3.2 the PSF for a number of non-uniform pupil distributions. In this example, we have chosen to compute the PSF for four identical optical systems (NA = 0.1), each influenced by different primary phase aberrations: spherical aberration, coma, astigmatism and a cocktail of the former three. We obtain the aberrated phase distribution, $\Phi(\rho, \theta)$, through Eq.(3.2) by defining a non-zero value for the Zernike phase aberration coefficient, α_n^m, pertaining to the desired aberration. In this way, spherical aberration, coma and astigmatism are introduced by a non-zero value of α_4^0, α_3^1 and α_2^2, respectively and the aberration cocktail consist of a distribution generated with a mix of the before mentioned α-coefficients. We then insert the resulting phase distribution into Eq.(3.10) to obtain the β-coefficients needed do compute the PSF. Although, this will in general result in a large number of non-zero β-coefficients, most of them will be very small. In this example, we therefore take into account only the dominant β_n^m. In Table 3.1, the β-coefficients are given that were ultimately used in generating the aberrated PSF's of Figure 3.2. The first row of Figure 3.2 clearly

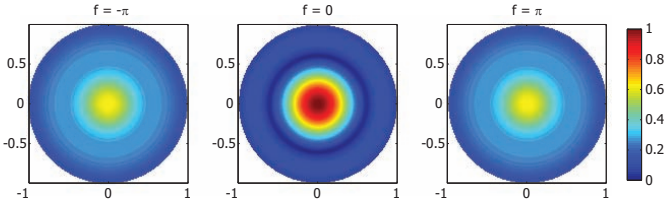

Figure 3.1: *The modulus of the electric field in three through-focus planes* $(f = -\pi, 0, \pi)$ *of the PSF for an aberration-free optical system* $(\mathrm{NA} = 0.1)$ *that is computed with the ENZ formalism. The maximum intensity is normalized to one and both the* x*- and* y*-axis are in units* λ/NA.

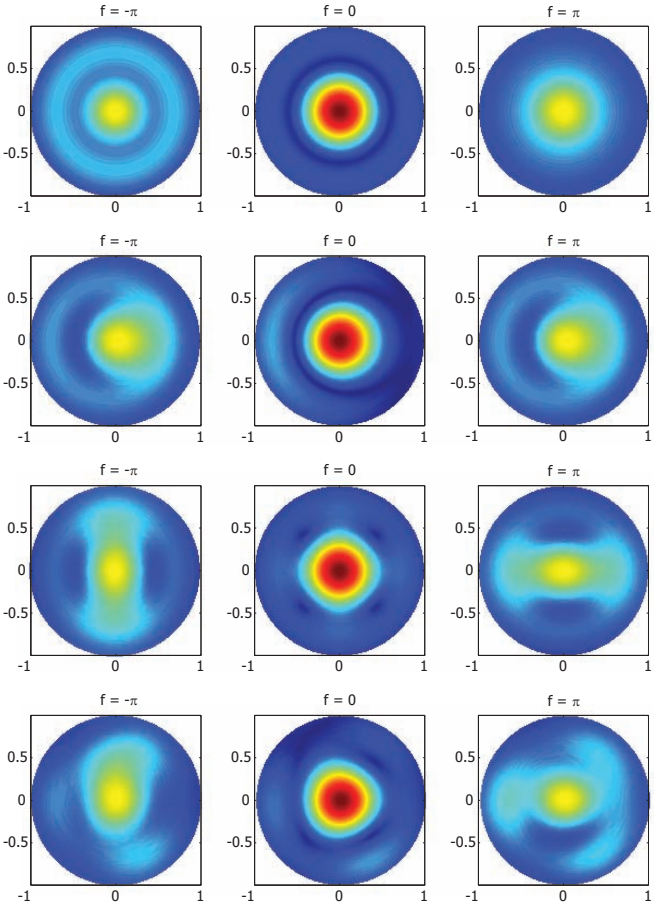

Figure 3.2: *The modulus of the electric field for three through-focus planes* $(f = -\pi, 0, \pi)$ *of the PSF that belongs to an optical system having a numerical aperture of* 0.1. *From top to bottom the PSF is influenced by spherical aberration, coma, astigmatism and a cocktail of various aberrations, respectively. The actual* β*-coefficients used for generating these PSF's are given in Table 3.1. The used color scheme and axis scaling is identical to that of Figure 3.1.*

	spherical	coma	astigmatism	cocktail
β_0^0	1.0	1.0	1.0	1.0
β_4^0	$0.5i$	0.0	0.0	$-0.25i$
β_3^{-1}	0.0	$0.5i$	0.0	-0.25
β_3^1	0.0	$0.5i$	0.0	0.25
β_2^{-2}	0.0	0.0	$0.5i$	$0.25i$
β_2^2	0.0	0.0	$0.5i$	$0.25i$
β_3^{-3}	0.0	0.0	0.0	$0.25i$
β_3^3	0.0	0.0	0.0	$0.25i$

Table 3.1: *Sets of β-coefficients used to generate the PSF's of Figure 3.2.*

shows the expected behavior that spherical aberration introduces an asymmetry around best focus ($f = 0$) and also the PSF's in the second and third row (coma and astigmatism) show the characteristic behavior that is expected for these aberrations. The final row, pertaining to the cocktail of aberrations, shows a complex behavior of the PSF that can not be predicted from the Zernike coefficients, illustrating the importance of PSF simulation for arbitrary sets of β-coefficients. In addition to the PSF's, we have for comparison also plotted the pupil distribution in Figure 3.3 that pertains to the used β-coefficients describing the aberration cocktail. In Chapter 5, where we discuss the applications of the ENZ theory, we have included an example in which we compute the PSF of a more realistic optical system, influenced by both transmission defects as well as phase aberrations.

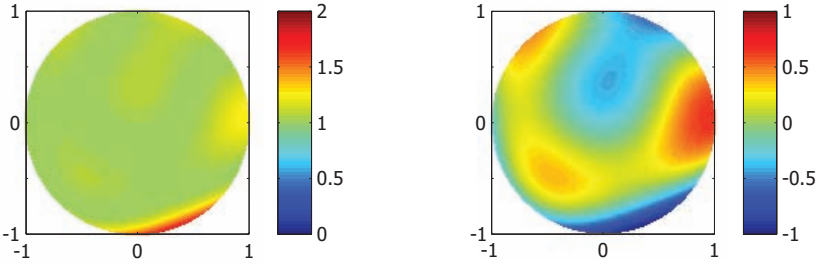

Figure 3.3: *The amplitude (left) and wavefront (right) in the exit pupil for an optical system that is described by the Zernike coefficients in the right-most column of Table 3.1. The axes are normalized with respect to the pupil radius and the color scheme on the left gives the relative amplitude whilst in the right-hand picture the colors pertain to the wavefront deviation in radians.*

3.2.3 Additional analytic result

Another analytic result from [7] is related to diffraction integrals of the type

$$T_n^m(r,f) = \int_0^1 \exp\left\{if\rho^2\right\} \rho^n J_m(2\pi r\rho)\rho d\rho \,, \tag{3.16}$$

where again n, m are integers with $n \geq 0$ and $n - |m| \geq 0$ and even. These integrals with a ρ-monomial in the integrand can be considered to be the building blocks for more general integrals containing a polynomial like a Zernike polynomial. Of course, they are also useful in the context of the aberration representation according to Seidel [15]. The Bessel series solution of this type of integral is given by

$$T_n^m(r,f) = \varepsilon_m \exp\left[if\right] \sum_{l=1}^{\infty} (-2if)^{l-1} \sum_{j=0}^{p} s_{lj} \frac{J_{|m|+l+2j}(2\pi r)}{(2\pi r)^l} \,. \tag{3.17}$$

with again $\varepsilon_m = -1$ for odd $m < 0$ and $\varepsilon_m = 1$ otherwise. The coefficients s_{lj} are given by

$$s_{lj} = (-1)^j \, \frac{|m|+l+2j}{q+1} \binom{p}{j} \binom{|m|+j+l-1}{l-1} \Big/ \binom{q+l+j}{q+1}, \tag{3.18}$$

for the same ranges as in the case of v_{lj}: $l = 1, 2, \ldots$ and $j = 0, 1, \ldots, p$.

3.2.4 Large defocus

As already discussed in [65], the series expression in Eq.(3.13) yields accurate results when f is restricted to the range $|f| \leq 5\pi$. When larger values of f are considered, the power-Bessel series representation breaks down due to serious loss of digits in Eq.(3.13). Typically, one has terms of the order of magnitude $|f|^l/l!$ in Eq.(3.13) while the V_{nm}'s themselves are of the order of unity. To avert the loss of digits when larger values of f are considered, there has been given an alternative Bessel-Bessel series expression in [65] that is accurate for arbitrary values of f. This series expression reads

$$V_n^m(r,f) = \varepsilon_m \exp(\tfrac{1}{2}if) \sum_{k=0}^{\infty} (2k+1) i^k j_k(\tfrac{1}{2}f) \sum_{l=\max(0,k-q,p-k)}^{k+p} (-1)^l \, w_{kl} \, \frac{J_{m+2l+1}(2\pi r)}{2\pi r}, \tag{3.19}$$

and requires the coefficients w_{kl} that are explicitly given in Appendix A.2. Some large defocus examples and an accuracy analysis of Eq.(3.19) are given in [48, 65].

3.3 Vectorial Extended Nijboer-Zernike theory

Optical systems that operate below a numerical aperture of 0.60 are well described by scalar diffraction theory and it was shown in Section 3.2 how, in this case, the PSF can be accurately computed. For optical systems with a larger numerical aperture, the influence of polarization effects becomes significant and, therefore, a complete vectorial treatment is required to accurately compute the PSF. In this section we will devise a vectorial version of the ENZ theory that gives a systematic framework to compute the PSF of high-NA optical systems.

3.3.1 ENZ representation of the exit pupil

In the vectorial version of the ENZ theory, we consider optical systems such as depicted in Figure 3.4. A point source at infinity generates a plane wave in the planar entrance pupil P_0. The general state of polarization in the entrance pupil of the system is determined by the field coefficients $a_x = p_x A$ and $a_y = p_y A$, with p_x and p_y complex numbers that define the polarization state, $[p_x, p_y]$, of the optical system and that satisfy the relation $|p_x|^2 + |p_y|^2 = 1$ for the purpose of normalization. After propagation through the optical system, this will generate in the exit pupil, P_1, a converging wavefront centered at the focal point F. It was shown in [66] that, for every point in the pupil, the electric field can be defined using only two polarization components that are always perpendicular to the unit propagation vector in that particular point. Then, using geometrical considerations similar to those used in Subsection 2.2.2, we can write the Cartesian electric field components in the exit pupil in terms of the field coefficients, a_x and a_y, in the entrance pupil (for the resulting expression, see Eqs.(2.19)-(2.21) with $E_{0,x}$ and $E_{0,y}$ replaced by a_x and a_y, respectively, and with $M = 0$).

To account for the spatially-varying amplitude and phase changes that are experienced by the x- and y-polarization components in the entrance pupil, while travelling through the optical system, we define their so-called complex transmission functions

$$\begin{aligned} t^x(\rho,\theta) &= A^x(\rho,\theta)\exp\left[i2\pi W(\rho,\theta)\right] \\ t^y(\rho,\theta) &= A^y(\rho,\theta)\exp\left[i2\pi W(\rho,\theta)+i\varepsilon(\rho,\theta)\right] \ , \end{aligned} \tag{3.20}$$

where A^x and A^y are real-valued functions that describe the change in field strengths of the x- and y-components, $W(\rho,\theta)$ is also real-valued and represents the wavefront aberration in units of λ, the wavelength of the light, due to optical path length variation common to both polarization states. The angle $\varepsilon(\rho,\theta)$ is the spatially varying phase difference that we have chosen to appear in the y-component. Nonzero values of ε are caused by birefringence or by polarization-dependent phase jumps at discontinuities in the optical system (e.g., air-glass transitions, optical surface coatings, etc.). As a result, the field distribution on the exit pupil sphere is completely defined by the field coefficients $[a_x, a_y]$ and their accompanying transmission functions t^x and t^y. Note that in Eqs.(2.19)-(2.21) these transmission functions are assumed identical and denoted by a single polarization independent function, $T_I(\rho,\theta)$.

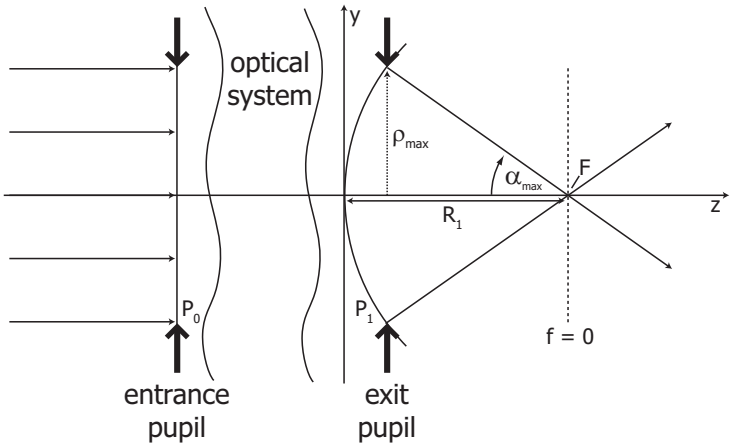

Figure 3.4: *The optical configuration considered in the ENZ theory. A point-source at infinity generates an incident plane-wave, having a polarization state* $[a_x, a_y]$*, in the flat entrance pupil denoted by* P_0*. This gives rise to a converging wavefront, centered at the focal point,* F*, in the exit pupil denoted by* P_1*. The position on the exit pupil sphere is defined by the cylindrical coordinates* (ρ, θ)*; the position in the image plane region is defined by the cylindrical coordinate system* (r, ϕ, f)*. The maximum aperture* (NA) *of the imaging pencil is defined as* $s_0 = \sin \alpha_{max}$*.*

The crucial step in the ENZ theory is the representation of the field on the exit pupil sphere in terms of radial Zernike polynomials. For this we introduce the Zernike expansions

$$\begin{aligned} a_x t^x(\rho,\theta) &= \sum_{n,m} \beta^m_{n,x} R^{|m|}_n(\rho) \exp[im\theta], \\ a_y t^y(\rho,\theta) &= \sum_{n,m} \beta^m_{n,y} R^{|m|}_n(\rho) \exp[im\theta], \end{aligned} \tag{3.21}$$

where the summation is over all integers n, m with $n - |m| \geq 0$ and even. Applying this expansion, together with the aforementioned reduced versions of Eqs.(2.19)-(2.21), we obtain the Cartesian field components in the exit pupil that can serve as input to the vectorial Debye integral.

3.3.2 ENZ expression for the vector PSF

Based on the Zernike expansions given above, it is possible to solve the vectorial version of the Debye diffraction integral given in Eq.(2.23). This solution was first presented in [9] and can be obtained as follows. We write the Cartesian field components in terms of the Zernike expansions of Eq.(3.21) and insert the resulting expressions into the Debye integral of Eq.(2.23). Then, using the expression

$\int_0^{2\pi} \exp(im\theta)\, \exp(i2\pi r\rho\cos(\theta-\phi))d\theta = 2\pi i^m J_m(2\pi r\rho)\exp(im\phi)$ with $J_m(x)$ the m-th order Bessel function of the first kind and after some lengthy manipulation, we obtain for the electric field in the focal region using column vector notation (for more details, see [9]),

$$\mathbf{E}(r,\phi,f) = \frac{-i\pi f_1 s_0^2}{\lambda}\exp\left(\frac{if}{u_0}\right)\sum_{n,m} i^m \exp[im\phi]\times$$
$$\left[\beta_{n,x}^m \begin{pmatrix} V_{n,0}^m + \frac{s_0^2}{2}\left(V_{n,2}^m\exp[2i\phi] + V_{n,-2}^m\exp[-2i\phi]\right) \\ \frac{s_0^2}{2}\left(-iV_{n,2}^m\exp[2i\phi] + iV_{n,-2}^m\exp[-2i\phi]\right) \\ s_0\left(-iV_{n,1}^m\exp[i\phi] + iV_{n,-1}^m\exp[-i\phi]\right)\end{pmatrix} + \right.$$
$$\left.\beta_{n,y}^m \begin{pmatrix} \frac{s_0^2}{2}\left(-iV_{n,2}^m\exp[2i\phi] + iV_{n,-2}^m\exp[-2i\phi]\right) \\ V_{n,0}^m + \frac{s_0^2}{2}\left(V_{n,2}^m\exp[2i\phi] - V_{n,-2}^m\exp[-2i\phi]\right) \\ -s_0\left(V_{n,1}^m\exp[i\phi] + V_{n,-1}^m\exp[-i\phi]\right)\end{pmatrix}\right]. \quad (3.22)$$

In the expression above we suppose that the incident light field is fully polarized. By allowing complex values for p_x and p_y, resulting in complex valued a_x and a_y in Eq.(3.21), we can thus accommodate general states of polarization, such as circular polarization ($[\sqrt{2}/2, \pm i\sqrt{2}/2]$), in Eq.(3.22).

The functions $V_{n,j}^m$ occurring in Eq.(3.22) depend on the normalized radial coordinate r and the defocus parameter f and are given by ($j = -2,-1,0,1,2$)

$$V_{n,j}^m(r,f) = \int_0^1 \rho^{|j|}\frac{\left(1+\sqrt{1-s_0^2\rho^2}\right)^{-|j|+1}}{(1-s_0^2\rho^2)^{1/4}}\exp\left[\frac{if}{u_0}\left(1-\sqrt{1-s_0^2\rho^2}\right)\right]\times$$
$$R_n^{|m|}(\rho)J_{m+j}(2\pi r\rho)\rho d\rho\ . \quad (3.23)$$

A series expansion can be devised to quickly obtain accurate values for the integral above. The functions that can be used in the expansion and the values of the corresponding expansion coefficients are given in Appendix A.4. The solution to the Debye integral given by Eqs.(3.22)-(3.23) is somewhat different from that given in [9] in a sense that we have now included the radiometric effect $(1-s_0^2\rho^2)^{1/4}$ in the V-functions instead of including it in the Zernike expansion of the transmission functions.

By applying the solution above, we can thus compute the PSF for a general system with given polarization in the entrance pupil. In Figure 3.5 the aberration-free PSF at high-NA is shown for x-polarized incident light ($p_x = 1$, $p_y = 0$). As we are now dealing with vector fields, we obtain the individual electric field components. In comparison with Figure 3.1 one clearly recognizes the elongated shape in the polarization direction that is characteristic for the PSF at high NA. For other incident polarization states the PSF can look quite different. To illustrate this we have included in Figure 3.6 the PSF for the following polarization states; y-polarization ($[0,1]$), diagonal polarization ($[\sqrt{2}/2, \sqrt{2}/2]$) and circular polarization (note that circular polarization also contains an orientation direction which is referred to as Right-Circular (RC) polarization ($[\sqrt{2}/2, -i\sqrt{2}/2]$) or Left-Circular (LC) polarization ($[\sqrt{2}/2, i\sqrt{2}/2]$). In a similar way as at low NA, we can compute

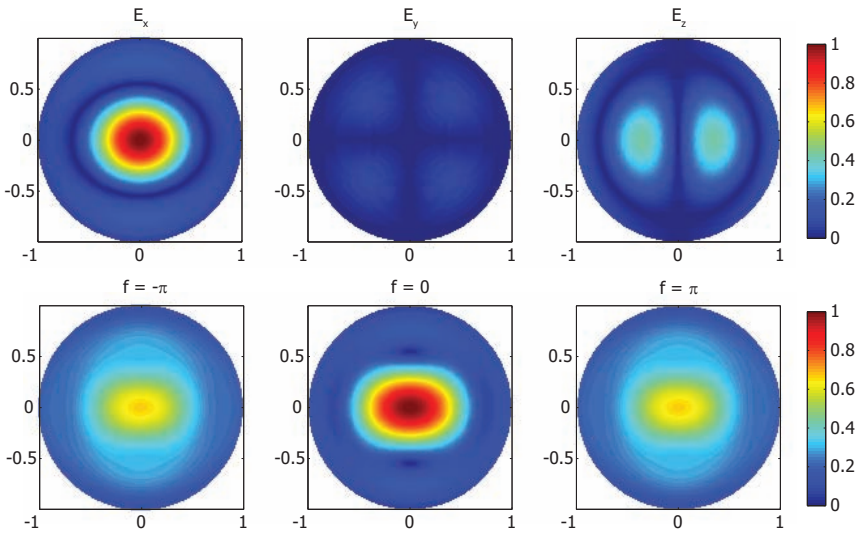

Figure 3.5: *The top row shows the absolute values of the individual electric field components in best focus* ($f = 0$). *The bottom row shows the modulus of the total electric field in three through-focus planes* ($f = -\pi, 0, \pi$). *The shown figures pertain to the x-polarized PSF for an aberration-free optical system* ($\mathrm{NA} = 0.95$) *that is computed with the ENZ formalism. The maximum intensity is normalized to one and both the x- and y-axis are in units* λ/NA.

.

the aberrated PSF. We simply include the aberration into the transmission functions of Eq.(3.20) and compute the resulting β-coefficients according to Eq.(3.21). As an example we reproduce the results given in Subsection 3.2.2 where we considered the PSF for a cocktail of aberrations at low NA (see right-most column of Table 3.1 and bottom row of Figure 3.2). The corresponding PSF at high NA, with a x-polarized incident beam, is given in Figure 3.7.

These examples nicely illustrate that, using Eqs.(3.22)-(3.24), it is possible to efficiently compute the electromagnetic field in the focal region generated by a general aberrated optical system imaging a point-source at infinity. The only requirement posed by ENZ theory is that the optical system is well described using the Debye approximation and that the exit pupil, which can have an arbitrary distribution due to various amplitude and phase deviations, can be described using Zernike functions. Note that this latter requirement can always be fulfilled as the Zernike polynomials form a complete set of basic functions. However, when non-circularly shaped pupils or phase jumps are present within the pupil it might be that impractically large numbers of Zernike coefficients are required.

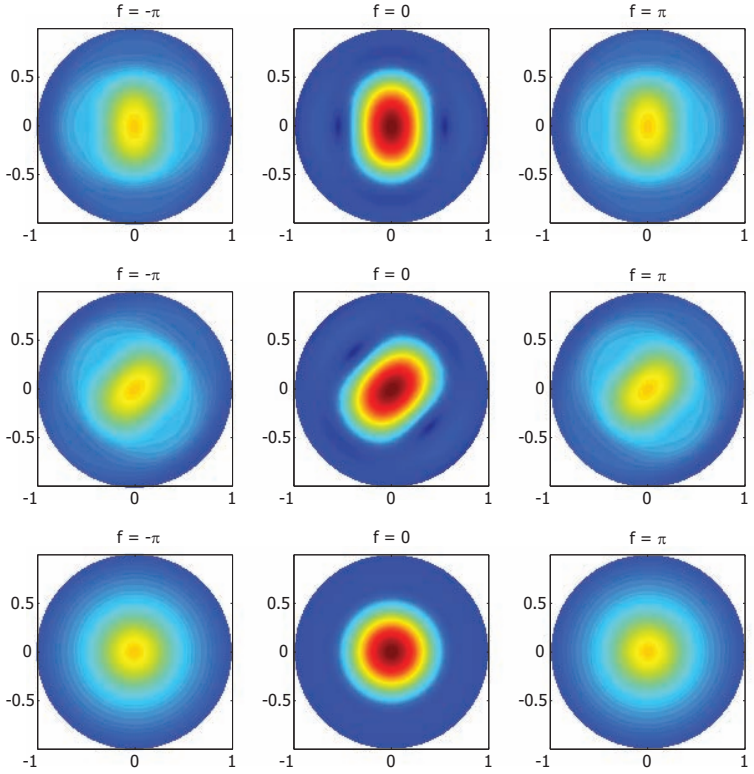

Figure 3.6: *The through-focus aberration-free PSF generated by an optical system having a* NA *equal to* 0.95*. The top row pertains to y-polarization* ($[0, 1]$)*, the middle row to diagonal polarization* ($[\sqrt{2}/2, \sqrt{2}/2]$) *and the bottom row to Right-Circular* ($[1, -i]$) *or Left-Circular* ($[1, i]$) *polarization, which have an identical PSF in the aberration-free case. Again the normalization and axis scaling is identical to that of Figure 3.5.*

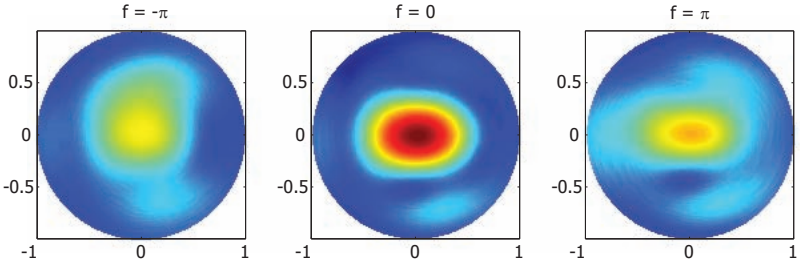

Figure 3.7: *The modulus of the total electric field for three through-focus planes* ($f = -\pi, 0, \pi$) *of the PSF that belongs to an optical system* (NA $= 0.95$*, incident polarization state* $[1, 0]$) *that is influenced by a cocktail of aberration defined by the* β*-coefficients in the right-most column of Table 3.1. The used color scheme and axis scaling is identical to that of Figure 3.5.*

3.3.3 Magnetic induction in the focal region

According to Maxwell's equations, the vector electric field attributed to a light-beam always coexist with a corresponding magnetic induction. In homogeneous space, for a plane wave, we have the relationship $\mathbf{B} = \sqrt{\varepsilon\mu}\,\mathbf{s} \times \mathbf{E}$, with $\mathbf{s}$ the unit propagation vector of the plane wave. In the optical domain, we are allowed to write $\mu = \mu_0$ with μ_0 the magnetic permeability of vacuum and $\varepsilon^{1/2} = n_1(\varepsilon_0)^{1/2}$, with n_1 the refractive index in image space. The unit propagation vector is determined for a certain value of the normalized pupil coordinates (ρ, θ) in the exit pupil, and is given by $\mathbf{s} = (-\sin(\alpha_1)\cos\theta, -\sin(\alpha_1)\sin\theta, \cos(\alpha_1))$. Using this quantity to obtain the magnetic induction on the exit pupil sphere and performing the Debye integral for the magnetic induction components we find the following quantities in the focal region (transmitted components in vector notation),

$$\mathbf{B}(r,\phi,f) = \frac{-i\pi n_1 f_1 s_0^2}{c\lambda}\exp\left(\frac{if}{u_0}\right)\sum_{n,m} i^m \exp[im\phi] \times$$
$$\left[\beta_{n,x}^m \begin{pmatrix} i\frac{s_0^2}{2}\left(-V_{n,2}^m\exp[2i\phi] + V_{n,-2}^m\exp[-2i\phi]\right) \\ V_{n,0}^m - \frac{s_0^2}{2}\left(V_{n,2}^m\exp[2i\phi] + V_{n,-2}^m\exp[-2i\phi]\right) \\ -s_0\left(V_{n,1}^m\exp[i\phi] + V_{n,-1}^m\exp[-i\phi]\right) \end{pmatrix} + \right.$$
$$\left. \beta_{n,y}^m \begin{pmatrix} -V_{n,0}^m - \frac{s_0^2}{2}\left(V_{n,2}^m\exp[2i\phi] + V_{n,-2}^m\exp[-2i\phi]\right) \\ +i\frac{s_0^2}{2}\left(V_{n,2}^m\exp[2i\phi] - V_{n,-2}^m\exp[-2i\phi]\right) \\ is_0\left(V_{n,1}^m\exp[i\phi] - V_{n,-1}^m\exp[-i\phi]\right) \end{pmatrix} \right], \quad (3.24)$$

with $c = \frac{1}{\sqrt{\varepsilon_0\mu_0}}$ the speed of light in vacuum. Having available both the electric and magnetic components in the focal region we have in principle all the required information to compute all other electromagnetic quantities such as the Poynting vector and the angular momentum. These quantities and the information they can provide us are the main topic of Section 3.7.

3.4 ENZ theory beyond the PSF

Although the ENZ theory presented in Sections 3.2 and 3.3 was developed to compute the PSF of optical systems under the influence of aberrations, we have shown in [45] that its range of application is not necessarily limited to point-objects. This can be understood by recognizing that the ENZ theory basically computes the field distribution in image space, given some general distribution in the exit pupil. Standard ENZ theory considers this non-uniformity in the exit pupil to come exclusively from amplitude and phase aberrations, but this does not imply that deformations originating from other sources can not be treated equally well. For example, considering an object different from a point-source at infinity will result in a non-uniformly distributed entrance pupil. Even when we would assume the imaging system to be perfect and for the time being neglect the radiometric effect, this would still result in a non-uniform exit pupil. Treating this exit pupil distribution according to ENZ theory will then result in a field distribution in the focal region constituting an image of the object.

In Section 2.2.2 we have derived an expression for the field in the exit pupil of an imaging system, given some general field in the entrance pupil that originates from a small arbitrarily shaped object located at a finite distance from the imaging system. Starting from Eqs.(2.19)-(2.21) we proceed by applying ENZ theory and represent the field components $E_{0,x}$ and $E_{0,y}$, including possible deformations introduced by the optical system and represented by $T_I(\rho,\theta)$, as a Zernike expansion

$$\begin{aligned} E_{0,x}(\rho,\theta)\; T_I(\rho,\theta) &= \sum_{n,m} \beta_{n,x}^m R_n^{|m|}(\rho)\exp(im\theta), \\ E_{0,y}(\rho,\theta)\; T_I(\rho,\theta) &= \sum_{n,m} \beta_{n,y}^m R_n^{|m|}(\rho)\exp(im\theta). \end{aligned} \tag{3.25}$$

Using these expansions and after a somewhat lengthy manipulation, the field components in the exit pupil can finally be written as

$$\begin{aligned} E_{1,x}(\rho,\theta) = \frac{f_1\, T_R}{2R_p\cos(\alpha_0)}\sqrt{\frac{n_0}{n_1}}\sum_{n,m} R_n^{|m|}(\rho)\exp(im\theta)\times \\ \left\{\beta_{n,x}^m\left[\{\cos(\alpha_1)+\cos(\alpha_0)\} - \left\{\frac{[\sin^2(\alpha_1)-\sin^2(\alpha_0)]\cos 2\theta}{[\cos(\alpha_0)+\cos(\alpha_1)]}\right\}\right]\right. \\ \left. -\beta_{n,y}^m\left[\frac{[\sin^2(\alpha_1)-\sin^2(\alpha_0)]\sin 2\theta}{[\cos(\alpha_0)+\cos(\alpha_1)]}\right]\right\}, \end{aligned} \tag{3.26}$$

$$\begin{aligned} E_{1,y}(\rho,\theta) = \frac{f_1\, T_R}{2R_p\cos(\alpha_0)}\sqrt{\frac{n_0}{n_1}}\sum_{n,m} R_n^{|m|}(\rho)\exp(im\theta)\times \\ \left\{\beta_{n,y}^m\left[\{\cos(\alpha_1)+\cos(\alpha_0)\} + \left\{\frac{[\sin^2(\alpha_1)-\sin^2(\alpha_0)]\cos 2\theta}{[\cos(\alpha_0)+\cos(\alpha_1)]}\right\}\right]\right. \\ \left. -\beta_{n,x}^m\left[\frac{[\sin^2(\alpha_1)-\sin^2(\alpha_0)]\sin 2\theta}{[\cos(\alpha_0)+\cos(\alpha_1)]}\right]\right\}, \end{aligned} \tag{3.27}$$

$$\begin{aligned} E_{1,z}(\rho,\theta) = \frac{f_1\, T_R\, s_0}{R_p\cos(\alpha_0)}\sqrt{\frac{n_0}{n_1}}\times \\ \sum_{n,m}\rho\, R_n^{|m|}(\rho)\exp(im\theta)\left\{\beta_{n,x}^m\cos\theta+\beta_{n,y}^m\sin\theta\right\}. \end{aligned} \tag{3.28}$$

To obtain the image produced by the optical system one should compute the Debye diffraction integral with the aid of the exit pupil field distribution defined by Eqs.(3.26)-(3.28). As we are interested in systems with a large numerical aperture, we have to deal with the full vectorial version of the Debye diffraction integral which is given in Eq.(2.23). The vector quantity $\mathbf{E_s}(\rho,\theta+\pi)$ in the integrand of the Debye-integral, is given by the field-invariant $R\mathbf{E_1}$, with R the distance along

the propagation direction towards or away from the image point. In our case $\mathbf{E_s}$ is simply given by $R_1\mathbf{E_1}$, where R_1 is the radius of the exit pupil sphere. Multiplication of R_1 with the geometrical amplitude factor f_1/R_p in Eqs.(3.26)-(3.28) and writing λ in terms of the vacuum wavelength, λ_0, and the refractive index in image space, n_1, it is possible to write the complete scaling factor $n_1 f_1 s_0^2 R_1/\lambda_0 R_p$ as $n_1 s_0^2 f_1/(\lambda_0[1 - M f_1/R_1])$ using the paraxial property $R_p = R_1 - M f_1$. Special cases arise when one of the pupils or both are located at infinity. For an exit pupil at infinity, the geometrical scaling factor reduces to $n_1 f_1 s_0^2/\lambda_0$. An entrance pupil at infinity poses a problem because the field components $E_{0,s}$ and $E_{0,p}$ tend to zero and the evaluation of the Zernike coefficients of Eq.(3.25) would be indefinite. In this case, the field components can be measured or calculated, far enough from the object itself, on a sphere with a predefined radius R_0 that will replace the actually infinite value of the radius. With the finite energy flow from the infinitely distant entrance pupil, the field components on the chosen sphere with radius R_0 can be obtained. Using the corresponding R_1-value for the exit pupil position, the quantity $R\mathbf{E_1}$, the ray invariant, is then uniquely obtained.

Taking the above considerations into account, we proceed by inserting Eqs.(3.26)-(3.28) into Eq.(2.23). Then, by again using the expression $\int_0^{2\pi} \exp(im\theta) \exp(i2\pi r\rho\cos(\theta-\phi))d\theta = 2\pi i^m J_m(2\pi r\rho)\exp(im\phi)$, we obtain after lengthy manipulations the following expression for the vector field in the focal region in column vector notation,

$$\mathbf{E_2}(r,\phi,f) = \frac{-i\pi n_1 f_1 s_0^2}{\lambda_0\,[1 - M f_1/R_1]}\sqrt{\frac{n_0}{n_1}}\,\exp\left(\frac{-if}{u_0}\right)\sum_{n,m}(-i)^m \exp[im\phi]\,\times$$
$$\left[\beta_{n,x}^m \begin{pmatrix} V_{n,0}^m - \left(\frac{s_{0,M}^2 - s_0^2}{2}\right)\left\{V_{n,+2}^m \exp[+2i\phi] + V_{n,-2}^m \exp[-2i\phi]\right\} \\ i\left(\frac{s_{0,M}^2 - s_0^2}{2}\right)\left\{V_{n,+2}^m \exp[+2i\phi] - V_{n,-2}^m \exp[-2i\phi]\right\} \\ -is_0\left\{V_{n,+1}^m \exp[+i\phi] - V_{n,-1}^m \exp[-i\phi]\right\} \end{pmatrix}\right.$$
$$\left. + \beta_{n,y}^m \begin{pmatrix} i\left(\frac{s_{0,M}^2 - s_0^2}{2}\right)\left\{V_{n,+2}^m \exp[+2i\phi] - V_{n,-2}^m \exp[-2i\phi]\right\} \\ V_{n,0}^m + \left(\frac{s_{0,M}^2 - s_0^2}{2}\right)\left\{V_{n,+2}^m \exp[+2i\phi] + V_{n,-2}^m \exp[-2i\phi]\right\} \\ -s_0\left\{V_{n,+1}^m \exp[+i\phi] + V_{n,-1}^m \exp[-i\phi]\right\} \end{pmatrix}\right]. \tag{3.29}$$

Comparing the above expression with Eq.(3.22), we see that the case of a more general object can be written very similarly to standard ENZ theory. However, due to the non-zero magnification, M, the $V_{n,j}^m$-functions occurring in the above expression are different and somewhat more complicated than those of Eq.(3.23). For integer $j = -2, \cdots, +2$, they are given as

$$V_{n,j}^m(r,f) = \int_0^1 \rho^{|j|} \frac{\left\{\left(1 - s_{0,M}^2\rho^2\right)^{\frac{1}{2}} + \left(1 - {s_0}^2\rho^2\right)^{\frac{1}{2}}\right\}^{-|j|+1}}{\left(1 - {s_0}^2\rho^2\right)^{\frac{1}{4}}\left(1 - s_{0,M}^2\rho^2\right)^{\frac{3}{4}}} \times$$
$$\exp\left[\frac{if}{u_0}\left(1 - \sqrt{1 - s_0^2\rho^2}\right)\right] R_n^{|m|}(\rho) J_{m+j}(2\pi r\rho)\rho d\rho, \tag{3.30}$$

and in accordance with standard ENZ analysis where a point-source at infinity was considered, one can devise a series expansion to quickly obtain accurate values of this integral. The functions that are used in the expansion and the values of the new expansion coefficients are given in Appendix A.5.

Also the corresponding expression for the magnetic induction vector can again be expressed in terms of the V-functions given above. The resulting expression becomes

$$\mathbf{B_2}(r,\phi,f) = \frac{-i\pi n_1^2 f_1 s_0^2}{\lambda_0\, c\,[1-Mf_1/R_1]}\sqrt{\frac{n_0}{n_1}}\,\exp\left(\frac{-if}{u_0}\right)\sum_{n,m}(-i)^m\exp[im\phi]\times$$
$$\left[\beta^m_{n,x}\begin{pmatrix} +i\left(\frac{s^2_{0,M}-s^2_0}{2}\right)\left\{V^m_{n,+2}\exp[+2i\phi]-V^m_{n,-2}\exp[-2i\phi]\right\} \\ +V^m_{n,0}+\left(\frac{s^2_{0,M}-s^2_0}{2}\right)\left\{V^m_{n,+2}\exp[+2i\phi]+V^m_{n,-2}\exp[-2i\phi]\right\} \\ -s_0\left\{V^m_{n,+1}\exp[+i\phi]+V^m_{n,-1}\exp[-i\phi]\right\}\end{pmatrix}\right.$$
$$\left.+\beta^m_{n,y}\begin{pmatrix} -V^m_{n,0}+\left(\frac{s^2_{0,M}-s^2_0}{2}\right)\left\{V^m_{n,+2}\exp[+2i\phi]+V^m_{n,-2}\exp[-2i\phi]\right\} \\ -i\left(\frac{s^2_{0,M}-s^2_0}{2}\right)\left\{V^m_{n,+2}\exp[+2i\phi]-V^m_{n,-2}\exp[-2i\phi]\right\} \\ +is_0\left\{V^m_{n,+1}\exp[+i\phi]-V^m_{n,-1}\exp[-i\phi]\right\}\end{pmatrix}\right]. \tag{3.31}$$

The expressions presented in this section form a generalization of standard vectorial ENZ theory. The results presented in Section 3.3 pertained to imaging from infinity ($M = 0$) and to equal refractive indices in object and image space, and the results presented here yield the same limiting value for this special case. Having available these new expressions based on ENZ theory, we can apply them in the ENZ imaging model presented in Section 2.2 to construct an efficient imaging algorithm. For a detailed analysis of an actual implementation of this imaging model we refer to [45, 67, 68] and in addition, we will illustrate its capabilities in Chapter 5 by presenting some image simulations of extended objects.

3.5 ENZ theory for a stratified image region

In the previous section, we have shown that the ENZ formalism can be adapted so that it can be used to compute the image of extended objects at a finite distance from the imaging system. In the derivation leading to Eq.(3.30), it was assumed that image space consist of a uniform medium with a constant refractive index. However, in many imaging processes, this assumption is not valid and image formation takes place in a non-uniform region. For example, in lithography, where the image is constructed in a layer of resist that is part of a multilayer wafer stack. In Section 2.4, we have analyzed the effects that are introduced by the layer transitions present in such a stratified image space configuration. This resulted in Eqs.(2.37)-(2.39), that give expressions for the effective pupil distribution governing the field in the h-th layer of a stratified region. Now, in order to arrive at a representation of this pupil distribution that, once it has been inserted in the diffraction integral, allows for a analytic solution, we again apply the ENZ

theory. We construct Zernike expansions for the quantities $E_{0,x/y}\, t_{h,s/p}\, T_I$ and $E_{0,x/y}\, r_{h,s/p}\, T_I$ that occur in Eqs.(2.37)-(2.39). At this point, it is also straightforward to include birefringence into the formalism by allowing non-identical aberration functions, $T_{I,x}$ and $T_{I,y}$, acting on the x- and y- components of the incident field, respectively. We thus define the following sets of Zernike expansions, containing forward propagating contributions

$$E_{0,x}(\rho,\theta)\; t_{h,s}(\rho)\; T_{I,x}(\rho,\theta) \;=\; \sum_{n,m} \beta^m_{n,x,t_s} R^{|m|}_n(\rho) \exp(im\theta), \tag{3.32}$$

$$E_{0,x}(\rho,\theta)\; t_{h,p}(\rho)\; T_{I,x}(\rho,\theta) \;=\; \sum_{n,m} \beta^m_{n,x,t_p} R^{|m|}_n(\rho) \exp(im\theta), \tag{3.33}$$

$$E_{0,y}(\rho,\theta)\; t_{h,s}(\rho)\; T_{I,y}(\rho,\theta) \;=\; \sum_{n,m} \beta^m_{n,y,t_s} R^{|m|}_n(\rho) \exp(im\theta), \tag{3.34}$$

$$E_{0,y}(\rho,\theta)\; t_{h,p}(\rho)\; T_{I,y}(\rho,\theta) \;=\; \sum_{n,m} \beta^m_{n,y,t_p} R^{|m|}_n(\rho) \exp(im\theta), \tag{3.35}$$

and similarly for the corresponding counter propagating ones

$$E_{0,x}(\rho,\theta)\; r_{h,s}(\rho)\; T_{I,x}(\rho,\theta) \;=\; \sum_{n,m} \beta^m_{n,x,r_s} R^{|m|}_n(\rho) \exp(im\theta), \tag{3.36}$$

$$E_{0,x}(\rho,\theta)\; r_{h,p}(\rho)\; T_{I,x}(\rho,\theta) \;=\; \sum_{n,m} \beta^m_{n,x,r_p} R^{|m|}_n(\rho) \exp(im\theta), \tag{3.37}$$

$$E_{0,y}(\rho,\theta)\; r_{h,s}(\rho)\; T_{I,y}(\rho,\theta) \;=\; \sum_{n,m} \beta^m_{n,y,r_s} R^{|m|}_n(\rho) \exp(im\theta), \tag{3.38}$$

$$E_{0,y}(\rho,\theta)\; r_{h,p}(\rho)\; T_{I,y}(\rho,\theta) \;=\; \sum_{n,m} \beta^m_{n,y,r_p} R^{|m|}_n(\rho) \exp(im\theta). \tag{3.39}$$

For the analysis of the electric vector field in layer h, we need these eight sets of coefficients. If the field should be calculated in another layer, the $t_{h,p/s}$ and $r_{h,p/s}$ coefficients change and new sets have to be constructed.

Using the Zernike expansions of Eqs.(3.32)-(3.39) together with Eqs.(2.37)-(2.39), expressions can be found for the forward and backward propagating Cartesian components of the electric and magnetic field. However, to continue the use of the $V^m_{n,j}$-type integrals that have been introduced in the earlier ENZ analysis with a homogeneous image space, we define the following sets of composite Zernike coefficients

$$\begin{aligned}
\beta^m_{n,x,t_+} &= \frac{\beta^m_{n,x,t_p} + \beta^m_{n,x,t_s}}{2} \;;\; \beta^m_{n,x,t_-} = \frac{\beta^m_{n,x,t_p} - \beta^m_{n,x,t_s}}{2}\,, \\
\beta^m_{n,y,t_+} &= \frac{\beta^m_{n,y,t_p} + \beta^m_{n,y,t_s}}{2} \;;\; \beta^m_{n,y,t_-} = \frac{\beta^m_{n,y,t_p} - \beta^m_{n,y,t_s}}{2}\,, \\
\beta^m_{n,x,r_+} &= \frac{\beta^m_{n,x,r_p} + \beta^m_{n,x,r_s}}{2} \;;\; \beta^m_{n,x,r_-} = \frac{\beta^m_{n,x,r_p} - \beta^m_{n,x,r_s}}{2}\,, \\
\beta^m_{n,y,r_+} &= \frac{\beta^m_{n,y,r_p} + \beta^m_{n,y,r_s}}{2} \;;\; \beta^m_{n,y,r_-} = \frac{\beta^m_{n,y,r_p} - \beta^m_{n,y,r_s}}{2}\,.
\end{aligned} \tag{3.40}$$

The Cartesian electric field components for each direction of incidence in layer h can now be evaluated, both for the forward and for the backward propagating field. Their directional or spectral dependence is determined by the normalized polar coordinates (ρ, θ) on the exit pupil sphere from where the propagating plane waves components in image space originate. The resulting expressions for forward and backward propagating Cartesian electric field components are

$$E^t_{h,x}(\rho,\theta) = \frac{f_1\ \cos^{1/2}(\alpha_1)}{2R_p\ \cos^{3/2}(\alpha_0)}\sqrt{\frac{n_0}{n_1}}\ \sum_{n,m} R_n^{|m|}(\rho)\exp(im\theta)\ \times$$
$$\Big\{\beta^m_{n,x,t_+}\left[\cos(\alpha_h)+\cos(\alpha_0)\right]\ +\beta^m_{n,x,t_-}\left[\cos(\alpha_h)-\cos(\alpha_0)\right]$$
$$+\Big[\ \beta^m_{n,x,t_+}\left[\cos(\alpha_h)-\cos(\alpha_0)\right]\ +\ \beta^m_{n,x,t_-}\left[\cos(\alpha_h)+\cos(\alpha_0)\right]\Big]\cos 2\theta$$
$$+\Big[\ \beta^m_{n,y,t_+}\left[\cos(\alpha_h)-\cos(\alpha_0)\right]\ +\ \beta^m_{n,y,t_-}\left[\cos(\alpha_h)+\cos(\alpha_0)\right]\Big]\sin 2\theta\ \Big\}, \tag{3.41}$$

$$E^r_{h,x}(\rho,\theta) = \frac{f_1\ \cos^{1/2}(\alpha_1)}{2R_p\ \cos^{3/2}(\alpha_0)}\sqrt{\frac{n_0}{n_1}}\ \sum_{n,m} R_n^{|m|}(\rho)\exp(im\theta)\ (-1)^m\ \times$$
$$\Big\{-\beta^m_{n,x,r_+}\left[\cos(\alpha_h)-\cos(\alpha_0)\right]\ -\beta^m_{n,x,r_-}\left[\cos(\alpha_h)+\cos(\alpha_0)\right]$$
$$+\Big[-\beta^m_{n,x,r_+}\left[\cos(\alpha_h)+\cos(\alpha_0)\right]\ -\beta^m_{n,x,r_-}\left[\cos(\alpha_h)-\cos(\alpha_0)\right]\Big]\cos 2\theta$$
$$+\Big[-\beta^m_{n,y,r_+}\left[\cos(\alpha_h)+\cos(\alpha_0)\right]\ -\beta^m_{n,y,r_-}\left[\cos(\alpha_h)-\cos(\alpha_0)\right]\Big]\sin 2\theta\ \Big\}, \tag{3.42}$$

$$E^t_{h,y}(\rho,\theta) = \frac{f_1\ \cos^{1/2}(\alpha_1)}{2R_p\ \cos^{3/2}(\alpha_0)}\sqrt{\frac{n_0}{n_1}}\ \sum_{n,m} R_n^{|m|}(\rho)\exp(im\theta)\ \times$$
$$\Big\{\beta^m_{n,y,t_+}\left[\cos(\alpha_h)+\cos(\alpha_0)\right]+\beta^m_{n,y,t_-}\left[\cos(\alpha_h)-\cos(\alpha_0)\right]$$
$$+\Big[-\beta^m_{n,y,t_+}\left[\cos(\alpha_h)-\cos(\alpha_0)\right]-\beta^m_{n,y,t_-}\left[\cos(\alpha_h)+\cos(\alpha_0)\right]\Big]\cos 2\theta$$
$$+\Big[\ \beta^m_{n,x,t_+}\left[\cos(\alpha_h)-\cos(\alpha_0)\right]+\beta^m_{n,x,t_-}\left[\cos(\alpha_h)+\cos(\alpha_0)\right]\Big]\sin 2\theta\ \Big\}, \tag{3.43}$$

$$E^r_{h,y}(\rho,\theta) = \frac{f_1\ \cos^{1/2}(\alpha_1)}{2R_p\ \cos^{3/2}(\alpha_0)}\sqrt{\frac{n_0}{n_1}}\ \sum_{n,m}\ R_n^{|m|}(\rho)\exp(im\theta)\ (-1)^m\ \times$$
$$\Big\{-\beta^m_{n,y,r_+}\left[\cos(\alpha_h)-\cos(\alpha_0)\right]\ -\beta^m_{n,y,r_-}\left[\cos(\alpha_h)+\cos(\alpha_0)\right]$$
$$+\Big[\ \ \beta^m_{n,y,r_+}\left[\cos(\alpha_h)+\cos(\alpha_0)\right]+\beta^m_{n,y,r_-}\left[\cos(\alpha_h)-\cos(\alpha_0)\right]\Big]\cos 2\theta$$
$$+\Big[-\beta^m_{n,x,r_+}\left[\cos(\alpha_h)+\cos(\alpha_0)\right]-\beta^m_{n,x,r_-}\left[\cos(\alpha_h)-\cos(\alpha_0)\right])\Big]\sin 2\theta\ \Big\}\,, \tag{3.44}$$

$$E^t_{h,z}(\rho,\theta) = \frac{f_1 s_{0,h}\ \cos^{1/2}(\alpha_1)}{R_p\ \cos^{3/2}(\alpha_0)}\sqrt{\frac{n_0}{n_1}}\ \sum_{n,m}\ \rho\ R_n^{|m|}(\rho)\exp(im\theta)\ \times$$
$$\Big\{\Big[\beta^m_{n,x,t_+}+\beta^m_{n,x,t_-}\Big]\cos\theta+\Big[\beta^m_{n,y,t_+}+\beta^m_{n,y,t_-}\Big]\sin\theta\Big\}\ , \tag{3.45}$$

$$E^r_{h,z}(\rho,\theta) = \frac{f_1 s_{0,h}\ \cos^{1/2}(\alpha_1)}{R_p\ \cos^{3/2}(\alpha_0)}\sqrt{\frac{n_0}{n_1}}\ \sum_{n,m}\ \rho\ R_n^{|m|}(\rho)\exp(im\theta)\ \times$$
$$(-1)^m\Big\{-\Big[\beta^m_{n,x,r_+}+\beta^m_{n,x,r_-}\Big]\cos\theta-\Big[\beta^m_{n,y,r_+}+\beta^m_{n,y,r_-}\Big]\sin\theta\Big\}\ . \tag{3.46}$$

Finally, these Cartesian spectral components have to be inserted in the diffraction integral. However, as already mentioned in Section 2.4, we can not directly apply Eq.(2.23), as it does not accommodate for counter propagating light contributions. Instead, the integral given in Eq.(2.40) should be used, in which the forward and backward propagating contributions are treated separately. Inserting Eqs.(3.41)-(3.46) and applying the same approach as before, the field in the h-th layer of the focal region can be written as (vector column notation)

$$\mathbf{E^t_{h,2}}(r,\phi,f) = \frac{-i\pi n_1 f_1 s_0^2}{\lambda_0\left[1-Mf_1/R_1\right]}\sqrt{\frac{n_0}{n_1}}\ \exp\left(\frac{-if}{u_{0,h}}\right)\sum_{n,m}(-i)^m\exp[im\phi]\ \times$$
$$\left[\beta^m_{n,x,t_+}\begin{pmatrix} V^m_{n,0,t_+}-\left(\frac{s^2_{0,M}-s^2_{0,h}}{2}\right)\Big\{V^m_{n,+2,t_+}\exp[+2i\phi]+V^m_{n,-2,t_+}\exp[-2i\phi]\Big\} \\ +i\left(\frac{s^2_{0,M}-s^2_{0,h}}{2}\right)\Big\{V^m_{n,+2,t_+}\exp[+2i\phi]-V^m_{n,-2,t_+}\exp[-2i\phi]\Big\} \\ -is_{0,h}\Big\{V^m_{n,+1,t_+}\exp[+i\phi]-V^m_{n,-1,t_+}\exp[-i\phi]\Big\}\end{pmatrix}\right.$$
$$\left.+\beta^m_{n,x,t_-}\begin{pmatrix} V^m_{n,0,t_-}-\left(\frac{s^2_{0,M}-s^2_{0,h}}{2}\right)\Big\{V^m_{n,+2,t_-}\exp[+2i\phi]+V^m_{n,-2,t_-}\exp[-2i\phi]\Big\} \\ +i\left(\frac{s^2_{0,M}-s^2_{0,h}}{2}\right)\Big\{V^m_{n,+2,t_-}\exp[+2i\phi]-V^m_{n,-2,t_-}\exp[-2i\phi]\Big\} \\ -is_{0,h}\Big\{V^m_{n,+1,t_-}\exp[+i\phi]-V^m_{n,-1,t_-}\exp[-i\phi]\Big\}\end{pmatrix}\right]$$

$$+\beta^m_{n,y,t_+}\begin{pmatrix} +i\left(\frac{s^2_{0,M}-s^2_{0,h}}{2}\right)\left\{V^m_{n,+2,t_+}\exp[+2i\phi]-V^m_{n,-2,t_+}\exp[-2i\phi]\right\} \\ V^m_{n,0,t_+}+\left(\frac{s^2_{0,M}-s^2_{0,h}}{2}\right)\left\{V^m_{n,+2,t_+}\exp[+2i\phi]+V^m_{n,-2,t_+}\exp[-2i\phi]\right\} \\ -s_{0,h}\left\{V^m_{n,+1,t_+}\exp[+i\phi]+V^m_{n,-1,t_+}\exp[-i\phi]\right\}\end{pmatrix}$$
$$+\beta^m_{n,y,t_-}\left[\begin{pmatrix} +i\left(\frac{s^2_{0,M}-s^2_{0,h}}{2}\right)\left\{V^m_{n,+2,t_-}\exp[+2i\phi]-V^m_{n,-2,t_-}\exp[-2i\phi]\right\} \\ V^m_{n,0,t_-}+\left(\frac{s^2_{0,M}-s^2_{0,h}}{2}\right)\left\{V^m_{n,+2,t_-}\exp[+2i\phi]+V^m_{n,-2,t_-}\exp[-2i\phi]\right\} \\ -s_{0,h}\left\{V^m_{n,+1,t_-}\exp[+i\phi]+V^m_{n,-1,t_-}\exp[-i\phi]\right\}\end{pmatrix}\right], \tag{3.47}$$

for the forward propagating contribution and in a similar fashion we get for the counter propagating contribution

$$\mathbf{E}^{\mathbf{r}}_{\mathbf{h},\mathbf{2}}(r,\phi,f)=\frac{-i\pi n_1 f_1 s_0^2}{\lambda_0\left[1-Mf_1/R_1\right]}\sqrt{\frac{n_0}{n_1}}\,\exp\left(\frac{if}{u_{0,h}}\right)\sum_{n,m}(-i)^m\exp[im\phi]\times$$
$$\left[\beta^m_{n,x,r_+}\begin{pmatrix} -V^m_{n,0,r_-}+\left(\frac{s^2_{0,M}-s^2_{0,h}}{2}\right)\left\{V^m_{n,+2,r_-}\exp[+2i\phi]+V^m_{n,-2,r_-}\exp[-2i\phi]\right\} \\ -i\left(\frac{s^2_{0,M}-s^2_{0,h}}{2}\right)\left\{V^m_{n,+2,r_-}\exp[+2i\phi]-V^m_{n,-2,r_-}\exp[-2i\phi]\right\} \\ -is_{0,h}\left\{V^m_{n,+1,r_-}\exp[+i\phi]-V^m_{n,-1,r_-}\exp[-i\phi]\right\}\end{pmatrix}\right.$$
$$+\beta^m_{n,x,r_-}\begin{pmatrix} -V^m_{n,0,r_+}+\left(\frac{s^2_{0,M}-s^2_{0,h}}{2}\right)\left\{V^m_{n,+2,r_+}\exp[+2i\phi]+V^m_{n,-2,r_+}\exp[-2i\phi]\right\} \\ -i\left(\frac{s^2_{0,M}-s^2_{0,h}}{2}\right)\left\{V^m_{n,+2,r_+}\exp[+2i\phi]-V^m_{n,-2,r_+}\exp[-2i\phi]\right\} \\ -is_{0,h}\left\{V^m_{n,+1,r_+}\exp[+i\phi]-V^m_{n,-1,r_+}\exp[-i\phi]\right\}\end{pmatrix}$$
$$+\beta^m_{n,y,r_+}\begin{pmatrix} -i\left(\frac{s^2_{0,M}-s^2_{0,h}}{2}\right)\left\{V^m_{n,+2,r_-}\exp[+2i\phi]-V^m_{n,-2,r_-}\exp[-2i\phi]\right\} \\ -V^m_{n,0,r_-}-\left(\frac{s^2_{0,M}-s^2_{0,h}}{2}\right)\left\{V^m_{n,+2,r_-}\exp[+2i\phi]+V^m_{n,-2,r_-}\exp[-2i\phi]\right\} \\ -s_{0,h}\left\{V^m_{n,+1,r_-}\exp[+i\phi]+V^m_{n,-1,r_-}\exp[-i\phi]\right\}\end{pmatrix}$$
$$\left.+\beta^m_{n,y,r_-}\begin{pmatrix} -i\left(\frac{s^2_{0,M}-s^2_{0,h}}{2}\right)\left\{V^m_{n,+2,r_+}\exp[+2i\phi]-V^m_{n,-2,r_+}\exp[-2i\phi]\right\} \\ -V^m_{n,0,r_+}-\left(\frac{s^2_{0,M}-s^2_{0,h}}{2}\right)\left\{V^m_{n,+2,r_+}\exp[+2i\phi]+V^m_{n,-2,r_+}\exp[-2i\phi]\right\} \\ -s_{0,h}\left\{V^m_{n,+1,r_+}\exp[+i\phi]+V^m_{n,-1,r_+}\exp[-i\phi]\right\}\end{pmatrix}\right], \tag{3.48}$$

with $s_{0,M}$ and $s_{o,h}$ already defined in Eq.(2.33). Again, the integrals $V^m_{n,j,t_\pm}$ occurring in the expressions above have changed compared to the case of imaging in homogeneous space. The $V^m_{n,j,t_\pm}$-functions, with $j=-2,-1,0,+1,+2$, are now

given by

$$V^m_{n,j,t_\pm}(r,f) = \int_0^1 \rho^{|j|} \frac{\left\{\left(1-s^2_{0,h}\rho^2\right)^{\frac{1}{2}} \pm \left(1-s^2_{0,M}\rho^2\right)^{\frac{1}{2}}\right\}^{-|j|+1}}{(1-s^2_0\rho^2)^{\frac{1}{4}}\left(1-s^2_{0,M}\rho^2\right)^{\frac{3}{4}}} \times \exp\left[\frac{if}{u_{0,h}}\left(1-\sqrt{1-s^2_{0,h}\rho^2}\right)\right] R^{|m|}_n(\rho) J_{m+j}(2\pi r\rho)\rho d\rho. \tag{3.49}$$

and we also immediately find for absorption-free media that

$$V^m_{n,j,r_\pm}(r,f) = \left(V^m_{n,j,t_\pm}(r,-f)\right)^* \ . \tag{3.50}$$

These integrals can also be computed efficiently and the corresponding recipe is provided in Appendix A.6.

As in Section 3.3.3, we also derive expressions for the magnetic induction in order to enable the calculation of the power flow and momentum flux in a specific layer of the multilayer stack. For this we require the unit propagation vector in the layer of interest, h, which has a refractive index n_h. This unit vector is thus given by

$$\begin{aligned}\hat{\mathbf{k}}_{\mathbf{h}}(\rho,\theta) &= \left(-\rho\, n_1 s_0 \cos\theta/n_h, -\rho\, n_1 s_0 \sin\theta/n_h, [1-(\rho\, n_1 s_0/n_h)^2]^{1/2}\right) \\ &= (-\sin(\alpha_h)\cos\theta, -\sin(\alpha_h)\sin\theta, \cos(\alpha_h)) \ .\end{aligned} \tag{3.51}$$

where we have used $\varepsilon^{1/2} = n_h(\varepsilon_0)^{1/2}$. Using this quantity to obtain the magnetic induction on the exit pupil sphere and performing the Debye integral for the magnetic induction components we find the following quantities in the focal region (transmitted components in vector notation),

$$\mathbf{B}^{\mathbf{t}}_{\mathbf{h},\mathbf{2}}(r,\phi,f) = \frac{-i\pi n_1 n_h f_1 s_0^2}{\lambda_0\, c\,[1-Mf_1/R_1]}\sqrt{\frac{n_0}{n_1}}\, \exp\left(\frac{-if}{u_{0,h}}\right)\sum_{n,m}(-i)^m \exp[im\phi] \times$$

$$\left[\beta^m_{n,x,t_+}\begin{pmatrix} +i\left(\frac{s^2_{0,M}-s^2_{0,h}}{2}\right)\left\{V^m_{n,+2,t_+}\exp[+2i\phi] - V^m_{n,-2,t_+}\exp[-2i\phi]\right\} \\ +V^m_{n,0,t_+} + \left(\frac{s^2_{0,M}-s^2_{0,h}}{2}\right)\left\{V^m_{n,+2,t_+}\exp[+2i\phi] + V^m_{n,-2,t_+}\exp[-2i\phi]\right\} \\ -s_{0,h}\left\{V^m_{n,+1,t_+}\exp[+i\phi] + V^m_{n,-1,t_+}\exp[-i\phi]\right\}\end{pmatrix}\right.$$

$$\left.+\beta^m_{n,x,t_-}\begin{pmatrix} +i\left(\frac{s^2_{0,M}-s^2_{0,h}}{2}\right)\left\{V^m_{n,+2,t_-}\exp[+2i\phi] - V^m_{n,-2,t_-}\exp[-2i\phi]\right\} \\ +V^m_{n,0,t_-} + \left(\frac{s^2_{0,M}-s^2_{0,h}}{2}\right)\left\{V^m_{n,+2,t_-}\exp[+2i\phi] + V^m_{n,-2,t_-}\exp[-2i\phi]\right\} \\ -s_{0,h}\left\{V^m_{n,+1,t_-}\exp[+i\phi] + V^m_{n,-1,t_-}\exp[-i\phi]\right\}\end{pmatrix}\right]$$

$$
+\beta^m_{n,y,t_+}\begin{pmatrix} -V^m_{n,0,t_+} + \left(\frac{s^2_{0,M}-s^2_{0,h}}{2}\right)\left\{V^m_{n,+2,t_+}\exp[+2i\phi] + V^m_{n,-2,t_+}\exp[-2i\phi]\right\} \\ -i\left(\frac{s^2_{0,M}-s^2_{0,h}}{2}\right)\left\{V^m_{n,+2,t_+}\exp[+2i\phi] - V^m_{n,-2,t_+}\exp[-2i\phi]\right\} \\ +is_{0,h}\left\{V^m_{n,+1,t_+}\exp[+i\phi] - V^m_{n,-1,t_+}\exp[-i\phi]\right\}\end{pmatrix}
$$

$$
+\beta^m_{n,y,t_-}\begin{pmatrix} -V^m_{n,0,t_-} + \left(\frac{s^2_{0,M}-s^2_{0,h}}{2}\right)\left\{V^m_{n,+2,t_-}\exp[+2i\phi] + V^m_{n,-2,t_-}\exp[-2i\phi]\right\} \\ -i\left(\frac{s^2_{0,M}-s^2_{0,h}}{2}\right)\left\{V^m_{n,+2,t_-}\exp[+2i\phi] - V^m_{n,-2,t_-}\exp[-2i\phi]\right\} \\ +is_{0,h}\left\{V^m_{n,+1,t_-}\exp[+i\phi] - V^m_{n,-1,t_-}\exp[-i\phi]\right\}\end{pmatrix}\Bigg]. \tag{3.52}
$$

The backward propagating components of the magnetic induction are obtained in a similar way, with the unit vector $\mathbf{s}$ replaced by its negative counterpart for each reflected plane wave component, and we obtain

$$
\mathbf{B}^{\mathbf{r}}_{\mathbf{h},\mathbf{2}}(r,\phi,f) = \frac{-i\pi n_1 n_h f_1 s_0^2}{\lambda_0\, c\,[1-Mf_1/R_1]}\sqrt{\frac{n_0}{n_1}}\,\exp\left(\frac{if}{u_{0,h}}\right)\sum_{n,m}(-i)^m\exp[im\phi]\times
$$

$$
\Bigg[\beta^m_{n,x,r_+}\begin{pmatrix} +i\left(\frac{s^2_{0,M}-s^2_{0,h}}{2}\right)\left\{V^m_{n,+2,r_-}\exp[+2i\phi] - V^m_{n,-2,r_-}\exp[-2i\phi]\right\} \\ +V^m_{n,0,r_-} + \left(\frac{s^2_{0,M}-s^2_{0,h}}{2}\right)\left\{V^m_{n,+2,r_-}\exp[+2i\phi] + V^m_{n,-2,r_-}\exp[-2i\phi]\right\} \\ s_{0,h}\left\{V^m_{n,+1,r_-}\exp[+i\phi] + V^m_{n,-1,r_-}\exp[-i\phi]\right\}\end{pmatrix}
$$

$$
+\beta^m_{n,x,r_-}\begin{pmatrix} +i\left(\frac{s^2_{0,M}-s^2_{0,h}}{2}\right)\left\{V^m_{n,+2,r_+}\exp[+2i\phi] - V^m_{n,-2,r_+}\exp[-2i\phi]\right\} \\ +V^m_{n,0,r_+} + \left(\frac{s^2_{0,M}-s^2_{0,h}}{2}\right)\left\{V^m_{n,+2,r_+}\exp[+2i\phi] + V^m_{n,-2,r_+}\exp[-2i\phi]\right\} \\ s_{0,h}\left\{V^m_{n,+1,r_+}\exp[+i\phi] + V^m_{n,-1,r_+}\exp[-i\phi]\right\}\end{pmatrix}
$$

$$
+\beta^m_{n,y,r_+}\begin{pmatrix} -V^m_{n,0,r_-} + \left(\frac{s^2_{0,M}-s^2_{0,h}}{2}\right)\left\{V^m_{n,+2,r_-}\exp[+2i\phi] + V^m_{n,-2,r_-}\exp[-2i\phi]\right\} \\ -i\left(\frac{s^2_{0,M}-s^2_{0,h}}{2}\right)\left\{V^m_{n,+2,r_-}\exp[+2i\phi] - V^m_{n,-2,r_-}\exp[-2i\phi]\right\} \\ -is_{0,h}\left\{V^m_{n,+1,r_-}\exp[+i\phi] - V^m_{n,-1,r_-}\exp[-i\phi]\right\}\end{pmatrix}
$$

$$
+\beta^m_{n,y,r_-}\begin{pmatrix} -V^m_{n,0,r_+} + \left(\frac{s^2_{0,M}-s^2_{0,h}}{2}\right)\left\{V^m_{n,+2,r_+}\exp[+2i\phi] + V^m_{n,-2,r_+}\exp[-2i\phi]\right\} \\ -i\left(\frac{s^2_{0,M}-s^2_{0,h}}{2}\right)\left\{V^m_{n,+2,r_+}\exp[+2i\phi] - V^m_{n,-2,r_+}\exp[-2i\phi]\right\} \\ -is_{0,h}\left\{V^m_{n,+1,r_+}\exp[+i\phi] - V^m_{n,-1,r_+}\exp[-i\phi]\right\}\end{pmatrix}\Bigg]. \tag{3.53}
$$

The expressions derived in this section give us access to the full electromagnetic field in a given uniform layer of a more general multilayered region. A stratified medium in image space may contain absorbing layers or layers where frustrated total reflection takes place via evanescent fields or plasmon creation. However, our implementation so far does not allow to calculate the field in a sublayer that itself shows absorption or where the plane wave spectrum comprises evanescent components. Especially in lithographic applications, where one wants to compute

the intensity distribution in a layer of photoresist that is absorptive, this poses a limitation. Research in order to extend the applicability of the formalism to also include this situation is ongoing.

In this section, we have dealt with a systematic analysis of image formation in layers in image space that are oriented perpendicular to the optical axis. Here, it is basically assumed that these layers extend infinitely into the x- and y-direction. When this assumption is not met, it becomes highly improbable that an analytic description of the focal field can be found. This is, for example, the case in lithographic imaging, where one tries to produce an image in a layer of resist that is deposited on top of a highly structured surface that resulted from preceding lithographic steps. Here we are faced with image formation in a region that can have almost arbitrary shapes and can consist of a high number of different materials. To obtain in this case the field in image space, one has to resort to numerical methods solving Maxwell's equations (see for example [69]).

3.6 NA-reduced and annular pupils

In many fields of optics one encounters optical systems that operate below their maximum numerical aperture (NA). For example, in lithography, the NA is varied to optimize the image performance of certain lithographic features [70]. In another field of optics, astronomy, one often has to deal with a pupil that has a central obstruction, and this can also be considered as a full pupil minus a NA-reduced pupil. Whenever the pupil of an optical system is not used to its full extent, this will result in a different behavior of the optical system in terms of its aberrations and imaging performance (see for example [62, 71–73]). In this section, we show how scaled and annularly shaped pupils, and their corresponding PSF's, can be efficiently described using the ENZ theory.

3.6.1 Zernike representation of a NA-reduced pupil

The basic theoretical results used to describe scaled pupils within the ENZ formalism are presented in [74]. Suppose we have a general pupil distribution $P(\rho, \theta)$, with corresponding set of Zernike coefficients β_n^m (see Eq.(3.10). We now seek to find the Zernike expansion of a reduced version of this pupil, where $0 \leq \rho \leq \varepsilon$ with ε being the reduction factor (see middle pupil in Figure 3.8). We have

$$P(\varepsilon\rho, \theta) = \sum_{n,m} \beta_n^m(\varepsilon)\, R_n^{|m|}(\rho) \exp(im\theta) \;, \qquad 0 \leq \rho \leq 1 \;, \quad 0 \leq \theta \leq 2\pi \;, \tag{3.54}$$

with $\beta_n^m(\varepsilon)$ the coefficients describing the reduced pupil. We would then like to relate the $\beta_n^m(\varepsilon)$ to the β_n^m occurring in the Zernike expansion of the unscaled pupil, $P(\rho, \theta)$. In [74], this relation is given as

$$\beta_n^m(\varepsilon) = \sum_{n'} \left(R_{n'}^n(\varepsilon) - R_{n'}^{n+2}(\varepsilon)\right) \beta_{n'}^m \;, \qquad n = |m|, |m|+2, \ldots \;, \tag{3.55}$$

where the summation is over $n' = n, n+2, ...$, and where the convention was used that $R_n^{n+2} = 0$.

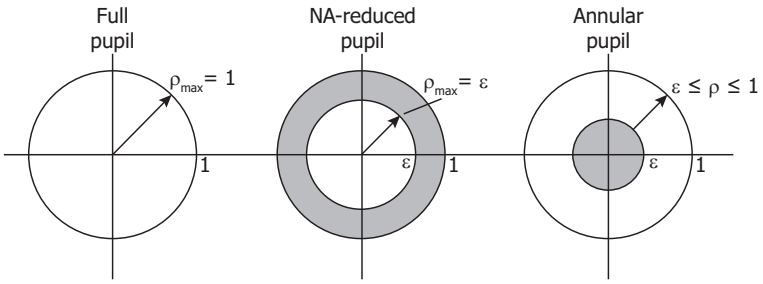

Figure 3.8: *Schematic representation of the pupil configurations discussed in this section. On the left we have the full pupil that is defined on the unit disk* $(0 \leq \rho \leq 1)$*. In the middle a scaled pupil is shown which, for example, can be obtained by obscuring the outer part of the pupil using a diaphragm* $(0 \leq \rho \leq \varepsilon)$*. On the right a so-called annular pupil is shown that is formed by obscuring the center part of the pupil using a disk* $(\varepsilon \leq \rho \leq 1)$*.*

Using Eq.(3.55), we are able to compute the Zernike coefficients describing the field on the reduced pupil, that results when only a fraction ε of the full pupil radius is considered, from the Zernike coefficients yielding the full pupil distribution. Using the same results, we can also treat an annular pupil simply by subtracting an NA-reduced pupil distribution from that of the full pupil. In [75] the scaling of pupils is discussed in more detail and in Chapter 5 we will also treat some examples in which the scaling of pupils is involved.

3.6.2 PSF of a NA-reduced pupil

When we consider the operation of an optical system using a subset of the full pupil, or in other words apply only a fraction of the maximum NA of the system, this will also have its influence on the PSF. Here we discuss this issue within the ENZ formalism. We again assume to have a smooth pupil function $P(\rho, \theta)$, $0 \leq \rho \leq 1$, $0 \leq \theta \leq 2\pi$. Now, reducing the numerical aperture (NA) to a fraction $\varepsilon \leq 1$ of its maximum value means that we set $P(\rho, \theta) = 0$ outside the disk $0 \leq \rho \leq \varepsilon$, $0 \leq \theta \leq 2\pi$ and leave P as it is inside the disk. In order to obtain convenient forms for the scalar field U, it is, in principle, possible to expand the new $P = P_\varepsilon$ as a Zernike series on the full disk $0 \leq \rho \leq 1$, $0 \leq \theta \leq 2\pi$. However, the resulting series has poorly decaying coefficients, due to the discontinuity at $\rho = \varepsilon$ (Ref. [75], Appendix C is explicit about this). We therefore choose for a different approach in which we observe that the new $U = U_\varepsilon$ is obtained as

$$\begin{aligned} U_\varepsilon(r, \phi, f) &= \frac{1}{\pi} \int_0^\varepsilon \int_0^{2\pi} \exp(if\rho^2)\, P(\rho, \theta)\, \exp\{2\pi i r \rho \cos(\theta - \phi)\}\, \rho\, d\rho\, d\theta \\ &= \frac{\varepsilon^2}{\pi} \int_0^1 \int_0^{2\pi} \exp(if\varepsilon^2\rho^2)\, P(\varepsilon\rho, \theta)\, \exp\{2\pi i r \varepsilon \rho \cos(\theta - \phi)\}\, \rho\, d\rho\, d\theta \end{aligned} \tag{3.56}$$

in which the last expression in Eq.(3.56) has been obtained from the middle one by changing the variable ρ, $0 \le \rho \le \varepsilon$, into $\varepsilon\rho$, $0 \le \rho \le 1$. From the Zernike expansion of the scaled pupil function given in Eq.(3.54), with $\beta_n^m(\varepsilon)$ given by Eq.(3.55), we then get

$$U_\varepsilon(r,\phi,f) = 2\varepsilon^2 \sum_{n,m} i^{|m|}\, \beta_n^m(\varepsilon)\, V_n^{|m|}(\varepsilon r, \varepsilon^2 f) \exp(im\phi) \ . \tag{3.57}$$

An alternative approach, leading to the same computation scheme for U_ε, is to insert the Zernike expansion of Eq.(3.10) into the first double-integral expression in Eq.(3.56). Using $Z_n^m(\rho,\theta) = R_n^m(\rho)\cos m\theta$, this leads to

$$U_\varepsilon(r,\phi,f) = 2 \sum_{n,m} i^{|m|}\, \beta_n^m\, V_n^{|m|}(r, f\,;\,\varepsilon) \cos m\phi \ , \tag{3.58}$$

where

$$V_n^m(r, f\,;\,\varepsilon) = \int_0^\varepsilon \exp(if\rho^2)\, R_n^{|m|}(\rho)\, J_m(2\pi r\rho)\, \rho\, d\rho \ . \tag{3.59}$$

With the substitution $\rho = \varepsilon\rho_1$, $0 \le \rho_1 \le 1$, in the latter integral and using (see Eq.(25) in [75])

$$R_{n'}^m(\varepsilon\rho) = \sum_n \left(R_{n'}^n(\varepsilon) - R_{n'}^{n+2}(\varepsilon)\right) R_n^m(\rho) \ , \qquad n' = m, m+2, \ldots \ , \tag{3.60}$$

to write $R_n^m(\varepsilon\rho_1)$ as linear combination of the $R_n^m(\rho_1)$, we get from Eq.(3.12)

$$V_n^m(r, f\,;\,\varepsilon) = \varepsilon^2 \sum_{n'} \left(R_n^{n'}(\varepsilon) - R_n^{n'+2}(\varepsilon)\right) V_{n'}^m(r\varepsilon, f\varepsilon^2) \ . \tag{3.61}$$

The advantage of Eq.(3.58) and Eq.(3.61) over Eq.(3.57) is that the expression of Eq.(3.58) is directly in terms of the Zernike coefficients of the unscaled pupil function and that the scaling operation is completely represented by the modification of V_n^m-functions as in Eq.(3.61).

In a similar fashion we can compute point-spread functions pertaining to a pupil function P that vanishes for $0 \le \rho < \varepsilon$. In this case, the scalar field U of the PSF corresponding to this P is given by

$$U(r,\phi,f) = 2 \sum_{n,m} i^{|m|}\, \beta_n^m\, W_n^{|m|}(r, f\,;\,\varepsilon) \cos m\phi \ , \tag{3.62}$$

where

$$\begin{aligned} W_n^m(r, f\,;\,\varepsilon) &= \int_\varepsilon^1 e^{if\rho^2}\, R_n^m(\rho)\, J_m(2\pi r\rho)\, \rho\, d\rho \ = \\ &= V_n^m(r,f) - V_n^m(r, f\,;\,\varepsilon) \ , \end{aligned} \tag{3.63}$$

with $V_n^m(r,f)$ and $V_n^m(r, f\,;\,\varepsilon)$ given in (3.12) and (3.61), respectively.

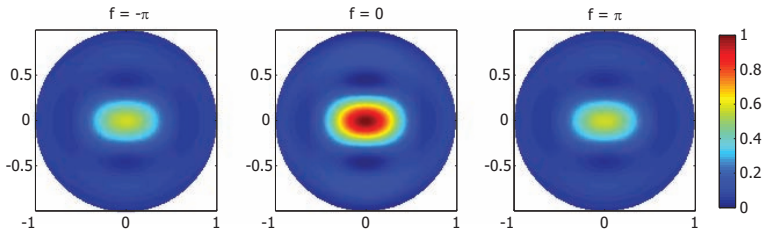

Figure 3.9: *The aberration-free PSF for an optical system* (NA = 0.95, *x-polarization*) *having an annular pupil with* $\varepsilon = 0.5$ (*see right-most image of Figure 3.8*). *Normalization and axis-scaling is identical to that of Figure 3.5.*

3.6.3 Pupil scaling in high-NA systems

So far, we have limited our discussion to scaled and annular pupils of scalar optical systems. However, in Section 3.3 we have introduced an ENZ-based approach to calculate the PSF of high-NA optical systems. This treatment of high-NA optical systems, though involved, is still based on the availability of computational schemes for the basic integrals $V_{n,j}^m$ (see for example Eq.(3.23). In the case that the pupil function is thresholded to zero in a set $\varepsilon \leq \rho < 1$, the integration ranges of the integrals in Eq.(3.23) have to be changed from $[0,1]$ to $[0,\varepsilon]$, yielding the high-NA versions of the $V_n^m(r,f\,;\,\varepsilon)$ in Eq.(3.59). Following the same approach as to arrive at Eq.(3.60) from Eq.(3.59), we get

$$V_{n,j}^m(r,f,s_0\,;\,\varepsilon) = \sum_{n'} \varepsilon^{|j|+2}(R_n^{n'}(\varepsilon) - R_n^{n'+2}(\varepsilon))\, V_{n',j}^m\Big(r\varepsilon, f\,\frac{u_0(\varepsilon)}{u_0}\,, s_0\varepsilon\Big)\ , \quad (3.64)$$

in which $u_0(\varepsilon) = 1-\sqrt{1-(s_0\varepsilon)^2}$. Hence, the calculation of point-spread functions for high-NA systems with thresholded pupil functions can still be done on the level of the Zernike coefficients of the full pupil function. Also, in the case of a pupil function obstructed in the disk $0 \leq \rho < \varepsilon$, we can do ENZ computation under high-NA conditions by replacing the W_n^m in Eq.(3.63) by

$$W_{n,j}^m(r,f,s_0\,;\,\varepsilon) = V_{n,j}^m(r,f,s_0) - V_{n,j}^m(r,f,s_0\,;\,\varepsilon)\ . \quad (3.65)$$

In Figure 3.9 the aberration free PSF is shown for an optical system in which the aperture is obscured in the region $0 \leq \rho \leq \frac{1}{2}$. In comparison to the second row of Figure 3.5 the PSF for an annular pupil has, as expected, an improved depth of focus. This is one of the main reasons why annular pupils are used in optics.

3.6.4 Pupils having a multi-ringed configuration

Taking the arguments above a bit further, we are also able to compute the PSF for optical systems having a multi-ringed pupil. Assume we have a pupil function $P(\rho,\theta)$, $0 \leq \rho \leq 1$, $0 \leq \theta \leq 2\pi$, with a Zernike expansion as in Eq.(3.10), and

numbers

$$0 = \varepsilon_0 < \varepsilon_1 < ... < \varepsilon_J = 1 \; ; \qquad a_1, a_2, ..., a_J \in C \; , \tag{3.66}$$

and consider as pupil function

$$\tilde{P}(\rho, \theta) = a_j \, P(\rho, \theta) \; , \qquad \varepsilon_{j-1} \leq \rho < \varepsilon_j \; , \quad 0 \leq \theta \leq 2\pi \; , \tag{3.67}$$

with j running from 1 to J. Then the point-spread function $\tilde{U}$ corresponding to $\tilde{P}$ is given by

$$\tilde{U}(r, \phi, f) = 2 \sum_{n,m} i^m \, \beta_n^m \, \tilde{V}_n^m(r, f) \cos m\phi \tag{3.68}$$

in which

$$\begin{aligned} \tilde{V}_n^m(r, f) &= \sum_{j=1}^{J} a_j \int_{\varepsilon_{j-1}}^{\varepsilon_j} e^{if\rho^2} \, R_n^m(\rho) \, J_m(2\pi r \rho) \, \rho \, d\rho \\ &= \sum_{j=1}^{J} a_j \, [V_n^m(r, f \, ; \, \varepsilon_j) - V_n^m(r, f \, ; \, \varepsilon_{j-1})] \end{aligned} \tag{3.69}$$

with $V_n^m(r, f \, ; \, \varepsilon)$ given in Eq.(3.61). These expressions could, for example, be used to simulate the performance of a Fresnel lens or zone plate that have a discontinues step-like phase or amplitude distribution in the pupil.

3.7 Electromagnetic quantities in the focal region

In this chapter, we produce expressions to compute the electric and magnetic field components in the focal region of an optical system for a variety of different cases. These basic quantities are needed to evaluate the optical quantities like energy density, intensity, linear impulse and angular momentum that are built up in and transported through the focal region. Although these quantities, time-averaged at optical frequencies, can be obtained in each point from the electromagnetic field vectors only, we will present in this section a detailed analysis to represent the electromagnetic quantities in focus in terms of the typical distributions associated with particular aberrations [76]. We will need these expressions, for example, in Chapter 4 when we address ENZ-based system characterization using intensity measurements in the focal region. In addition, these expressions, in contrast with the common numerical integration approach, provide us with valuable insight in the physical mechanisms that generate all the interesting phenomena that occur when optical beams are strongly focused.

3.7.1 Expression for the electric energy density

The time averaged value of the electric field energy density $\langle w_e \rangle$, which is related to the intensity as $I = \frac{c}{n_r}\langle w_e \rangle$, is given by

$$\langle w_e \rangle = \frac{\epsilon_0}{2} n_r^2 |\mathbf{E}|^2 \, , \tag{3.70}$$

with the relative dielectric constant given by $\epsilon = n_r^2$. The electric field components in the presence of aberrations in a high-numerical-aperture system (object at $-\infty$), as given by Eq.(3.22), are needed to compute the scalar product $\mathbf{E}^* \cdot \mathbf{E}$. The direct evaluation of $\langle w_e \rangle$ leads to a quadruple sum over the indices n, m, $n^{'}$ and $m^{'}$ that appear in the products of the electric field components. For notational purposes, we introduce

$$\begin{aligned} G_{kl}(\beta_1, \beta_2) &= \sum_{n,m} i^m \exp\left[im\phi\right] \; \beta_{n,1}^m V_{n,k}^m(r,f) \exp\left[ik\phi\right] \times \\ &\qquad \sum_{n',m'} i^{-m'} \exp\left[-im'\phi\right] \beta_{n',2}^{m'\,*} V_{n',l}^{m'\,*}(r,f) \exp\left[-il\phi\right] \\ &= \sum_{n,m,n',m'} \exp\left[i(m-m')\pi/2\right] \; \exp\left[i(m-m'+k-l)\phi\right] \times \\ &\qquad \beta_{n,1}^m \beta_{n',2}^{m'\,*} V_{n,k}^m(r,f) V_{n',l}^{m'\,*}(r,f) \;\; , \end{aligned} \tag{3.71}$$

where the function G_{kl} has the sets of Zernike coefficients $\beta_{n,1}^m$ and $\beta_{n,2}^m$ as variables, in shorthand notation written as β_1 and β_2 in the argument of G_{kl}. The indices $\{kl\}$ stem from the various combinations of $V_{n,j}^m \exp[i(j\phi)]$-functions that occur in the summation. Using Eq.(3.22) and Eq.(3.71) the electric energy density can be written as (for details see [48], §3)

$$\begin{aligned} \langle w_e(r,\phi,f) \rangle = \frac{\epsilon_0 n_r^2 k_0^2 f_1^2 s_0^4}{8} \Big[& G_{0,0}(\beta_x,\beta_x) + G_{0,0}(\beta_y,\beta_y) \\ & + s_0^2 \Re\left\{ G_{0,2}(\beta_x,\beta_x) + iG_{0,2}(\beta_x,\beta_y) + iG_{0,2}(\beta_y,\beta_x) - G_{0,2}(\beta_y,\beta_y) \right\} \\ & + s_0^2 \Re\left\{ G_{0,-2}(\beta_x,\beta_x) - iG_{0,-2}(\beta_x,\beta_y) - iG_{0,-2}(\beta_y,\beta_x) - G_{0,-2}(\beta_y,\beta_y) \right\} \\ & + \frac{s_0^4}{2} \left\{ G_{2,2}(\beta_x,\beta_x) + iG_{2,2}(\beta_x,\beta_y) - iG_{2,2}(\beta_y,\beta_x) + G_{2,2}(\beta_y,\beta_y) \right\} \\ & + \frac{s_0^4}{2} \left\{ G_{-2,-2}(\beta_x,\beta_x) - iG_{-2,-2}(\beta_x,\beta_y) + iG_{-2,-2}(\beta_y,\beta_x) + G_{-2,-2}(\beta_y,\beta_y) \right\} \\ & + s_0^2 \left\{ G_{1,1}(\beta_x,\beta_x) + iG_{1,1}(\beta_x,\beta_y) - iG_{1,1}(\beta_y,\beta_x) + G_{1,1}(\beta_y,\beta_y) \right\} \\ & + s_0^2 \left\{ G_{-1,-1}(\beta_x,\beta_x) - iG_{-1,-1}(\beta_x,\beta_y) + iG_{-1,-1}(\beta_y,\beta_x) + G_{-1,-1}(\beta_y,\beta_y) \right\} \\ & + 2s_0^2 \Re\left\{ -G_{1,-1}(\beta_x,\beta_x) + iG_{1,-1}(\beta_x,\beta_y) + iG_{1,-1}(\beta_y,\beta_x) + G_{1,-1}(\beta_y,\beta_y) \right\} \Big] . \end{aligned} \tag{3.72}$$

with k_0 the vacuum wave number and f_1 again the focal length of the imaging system. The indices x, y of β in the arguments of the G_{kl}-functions refer to the

Zernike coefficients, $\beta_{n,x}^m$ and $\beta_{n,y}^m$, used to describe the x and y field components in the pupil. The expression above is, within the framework of the approximations related to the Debye integral, a rigorous expression for the energy density in the focal region for a general optical system suffering from transmission defects, wavefront aberration and spatially varying birefringence over the pupil cross-section.

In the often occurring case that the optical system is free of birefringence we can write the aberration coefficients as $\beta_{n,x}^m = p_x \beta_n^m$ and $\beta_{n,y}^m = p_y \beta_n^m$, respectively. As a result the electric energy density can be written as

$$\begin{aligned}\langle w_e(r,\phi,f)\rangle = \frac{\epsilon_0 n_r^2 k_0^2 f_1^2 s_0^4}{8} \Big[& G_{0,0}(\beta,\beta) \\ & + s_0^2 \left\{ \left[|p_x|^2 - |p_y|^2 \right] \Re\{G_{0,2}(\beta,\beta)\} - 2\Re(p_x p_y^*)\Im\{G_{0,2}(\beta,\beta)\} \right\} \\ & + s_0^2 \left\{ \left[|p_x|^2 - |p_y|^2 \right] \Re\{G_{0,-2}(\beta,\beta)\} + 2\Re(p_x p_y^*)\Im\{G_{0,-2}(\beta,\beta)\} \right\} \\ & + \frac{s_0^4}{2} \left[\left\{ 1 - 2\Im(p_x p_y^*) \right\} G_{2,2}(\beta,\beta) + \left\{ 1 + 2\Im(p_x p_y^*) \right\} G_{-2,-2}(\beta,\beta) \right] \\ & + s_0^2 \left[\left\{ 1 - 2\Im(p_x p_y^*) \right\} G_{1,1}(\beta,\beta) + \left\{ 1 + 2\Im(p_x p_y^*) \right\} G_{-1,-1}(\beta,\beta) \right] \\ & - 2s_0^2 \left\{ \left[|p_x|^2 - |p_y|^2 \right] \Re\left\{ G_{+1,-1}(\beta,\beta) \right\} + 2\Re(p_x p_y^*)\Im\left\{ G_{+1,-1}(\beta,\beta) \right\} \right\} \Big] . \end{aligned} \tag{3.73}$$

This analytic expression, representing the energy density in the focal region, will be used in Section 4.2 to construct the vectorial ENZ inversion scheme.

3.7.2 Expression for the Poynting vector

To examine the energy flow through the focal region, the time averaged value of the Cartesian components of the Poynting vector S has to be found. The expression for the time averaged Poynting vector is given by

$$\langle \mathbf{S} \rangle = \frac{\epsilon_0 c^2}{2} \Re\left\{ \mathbf{E} \times \mathbf{B}^* \right\} . \tag{3.74}$$

We introduce the vector $\mathbf{q} = [c/(n_r \gamma^2 s_0^4)](\mathbf{E} \times \mathbf{B}^*)$, with $\gamma = \frac{\pi R_1}{\lambda}$ and, using Eqs.(3.22) and (3.24) for the electromagnetic field vectors, we obtain, after some lengthy manipulation, the following expressions for the components q_x, q_y and q_z,

$$\begin{aligned} q_x \;=\; & s_0 \Big\{ -2ip_x^* p_y [\Im(G_{0,1}) + \Im(G_{0,-1})] \\ & \qquad + i \left\{ |p_x|^2 \left[G_{1,0} - G_{-1,0} \right] - |p_y|^2 \left[G_{0,1} - G_{0,-1} \right] \right\} \Big\} \\ & - s_0^3 \Big\{ \left[1 - 2\Im(p_x p_y^*) \right] \Im(G_{2,1}) - \left[1 + 2\Im(p_x p_y^*) \right] \Im(G_{-2,-1}) \\ & \qquad + 2i\Re(p_x p_y^*)\Im(G_{1,-2} - G_{2,-1}) + i \left[|p_x|^2 - |p_y|^2 \right] \Re(G_{1,-2} - G_{2,-1}) \Big\}, \end{aligned} \tag{3.75}$$

$$
\begin{aligned}
q_y &= s_0\Big\{2ip_xp_y^*[\Re(G_{0,1})-\Re(G_{0,-1})] \\
&\quad +|p_x|^2\left[G_{0,1}+G_{0,-1}\right]+|p_y|^2\left[G_{1,0}+G_{-1,0}\right]\Big\} \\
&\quad +s_0^3\Big\{\left[1-2\Im(p_xp_y^*)\right]\Re(G_{2,1})+\left[1+2\Im(p_xp_y^*)\right]\Re(G_{-2,-1}) \\
&\quad +2i\Re(p_xp_y^*)\Re(G_{1,-2}-G_{2,-1})-i\left[|p_x|^2-|p_y|^2\right]\Im(G_{1,-2}-G_{2,-1})\Big\}\ ,
\end{aligned}
\tag{3.76}
$$

$$
\begin{aligned}
q_z &= G_{0,0}-s_0^2\Big\{i\left[|p_x|^2-|p_y|^2\right]\Im(G_{0,2})+2i\Re(p_xp_y^*)\Re(G_{0,2}) \\
&\quad +i\left[|p_x|^2-|p_y|^2\right]\Im(G_{0,-2})-2i\Re(p_xp_y^*)\Re(G_{0,-2})\Big\} \\
&\quad -\frac{s_0^4}{2}\Big\{\left[1-2\Im(p_xp_y^*)\right]G_{2,2}+\left[1+2\Im(p_xp_y^*)\right]G_{-2,-2}\Big\}.
\end{aligned}
\tag{3.77}
$$

where we have again used a notation based on the G_{kl}-functions defined in Eq.(3.71) and the general property $G_{kl}^*(\beta_1,\beta_2)=G_{lk}(\beta_2,\beta_1)$. To find the time-averaged energy flow and to eliminate the reactive part of the Poynting vector, the real parts of the above expressions for q_x, q_y and q_z should be inserted into the general expression of Eq.(3.74), leading to

$$
\begin{aligned}
S_x &= \frac{\epsilon_0 c n_r \gamma^2 s_0^5}{2}\Big\{-2\Im(p_xp_y^*)\Im\left(G_{0,1}+G_{0,-1}\right)+\Im\left(G_{0,1}-G_{0,-1}\right) \\
&\quad +s_0^2\Big[2\Im(p_xp_y^*)\Im\left(G_{2,1}+G_{-2,-1}\right)-\Im\left(G_{2,1}-G_{-2,-1}\right)\Big]\Big\}\ ,
\end{aligned}
\tag{3.78}
$$

$$
\begin{aligned}
S_y &= \frac{\epsilon_0 c n_r \gamma^2 s_0^5}{2}\Big\{-2\Im(p_xp_y^*)\Re\left(G_{0,1}-G_{0,-1}\right)+\Re\left(G_{0,1}+G_{0,-1}\right) \\
&\quad +s_0^2\Big[-2\Im(p_xp_y^*)\Re\left(G_{2,1}-G_{-2,-1}\right)+\Re\left(G_{2,1}+G_{-2,-1}\right)\Big]\Big\}\ ,
\end{aligned}
\tag{3.79}
$$

$$
\begin{aligned}
S_z &= \frac{\epsilon_0 c n_r \gamma^2 s_0^4}{2}\Big\{\Big[G_{0,0}-\frac{s_0^4}{2}\left(G_{2,2}+G_{-2,-2}\right)\Big] \\
&\quad +s_0^4\,\Im(p_xp_y^*)\left(G_{2,2}-G_{-2,-2}\right)\Big\}.
\end{aligned}
\tag{3.80}
$$

3.7.3 Expression for the linear momentum flow

The linear momentum density of the electromagnetic field is a vector $\vec{m}$ which can be obtained form the Poynting vector S by multiplying it with the factor $\frac{2}{c^2}$ for the vacuum case. The corresponding flow of momentum is given by the Maxwell stress tensor $\mathbf{T}$ whose entries T_{ij} with $i,j=(x,y,z)$ have the dimension of pressure and are given by

$$\begin{pmatrix} \frac{1}{2}\left(\epsilon_0|\mathbf{E}|^2+\frac{1}{\mu_0}|\mathbf{B}|^2\right) & -\epsilon_0 E_x E_y^* - \frac{1}{\mu_0}B_x B_y^* & -\epsilon_0 E_x E_z^* - \frac{1}{\mu_0}B_x B_z^* \\ -\epsilon_0|E_x|^2 - \frac{1}{\mu_0}|B_x|^2 & & \\ -\epsilon_0 E_y E_x^* - \frac{1}{\mu_0}B_y B_x^* & \frac{1}{2}\left(\epsilon_0|\mathbf{E}|^2+\frac{1}{\mu_0}|\mathbf{B}|^2\right) & -\epsilon_0 E_y E_z^* - \frac{1}{\mu_0}B_y B_z^* \\ & -\epsilon_0|E_y|^2 - \frac{1}{\mu_0}|B_y|^2 & \\ -\epsilon_0 E_z E_x^* - \frac{1}{\mu_0}B_z B_x^* & -\epsilon_0 E_z E_y^* - \frac{1}{\mu_0}B_z B_y^* & \frac{1}{2}\left(\epsilon_0|\mathbf{E}|^2+\frac{1}{\mu_0}|\mathbf{B}|^2\right) \\ & & -\epsilon_0|E_z|^2 - \frac{1}{\mu_0}|B_z|^2 \end{pmatrix}. \tag{3.81}$$

The physical interpretation of the Maxwell stress tensor and its symmetry properties are discussed in various textbooks, see [77]. We now give the expressions for the transport of x, y and z-linear momentum in the three orthogonal directions for a focused beam with arbitrary aperture by evaluating the stress tensor element T_{ij}. Taking the time-averaged real parts of the elements of expression (3.81) we obtain

$$\begin{aligned}
T_{xx} &= \epsilon_0\gamma^2 s_0^6 \{[G_{1,1}+G_{-1,-1}-\Re(G_{2,0}+G_{-2,0})] \\
&\quad -2\Im(p_x p_y^*)\left[(G_{1,1}-G_{-1,-1})-\Re(G_{2,0}-G_{-2,0})\right]\}, && (3.82)\\
T_{xy} &= \epsilon_0\gamma^2 s_0^6 \{-\Im(G_{2,0}-G_{-2,0}) \\
&\quad +2\Im(p_x p_y^*)\Im(G_{2,0}+G_{-2,0})\}, && (3.83)\\
T_{xz} &= \epsilon_0\gamma^2 s_0^5 \{-\Im\left[G_{1,0}-G_{-1,0}+s_0^2(G_{1,2}-G_{-1,-2})\right] \\
&\quad +2\Im(p_x p_y^*)\Im\left[(G_{1,0}+G_{-1,0})+s_0^2(G_{1,2}+G_{-1,-2})\right]\}, && (3.84)\\
T_{yx} &= T_{xy}\,, && (3.85)\\
T_{yy} &= \epsilon_0\gamma^2 s_0^6 \{[G_{1,1}+G_{-1,-1}+\Re(G_{2,0}+G_{-2,0})] \\
&\quad -2\Im(p_x p_y^*)\left[(G_{1,1}-G_{-1,-1})+\Re(G_{2,0}-G_{-2,0})\right]\}, && (3.86)\\
T_{yz} &= \epsilon_0\gamma^2 s_0^5 \{\Re\left[G_{1,0}+G_{-1,0}-s_0^2(G_{1,2}+G_{-1,-2})\right] \\
&\quad -2\Im(p_x p_y^*)\Re\left[(G_{1,0}-G_{-1,0})-s_0^2(G_{1,2}-G_{-1,-2})\right]\}, && (3.87)\\
T_{zx} &= T_{xz}\,, && (3.88)\\
T_{zy} &= T_{yz}\,, && (3.89)\\
T_{zz} &= \epsilon_0\gamma^2 s_0^4 \left\{\left[G_{0,0}-s_0^2(G_{1,1}+G_{-1,-1})+\frac{s_0^4}{2}\,(G_{2,2}+G_{-2,-2})\right]\right. \\
&\quad \left.+2\Im(p_x p_y^*)\left[s_0^2(G_{1,1}-G_{-1,-1})-\frac{s_0^4}{2}(G_{2,2}-G_{-2,-2})\right]\right\}. && (3.90)
\end{aligned}$$

The value of T_{ij} yields the transport of the i-component of the linear momentum vector in the direction j. The diagonal elements of the stress tensor are called the

normal pressure components, the off-diagonal elements the shear pressure components. The conservation of a linear momentum component i is given by

$$\frac{\partial m_i}{\partial t} + \frac{\partial T_{ix}}{\partial x'} + \frac{\partial T_{iy}}{\partial y'} + \frac{\partial T_{iz}}{\partial z'} = 0, \tag{3.91}$$

where we have used real-space Cartesian coordinates (x', y', z'). In our normalized system of coordinates, the conservation law reads

$$\frac{\partial m_i}{\partial t} + \frac{s_0}{\lambda}\left[\frac{\partial T_{ix}}{\partial x} + \frac{\partial T_{iy}}{\partial y}\right] - \frac{2\pi\left[1-\sqrt{1-s_0^2}\right]}{\lambda}\frac{\partial T_{if}}{\partial f} = 0\,, \tag{3.92}$$

where the quantities have now been expressed using the normalized coordinates (x, y, f).

3.7.4 Expression for the angular momentum flow

Angular momentum in a focused beam stems from intrinsic or spin momentum of the photons in the beam or from a special geometrical structure of the beam. The angular momentum density $\vec{j}$ and the corresponding tensor $\mathbf{M}$ with the flow components M_{ij} are related through the angular momentum conservation law, which in our normalized coordinates is expressed as

$$\frac{\partial j_i}{\partial t} + \frac{s_0}{\lambda}\left[\frac{\partial M_{ix}}{\partial x} + \frac{\partial M_{iy}}{\partial y}\right] - \frac{2\pi\left[1-\sqrt{1-s_0^2}\right]}{\lambda}\frac{\partial M_{if}}{\partial f} = 0\,. \tag{3.93}$$

The angular momentum density with vector components j_i is directly obtained from the Poynting vector by the relation

$$\mathbf{j} = \epsilon_0 \mathbf{r} \times (\mathbf{E} \times \mathbf{B}^*). \tag{3.94}$$

The momentum flux density tensor elements M_{ij} bear a direct relationship to the Maxwell stress tensor elements T_{ij}, according to

$$\mathbf{M} = \mathbf{r} \times \mathbf{T}\ , \tag{3.95}$$

in which the elements of $\mathbf{M}$ are evaluated using $M_{ij} = \sum_{mn} \epsilon_{imn} r_m T_{nj}$ with ϵ_{imn} the Levi-Civita symbol and where, as before, T_{nj} are the time-averaged values of the Maxwell stress-tensor elements. This, for example, results in the following expression for $M_{zz}(r, f, \phi)$, the axial angular momentum flux density through a surface perpendicular to the z-axis

$$M_{zz} = \frac{\lambda r}{s_0}\ \left[T_{yz}\cos\phi - T_{xz}\sin\phi\right], \tag{3.96}$$

where we have used the relation $r = r^{'} s_0/\lambda$ between the real-space coordinate $r^{'}$ and the dimensionless coordinate r (note, $\lambda = 2\pi c/\omega$). The substitution of the

tensor elements yields, after some rearrangement,

$$\begin{aligned} M_{zz} &= \epsilon_0\gamma^2 s_0^4 \lambda r \Big[\left\{ \Re\left[G_{1,0} + G_{-1,0} - s_0^2(G_{1,2} + G_{-1,-2})\right]\cos\phi \right. \\ &\qquad \left. + \Im\left[(G_{1,0} - G_{-1,0}) + s_0^2(G_{1,2} - G_{-1,-2})\right]\sin\phi \right\} \\ &\quad -2\Im(p_x p_y^*)\left\{ \Re\left[G_{1,0} - G_{-1,0} - s_0^2(G_{1,2} - G_{-1,-2})\right]\cos\phi \right. \\ &\qquad \left. + \Im\left[(G_{1,0} + G_{-1,0}) + s_0^2(G_{1,2} + G_{-1,-2})\right]\sin\phi \right\} \Big]. \end{aligned} \tag{3.97}$$

3.7.5 The aberration-free system as a special case

In this section, we produce analytic expressions for the various electromagnetic quantities in the focal region. The added value provided by these expressions is that they allow a better understanding of the physical principles that contribute to the various phenomena observed in a focal spot. We could, for example, reduce the general expressions for the Poynting vector components to their simpler form in the case of an aberration-free imaging system. In that case, we put $\beta_n^m = 0$ with the exception of β_0^0 that we give the value of unit electric field strength. The G-functions then reduce to

$$G_{kl}(\beta) = \exp\{i(k-l)\phi\}\,\Psi^0_{0;k,l}(r,f), \tag{3.98}$$

with the shorthand notation $\Psi^0_{0;k,l}(r,f) = V^0_{0,k}(r,f)V^{0*}_{0,l}(r,f)$. After some manipulation, the Cartesian Poynting vector components are found to be

$$\begin{aligned} P_{x,r} &= 2s_0\Big[2\Im(p_x p_y^*)\Re\{\Psi^0_{0;0,1}(r,f)\}\sin\phi + \Im\{\Psi^0_{0;0,1}(r,f)\}\cos\phi\Big] \\ &\quad +2s_0^3\Big[2\Im(p_x p_y^*)\Re\{\Psi^0_{0;2,1}(r,f)\}\sin\phi - \Im\{\Psi^0_{0;2,1}(r,f)\}\cos\phi\Big], \end{aligned} \tag{3.99}$$

$$\begin{aligned} P_{y,r} &= 2s_0\Big[-2\Im(p_x p_y^*)\Re\{\Psi^0_{0;0,1}(r,f)\}\cos\phi + \Im\{\Psi^0_{0;0,1}(r,f)\}\sin\phi\Big] \\ &\quad +2s_0^3\Big[-2\Im(p_x p_y^*)\Re\{\Psi^0_{0;2,1}(r,f)\}\cos\phi - \Im\{\Psi^0_{0;2,1}(r,f)\}\sin\phi\Big], \end{aligned} \tag{3.100}$$

$$P_{z,r} = \Psi^0_{0;0,0}(r,f) - s_0^4\Psi^0_{0;2,2}(r,f)\,. \tag{3.101}$$

Because of the basic circular symmetry of many diffraction problems, it is appropriate to express the Poynting vector components in cylindrical coordinates and we find for the polar components

$$\begin{aligned} P_r &= 2s_0\,\Im\left[\Psi^0_{0;0,1}(r,f) - s_0^2\Psi^0_{0;2,1}(r,f)\right], \\ P_\phi &= -4s_0\Im(p_x p_y^*)\,\Re\left[\Psi^0_{0;0,1}(r,f) - s_0^2\Psi^0_{0;2,1}(r,f)\right]. \end{aligned} \tag{3.102}$$

Some conclusions can be drawn from the above expressions. Using the property $\Psi^0_{0;k,l}(r,-f) = \Psi^{0*}_{0;0,0}(r,f)$, we can state that

- On-axis ($r = 0$), the power flow is directed along the axis of the beam.
- The radial component changes sign through focus.
- The azimuthal component is only present if the incident radiation is not linearly polarized ($arg(p_x) \neq arg(p_y)$), see [78], [66]. This corresponds to the presence of angular momentum in the focused beam.
- The azimuthal component is maximum in the case of circularly polarized light.
- The azimuthal component maintains its sign on both sides of the optimum focus.
- For large s_0, all components can locally change sign with respect to their average values if the (r,f)-dependent function becomes zero. This can give rise to regions where the energy flow is in the negative z-direction and also to the appearance of vortices in the energy flow pattern.
- Regardless of the incident state of polarization, the z-component possesses circular symmetry. This is because the Poynting vector describes the energy flow of both electric and magnetic energy. Any lack of circular symmetry in the energy densities of these contributions is cancelled in their sum.
- In the low-aperture case, the z-component is the only surviving one.

In Figure 3.10, we present some graphs that illustrate the observations made above for the aberration-free case. With the upper row (linear polarization in the x-direction) as a reference, we see in the second row the influence of circular polarization in the entrance pupil on the flow pattern in the focal region. The state of polarization is right-handed, the flow circulation in focus becomes left-handed. Everywhere on the optical axis the azimuthal component is zero. The beam possesses a certain amount of angular momentum. With the positive z-direction as the viewing direction, we observe that the rotation sense of the electric field vector is left-handed for RC-polarized light and this rotation sense is in accordance with the sign of the angular momentum of the electric field distribution in the focal region. In the bottom row, we have plotted the power flow in the case of radial polarization. Because of the interchangeability of the **E**- and **B**-vector between radial and azimuthal polarization, the flow pattern would have been the same for azimuthal polarization. It is important to remark that the z-component of the Poynting vector is zero everywhere on-axis, despite the fact that the energy density is finite on-axis in the case of radial polarization. The same holds for the magnetic energy density in the case of azimuthal polarization. However, because of the vanishing transversal components of either the electric (radial polarization) or magnetic (azimuthal) field components on the z-axis, there is no power flow possible in the z-direction on the axis itself.

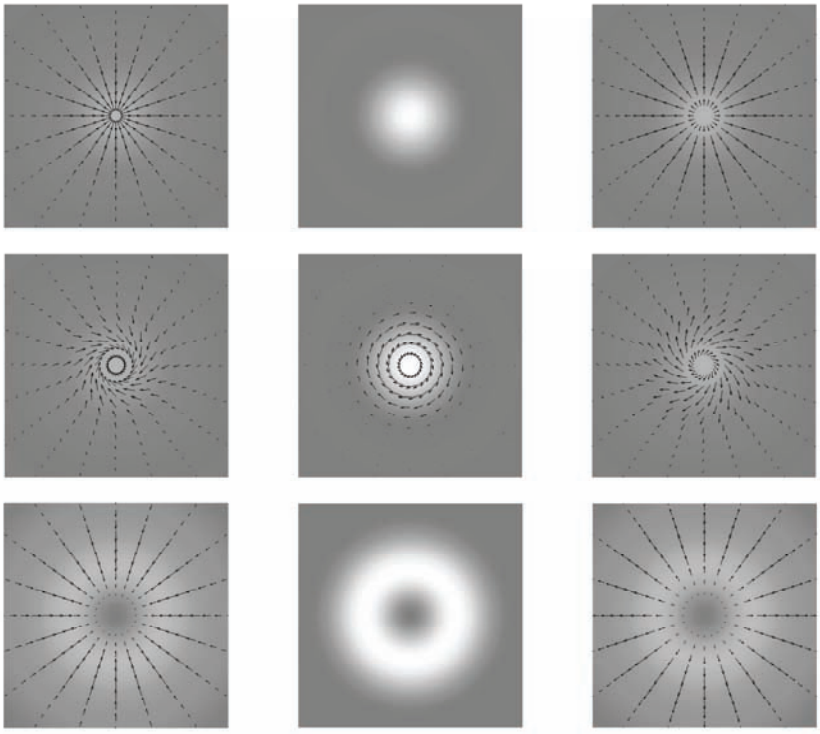

Figure 3.10: *Flow lines of the Poynting vector in the focal region of an ideal imaging system* ($s_0 = 0.95$) *for various states of polarization in the entrance pupil. Left column:* $f = \pi$*; central column:* $f = 0$*, right column:* $f = -\pi$*. Lateral dimensions in* x*- and* y*-direction are* $-1.11 \leq x, y \leq +1.11$*. Upper row: linear polarization along the* x*-axis. Middle row: Right-handed circularly polarized light* ($p_x = 1,\ p_y = -i$)*. Bottom row: radial polarization.*

In addition, we can also examine the particular behavior of the linear and angular momentum flux components in the focal region of an aberration-free imaging system. A first analysis applies to a linearly polarized beam with the field vector in the entrance pupil oriented along the x-axis, $[p_x, p_y] = [1, 0]$. We start with a relatively low value for the NA, (s_0=0.01). The starting point of the analysis is given by the three components of the linear momentum density; in vacuum they can be obtained from the Poynting vector by multiplication with a factor of $1/c^2$. The stress tensor elements were given in Eqs.(3.82)-(3.90). For the aberration-free case, the T_{zj} components are generally dominating and these can then be written as

$$\begin{aligned} T_{zx} \quad = \quad & -2\epsilon_0\gamma^2 s_0^5 \Big\{ \Im\left[V_{0;1}^0 (V_{0;0}^0 + s_0^2 V_{0;2}^0)^*\right] \cos\phi \\ & -2\Im(p_x p_y^*)\Re\left[V_{0;1}^0 (V_{0;0}^0 + s_0^2 V_{0;2}^0)^*\right] \sin\phi \Big\}, \end{aligned} \tag{3.103}$$

$$T_{zy} = -2\epsilon_0\gamma^2 s_0^5 \Big\{ \Im\left[V_{0;1}^0 (V_{0;0}^0 - s_0^2 V_{0;2}^0)^*\right] \sin\phi + 2\Im(p_x p_y^*)\Re\left[V_{0;1}^0 (V_{0;0}^0 - s_0^2 V_{0;2}^0)^*\right] \cos\phi \Big\}, \quad (3.104)$$

$$T_{zz} = \epsilon_0\gamma^2 s_0^4 \left\{ \left|V_{0,0}^0\right|^2 - 2s_0^2 \left|V_{0,1}^0\right|^2 + s_0^4 \left|V_{0,2}^0\right|^2 \right\}. \quad (3.105)$$

The stress tensor elements are represented in Figure 3.11, rows one to three, where, as expected, a dominating T_{zz} flux component is visible. All other elements are small, especially T_{xx}, T_{xy}, T_{yx} and T_{yy}, and their patterns remain invisible with the applied color shading. The transition from low numerical aperture to high NA (s_0=0.95) gives rise to a lack of circular symmetry in the separate electric or magnetic energy density. Electromagnetic cross-terms like the Poynting vector $\vec{S}$ and the linear and angular momentum densities, $\vec{m}$ and $\vec{j}$, maintain their circular symmetry; the flux components T and M do not have this property. When comparing the T-components in Figure 3.12 with its low-NA values, it becomes apparent that especially the elements T_{xx}, $T_{xy} = T_{yx}$ and T_{yy} have increased in relative value with respect to T_{zz}. We also take a look at the angular momentum flux components in the nominal focal plane (rows four to six of Figure 3.11). The only appreciable components are M_{xz} and M_{yz} and, in combination, they give rise to a tangentially oriented flux component that varies with the radial coordinate r. The high-NA effect on the M-components is the appearance of substantial z-flux components in the x- and y-direction. The net result is an in-plane tangential flow pattern of z-angular momentum, but the z-flow component of the z-angular momentum stays rigorously zero neither is there net transport of z-angular momentum through a plane z=constant. This can be understood by taking a closer look at Eq.(3.97). In the nominal focal plane, all functions $V_{n,k}^m$ are real and in the absence of aberrations the expression given in Eq.(3.97) reduces to

$$M_{zz} = -4\epsilon_0\gamma^2 s_0^4 \lambda\, r\, \Im(p_x p_y^*) \left[V_{0,1}^0 (V_{0,0}^0 - s_0^2 V_{0,2}^0)\right]. \quad (3.106)$$

So, in order to have a contribution to M_{zz} in the aberration-free case, the factor $\Im(p_x p_y^*)$ should be non-zero, and this will only be true for a beam that contains spin momentum. If we therefore switch to an incident beam having a left-handed circular polarization, $[p_x, p_y] = [1, i]/\sqrt{2}$, we effectively introduce spin momentum (see Figure 3.13). Regarding the T- flux components, the main difference with the linearly polarized incident beam is found in the nonzero T_{zx}-, T_{zy}-, T_{xz}- and T_{yz}-components. This is equivalent to a tangential flow pattern of z- linear momentum, on top of the main flow component T_{zz}. The main difference with linear incident polarization for the M-components is the appearance of a non-zero M_{zz}-component, created by the nonzero linear momentum components T_{xz} and T_{yz}. This is the result of the spin momentum in the incident beam.

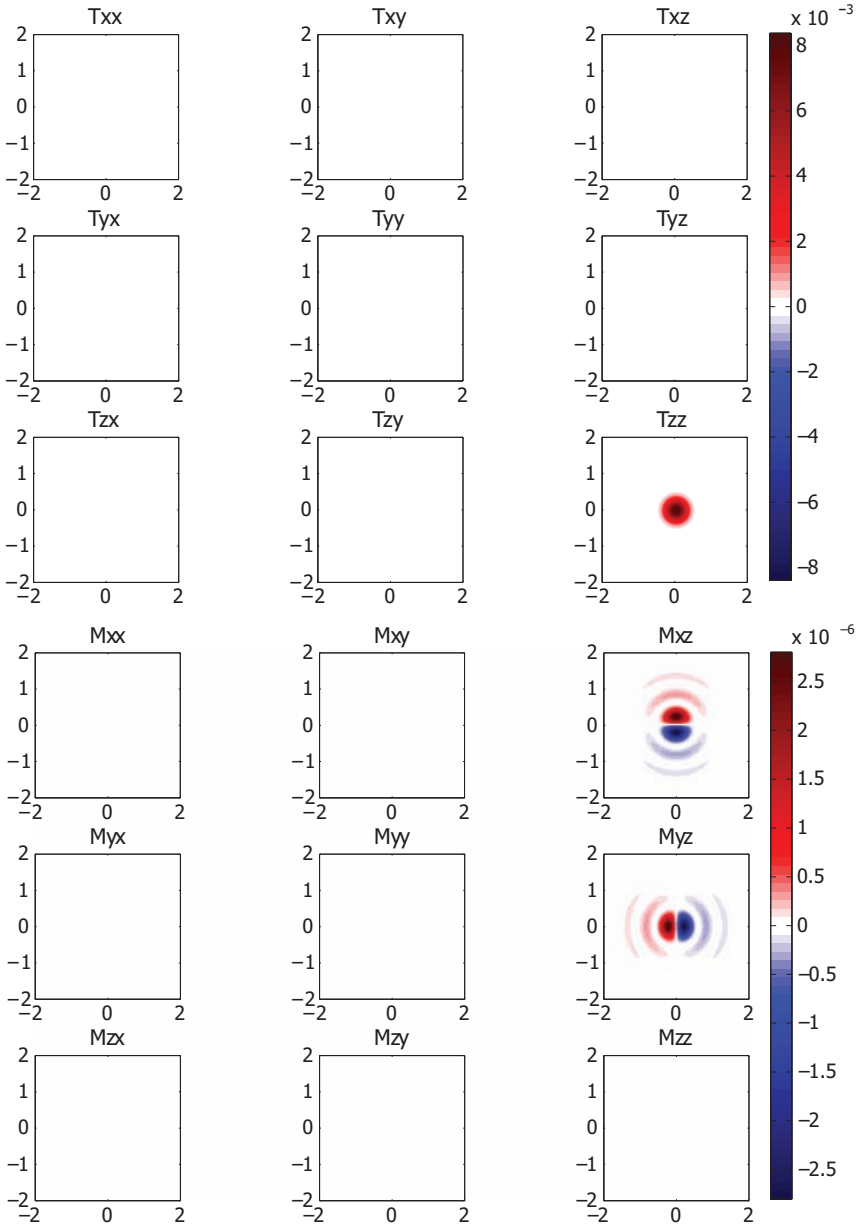

Figure 3.11: *The linear momentum flux components T_{ij} are represented in rows one to three, the radial momentum flux components M_{ij} in rows four to six. The numerical aperture of the focusing beam is kept in the paraxial range ($s_0 = 0.01$). The x- and y-axis are again given in units $\lambda/\,\mathrm{NA}$.*

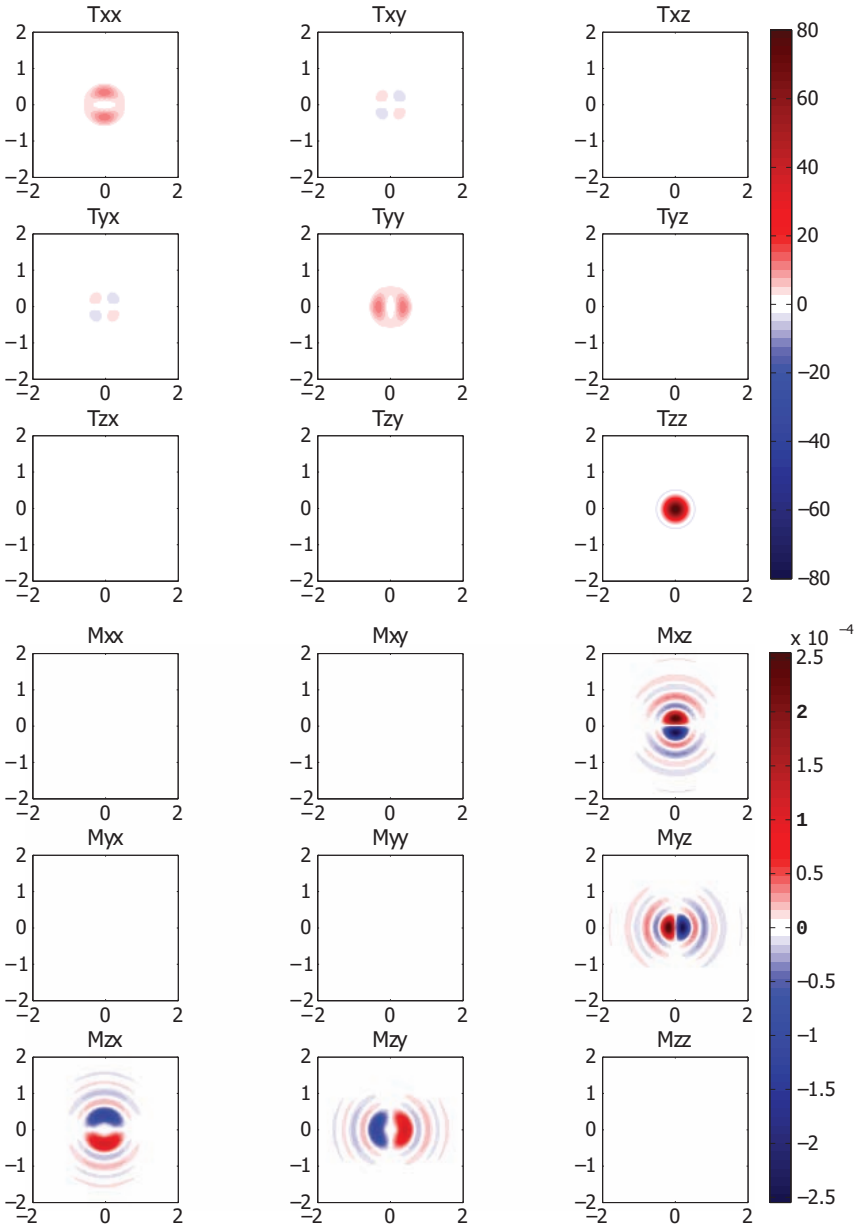

Figure 3.12: *The linear momentum flux components T_{ij} are represented in rows one to three, the radial momentum flux components M_{ij} in rows four to six. The numerical aperture s_0 of the focusing beam amounts to 0.95, linear polarization along the x-axis, $[p_x, p_y] = [1, 0]$. Axis scaling identical to Figure 3.11.*

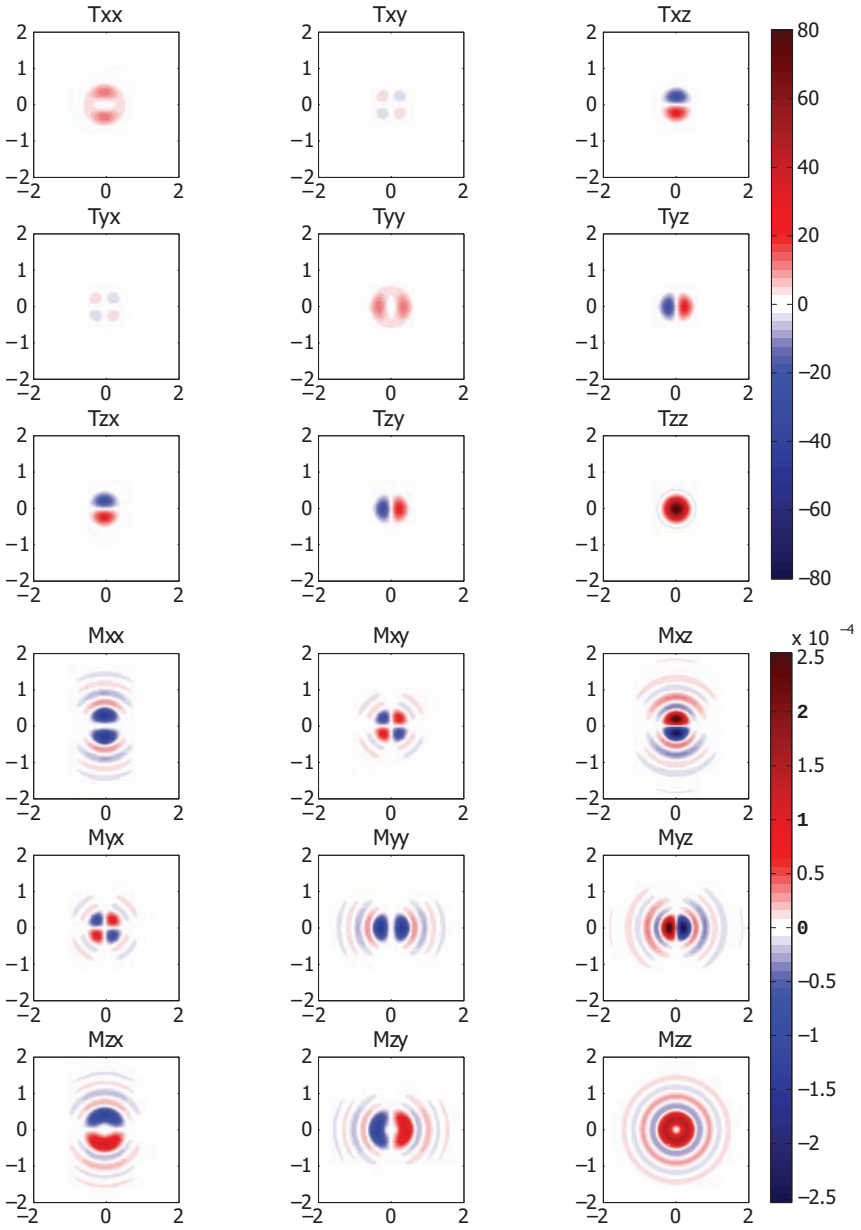

Figure 3.13: *Row one to three: graphs of the linear momentum flux components T_{ij} in the nominal focal plane; row four to six: the M_{ij}-flux components in the same plane. The numerical aperture s_0 of the focusing beam amounts to 0.95, left-handed circular polarization, $[p_x, p_y] = [1, i]/\sqrt{2}$. Axis scaling identical to Figure 3.11.*

3.8 Accuracy and convergence of the ENZ-based methods

In this section, we expand on the convergence properties and anticipated accuracy of the ENZ formalism introduced in the preceding sections. Such considerations are important to be able to qualitatively relate the ENZ formalism to other methods.

3.8.1 Computation of the ENZ basic integral

In the preceding sections of this chapter, we have seen that a given Zernike circle polynomial, used in the expansion of the pupil distribution, has a contribution to the image that is given by an integral expression. These integrals, which we refer to as the ENZ basic integrals, can be evaluated using series expansions provided by the ENZ theory. These series expansions, included in Appendix A, thus largely determine the accuracy and convergence properties of the ENZ formalism.

When we study the various calculation schemes for the ENZ basic functions given in Appendix A, we see that their computation involves an infinite sum. During the actual computation of the ENZ basic integrals, this infinite sum is cut off at a certain finite value. In Figure 3.14, we show the relation between the RMS error present in the computed ENZ basic integral ($V_{n,j}^m(r,f)$ given in Appendix A.5) and the maximum value, t_{max}, included in the summation over t. One can see that a modest amount of terms, say $t_{max} = 25$, already results in an accuracy of 10^{-4}. Furthermore, we see a steady decrease in the RMS, for increasing t_{max}, down to 10^{-12}. From this we can conclude that the $V_{n,j}^m(r,f)$-functions can always be computed down to the accuracy required by a particular application and as a result the computation of the ENZ basic functions does not impose a limit on the accuracy of the ENZ method. Of course, a higher accuracy does imply a larger computational burden. This is, however, of limited importance when we apply the ENZ formalism. As the $V_{n,j}^m(r,f)$-functions exclusively depend on the specifications of the imaging system and are thus independent of the pupil distribution being imaged, the ENZ basic functions can be calculated in advance and be stored in a look-up table. As a result, a highly accurate simulation, in which a general pupil is imaged, can be reduced to a weighted summation over pre-calculated data values where the Zernike expansion coefficients describing the pupil act as the weight factors.

Please note that the various series expressions given in Appendix A can be divided into two groups; those based on a power-Bessel expansion yielding accurate results for a limited range of f and those based on a Bessel-Bessel expansion accurate for all f [65]. In both cases, the computational burden increases for larger values of f, but with the Bessel-Bessel expansion it is always possible to determine the ENZ basic functions with the desired accuracy. The range of f for which the ENZ formalism can be applied is therefore only limited by the practical calculation time, not by the convergence of the calculation method. Because of this basic accuracy, the method could be used to check numerical methods (e.g. Fourier transform methods) with respect to the required sampling density for achieving a desired precision.

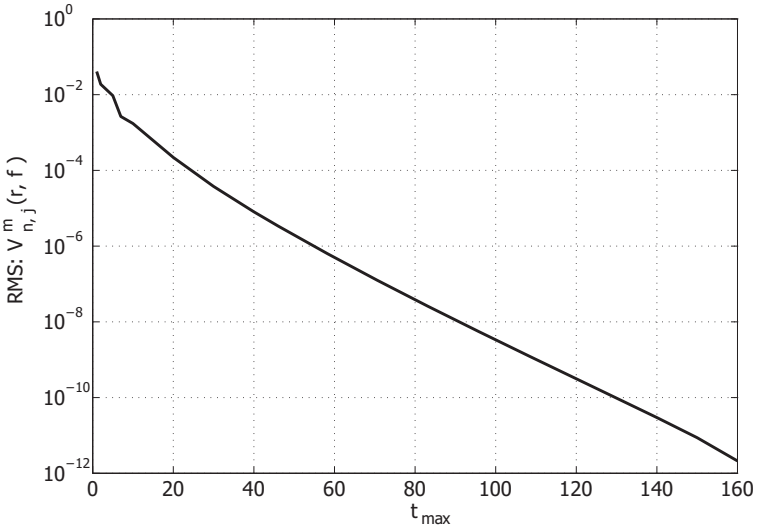

Figure 3.14: *The Root Mean Square (RMS) error present in the $V_{n,j}^{m}(r,f)$-functions when approximated by the series expansion in which the infinite sum is replaced by a summation over $t = 1, 2...t_{max}$ (see Appendix A.5).*

3.8.2 Pupil expansion accuracy

The second operation that has a strong influence on the overall accuracy of the ENZ formalism is the expansion of the pupil in terms of Zernike circle polynomials. As the Zernike polynomials constitute a complete set on the unit disk and can be computed accurately for arbitrary degree and order (see [79]) it is always possible to exactly represent a given pupil function on the unit disk in terms of Zernike polynomials. Nonetheless, the required number of Zernike polynomials required for an accurate representation of a general pupil function can become impractically large. Therefore, in practice, the expansion of the pupil is normally stopped when the desired fitting accuracy in the pupil is reached. As a result, the pupil representation will contain a certain residual error and this will also introduce a certain error in the corresponding computed image.

To illustrate that the fitting accuracy in the pupil strongly depends on the pupil distribution itself we consider the following example. Let us assume that we have three mask objects as depicted in the top row of Figure 3.15. To image these objects coherently using the ENZ approach presented in Section 3.4, we should compute the pupil distributions these objects produce when illuminated for example by an x-polarized plane wave. Now assume we have this data available through some means of electromagnetic simulation. The next step is to determine the Zernike expansions of the resulting pupil distributions. In the bottom row of Figure 3.15 we have included graphs showing the residual RMS fitting error in the pupil for all three objects versus the maximum radial and azimuthal order of the Zernike polynomials, n and m, used in the expansion. These simulations clearly illustrate that the number of Zernike polynomials required to obtain a certain de-

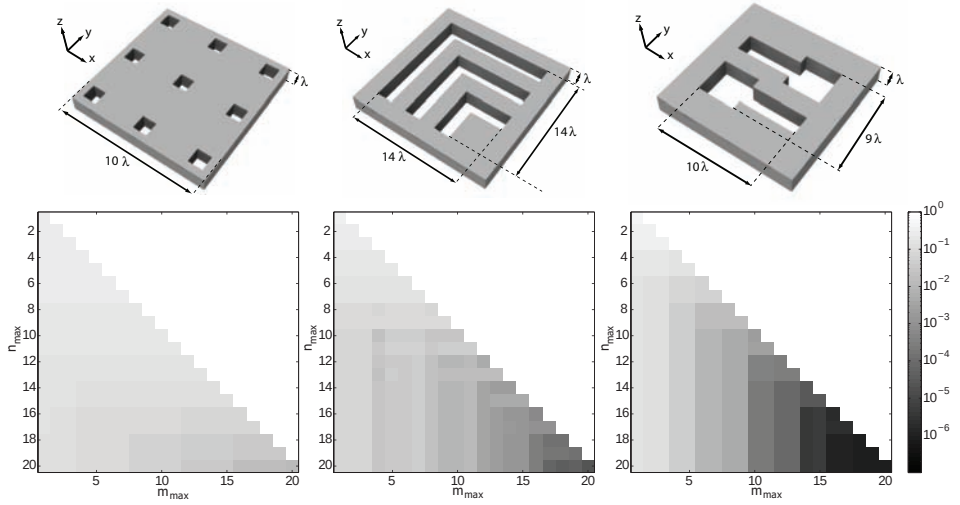

Figure 3.15: *For three different objects (top row), the Root Mean Square (RMS) error present in the Zernike approximation of the electric field components in the entrance pupil (bottom row) is shown. The system settings for the three objects are, from left to right: normal incidence TM polarized plane wave illumination with an object side numerical aperture of* 0.525 *and, for the middle and right object, normal incidence TE-polarization with an object side numerical aperture of* 0.2375*. Note that the indicated dimensions of the objects are given at the mask-scale.*

gree of fitting accuracy for the field in the entrance pupil, strongly varies between different objects. In general, one would expect the required number of Zernike polynomials to depend on the size and complexity of the objects. Nevertheless, a complex object doesn't necessary imply the need for a large number of Zernike functions for an accurate fit. A complex object can produce a relatively smooth pupil distribution which would then require a limited number of Zernike polynomials to be fitted accurately. On the other hand, a fairly simple structure with a high degree of periodicity, can produce a sharply modulated pupil distribution that closely resembles the diffraction pattern that would arise in the case of a purely periodic object. In this case, the number of Zernike polynomials required to obtain an accurate fit is fairly large. Thus, in general, the number of Zernike functions required for an accurate pupil fit strongly depends on the degree of modulation in the pupil which by itself is influenced by many factors such as the nature of the object. A general recipe to determine the maximum number of Zernikes required for an accurate fit beforehand is thus unrealistic and the number of Zernikes is therefore determined iteratively until the desired fitting accuracy is reached.

From the above discussion we can conclude that, for general optical systems, the fitting accuracy in the pupil should always be monitored in order to assure reliable simulation results with the ENZ methods. Nevertheless, there are circumstances in which the Zernike expansion of the pupil is exact. This is, for example,

the case when we consider the computation of the PSF for an aberration free system, in which case the pupil is defined by a single Zernike coefficient. Also for other simulation tasks where a pupil is specified by a finite number of Zernike coefficients, there is no error introduced by the pupil representation itself and the accuracy in the computed image is completely determined by the residual error present in the ENZ basic functions.

3.8.3 Overall ENZ accuracy

In the preceding subsections we have identified two operations in the ENZ formalism that can contribute to inaccuracies in the computed focal distributions. One of these sources, the residual error in the computation of the ENZ basic functions using series expansions, was shown to be reducible down to machine precision if there is enough computational power available. That this will also give rise to relatively large computation times was shown to be of minor importance as the ENZ basic functions should, in principle, only be computed a single time for a given optical system after which the results can be used repeatedly. Of course the summation of these basic functions, to obtain the actual distribution, requires some computational effort proportional to the number Zernike terms included in the pupil expansion. However, this contribution is always very small compared to the computational effort required to generate the ENZ basic functions, but can become a significant part of the overall image computation time when many points in image space are to be computed. The accuracy of the ENZ basic functions will thus never have to be the limiting factor in the overall accuracy of the ENZ method. In other words, the overall ENZ accuracy is determined by the quality of the pupil representation. This also means that if the pupil is exact, the image can also be obtained with an accuracy down to machine precision. For arbitrary pupil distributions we would like to know the relation between the residual error in the pupil and the resulting error in image space. As an example, we again consider the imaging of the objects depicted in the first row of Figure 3.15. Then, for increasingly accurate pupil representations, we have computed the corresponding RMS accuracy in the image volume and have plotted the results in Figure 3.16. The figure clearly illustrates a similar behavior for the RMS errors of all three objects studied. Note that the lines representing the contact holes and elbow structure do not cover the full range of the RMS errors in entrance pupil expansions, because for the maximum number of Zernike terms used in these examples ($m_{max} = n_{max} = 20$), the best obtained accuracies were 10^{-2} and 10^{-4} respectively. It is interesting to note that a pupil field accuracy of 10^{-3} already yields an intensity fidelity in the image region that is better than 10^{-4}, despite the nonlinearities that arise in the creation of the intensity distribution in the image. It can thus be said that the best obtainable accuracy in image space is always better than the accuracy of the pupil expansion.

Please note that, strictly speaking, we are discussing here the accuracy to which the ENZ methods can compute the Debye-type diffraction integrals. The computed ENZ images will only accurately reflect the actual images produced by an optical system if this optical system is well described by these Debye integrals.

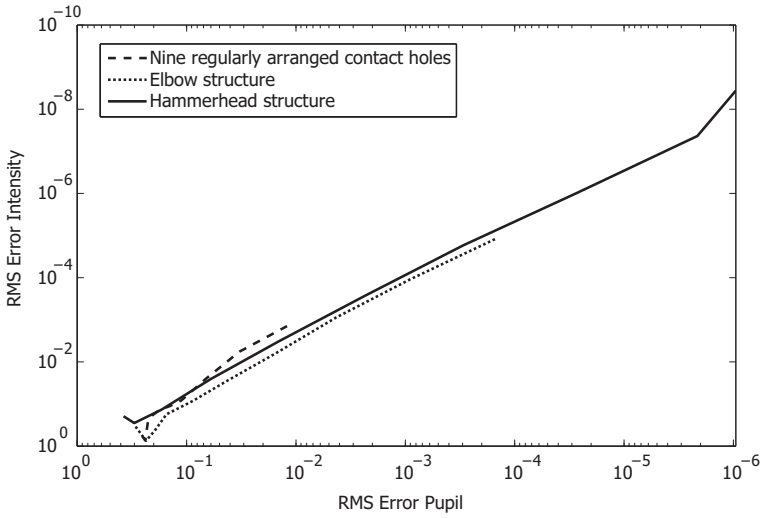

Figure 3.16: *For the same three objects as in Figure 3.15, the RMS error for the intensity in the image volume is shown as a function of the RMS error in the Zernike expansion of the pupil fields. The area over which the RMS intensity error was calculated, was a circle that circumscribes the square images. The final RMS-value was obtained by averaging the RMS intensity errors from various through-focus images.*

If an optical system operates outside the Debye regime, which is, for example, the case for microlenses (see Section 4.5), the above presented analysis regarding the accuracy of the produced images is no longer valid. Although the ENZ method can still yield valuable results for optical systems not strictly satisfying the Debye approximations, the error included in this case can not be quantified in a general manner and should be analyzed separately.

3.8.4 Computational considerations

The accuracy of a method should always be discussed in relation to the computational burden involved with it. As already discussed above, the ENZ methods are composed of two largely independent modules, and as a result the computational complexity should be evaluated likewise. We will only consider the computational complexity involved in going from the pupil distribution to the image. Evaluation of the computational effort required to obtain the pupil distribution with a sufficient accuracy is outside the scope of this thesis.

Suppose we have a pupil distribution defined by a set of data points. To get from this information the Zernike expansion of the pupil one can apply a least-squares fitting operation. In our case, we use the least-squares fitting algorithm included in Matlab (Standard Matlab function *mldivide.m* [80]), which is based on QR factorization with column pivoting, to obtain the Zernike coefficients describing the pupil. The computational complexity of this algorithm is $O(N_Z^3)$, where

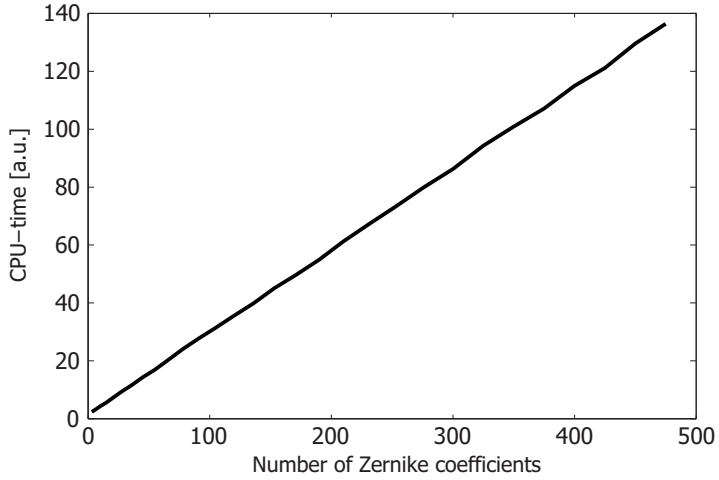

Figure 3.17: *The relation between the computation time and the total number of Zernike coefficients used in the expansion of the entrance pupil field is shown.*

N_Z is the total number of Zernike coefficients to be fitted.

The computational complexity of the second module, which computes the field in the focal region given the Zernike coefficients describing the pupil, can be deduced from Eq.(3.29). Recall that the $V_{n,j}^m$ functions are independent of the object and can therefore be calculated in advance. As a result, all terms between the large parentheses on the second and third line of Eq.(3.29) are fixed for a given set of (r, ϕ, f). The computational task is thus reduced to computing

$$\mathbf{E_2}(r,\phi,f) = C_1(f) \sum_{n,m} \left[\beta_{n,x}^m \mathbf{C}_2(m,n,r,\phi,f) + \beta_{n,y}^m \mathbf{C}_3(m,n,r,\phi,f) \right], \quad (3.107)$$

where C_1, $\mathbf{C}_2$ and $\mathbf{C}_3$ all represent data stored in a look-up table. Consequently, the computational complexity is proportional to

$$N_f \times N_r \times N_\phi \times 2N_Z \ , \quad (3.108)$$

where N_f, N_r and N_ϕ are the number of sampling points in the focal, radial and azimuthal directions of our cylindrical coordinate system, (f, r, ϕ), in the focal volume. The expression in Eq.(3.108) thus predicts a linear relation between the CPU-time and N_Z, the number of Zernike coefficients used in the computation. This behavior is clearly visible in Figure 3.17, where we have plotted the CPU-time versus the number of Zernike coefficients.

On comparing the computational complexities determined above, we can conclude that both parts of the ENZ formalism can be dominant. Whenever $N_f \times N_r \times N_\phi \ll N_Z^2$, the least-squares fitting operation to determine the Zernike expansion coefficients of the pupil, will dominate the required computational workload, while in case that $N_f \times N_r \times N_\phi \gg N_Z^2$, the computational contribution of the image construction will be more important.

3.9 Summary and discussion

In this chapter, we have presented the mathematical formulation of the Extended Nijboer-Zernike theory. Starting from the original work by Zernike and Nijboer (Section 3.1), we have devised both a scalar (Section 3.2) and a vectorial version (Section 3.3) of the ENZ formalism to compute the PSF for general optical systems in a systematic and semi-analytic manner. In addition, we have shown that the ENZ theory can be further generalized to allow the computation of the through-focus image behavior of more general extended objects (Section 3.4). This is realized by exploiting the fact that ENZ theory allows the computation of the focal distribution given a general nonuniform field distribution in the exit pupil. Whether this exit pupil distribution is generated by an aberrated optical system imaging a point-source, or by a more complicated object, does not affect the ENZ imaging principle. In Section 3.5, ENZ-based imaging is further generalized by allowing a stratified configuration in image space. It is shown that, by keeping track of all the refracted and reflected light coming from the layer interfaces, it is possible to accommodate their nett effect into the Zernike coefficients describing the field in a given layer of the focus. Furthermore, also the optical system itself can pose complications in applying the ENZ theory. For example, an optical system could be operated using only a fraction of its maximum NA or could be obscured in a central region. In both cases, part of the full pupil does not contribute to the formation of the image, and in Section 3.6 we have shown how to efficiently incorporate these circumstances. In Section 3.7, we have applied the ENZ theory to other electromagnetic quantities in the focal region, such as the Poynting vector, linear momentum flow and angular momentum flow. This has resulted in analytic expressions for these quantities that provide far more insight at the physical phenomena occurring in the focal region than a standard numerical computation based on the electric and magnetic fields. To illustrate this, Section 3.7 includes an analysis of the various electromagnetic quantities in the focal region for aberration free optical systems. Finally, in Section 3.8 we have expanded on the accuracy of the ENZ formalism and the corresponding computational effort required. This showed that in principle the accuracy of the ENZ methods is only limited by the residual error present in the Zernike expansion of the pupil. To conclude we have derived an expression that gives the lower limit of computational operations required to construct an ENZ-based image.

Chapter 4

Optical system quality assessment using the ENZ theory

Nowadays, the perfection of optical instruments has reached a level that was thought to be impossible in the still recent past. Especially since the 1970's, the quality of optical imaging systems (telescopes, microscope objectives, high-quality projection lenses for optical lithography, space observation cameras) has been pushed to the extreme limits. The residual aberrations present in such high quality imaging systems are to be reduced to a minute fraction of the wavelength to meet the very stringent specifications. To obtain an optical quality of this level, we also require extremely accurate measurement techniques. In most cases, interferometric methods are applied for this purpose as their achievable precision is very high. However, they have the disadvantage that they require refined and delicate optical set-ups and, in practice, special laser sources to achieve sufficient signal-to-noise ratio.

An appealing alternative to interferometric methods would be a direct measurement of the PSF intensity if it is possible to derive from such an intensity distribution the relevant quality data of the optical system. The difficulty of this approach lies in the fact that, in the optical domain, the PSF is only experimentally accessible in terms of the energy density or the energy flow. These quantities are both non-linear functions of the basic electromagnetic field components in the focal region and this relationship leads to an ill-posed inversion problem that has to be solved in order to obtain the system characteristics that determine the quality of the optical system. Nevertheless, several characterization methods that go in this direction can be found in the literature. The first publications on this type of inversion problems go back to Gerchberg [81, 82] and Frieden [83]. In attempts to improve the stability of the inversion process, extra information from e.g. the pupil intensity distribution (optical far field intensity) or from several image planes in the focal region were incorporated in methods like the "phase diversity method" proposed by Gonsalves [84], or the multiple images phase retrieval method in elec-

tron microscopy by van Dijck [85]). A comparison of 'phase retrieval' methods is found in [86]; later developments are found in [87–90]. In this chapter, we will devise another characterization method based on the analytic results for the PSF of a general optical system provided by the Extended Nijboer-Zernike (ENZ) diffraction theory.

In the previous chapter, we have introduced and discussed the ENZ theory as a convenient and systematic formalism to compute the point-spread function (PSF) produced by a general optical system. In addition to this, we have also shown that it is possible to compute the through-focus image behavior of more general extended objects using the same basic tool set. In this chapter, however, we will again focus on the PSF's of optical systems and show that an analysis of their through-focus intensity behavior according to ENZ theory yields all the required information to reconstruct the aberration function of an optical system. In Section 4.1, the basic principles of ENZ-based aberration retrieval are discussed and applied to the analysis of PSF's formed by general optical systems having a small numerical aperture (NA). The same retrieval approach is applied to optical systems having a high-NA in Section 4.2, where in this case the analysis is based on the vectorial version of the ENZ diffraction theory. The maximum size of wavefront deviation that can be handled by the retrieval methods given in Sections 4.1 and 4.2 is limited due to the application of a small aberration assumption which is needed to arrive at workable retrieval expressions. We will show in Section 4.3 that the range of aberration magnitudes for which the ENZ retrieval formalism yields accurate results can be strongly increased by the introduction of a so-called predictor-corrector scheme.

At this point we have succeeded in devising an optical system characterization method based on the ENZ diffraction theory. Nevertheless, the results introduced in Sections 4.1-4.3 pertain to the retrieval of polarization independent aberrations present in optical systems operating within the Debye approximation. To further extend the applicability of our retrieval method we discuss in Section 4.4 the retrieval of polarization dependent aberrations. The representation of such birefringence is done according to the Jones pupil formalism and it will be shown that this pupil can be reconstructed from at least four consecutive ENZ retrieval operations all having different incident polarization states. Moreover, we would also like to be able to analyze optical systems that operate outside the Debye regime. For these systems the Rayleigh integral can be used and we therefore analyze in Section 4.5 the difference between the Debye integral and the Rayleigh integral. This will result in a correction of the Debye integral that, when it is inserted in the ENZ retrieval formalism, enables the analysis of optical systems operating well outside the Debye regime.

In addition to the ENZ-based quality assessment, we will also discuss in Section 4.6 the somewhat less advanced but nevertheless widely used quality measure provided by the Strehl ratio. An analysis of this quantity for systems having a large NA will show rather unexpected and counterintuitive behavior. Using our ENZ-inspired analysis of the Strehl ratio, we will explain these phenomena and define the merit of a quantity such as the Strehl ratio for systems with a large NA. Finally, some concluding remarks are given in Section 4.7.

4.1 Extended Nijboer-Zernike aberration retrieval

In Sec. 3.2 we have seen how to compute the through-focus complex amplitude, $U(r,\phi;f)$, of a general aberrated optical system, based on the Zernike expansion coefficients, β_n^m, of its pupil function, $P(\rho,\theta)$. We now consider the *inverse* problem and derive a method to reconstruct $P(\rho,\theta)$ from measurement data taken from the focal region.

4.1.1 Analytic expression for the intensity in the focal region

In the optical domain, it is in general not possible to directly measure $U(r,\phi;f)$. Instead, we have available the intensity as the measurable quantity. In the scalar regime, the intensity, $I(r,\phi;f)$, is proportional to the squared modulus of the complex amplitude, $U(r,\phi;f)$. As a result, the theoretical intensity can also be written as a function of the Zernike coefficients, β_n^m, using Eq.(3.11),

$$I_{theory}(r,\phi;f) \propto |U_{theory}(r,\phi;f)|^2 = \left| 2\sum_{n,m} i^{|m|}\beta_n^m V_n^{|m|}(r,f)\exp(im\phi) \right|^2 . \quad (4.1)$$

The squared modulus operation in Eq.(4.1) can make the evaluation of this expression quite involved. However, as we have limited ourselves to the evaluation of optical systems of high quality, we may assume that the phase aberrations and transmission defects are small. In this case Eq.(4.1) can be replaced by the approximate expression

$$\begin{aligned} I(r,\phi,f) \quad &\approx \quad 4(\beta_0^0)^2\,|V_0^0(r,f)|^2 \\ &\quad +8\beta_0^0 \sum_{n=0}^{\infty}\sum_{m=-\infty}^{+\infty} \Re\left\{ i^{-m}\beta_n^m{}^*\, V_0^0(r,f)\, V_n^m{}^*(r,f)\exp[-im\phi] \right\}, \quad (4.2) \end{aligned}$$

where the term with $m = n = 0$ has to be omitted in the summation. The coefficient β_0^0 is chosen to be real and positive; any nonzero phase of β_0^0 can be accounted for by a phase offset in the coefficients β_n^m with $n = m \neq 0$ as the absolute phase of the wavefront in the exit pupil is of no concern when measuring the image intensity. The approximation in Eq.(4.2) is justified when β_0^0 is the dominant coefficient in the Zernike expansion of the pupil function, thus allowing the deletion of any quadratic terms in β that do not contain a β_0^0 coefficient. In Eq.(4.2), the leading term is the aberration-free intensity pattern, for $f = 0$ equal to the Airy disc intensity.

Although the parametric representation of the pupil function with the aid of the β-coefficients is mathematically efficient and compact, the relationship between the amplitude and phase part of the pupil function and the structure of the intensity distribution in the focal volume tends to become obscure. For that reason, we temporarily resort to the more common harmonic representation with possibly complex β_c- and β_s-coefficients for the cosine and sine terms and the following

relationship with the general β-coefficients

$$\beta_n^m = \frac{\beta_{n,c}^m}{2} - i\frac{\beta_{n,s}^m}{2}, \qquad \beta_n^{-m} = \frac{\beta_{n,c}^m}{2} + i\frac{\beta_{n,s}^m}{2}. \tag{4.3}$$

When the pupil function shows only weak phase aberration, one uses the approximate representation

$$P(\rho,\theta) \approx 1 + i\Phi(\rho,\theta) = 1 + i{\sum_{nm}}' R_n^m(\rho)\left[\alpha_{n,c}^m \cos\theta + \alpha_{n,s}^m \sin\theta\right]. \tag{4.4}$$

The prime on top of the summation sign indicates that the term with $n = m = 0$ should be excluded from the summation. The corresponding β-coefficients are given by

$$\beta_n^m = i\frac{\alpha_{n,c}^m}{2} + \frac{\alpha_{n,s}^m}{2}, \qquad \beta_n^{-m} = i\frac{\alpha_{n,c}^m}{2} - \frac{\alpha_{n,s}^m}{2},$$

and

$$\beta_{n,c}^m = i\alpha_{n,c}^m, \qquad \beta_{n,s}^m = i\alpha_{n,s}^m, \qquad \beta_0^0 = 1, \tag{4.5}$$

with the real coefficients $\alpha_{n,c}^m$ and $\alpha_{n,s}^m$ now specifically linked to the phase part of the pupil function. For this latter, frequently occurring practical case, Eq.(4.2) can be written out in detail to make visible the separate ϕ- and (r,f)-dependencies in the intensity distribution in the focal region. These dependencies will be exploited later in the retrieval scheme. After some manipulation, Eq.(4.2) is written according to

$$\begin{aligned} I(r,\phi,f) \quad \approx \quad & \Psi_0^0 + {\sum_{n,m}}' \left\{ \Re\left[\Psi_n^m(r,f)\right]\left(\Re[\beta_{n,c}^m]\cos m\phi + \Re[\beta_{n,s}^m]\sin m\phi\right)\right. \\ & \left. + \Im\left[\Psi_n^m(r,f)\right]\left(\Im[\beta_{n,c}^m]\cos m\phi + \Im[\beta_{n,s}^m]\sin m\phi\right)\right\}, \end{aligned} \tag{4.6}$$

where we have introduced the function

$$\Psi_n^m(r,f) = \gamma_m i^{-m} V_0^0(r,f) V_n^{m\,*}(r,f) \tag{4.7}$$

with $\gamma_0 = 4$ and $\gamma_m = 8$ for $m = 1, 2, \ldots$. With the phase-only pupil function and the coefficients according to Eq.(4.4) we find

$$I(r,\phi,f) \approx \Psi_0^0 + {\sum_{n,m}}' \Im\left[\Psi_n^m(r,f)\right]\left(\alpha_{n,c}^m \cos m\phi + \alpha_{n,}^m \sin m\phi\right). \tag{4.8}$$

This expression represents a set of equations in the unknown coefficients $\alpha_{n,c}^m$ and $\alpha_{n,s}^m$ of which a certain set is needed to represent in a sufficiently accurate way the phase part of the pupil function Φ. Various methods can be applied to solve for the unknown coefficients, like point-matching or a least-squares solution. Below, we present an approach that is based on the formation of a set of linear equations using inner products, that is described in [14, 64].

4.1.2 Aberration retrieval scheme (scalar case)

To solve for the unknown aberration coefficients, $\alpha_{n,c}^m$ and $\alpha_{n,s}^m$ in Eq.(4.8), we proceed as follows. We first carry out a harmonic analysis of the intensity data in the focal volume by evaluating

$$\Upsilon_c^m(r,f) = \frac{1}{2\pi}\int_0^{2\pi} I(r,\phi,f)\cos m\phi \; d\phi, \tag{4.9}$$

and the corresponding sine-transform $\Upsilon_s^m(r,f)$. Carrying out the same harmonic analysis on the right-hand side of Eq.(4.8) we obtain the equations

$$\begin{aligned} \Upsilon_c^m(r,f) &= \delta_{mm}\Psi_0^0(r,f) + \frac{1}{2}\sum_n \alpha_{n,c}^m \Im\left[\Psi_n^m(r,f)\right], \\ \Upsilon_s^m(r,f) &= \frac{1}{2}\sum_n \alpha_{n,s}^m \Im\left[\Psi_n^m(r,f)\right], \end{aligned} \tag{4.10}$$

with δ_{mm} the Kronecker symbol. We then define the (normalized) inner product of two functions Ψ_n^m, given in Eq.(4.7), by

$$(\Psi_1(r,f),\Psi_2(r,f)) = \frac{1}{2\pi R^2 F}\int_0^R\int_{-F}^F \Psi_1(r,f)\Psi_2^*(r,f)\; r dr df, \tag{4.11}$$

where the integration extends over the focal volume up to certain limits within which reliable data have been made available by measurement. We now apply the inner product operation to both sides of Eq.(4.10) and obtain

$$\begin{aligned} (\Upsilon_c^m, \Im[\Psi_{n'}^m]) &= \delta_{mm}\left(\Psi_0^0, \Im[\Psi_{n'}^m]\right) + \frac{1}{2}\sum_n \alpha_{n,c}^m \left(\Im[\Psi_n^m(r,f)], \Im[\Psi_{n'}^m]\right), \\ (\Upsilon_s^m, \Im[\Psi_{n'}^m]) &= \frac{1}{2}\sum_n \alpha_{n,s}^m \left(\Im[\Psi_n^m(r,f)], \Im[\Psi_{n'}^m]\right). \end{aligned} \tag{4.12}$$

By choosing a sufficiently large number of $n^{'}$ values, a preferably square system of equations is constructed for each specific value of the harmonic component m, and upon solving these systems we obtain estimates for the desired α- and β-coefficients. The inner products on the right-hand side of Eq.(4.12) are calculated beforehand, a single time. The inner products on the left-hand side depend on the measurement data and have to be calculated anew for each system measurement. The solution of the system of equations is further facilitated by the fact that the matrix system of linear equations, built via the inner product method, is sparse with an almost perfect diagonal structure; this is because of the 'almost' orthogonality properties of the elementary functions $\Psi_n^m(r,f)$ over the two-dimensional (r,f)-integration domain in the focal region. For more information and some examples concerning scalar ENZ retrieval we refer to [12–14, 64].

4.1.3 ENZ-based retrieval of scaled and annular pupils (scalar case)

In Section 3.6 it was shown that the ENZ formalism can also be used to efficiently calculate the PSF of an optical system that is operated using only a radial subset of its full pupil. We now also consider the inverse operation for this class of systems.

Let us assume we want to reconstruct the scaled pupil function, $P(\epsilon\rho, \theta)$, defined in Eq.(3.54) from intensity data taken from the focal region. On comparing Eq.(3.58) with the expression for the full pupil case, Eq.(3.11), we immediately see that retrieval of the β-coefficients describing the reduced pupil can be performed using the same scheme as given above, simply by substituting $V_n^m(r, f; \epsilon)$ for $V_n^m(r, f)$. What in fact happens, if $\epsilon < 1$ in Eq.(3.54), is that the effective NA of the optical systems is reduced and we thus only require a new set of basic functions, $V_n^m(r, f; \epsilon)$, that pertain to this new NA setting, to perform the inversion scheme.

If a pupil function is known to be centrally obstructed in the region $0 \leq \rho \leq \epsilon$, aberration retrieval can also be practiced with the above sketched approach by appropriately modifying the V_n^m-functions involved. In this case, as described in Section 3.6.2, the amplitude in the focal region is given by the expression in Eq.(3.62). From this expression we thus find that the V_n^m-functions in the inversion scheme should be replaced by the W_n^m-functions defined in Eq.(3.63), in order to enable reconstruction of an annularly shaped pupil. Please note that in both the scaled and annular pupil case, the retrieved β-coefficients pertain to the contributing part of the pupil function only. The retrieved β-coefficients do give a possible solution of the pupil-function in the excluded pupil area but there are many more possible solutions especially if the total number of Zernike coefficients is large (Some discussion on this non-uniqueness problem is given in [75]).

4.2 ENZ aberration retrieval at high-NA

In the foregoing section, we have extensively discussed the retrieval mechanism for the complex pupil function using the scalar imaging model. In this section, we replace the scalar through-focus intensity distribution by its vector equivalent and then apply this new expression to basically the same retrieval procedure. The complications that arise in the vector imaging model stem from the influence of the state of polarization in the exit pupil on the intensity distribution in the focal region, see Section 3.3. In most cases, the state of polarization in the exit pupil is uniquely determined by the state of polarization in the entrance pupil. This direct relationship disappears when the optical system introduces birefringence. The vector imaging model is capable to keep track of this birefringence and, using more than one set of through-focus images with different states of polarization in the entrance pupil, it is even possible to retrieve also the birefringence properties of the system. We first present a linearized expression for the intensity distribution in the focal volume in the absence of birefringence and use this expression in a vector diffraction retrieval scheme. Retrieval in the presence of birefringence is addressed further on in this section but will not be worked out in full detail.

4.2.1 Approximated linearized intensity in the focal volume

In order to reconstruct the pupil distribution of a high-NA optical system, we require a theoretical expression for the intensity or energy density in the focal volume. In Section 3.7, it was shown that the energy density, $\langle w_e(r,\phi,f)\rangle$, of an optical system free of birefringence can be conveniently represented by Eq.(3.73), making use of the G_{kl}-functions of Eq.(3.71). Next, this expression for $\langle w_e(r,\phi,f)\rangle$ should serve as the analytic input for a similar procedure as was used in the low-NA scalar retrieval case. The analysis in such an ENZ retrieval scheme is based on an evaluation of the typical azimuthal dependencies that are present in the focal distribution. To apply the same approach in the high-NA case, we therefore require a representation of $\langle w_e(r,\phi,f)\rangle$ in which the azimuthal dependence is explicit. This can be achieved by rewriting the G_{kl}-functions of Eq.(3.71) in such a way that terms with equal azimuthal dependence $\exp(im\phi)$ are combined. This can be achieved by using the diagonalization scheme given in [48], Eq.(3.3), and this results in

$$
\begin{aligned}
G_{kl}(\beta_1,\beta_2) \;=\; & \exp\left[i(k-l)\phi\right]\Bigg[\sum_n\sum_m \beta_{n,1}^{m}\beta_{n,2}^{m*}V_{n,k}^{m}V_{n,l}^{m*} \\
& + \sum_{\mu=1}^{\mu_{max}}\Bigg\{\exp\left[-i\mu\pi/2\right]\exp\left[-i\mu\phi\right]\sum_m\sum_n \beta_{n,1}^{m}\beta_{n,2}^{m+\mu*}V_{n,k}^{m}V_{n,l}^{m+\mu*} \\
& \qquad + \exp\left[i\mu\pi/2\right]\exp\left[i\mu\phi\right]\sum_m\sum_n \beta_{n,1}^{m+\mu}\beta_{n,2}^{m*}V_{n,k}^{m+\mu}V_{n,l}^{m*}\Bigg\} \\
& + \sum_{\nu=1}^{\nu_{max}}\Bigg\{\sum_n\sum_m\left(\beta_{n,1}^{m}\beta_{n+\nu,2}^{m*}V_{n,k}^{m}V_{n+\nu,l}^{m*}+\beta_{n+\nu,1}^{m}\beta_{n,2}^{m*}V_{n+\nu,k}^{m}V_{n,l}^{m*}\right) \\
& \qquad + \sum_{\mu=1}^{\mu_{max}}\Bigg(\exp\left[-i\mu\pi/2\right]\exp\left[-i\mu\phi\right]\sum_n\sum_m\Big[\beta_{n,1}^{m}\beta_{n+\nu,2}^{m+\mu*}V_{n,k}^{m}V_{n+\nu,l}^{m+\mu*} \\
& \qquad\qquad + \beta_{n+\nu,1}^{m}\beta_{n,2}^{m+\mu*}V_{n+\nu,k}^{m}V_{n,l}^{m+\mu*}\Big] + \exp\left[i\mu\pi/2\right]\exp\left[+i\mu\phi\right]\times \\
& \qquad\qquad \sum_n\sum_m\Big[\beta_{n,1}^{m+\mu}\beta_{n+\nu,2}^{m*}V_{n,k}^{m+\mu}V_{n+\nu,l}^{m*}+\beta_{n+\nu,1}^{m+\mu}\beta_{n,2}^{m*}V_{n+\nu,k}^{m+\mu}V_{n,l}^{m*}\Big]\Bigg)\Bigg\}\Bigg],
\end{aligned}
\tag{4.13}
$$

where we have suppressed in the notation the (r,f)-dependence of the V-functions. Then, again under the assumption that for our high-quality imaging systems β_0^0 is the dominant coefficient, we can further simplify theexpressions by using the

linearized version of $G_{k,l}$ according to

$$G_{k,l}(\beta,\beta) \;=\; \frac{\beta_0^0}{2}\,\exp\{i(k-l)\phi\}\,\times \\ \sum_{\nu}\sum_{\mu}(2-\delta_{\nu\mu})\left\{\beta_\nu^{\mu *}\Psi^{\mu *}_{\nu;k,l}(r,f)\exp(-i\mu\phi)+\beta_\nu^{\mu}\Psi^{\mu}_{\nu;l,k}(r,f)\exp(+i\mu\phi)\right\}. \tag{4.14}$$

In this expression, μ assumes both positive and negative values and $\delta_{\nu\mu}$ stands for the Kronecker symbol. We have also introduced the shorthand notation

$$\Psi^{\mu}_{\nu;k,l}(r,f) = (+i)^{\mu}V^{0*}_{0,k}(r,f)V^{\mu}_{\nu,l}(r,f)\;. \tag{4.15}$$

Using the approximated $G_{k,l}$-functions given in Eq.(4.14) and inserting them in Eq.(3.73) we obtain an expression for $\langle w_e(r,\phi,f)\rangle$ that is well suited to serve as the analytic input for the vectorial ENZ retrieval scheme described below.

4.2.2 Aberration retrieval scheme (vector case)

Like in the scalar case, the retrieval scheme for obtaining the complex pupil function is based on a Fourier analysis of the measured and the analytically proposed intensity data. In contrast with the analysis of Section 4.1.2 where we have dealt with separate expressions for the cosine and sine harmonic components as they provide a clear interpretation of the expressions, we will retain here to the complex exponential notation $\exp(im\theta)$ and the complex β-coefficients with m-indices running from $-\infty$ to $+\infty$. We make this choice because at high-NA, a representation using sine and cosine terms does not yield any benefit in terms of understanding the underlying processes due to the complexity of the expressions at high-NA. Therefore, the harmonic dependence in the focal region is represented by the complex exponentials $\exp(im\phi)$ and the Fourier decomposition is carried out with respect to the azimuthal harmonics in the through-focus intensity distribution. To this goal, we evaluate

$$\Upsilon^{m}_{an}(r,f) = \frac{1}{2\pi}\int_{-\pi}^{+\pi}\langle w_e(r,\phi,f)\rangle\exp(im\phi)d\phi\;, \tag{4.16}$$

with the subscript (an) referring to the analytically calculated intensity distribution. A comparable operation is performed on the measured intensity data, that we assume known in the focal volume, and this yields

$$\Upsilon^{m}(r,f) = \frac{1}{2\pi}\int_{-\pi}^{+\pi} I_{measured}(r,\phi,f)\exp(im\phi)d\phi\;. \tag{4.17}$$

We then insert the analytic expression for $\langle w_e(r,\phi,f)\rangle$, together with the linearized expression for G_{kl}, into Eq.(4.16) and, after some lengthy manipulation, we obtain

the following expression for Υ^m_{an} (see [48, 91–93] for more details)

$$
\begin{aligned}
\Upsilon^m_{an}(r,f) \approx \frac{\beta^0_0}{2}\sum_\nu \Bigg(& \\
& \beta^{m*}_\nu(2-\delta_{\nu,m})\left[\Psi^{m*}_{\nu;0,0} + s_0^2\left\{\left(\Psi^{m*}_{\nu;1,1}+\Psi^{m*}_{\nu;-1,-1}\right)+\frac{s_0^2}{2}\left(\Psi^{m*}_{\nu;2,2}+\Psi^{m*}_{\nu;-2,-2}\right)\right.\right. \\
& \left.\left. -2\Im(p_x p_y^*)\left[\left(\Psi^{m*}_{\nu;1,1}-\Psi^{m*}_{\nu;-1,-1}\right)+\frac{s_0^2}{2}\left(\Psi^{m*}_{\nu;2,2}-\Psi^{m*}_{\nu;-2,-2}\right)\right]\right\}\right] \\
& +\beta^{-m}_\nu(2-\delta_{\nu,m})\left[\Psi^{-m}_{\nu;0,0} + s_0^2\left\{\left(\Psi^{-m}_{\nu;1,1}+\Psi^{-m}_{\nu;-1,-1}\right)+\frac{s_0^2}{2}\left(\Psi^{-m}_{\nu;2,2}+\Psi^{-m}_{\nu;-2,-2}\right)\right.\right. \\
& \left.\left. -2\Im(p_x p_y^*)\left[\left(\Psi^{-m}_{\nu;1,1}-\Psi^{-m}_{\nu;-1,-1}\right)+\frac{s_0^2}{2}\left(\Psi^{-m}_{\nu;2,2}-\Psi^{-m}_{\nu;-2,-2}\right)\right]\right\}\right] \\
& +\beta^{(m-2)*}_\nu\ \left[|p_x|^2-|p_y|^2+2i\Re(p_x p_y^*)\right](2-\delta_{\nu,m-2})\ \times \\
& \qquad\qquad \frac{s_0^2}{2}\left\{\Psi^{(m-2)*}_{\nu;-2,0}+\Psi^{(m-2)*}_{\nu;0,2}-2\Psi^{(m-2)*}_{\nu;-1,+1}\right\} \\
& +\beta^{(m+2)*}_\nu\ \left[|p_x|^2-|p_y|^2-2i\Re(p_x p_y^*)\right](2-\delta_{\nu,m+2})\ \times \\
& \qquad\qquad \frac{s_0^2}{2}\left\{\Psi^{(m+2)*}_{\nu;2,0}+\Psi^{(m+2)*}_{\nu;0,-2}-2\Psi^{(m+2)*}_{\nu;+1,-1}\right\} \\
& +\beta^{(-m-2)}_\nu\ \left[|p_x|^2-|p_y|^2-2i\Re(p_x p_y^*)\right](2-\delta_{\nu,-m-2})\ \times \\
& \qquad\qquad \frac{s_0^2}{2}\left\{\Psi^{(-m-2)}_{\nu;-2,0}+\Psi^{(-m-2)}_{\nu;0,2}-2\Psi^{(-m-2)}_{\nu;-1,+1}\right\} \\
& +\beta^{(-m+2)}_\nu\ \left[|p_x|^2-|p_y|^2+2i\Re(p_x p_y^*)\right](2-\delta_{\nu,-m+2})\ \times \\
& \qquad\qquad \frac{s_0^2}{2}\left\{\Psi^{(-m+2)}_{\nu;2,0}+\Psi^{(-m+2)}_{\nu;0,-2}-2\Psi^{(-m+2)}_{\nu;+1,-1}\right\}\Bigg), \qquad (4.18)
\end{aligned}
$$

where p_x and p_y denote the relative strengths of the x- and y-polarization components of the incident field. We recall that the expression above is not exact but applies to the linearized approximation of the $G_{k,l}$-functions. The equations to be solved for each separate m-value now read

$$\Upsilon^m(r,f) \approx \Upsilon^m_{an}(r,f)\ . \qquad (4.19)$$

In practice, we merge the equations resulting for different values of m into one large system of linearized equations. Then, like in the scalar case, the practical solution procedure consists of taking inner products, as defined by Eq.(4.11), on both sides with the functions $\Psi^m_{n;k,l}(r,f)$ and subsequently solving the linear system to obtain estimates for the β-coefficients. Note that, in the vector retrieval case, the functions $\Upsilon^m(r,f)$, $\Upsilon^m_{an}(r,f)$ and $\Psi^m_{n;k,l}(r,f)$ are all complex and the practical integration limits in the inner products operation are determined by the axial and lateral range of the collected intensity data. For more information on the high-NA retrieval scheme and some practical examples we refer to [91,92,94,95]. In addition, we have included in Section 5.5 an example in which we characterize a high-NA optical system in simulation by analyzing synthetic through-focus intensity data according to the ENZ inversion scheme.

4.2.3 ENZ-based retrieval of scaled and annular pupils (vector case)

In exactly the same manner as in the scalar case, the vectorial ENZ retrieval scheme can be adapted to apply to optical systems having a scaled or annular pupil. To reconstruct a scaled or annular pupil function, one should replace the basic functions $V_{n,j}^m$ occurring in the retrieval scheme above, by their scaled or annular counterparts defined in Eq.(3.64) and Eq.(3.65), respectively. Again, the set of β-coefficients that result in this case, of course, pertains to the contributing reduced or annular part of the pupil only and does not necessarily give any additional information on the part of the pupil functions that was excluded from the image formation process. An example of pupil function reconstruction on an annular pupil using ENZ retrieval is given in Chapter 5 or one can consult [75,96] for more information.

4.3 Retrieval of larger aberrations

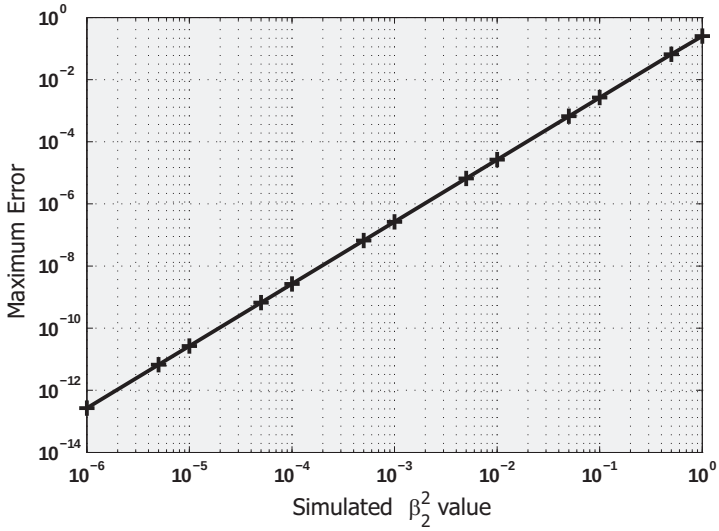

Figure 4.1: *Relation between the absolute size of β_2^2 and the maximum error present in the retrieved β-coefficients, for an otherwise perfect optical system (x-polarization,* NA $= 0.95$*).*

In Sections 4.1 and 4.2 we have shown how to construct a linear systems of equations that, on solving them, produces an estimate for the Zernike coefficients describing the aberrational state of the optical system. The formulation in terms of linear equations was possible because of the applied linearization with respect to the dominant Zernike coefficient β_0^0. Such a linearization is allowed when we assume that the aberrations (β_n^m-coefficients with $n, m \neq 0$) are small compared to β_0^0. Nevertheless, the linearization does introduce an error in the estimates of the

β_n^m-coefficients. In [92] it was shown that this error is proportional to the square of the largest β_n^m-coefficient with $n, m \neq 0$. In Figure 4.1 this behavior is illustrated by plotting the retrieval error versus the size of the aberration present in the optical system. Evaluation of Figure 4.1 tells us that if we require an accuracy in the retrieved coefficients better than 10 mλ, the total aberration should remain below 0.1 λ. Although advanced optical systems are generally within this limit, it can happen that they have larger aberrations, for example, due to a misalignment of some of its components. To be able to accurately apply the proposed ENZ retrieval scheme to such systems, we present in the remainder of this section an iterative procedure that significantly extends the range of aberration magnitude for with the method yields accurate results.

4.3.1 The predictor-corrector procedure

As already stated above, the basic ENZ retrieval approach, presented in Sections 4.1 and 4.2, is not exact and this becomes problematic for systems containing medium-to-large aberrations. In order to improve the retrieval accuracy, we should somehow estimate the error introduced by the linearization and compensate for it. In [64] and [92] it was shown, for the scalar and vectorial case respectively, that a so-called predictor-corrector procedure can be applied for this purpose. In Figure 4.2 a schematic representation of this procedure is given and below we will work out the details for the high-NA vectorial case.

We assume that a measured through-focus intensity distribution I_m is available that is to be represented in the form

$$I_m \propto |\mathbf{E}|^2 = \left(\beta_0^0\right)^2 \chi_{0,0}^{0,0} + 2 \sum_{n,m}{}' \beta_0^0 \beta_n^{m*} \chi_{n,0}^{m,0} + \sum_{n,m}{}' \sum_{n',m'}{}' \beta_n^m \beta_{n'}^{m'*} \chi_{n,n'}^{m,m'} \quad . \tag{4.20}$$

Here $\chi_{0,0}^{0,0}$ and $\chi_{n,0}^{m,0}$ pertain to the dominant aberration-free auto-term and the dominant cross-terms, respectively, that arise in accordance with Eqs.(4.13)-(4.15), and $\chi_{n,n'}^{m,m'}$ is an elaborate term, that involves products $V_{n;j}^m V_{n';j'}^{m'*}$, pertaining to small cross-terms. The primes on the summation symbols in Eq.(4.20) indicate that the terms with $n = m = 0$ and $n' = m' = 0$ should be deleted. In the basic retrieval scheme, we choose the β's in the small cross-term deleted version

$$\left(\beta_0^0\right)^2 \chi_{0,0}^{0,0} + 2 \sum_{n,m}{}' \beta_0^0 \beta_n^{m*} \chi_{n,0}^{m,0} \tag{4.21}$$

of Eq.(4.20) such that the match between Eq.(4.21) and I_m is maximal; this is done in accordance with Eqs.(4.17)-(4.19). The resulting β's are denoted by $\beta_n^m(1)$ and form a first estimate of the β's in Eq.(4.20) that serve to represent I_m.

In the basic retrieval scheme, matching is done with the small cross-terms deleted. Now that an estimate $\beta_n^m(1)$ has been found, the small cross-term expression in Eq.(4.20) can be estimated as

$$\sum_{n,m}{}' \sum_{n',m'}{}' \beta_n^m(1) \beta_{n'}^{m'*}(1) \chi_{n,n'}^{m,m'} \tag{4.22}$$

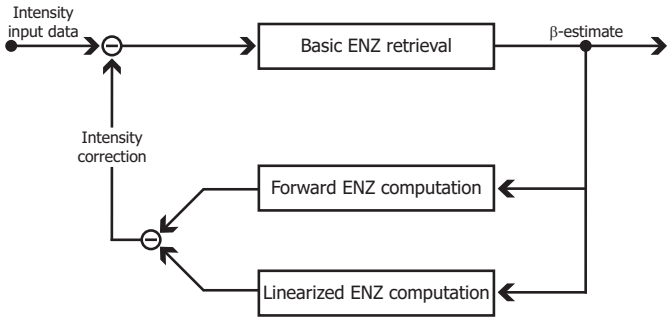

Figure 4.2: *Schematic representation of the predictor-corrector procedure. Input intensity data is taken from an unknown optical system and serves as input for the basic ENZ retrieval (Eq.(4.21)). This will give a set of β-coefficients denoted $\beta(1)$ and serves as input to both the complete and linearized forward ENZ computations. The two resulting intensity distributions are subtracted according to Eq.(4.23). This results in an intensity correction term that is applied to the original input intensity. After this a second iteration can be started with the corrected intensity as input and this process is repeated until convergence in the β-estimates is reached.*

in which the unknown β_n^m are replaced by their first estimates $\beta_n^m(1)$. A direct computation of Eq.(4.22) is, especially in the vectorial case, quite involved since the $\chi_{n,n'}^{m,m'}$ are complicated expressions, and so we proceed in a different manner. We compute, using the forward scheme for computing the field components E_i in Eq.(3.22), the through-focus intensity point-spread function $I(1) = |\mathbf{E}(1)|^2$ of the optical system with pupil function $P(1)$ of Eq.(3.10) where we have set $\beta_n^m = \beta_n^m(1)$ throughout. Then, in accordance with Eq.(4.20), the quantity Eq.(4.22) is given by

$$I(1) - \left(\beta_0^0(1)\right)^2 \chi_{0,0}^{0,0} - 2{\sum_{n,m}}' \beta_0^0(1)\beta_n^{m*}(1)\chi_{n,0}^{m,0} \ , \tag{4.23}$$

and the computation of this quantity is feasible in a very acceptable time.

Having available now Eq.(4.22), we perform basic retrieval with the I_m replaced by

$$I_m - {\sum_{n,m}}' {\sum_{n',m'}}' \beta_n^m(1)\beta_{n'}^{m'*}(1)\chi_{n,n'}^{m,m'} \ . \tag{4.24}$$

Hence, the β's in Eq.(4.21) now maximize the match between Eqs.(4.21) and (4.24) to yield a new collection of coefficients $\beta_n^m(2)$. This whole process of adjusting I_m is repeated until convergence is reached. When convergence is reached, we have obtained coefficients $\beta_n^m(\infty)$ that satisfy

$$I_m - {\sum_{n,m}}' {\sum_{n',m'}}' \beta_n^m(\infty)\beta_{n'}^{m'*}(\infty)\chi_{n,n'}^{m,m'} = \left(\beta_0^0(\infty)\right)^2 \chi_{0,0}^{0,0} - 2{\sum_{n,m}}' \beta_0^0(\infty)\beta_n^{m*}(\infty)\chi_{n,0}^{m,0} \ . \tag{4.25}$$

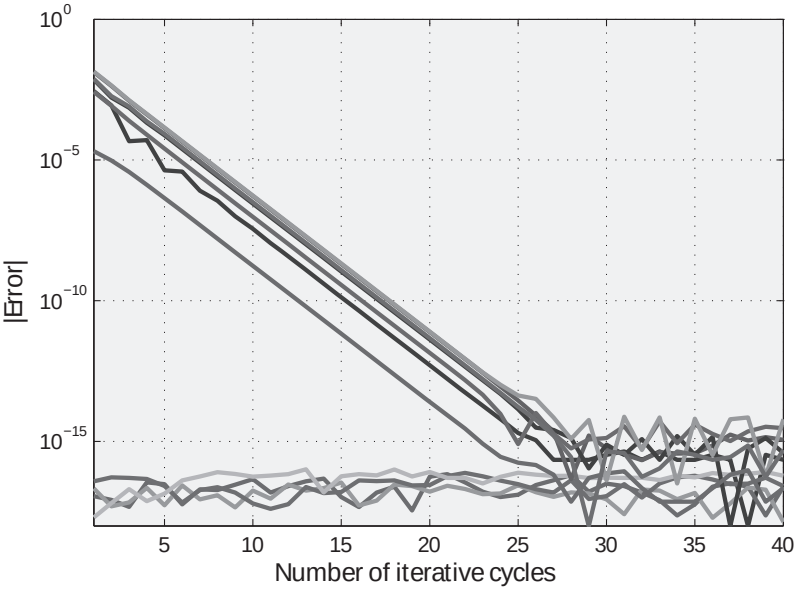

Figure 4.3: *A plot of the residual errors remaining in the retrieved β-values versus the number of iterative steps taken in the predictor-corrector procedure. The lines pertain to various aberration terms that were either initially present or that were erroneously detected at the start of the iterative retrieval process. The end value is determined by machine precision.*

By bringing the double summation at the left-hand side of Eq.(4.25) to the right-hand side of Eq.(4.25), we see that we have managed to represent I_m in the form Eq.(4.20) using $\beta_n^m = \beta_n^m(\infty)$. Although the predictor-corrector scheme is presented here for the vectorial case, it can as well be applied in the scalar case by simply replacing the vectorial expressions by their scalar counterparts given in Section 4.2.

To illustrate the large gain of accuracy introduced by the predictor-corrector procedure we have included Figure 4.3 that shows the residual error present in the retrieved β-coefficients versus the number of iteration cycles for a typical ENZ retrieval task. The predictor-corrector procedure reduces the residual error of the reconstruction algorithm all the way down to machine precision. As a result, this approach extends the range of aberration magnitudes for which ENZ system characterization yields accurate results up to aberration magnitudes of 0.3λ RMS. Beyond this range, also the predictor-corrector procedure breaks down, probably due to phase wrapping effects occurring in the reconstructed pupil distribution. Note that in an actual system characterization experiment the maximum obtainable accuracy of the predictor-corrector approach is also affected by noise in the measurement data. However, the influence of noise on ENZ retrieval is limited and this will be illustrated and further discussed in Chapter 5 where we present some aberration retrieval applications in which the predictor-corrector procedure is applied.

4.4 ENZ-based retrieval for birefringent optical systems

In birefringent optical systems, the different polarization components of the incident beam acquire different amounts of aberrations while propagating through the optical system. To analyze the state of polarization in the exit pupil in the presence of birefringence, we use the Jones matrix analysis [97]. The matrix relation between the x- and y-components of the input and output electric fields is in general given by [98]

$$\begin{pmatrix} E_x \\ E_y \end{pmatrix} = \begin{pmatrix} m_{11} & m_{12} \\ m_{21} & m_{22} \end{pmatrix} \begin{pmatrix} a_j \\ b_j \end{pmatrix} \tag{4.26}$$

where the complex amplitudes of the x- and y components of the incident electric field at the j-th exposure have been denoted by (a_j, b_j). In order to determine the birefringence of the optical system we basically need to evaluate the four complex matrix elements m_{ij} for each sample point in the exit pupil, leading to eight independent quantities to be determined. We now choose to exclude dichroism. In this case the matrix above has a special structure [66,99–102] and can be written as

$$M = \begin{pmatrix} m_{11} & m_{12} \\ -m_{12}^* & m_{11}^* \end{pmatrix} , \tag{4.27}$$

with the property $|m_{11}|^2 + |m_{12}|^2 = 1$. The eigenstates of this matrix are elliptical in general. Once the eigenvalues and eigenstates have been found, the orientation and the value of the phase birefringence are known.

Because of the special structure of the unitary matrix M, three independent quantities need to be determined on top of the geometrical wavefront aberration and transmission defects of the system. We thus need four retrieval operations to determine the complex quantities m_{11} and m_{12} plus the polarization-independent geometrical defects of the system. Preferred polarization states (a_j, b_j) are two orthogonal linear polarization states, e.g. $(1, 0)$ and $(0, 1)$ and the circular ones, viz. $(1, i)/\sqrt{2}$ for left-circularly polarized and $(1, -i)/\sqrt{2}$ for right-circularly polarized light. The four exposures with the preferred polarization states lead, after retrieval, to four different sets of β-coefficients, $\beta^m_{n;(1,0)}$, $\beta^m_{n;(0,1)}$, $\beta^m_{n;(1,i)}$ and $\beta^m_{n;(1,-i)}$. From the four sets of β-coefficients we obtain the complex amplitude in a general point of the exit pupil for four different polarization states. This is basically sufficient to uniquely determine the size and the orientation of the cumulative birefringence of the optical system in that specific point of the exit pupil. In addition, we obtain the geometrical defects of the system that are independent of the state of polarization of the incident light.

4.5 ENZ-based retrieval beyond the Debye regime

The ENZ theory is based on the Debye diffraction integral and consequently also the ENZ inversion scheme will only produce sensible results for optical systems that are operating within the Debye regime. In optics this generally does not pose severe

limitations as the vast majority of optical systems are well described according to the Debye approximations. Nevertheless, in some cases, especially during ENZ inversion experiments, it is inevitable to deal with the Rayleigh integral. In this section, we explain why and in addition we show that it is possible to approximate the Rayleigh integral with the analytically solvable Debye integral, by introducing a scaling factor for the variables f and r.

4.5.1 Rayleigh vs Debye

One exception of optical systems not well described by the Debye integral is formed by tiny microlenses. As they have an aperture of typically only a few hundred wavelengths in diameter, they require a description according to the exact Rayleigh integral. Also, in another more unexpected situation, the Debye representation breaks down, namely, during experiments meant to collect data for the ENZ inversion scheme. As the object used in the inversion experiment is point-like, its image size is typically of the same size as the Airy-spot. Consequently, direct and accurate recording of this tiny pattern using a CCD-camera is not possible, because the spot extends over only a few pixels. Therefore, in general, an enlarged image of the focal spot is generated on the CCD-camera, using an additional lens. This operation reduces the effective NA inversely proportional with the applied magnification of the image. In many practical situations this means that the effective NA takes a value below 0.01 and in this range the Debye integral is no longer valid and only the Rayleigh integral yields accurate results. In fact, the net effect of extremely small NA values is very similar to that of very small apertures as is illustrated in Figure 4.4. There, we show on top the through-focus axial intensity computed with both the Rayleigh and Debye integral. As this computation was performed within the Debye regime, both curves match very well. The four graphs below pertain to the same computation, only there we have changed one of the parameters used in the top graph so that the resulting system is outside the Debye regime. In the two left-most graphs we have changed the aperture so that the simulated systems represent two microlenses having a diameter of $100\,\mu$m and $50\,\mu$m, respectively. In the two figures on the right we have changed the effective NA of the system to 0.02 and 0.01, respectively. Comparison between the figures on the left and right shows that their effect on pushing the Debye integral away from its exact Rayleigh counterpart is identical.

4.5.2 Correction of the Debye integral

When one compares mathematical expressions for the Rayleigh and Debye integrals (see for example [48], Eqs.(2.15) and (2.17) or [103]), one finds that the difference between them is twofold. Both their amplitude factor, which can be taken outside the integral, as well as their phase exponentials, inside the integral, are different. According to our analysis, which we intend to present in detail in [104], it is possible to represent the Rayleigh integral in terms of the Debye integral by applying a scaling operation, to both the lateral and axial variables,

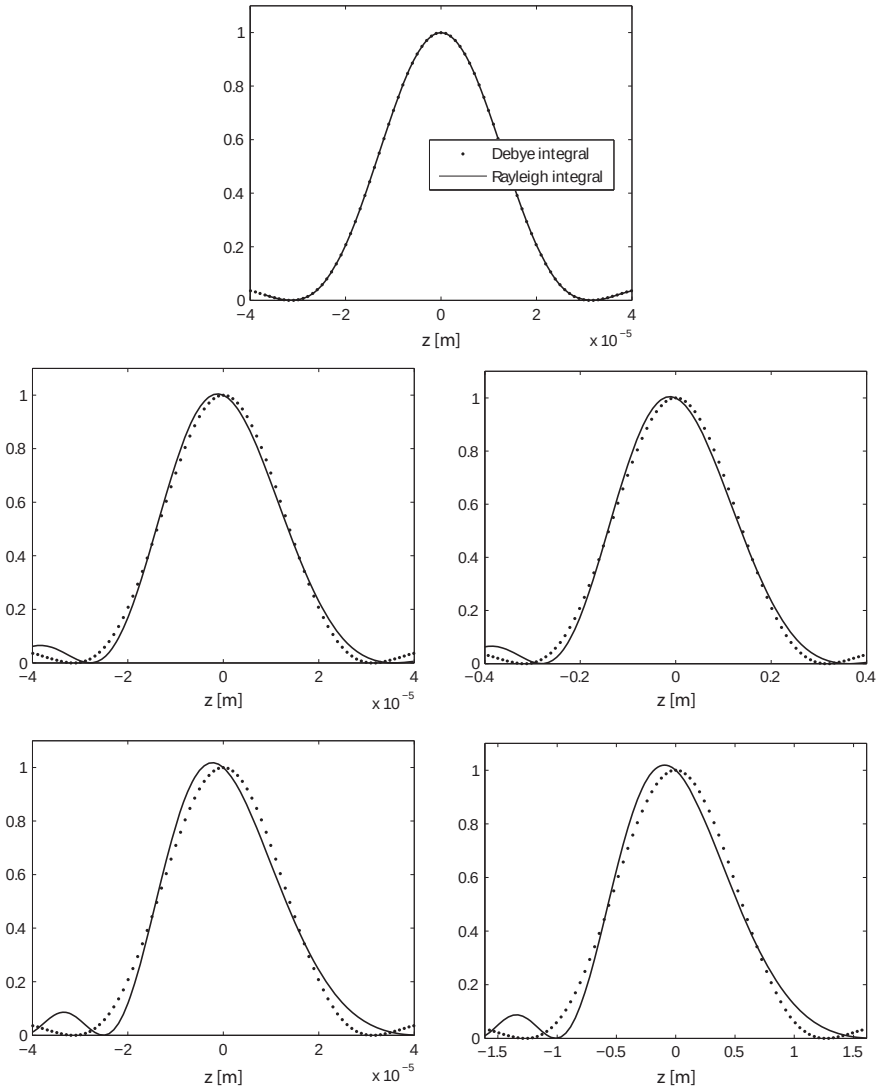

Figure 4.4: *Axial PSF intensity according to both the Rayleigh and Debye integrals. The top graph shows the PSF generated by a perfect,* 1 cm *diameter, lens* (NA = 0.2, $\lambda = 633\,\mathrm{nm}$) *that is well within the Debye regime. The four graphs below we have started from the same settings as the graph on top, however changing one parameter so that the resulting system is outside the Debye regime. In the left two graphs we have changed the aperture to a diameter of* $100\,\mu$m *and* $50\,\mu$m*, respectively, and for the two graphs on the right we have reduced the NA to a value of* 0.02 *and* 0.01*, respectively.*

that reads

$$r' = \frac{r}{1 - \frac{\lambda f}{\pi s_0^2 R_1}} \ , \tag{4.28}$$

$$f' = \frac{f}{1 - \frac{\lambda f}{\pi s_0^2 R_1}} \ . \tag{4.29}$$

This rather simple modification significantly improves the agreement between the Debye and Rayleigh curves. In fact if we apply Eqs.(4.28) and (4.29) to all examples presented in Figure 4.4, the corrected Debye curves will be visually identical to the Rayleigh curve.

Because of the very basic nature of the correction presented here it can be straightforwardly implemented throughout the complete ENZ formalism. What results is an even more versatile version of the ENZ toolset, that can also be applied to compute PSF's of microlenses and allows the application of ENZ inversion to measurement data collected using an additional lens to magnify the image on the recording media.

4.6 ENZ theory and the Strehl ratio

In Section 2.5 we have briefly introduced the Strehl ratio as a commonly used single valued quality measure. The popularity of the Strehl ratio can be largely explained by the fact that, for optical systems having a low-NA and containing only a small amount of phase aberration, this quantity can be represented by a simple analytic approximation. Unfortunately, at larger NA, such a simple relationship does not exist and the discussion of optical quality in terms of Strehl ratio becomes, in this case, more complex. In fact, the analysis of the Strehl ratio at high-NA can lead to some rather counterintuitive results and these will be discussed in this section.

4.6.1 Analytic expressions for the Strehl ratio (low-NA)

Under the condition that we are only dealing with a limited phase excursion in the pupil, the Strehl ratio S can be approximated in terms of the Zernike expansion coefficients α pertaining to the phase aberration Φ defined in Eq.(3.2). For this purpose we insert Eq.(3.2) into Eq.(2.43) and apply a series expansion up to the second order of the integrand in the numerator. The Strehl ratio, S, can then be written as

$$S \approx S(\alpha) := 1 - {\sum_{n,m}}' \frac{(\alpha_n^m)^2}{\varepsilon_m (n+1)} \tag{4.30}$$

where we have used that $A(\rho, \theta) = 1$ and $\varepsilon_0 = 1$, $\varepsilon_1 = \varepsilon_2 = ... = 2$, represents Neumann's symbol. Like in previous summations, the prime implies that the term with $(n, m) = (0, 0)$ is omitted. Examination of Eq.(4.30) clearly shows the expected behavior that S is reduced whenever the number and/or magnitude of the Zernike coefficients, α_n^m, pertaining to the expansion of the phase aberration, $\Phi(\rho, \theta)$, is increased.

4.6.2 Analytic expressions for the Strehl ratio (high-NA)

In the high-NA case, the assumptions made to arrive at Eq.(4.30) are not valid. In order to arrive at an equivalent expression for the Strehl ratio at high-NA, the complete definition of S, already given in Eq.(2.45), should be considered

$$S = \frac{\left| \frac{1}{\pi} \int_0^{2\pi} \int_0^1 A_l(\rho,\theta) \exp\{i[\Phi(\rho,\theta) + f\Delta(\rho)]\} \rho d\rho d\theta \right|^2}{\left| \frac{1}{\pi} \int_0^{2\pi} \int_0^1 A_l(\rho,\theta) \rho d\rho d\theta \right|^2} . \tag{4.31}$$

For this purpose we introduce the Zernike expansions of the various functions encountered in the integrands of Eq.(4.31). Regarding the exponential phase function, in line with standard ENZ aberration analysis of Φ, we write

$$\begin{aligned}
\Phi(\rho,\theta) &= \sum_{n,m} \alpha_n^m R_n^m(\rho) \cos m\theta \, , \\
\Phi_1(\rho,\theta) &= \left(\sum_{n,m} \alpha_n^m R_n^m(\rho) \cos m\theta \right) - \alpha_0^0 R_0^0(\rho) \, , \\
\Delta(\rho,\theta) &= \frac{1 - \sqrt{1 - s_0^2 \rho_0^2}}{1 - \sqrt{1 - s_0^2}} = \sum_{n,m} \gamma_{2n}^0 R_n^m(\rho) \, , \\
\Delta_1(\rho,\theta) &= \left(\sum_{n,m} \gamma_{2n}^0 R_n^m(\rho) \right) - \gamma_0^0 R_0^0(\rho) \, .
\end{aligned} \tag{4.32}$$

The defocus phase term Δ has been developed into a radially symmetric Zernike expansion with even index coefficients γ_{2n}^0; the values of these coefficients are basically obtained by evaluating the inner products of Δ with the relevant radial Zernike polynomial (a recipe to determine the coefficients γ_{2n}^0 is included in Appendix B, for more details see [63]). We have introduced the functions Φ_1 and Δ_1 to split off the constant phase terms that are irrelevant for the determination of optimum focus and Strehl ratio. Note that we have again limited ourselves in this aberration analysis to $\cos m\theta$-dependent aberration terms, but an extension of the analysis to the general case including aberration terms with arbitrary azimuthal dependence is straightforward.

With $A_E(\rho,\theta) \equiv 1$, the amplitude function A_l of Eq.(2.44) is split into

$$\begin{aligned}
A_l(\rho,\theta) &= \left[\frac{1 + \sqrt{1 - s_0^2\rho^2} - [1 - \sqrt{1 - s_0^2\rho^2}] \cos 2\theta}{2(1 - s_0^2\rho^2)^{1/4}} \right] \\
&= A^0(\rho) - A^2(\rho) \cos 2\theta \, ,
\end{aligned} \tag{4.33}$$

with

$$A^0(\rho) = \sum_{n=0}^{\infty} a_{2n}^0 R_{2n}^0(\rho) \, , \qquad A^2(\rho) = \sum_{n=1}^{\infty} a_{2n}^2 R_{2n}^2(\rho) \, . \tag{4.34}$$

The expressions for the coefficients a_{2n}^0 and a_{2n}^2 as a function of s_0 can again be found in Appendix B.

To calculate the approximated Strehl ratio we start by expanding the exponential of the integrand in the numerator of Eq.(4.31) up to second order according to $\exp(ix) = 1 + ix - \frac{1}{2}x^2$. The numerator of Eq.(4.31) is equal to $|U|^2$, with the complex amplitude U given by

$$\begin{aligned} U &= \frac{1}{\pi}\int_0^{2\pi}\int_0^1 A_l(\rho,\theta)\exp\{i[\Phi_1(\rho,\theta)+f\Delta_1(\rho)]\}\rho d\rho d\theta \\ &\approx \frac{1}{\pi}\int_0^{2\pi}\int_0^1 \left(A^0(\rho)-A^2(\rho)\cos 2\theta\right)\left[1+i\left\{\Phi_1(\rho,\theta)+f\Delta_1(\rho)\right\}\right. \\ &\qquad \left.-\frac{1}{2}\left\{\Phi_1(\rho,\theta)+f\Delta_1(\rho)\right\}^2\right]\rho d\rho d\theta. \quad (4.35) \end{aligned}$$

Using the notation

$$\Phi_1^m(\rho) = \sum_{0\neq n=m,m+2,\cdots} \alpha_n^m R_n^m(\rho) = \frac{\epsilon_m}{2\pi}\int_0^{2\pi}\Phi_1(\rho,\theta)\cos m\theta\, d\theta, \quad (4.36)$$

for $m = 0, 2$ and with $\epsilon_0 = 1,\ \epsilon_2 = 2$, we write

$$\begin{aligned} U &\approx 2\int_0^1 A^0(\rho)\rho d\rho + 2i\int_0^1 A^0(\rho)\left\{\Phi_1^0(\rho)+f\Delta_1(\rho)\right\}\rho d\rho \\ &\quad -\frac{1}{2\pi}\int_0^{2\pi}\int_0^1 A^0(\rho)\left\{\Phi_1(\rho,\theta)+f\Delta_1(\rho)\right\}^2\rho d\rho d\theta \\ &\quad -i\int_0^1 A^2(\rho)\Phi_1^2(\rho)\rho d\rho \\ &\quad +\frac{1}{2\pi}\int_0^{2\pi}\int_0^1 A^2(\rho)\left\{\Phi_1(\rho,\theta)+f\Delta_1(\rho)\right\}^2\cos 2\theta\rho d\rho d\theta. \quad (4.37) \end{aligned}$$

Deleting 4^{th} order terms, expanding squares and carrying out integrations (using Eq.(4.36)), we obtain

$$\begin{aligned} |U|^2 &\approx (a_0^0)^2 - \frac{a_0^0}{\pi}\int_0^{2\pi}\int_0^1 A^0(\rho)\left\{\Phi_1(\rho,\theta)\right\}^2\rho d\rho d\theta \\ &\quad -4a_0^0\, f\int_0^1 A^0(\rho)\Delta_1(\rho)\Phi_1^0(\rho)\rho d\rho \\ &\quad -2a_0^0\, f^2\int_0^1 A^0(\rho)\left\{\Delta_1(\rho)\right\}^2\rho d\rho \\ &\quad +\frac{a_0^0}{\pi}\int_0^{2\pi}\int_0^1 A^2(\rho)\left\{\Phi_1(\rho,\theta)\right\}^2\cos 2\theta\rho d\rho d\theta \\ &\quad +2a_0^0\, f\int_0^1 A^2(\rho)\Delta_1(\rho)\Phi_1^2(\rho)\rho d\rho \\ &\quad +\left(\int_0^1 A^2(\rho)\Phi_1^2(\rho)\rho d\rho\right)^2 \end{aligned}$$

$$- \left(2 \int_0^1 A^2(\rho) \Phi_1^2(\rho) \rho d\rho \right) \left(2 \int_0^1 A^0(\rho) \left\{ \Phi_1^0(\rho) + f \Delta_1(\rho) \right\} \rho d\rho \right)$$
$$+ \left(2 \int_0^1 A^0(\rho) \left\{ \Phi_1^0(\rho) + f \Delta_1(\rho) \right\} \rho d\rho \right)^2 . \quad (4.38)$$

The expression above, together with the definition of S given in Eq.(4.31) can be used to accurately compute the Strehl ratio for high-NA optical systems. One should bear in mind that the Strehl ratio is defined as the maximum of Eq.(4.31) and that the f value for which this maximum is obtained in high-NA systems depends on both the phase aberrations as well as the NA-dependent amplitude factor.

Position of maximum intensity

The f position for which the on-axis intensity is maximum can also be approximated analytically. In [63] it was reasoned that the last two terms of Eq.(4.38) are small enough to be neglected. Then, if we differentiate the remaining terms with respect to f we obtain

$$\begin{aligned} \frac{\partial |U|^2}{\partial f} &= -2a_0^0 \left[2 \int_0^1 A^0(\rho) \Delta_1(\rho) \Phi_1^0(\rho) \rho d\rho \right. \\ &+ \left. 2f \int_0^1 A^0(\rho) \left\{ \Delta_1(\rho) \right\}^2 \rho d\rho - \int_0^1 A^2(\rho) \Delta_1(\rho) \Phi_1^2(\rho) \rho d\rho \right] . \quad (4.39) \end{aligned}$$

Setting this equal to 0, we then find

$$f = - \frac{\int_0^1 A^0(\rho) \Delta_1(\rho) \Phi_1^0(\rho) \rho d\rho - \frac{1}{2} \int_0^1 A^2(\rho) \Delta_1(\rho) \Phi_1^2(\rho) \rho d\rho}{\int_0^1 A^0(\rho) \left\{ \Delta_1(\rho) \right\}^2 \rho d\rho} . \quad (4.40)$$

Using the results from Appendix B,

$$A^0(\rho) \Delta_1(\rho) = \sum_{n=0}^{\infty} C_{2n}^0 R_{2n}^0(\rho), \qquad A^2(\rho) \Delta_1(\rho) = \sum_{n=1}^{\infty} E_{2n}^2 R_{2n}^2(\rho), \quad (4.41)$$

we get the final expression for the optimum focus setting

$$f = - \frac{\sum_{n=1}^{\infty} \frac{C_{2n}^0 \alpha_{2n}^0}{2(2n+1)} - \frac{1}{2} \sum_{n=1}^{\infty} \frac{E_{2n}^2 \alpha_{2n}^2}{2(2n+1)}}{\sum_{n=1}^{\infty} \frac{C_{2n}^0 \gamma_{2n}^0}{2(2n+1)}} \quad (4.42)$$

from orthogonality of the Zernike polynomials, normalized according to

$$\int_0^1 \left\{ R_n^m(\rho) \right\}^2 \rho d\rho = [2(n+1)]^{-1}. \quad (4.43)$$

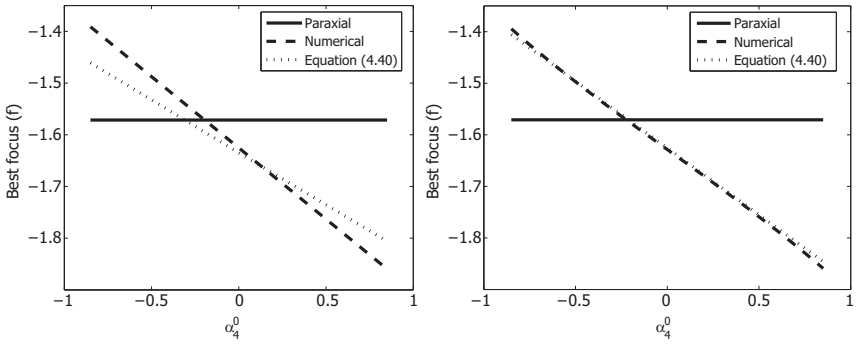

Figure 4.5: *Best-focus setting f as a function of the Zernike coefficient of spherical aberration α_4^0 in three different cases: paraxial approximation, numerical evaluation and our analysis of best focus setting according to Eq.(4.40). The initial defocusing coefficient α_2^0 is $\pi/4$. The paraxial approximation predicts a constant best focus setting at $f = -\pi/2$, the numerical evaluation shows a deviation from this value, even when $\alpha_4^0 = 0$. In both graphs, we have also presented the focus setting according to Eq.(4.40), in the left-hand graph without taking into account the high-NA amplitude nonuniformity, in the right-hand graph this effect has been included.*

As an incidental note, we observe that

$$\begin{aligned}
\sum_{n=1}^{\infty} \frac{C_{2n}^0\, \alpha_{2n}^0}{2(2n+1)} &= \int_0^1 A^0(\rho)\Delta_1(\rho)\Phi_1^0(\rho)\rho d\rho\,, \\
\frac{1}{2}\sum_{n=1}^{\infty} \frac{E_{2n}^2\, \alpha_{2n}^2}{2(2n+1)} &= \frac{1}{2}\int_0^1 A^2(\rho)\Delta_1(\rho)\Phi_1^2(\rho)\rho d\rho\,, \\
\sum_{n=1}^{\infty} \frac{C_{2n}^0 \gamma_{2n}^0}{2(2n+1)} &= \int_0^1 A^0(\rho)\left(\Delta_1(\rho)\right)^2 \rho d\rho\,. \qquad (4.44)
\end{aligned}$$

When substituting the identities above in Eq.(4.42) we observe that the inner product ($\rho d\rho$ on $0 \le \rho \le 1$) of the functions $(fA^0\Delta_1 + A^0\Phi_1^0 - \frac{1}{2}A^2\Phi_1^2)$ and Δ_1 has been made zero by the particular choice of f. This means that the aberration function corresponding to "best" focus does not contain a high-NA defocus term of the form $\Delta_1 = (\Delta(\rho) - \gamma_0^0)$. The appearance of the high-NA amplitude functions A^0 and A^2 in the aberration function $(fA^0\Delta_1 + A^0\Phi_1^0 - \frac{1}{2}A^2\Phi_1^2)$ means that the true phase aberration $f\Delta_1 + \Phi_1$ has been automatically weighted with the high-NA amplitude functions in obtaining the optimum focus setting.

In Figure 4.5 we have provided an example showing that it is insurmountable to include the amplitude function $A_l(\rho, \theta)$ in order to obtain accurate predictions on the Strehl ratio at high NA. Figure 4.5 shows the focus offset that is found according to three different approaches when the spherical aberration coefficient α_0^4 is varied. The solid line represents the focus setting according to the paraxial approximation and, as it was to be expected, it does not show any dependence of the focus setting on the presence of spherical aberration. In the left-hand graph of

Figure 4.5 we have shown the behavior of f according to our analytic treatment in the case that the amplitude nonuniformity according to Eq.(4.33) was omitted from the analysis (dotted curve, labeled 'Eq.(4.40)'). This approach is in line with the common opinion that phase defects are significant in the evaluation of the Strehl ratio but amplitude non-uniformities are not. We can see that the difference with the exact, numerically obtained data that include the high-NA amplitude effects (dashed curve, labeled "numerical") is still appreciable although there is a considerable positive correlation with Eq.(4.40). The right-hand figure applies to the same cases with the exception that the amplitude nonuniformity now has been included in our analytic results (dotted curve). The correspondence with the non-approximated numerical calculations (dashed curved) becomes very satisfactory, showing the significant role played by the amplitude nonuniformity in the evaluation of optimum focus for a high-numerical-aperture beam. For more details and examples regarding Strehl ratio at high NA we refer to [63].

4.6.3 Meaning of Strehl ratio at high-NA

Maximum Strehl ratio is an important criterion in the design and experimental optimization of an optical system. Its simple relationship with minimum quadratic wavefront deviation is not maintained in the high numerical aperture case. For finding the focus setting with maximum Strehl ratio, it is essential to use the rigorous expressions given in this section. Our analysis shows that the focal setting that is commonly derived from a Zernike expansion of the aberration function needs to be adapted at high-NA values to find the image plane with the highest possible Strehl ratio. Also the amplitude nonuniformity in the exit pupil that is inherent to high-NA imaging has a non-negligible influence in determining this optimum focus setting and calculating the maximum Strehl ratio. Altogether it is clear that the Strehl ratio shows a far more complex behavior at high-NA. Therefore it is important to recognize that the laws deduced from its low-NA definition can not be applied unquestionably in the high-NA case and that this is still something that has to fully penetrate the awareness of the optical community.

4.7 Summary and discussion

In this chapter we have discussed the possibility of doing quality assessments of optical systems according to the ENZ diffraction theory. In Section 4.1 we have shown, for the low-NA case, how a linear system of equations can be constructed that, upon solving, yields an unambiguous set of Zernike coefficients describing the optical system under consideration. In Section 4.2 it was shown that, although the expressions in the high-NA case get far more complex, the same inversion approach can still be successfully applied. It should be noted here that the retrieved β-coefficients describe the complex field distribution in the exit pupil according to Eq.(3.21). In the forward direction this expansion is unique. In the reverse direction however, obtaining the functions A and Φ from the β-coefficients, the uniqueness of such an expansion can be questioned. This is because of the contribution to both the real and imaginary part by the exponential. As a result

there is a potential problem in uniquely determining the actual aberrations acting on the optical system. However, this problem can be overcome by applying phase-unwrapping techniques, like in optical interferometry [105], to recover the functions A and Φ independently if they show a smooth behavior.

In Section 4.3, we have dealt with the fact that both the low- and high-NA inversion schemes are not exact. They are constructed using a linearization which is justified under the assumption that the aberrations are relatively small. When the aberrations get larger and their corresponding β-coefficients approach the same order of magnitude as the dominant aberration free β-coefficient, β_0^0, the ENZ retrieval method no longer gives accurate results. This is dealt with in Section 4.3 by introducing a so-called predictor-corrector approach. This iterative procedure significantly extends the range of aberration magnitudes for which ENZ-based aberration retrieval yields accurate results up to values as large as 0.3λ RMS.

Until Section 4.4, our discussions were limited to optical systems containing aberrations that are polarization independent. Nevertheless, the ENZ retrieval scheme can also be applied to optical systems that contain birefringence. The birefringence of an optical system is described by its Jones pupil. In Section 4.4 it is described how the Jones pupil can be derived from at least four consecutive ENZ retrieval operations all having a different state of polarization for the incident beam.

All the interesting features presented in Sections 4.1 to 4.4 are enabled by the analytic results provided by the ENZ diffraction theory. However, the ENZ diffraction theory is only valid for optical systems that operate in the Debye regime. As a result, ENZ retrieval performed on an optical system that does not comply with the Debye approximations will yield inaccurate results. For example, systems with a very small NA or systems in which the aperture diameter is less than a few hundred wavelengths, should be described using the Rayleigh integral. This integral is an accurate description of the focal region for a far larger range of numerical aperture values and aperture diameters than its Debye counterpart. Its disadvantage is that, until now, no general semi-analytic solution to this integral is available and, as a consequence, it can also not be used to construct an ENZ-like inversion scheme. In order to still allow the characterization of optical systems slightly outside the Debye regime, we have introduced a correction in Section 4.5. In this correction, the Rayleigh integral is approximated by the Debye integral by the introduction of a scaling term acting on the variables r and f occurring in the ENZ basic functions. By incorporating these adapted basic functions in the standard ENZ inversion scheme we enable the characterization of optical systems with very small NA or aperture diameter that were otherwise excluded from ENZ analysis.

Finally, in Section 4.6 we have dealt with the Strehl ratio as a quality measure for advanced optical systems. Using the Zernike representation of aberrations it is shown that at low NA a simple approximate analytic expression is available to predict the Strehl ratio. Applying a similar analysis to the Strehl ratio at high NA does not lead to a similar concise result. To evaluate the Strehl ratio at high NA one should deal with a complex expression that depends on both the amplitude and the phase deviations present in the exit pupil. This complex

relation makes that some generally accepted assumptions regarding the Strehl ratio are not valid at high NA. For example, the location of highest Strehl ratio depends on both the aberrations and the amplitude in the pupil and as a result is not found at the position predicted by geometrical optics. This also implies that, if one optimizes the performance of an optical system by fine tuning some components while monitoring the Strehl ratio in a single plane, the optimum focus setting can change, resulting in false adjustments.

Chapter 5

Applications of the ENZ diffraction theory

Following the mainly theoretical considerations presented in Chapters 2-4, we discuss in this chapter a variety of applications in which the ENZ diffraction theory can be effectively applied. Although some experimental work in relation to the ENZ theory has been reported over the years [12–14, 94, 95, 106, 107], the availability of experimental results related to the advanced optical systems considered in this thesis remains limited. As a result, most applications discussed in this chapter are presented using simulations. These simulation results are obtained using self written software tools, developed in either C^{++} or Matlab, that are based on the expressions presented in this thesis. As a result, all examples shown in this chapter are reproducible for the reader with a limited amount of effort.

In Section 5.1, we start with some examples on the most obvious application of the ENZ theory; the computation of PSF's for general optical systems. Following the very basic examples already presented in Chapter 3, we focus in this chapter on the application of the ENZ formalism to optical systems that are either more realistic or present in some other way a challenge with respect to their simulation. The examples treated in this section clearly show that the ENZ formalism is a very versatile method to accurately compute the PSF of general optical system as long as they are within the Debye diffraction regime.

Apart from generating the PSF, we have seen in this thesis that the ENZ theory also gives direct access to the electric and magnetic fields in the focal region. In Section 3.7, this was used to devise expressions to accurately compute and analyze electromagnetic quantities like the Poynting vector and to study momentum transfer in the focal region. In Section 5.2, we apply these possibilities to some specific optical systems in order to visualize the transport of energy in their focal region and to study and possibly alter the transfer of momentum. Especially in the case that a helical phase object is present in the optical system, the application of the ENZ formalism will turn out to be far more efficient than the commonly used methods based on Gauss-Laguerre modes.

Besides the study of aberrated PSF's in the focal region it was shown in Section 3.4 that also the through-focus behavior of more complicated objects can be computed using the ENZ formalism. In Section 5.3, this application of the ENZ theory is illustrated by simulating the aerial image of a complex isolated mask structure produced by a lithographic exposure apparatus. In addition we illustrate the computational advantage of a non-periodic method when the image of an isolated object should be computed with a high accuracy. This is followed in Section 5.4 by more image computations, only this time dealing with a stratified configuration in image space. The formation of images in a stratified region is made possible by the analysis presented in Section 3.5 and we illustrate its capabilities by computing the intensity distribution in a layer of optical resist and by studying the air-gap effect of a solid-immersion disk read-out system.

Then, finally, in Section 5.5, we focus on applications of the ENZ inversion scheme. The development of an optical system characterization method based on through-focus intensity measurements was the main motivation for developing the ENZ diffraction theory. We will give three examples in which ENZ aberration retrieval is applied to different systems. These include a high-NA optical system, an optical system having an annular pupil and a microlens which, strictly speaking, is not accurately described by the underlying Debye diffraction theory. As the final application of the chapter we mention the possibility of accurately determining system parameters through minimization of the total retrieved aberration. This will show that for a well-corrected optical system, the aberration retrieved with the ENZ formalism will be minimum when the correct system parameters are used.

5.1 Computing the impulse response of an optical system

The most obvious application of the ENZ diffraction theory is the computation of the optical impulse response or point-spread function (PSF) of general optical systems. The ability to accurately and efficiently compute the PSF is important in judging and predicting the image performance of an optical system and to study the effects of specific aberrations. In Chapter 3, we have already computed the PSF for some very basic systems in order to illustrate the capabilities of the ENZ formalism. Although these examples did provide the necessary insight, they generally did not pertain to realistic optical systems. In this section, we present some more advanced applications of ENZ-based PSF computations and treat some examples that more closely resemble real-life optical systems.

5.1.1 Field distribution of a focused laser beam

Suppose we have a laser beam ($\lambda = 633\,\text{nm}$) with a relatively large diameter which is generated by some unknown optical system and we focus this beam (NA focusing lens = 0.95) in order to scan some surface. To obtain an accurate prediction on the maximum achievable scanning resolution and corresponding tolerances, we should know the size of the focal spot that is produced by the lens given a certain field distribution of the incident beam. One method to obtain this quantity is to measure the field in focus directly. However, this is often not feasible due to the limited lateral resolution of the detector. As a result we will often have to rely on a model or simulation to estimate the extent of the focal spot. One could for example take the diffraction-limited Airy spot as a first estimate, which can be computed using the wavelength of the laser light and the lens specifications. However, if the beam contains appreciable structure or nonuniformity in its wavefront or the focusing lens has non-negligible aberrations, the Airy distribution will be a poor representation of the actual spot. A far better prediction of the shape of the focal spot can be achieved using the ENZ formalism described in Section 3.3. In order to apply the ENZ theory, we require that the field distribution in the exit pupil is known. For the system described above this distribution is determined by the amplitude and phase distribution of the laser beam in conjunction with the complex transmission function of the focusing lens. As an example, we obtained experimentally the amplitude distribution, A_{beam}, and wavefront deviation, Φ_{beam}, through a measurement with a wavefront analyzer (see Figure 5.1) of a x-polarized collimated laser beam. Based on these measurements, we can construct the complex field distribution in the entrance pupil of the focusing lens using Eq.(3.8). To derive from this the exit pupil distribution, we should apply the complex transmission function of the focusing lens. Now assume we have available the set of Zernike coefficients, α_n^m, describing the phase aberration of the lens, Φ_{lens}, according to Eq.(3.2) and that the lens does not impose any additional amplitude effects, $A_{lens} \equiv 1$ (see top row Figure 5.2). The field in the exit pupil is then completely defined by A_{beam} and $\Phi = \Phi_{beam} + \Phi_{lens}$. Inserting these quantities in Eq.(3.8) to obtain the expression for the exit pupil distribution (see middle row

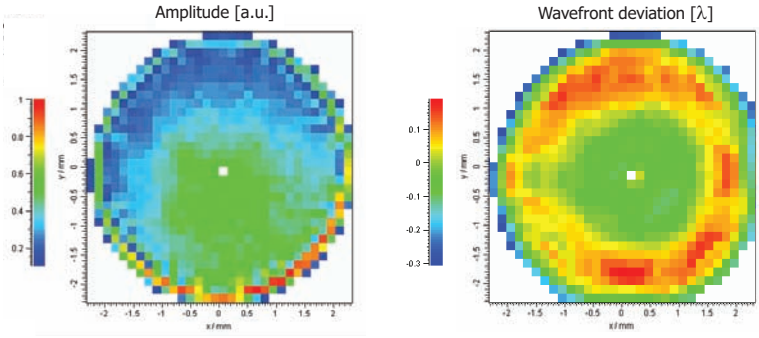

Figure 5.1: *Screen shot taken from a software package to read-out a wavefront sensor (Optocraft SHSLab wavefront sensor). The data is taken from a relatively poor laser beam at a plane just before the focusing lens. On the left the normalized intensity is shown, on the right the wavefront deviation in lambda units.*

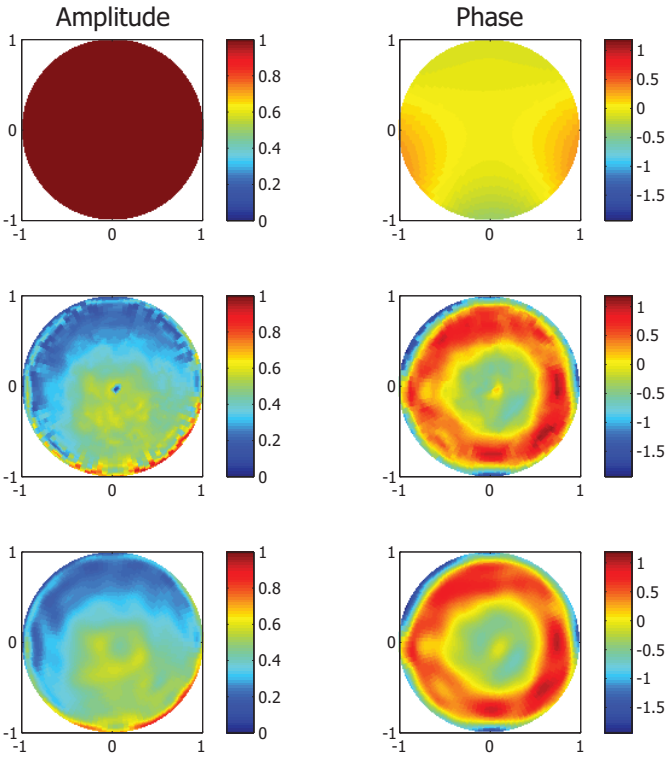

Figure 5.2: *The top row shows the amplitude and phase (in radians) of the normalized transmission function of the focusing lens. In the second row, the combined contribution of the incident beam and lens transmission is shown, thus effectively showing the exit pupil distribution. The bottom row presents graphs that were obtained using the Zernike expansion of the pupil with the maximum expansion order given by* $m_{max} \leq n_{max} \leq 20$.

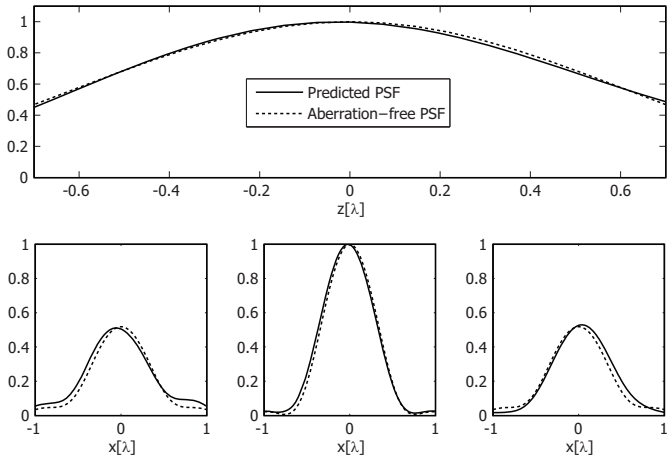

Figure 5.3: *Comparison between a spot generated from the pupil distribution in the bottom row of Figure 5.2 and an aberration-free spot (both are normalized to one,* NA = 0.95*). The top graph shows an intensity trace along the optical axis. The bottom row shows an intensity trace along the x-axis for the three different focal position indicated by the vertical lines in the top graph. The outer two graphs correspond to the out-of-focus planes that have a maximum intensity that is half the maximum intensity in focus.*

Figure 5.2) and using this expression as the left-hand input of Eq.(3.21), we find the relation between the exit pupil distribution and the Zernike expansion coefficients required to compute the PSF according to the ENZ formalism. Note that in this particular case the incident beam is fully x-polarized making $a_y t^y(\rho, \theta) = 0$ and consequently also all $\beta^m_{n,y}$ equal to zero. The actual computation of the $\beta^m_{n,x}$ coefficients is performed using a least-squares fitting operation which is, in our experience, by far the most efficient approach.

Having available the β-coefficients, we can directly apply the ENZ formalism and compute the electric field and intensity distribution in the focal region. This allows us, for example, to examine the on-axis through-focus intensity (top graph Figure 5.3) or to plot the intensity along the x-axis for several through-focus planes (bottom row of Figure 5.3). Based on these figures one could conclude that the spot is relatively good, as its behavior is not very much different from the aberration-free spot (also plotted in Figure 5.3). However, if we plot the electric field components or intensity in the xy-plane (see Figure 5.4), which data is readily available when using the ENZ formalism, we see a rather different picture. Although the spot in focus is still rather good, we have to conclude that the spot deteriorates much faster, when moving out of focus, than we would have concluded from Figure 5.3 alone. For our scanning system, this means that the axial movement tolerance will be far worse than the expected tolerance based on an analysis that does not take the beam shape and lens aberrations into account.

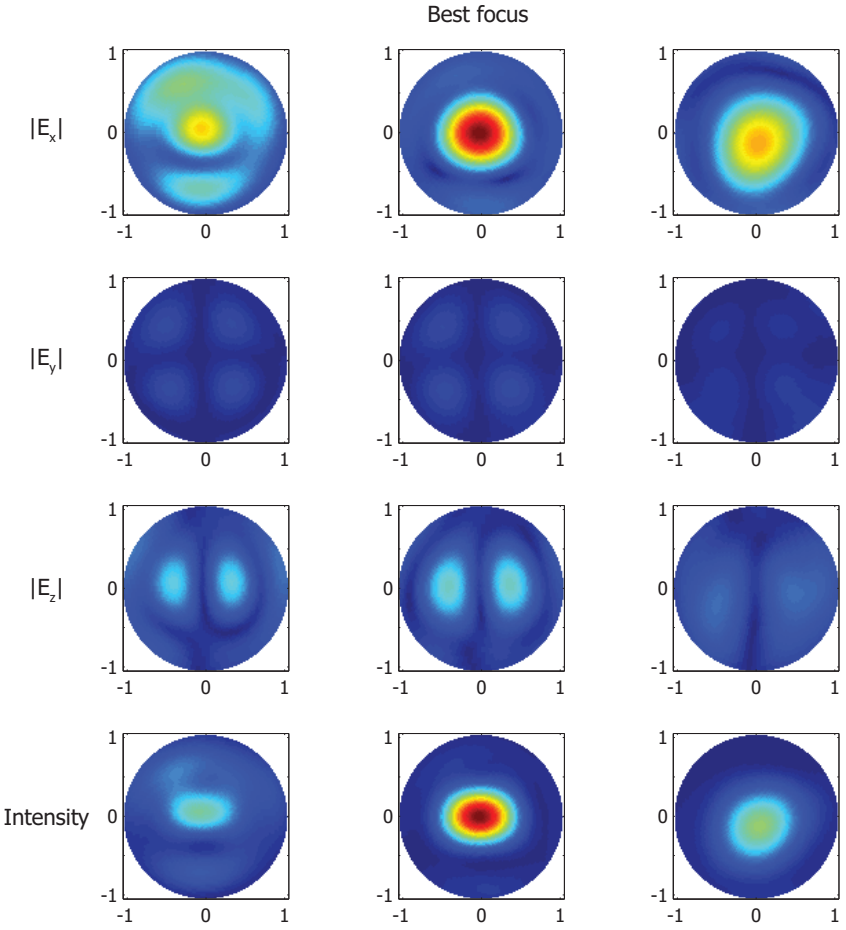

Figure 5.4: *The absolute values of the three Cartesian electric field components (row one to three) and the intensity distribution (row four) for several xy-planes in the focal region generated from the pupil distribution in the bottom row of Figure 5.2. The columns pertain to the same axial positions as in the bottom row of Figure 5.3. The first three rows are normalized to the maximum electric field amplitude, the bottom row to the maximum intensity and the x- and y-axis are given in units λ. The focusing lens has a numerical aperture* NA = 0.95.

5.1.2 Evaluation of a strongly defocused PSF

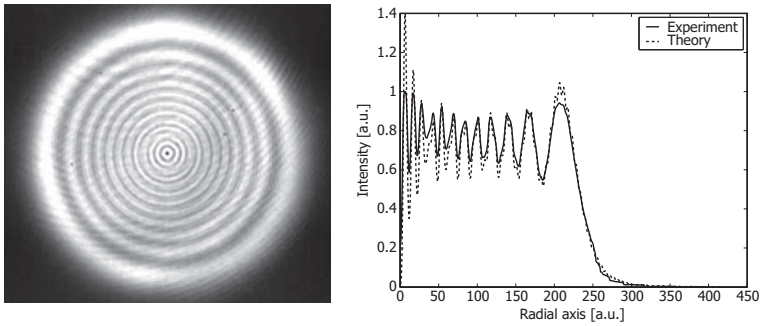

Figure 5.5: *On the left we show the measured intensity distribution in a strongly defocused image plane. Note that the axial intensity corresponds to a minimum due to the presence of an even number of Fresnel zones in the aperture as seen from the defocused position. On the right we show a comparison between the measured intensity and its calculated best-fit. The best fit between measurement and simulation was obtained for a value of* $f = 75$.

Although the ENZ formalism is meant to compute the distribution of converging fields, its application is not limited to positions close to best focus. In fact, using the results of Subsection 3.2.4, very large values of f are allowed pertaining to image planes far from focus (see also [48]). We illustrate this appealing feature in Figure 5.5. In the left part of this figure a measured intensity distribution is shown for a strongly defocused image plane. By matching this data to our theoretical frame-work, from which the results of the radial axis profile are shown in the right part of Figure 5.5, we found that the unknown position of the defocused plane pertains to a value of 75 radians for the defocus parameter f. The fact that the measured intensity data shows a less pronounced modulation may be attributed to some scattered background light and due to a diaphragm rim that is not perfectly spherical.

5.1.3 PSF generation for non-standard pupil shapes

Generally, most optical systems for which a PSF should be computed have a circular aperture. However, optical systems exist for which this is not the case. For example, in astronomy, the circular aperture is often obstructed in the center by a secondary mirror or measurement equipment. This effectively means that one has to deal with an aperture that is annularly shaped. Any nonstandard shaped aperture can in principle be regarded circular by enclosing it by an imaginary circular aperture and putting the area outside the actual aperture equal to zero. ENZ evaluation of such a system can then be performed straightforwardly using the standard Eqs.(3.21)-(3.23), where the actual aperture has been replaced by its imaginary circular counterpart. There is, however, the problem that, due to the sharp step-like behavior present in the comprising aperture, the expansion of

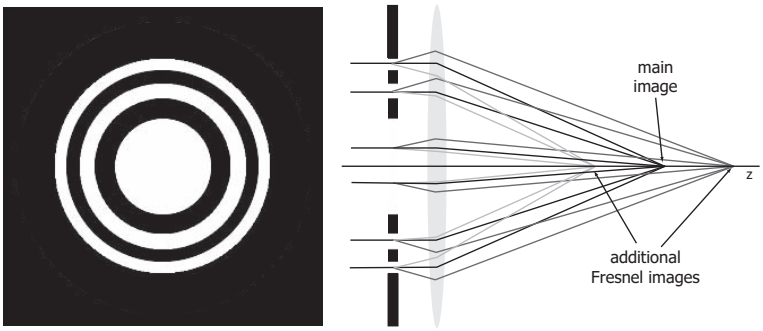

Figure 5.6: *A Fresnel lens or zone plate. White and black areas represent full and zero transmission, respectively. On the right, we have schematically depicted the formation of additional Fresnel images by this optical element.*

the pupil function on this aperture will, in general, require an enormous amount of expansion coefficients to become accurate. An alternative approach has been presented in Section 3.6 where it has been shown that both NA-reduced and annularly shaped pupils can be described in a more efficient manner using the ENZ formalism. This approach exploits the fact that these pupils can be seen as either a NA-reduced version of the actual pupil or as a full circular pupil minus another smaller circular pupil. These observations led to the construction of alternative ENZ basic function (Eqs.(3.61) and (3.63)-(3.65)) that should replace the standard V-functions during the computation of the PSF of non-standard pupil shapes. In Section 3.6, Figure 3.9, we have already shown the through-focus PSF for an aperture that is obstructed in the disk $0 \leq \rho \leq \frac{1}{2}$. In the complementary situation, when the pupil is obscured in the region $\frac{1}{2} \geq \rho \geq 1$, we are simply dealing with a standard PSF computation in which the numerical aperture is half that of the actual system.

To further illustrate this feature of the ENZ formalism, we consider an optical system including a Fresnel zone plate (see left part of Figure 5.6). Such an optical component basically consists of a pupil that is obscured in several concentric rings of increasing radius. The effect of this selective obscuration is that there will now be additional positions along the optical axes where constructive interference can take place provided that the width and position of the transmitting and obscuring regions are chosen correctly. On the right-hand side of Figure 5.6 we have schematically depicted the formation of these additional Fresnel images. In principle, we could evaluate this system using the standard ENZ formalism. However, because every ring introduces a step-like feature in the pupil, a standard Zernike representation of this pupil would require an enormous amount of Zernike coefficients in order to be accurate. We therefore proceed by applying the results presented in Subsection 3.6.4 that do allow for an efficient computation of the PSF when a Fresnel element is present. To apply Eq.(3.69), the locations of the transitions between dark and bright regions should be known. In terms of the pupil parameters used in the ENZ theory, the location of these interfaces are given in

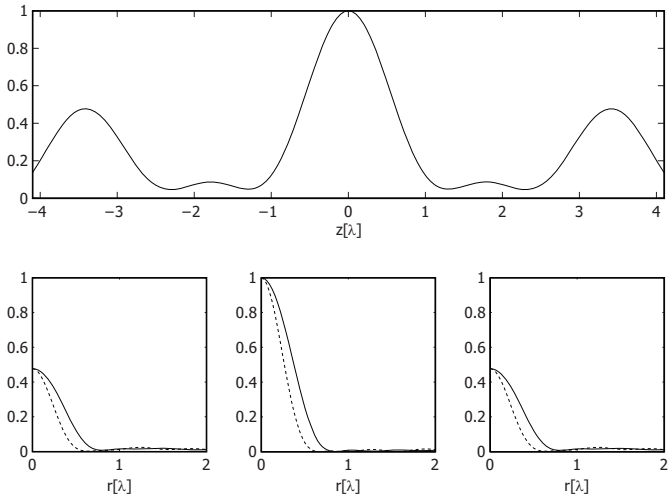

Figure 5.7: *Resulting PSF distribution when a Fresnel zone plate is present in the pupil. The top graph shows an intensity trace along the optical axis clearly illustrating the formation of a plus and minus first order Fresnel image. In the bottom row the intensity in the transverse direction is plotted for all three planes in which an image is formed. The solid and dashed curves pertain to an image trace in the radial x and y directions, respectively.*

good approximation ($R_1 >> \lambda_0$) by

$$\varepsilon_j \approx \frac{\sqrt{1-\left(1-\frac{j\lambda}{2\Delta z}\right)^2}}{s_0} \quad j = 1, 2 \cdots J \,, \tag{5.1}$$

where Δz is the desired distance between the primary and secondary images. Inserting these values into Eq.(3.69) and letting a_j be zero for even and one for odd values of j, we obtain the adapted V-functions, $\tilde{V}_n^m(r, f)$. These can be directly used in conjunction with Eq.(3.22) to compute the field in the focal region of an optical system having a Fresnel zone plate in the pupil. To illustrate this application we simulate an optical system (NA $= 0.95$, x-polarized incident beam) that contains a Fresnel zone plate that is designed to generate first order Fresnel images at a distance of 3.5λ from best focus. In Figure 5.7 the resulting PSF is shown clearly illustrating the formation of the satellite Fresnel images (top graph). In addition, we also show radial traces for all three intensity maxima and these could, for example, be used to determine the full width half maximum (FWHM) of these additional spots. Note that the satellite images are not located at exactly 3.5λ and that the intensity does not become zero in between the maxima. This is because the outermost bright ring following from Eq.(5.1) does not completely fit in the pupil, thus preventing complete constructive and destructive interference to take place.

5.2 Study of electromagnetic quantities in the focal region

Another advantage of image computations using the ENZ formalism is that it provides, with very small extra effort, not only the electric energy density but also the complete vectorial electric and magnetic fields in the focal region. These fields, in turn, give access to all the electromagnetic quantities in focus according to the expressions provided in Section 3.7. In fact, we have even shown that it is possible to derive analytic expressions for the various electromagnetic quantities in the focal region in terms of the ENZ basic functions. The main advantage of this is that it can provide us with additional insight and to illustrate this we have, in Subsection 3.7.5, discussed in detail the aberration-free optical system. In this section, we discuss some more interesting cases in which the full access to electromagnetic quantities enhances our knowledge and understanding of the physical processes occurring during image formation and the additional phenomena introduced by aberrations. For more details on the examples discussed in this section see [76].

5.2.1 Visualization of vortices in the energy flow

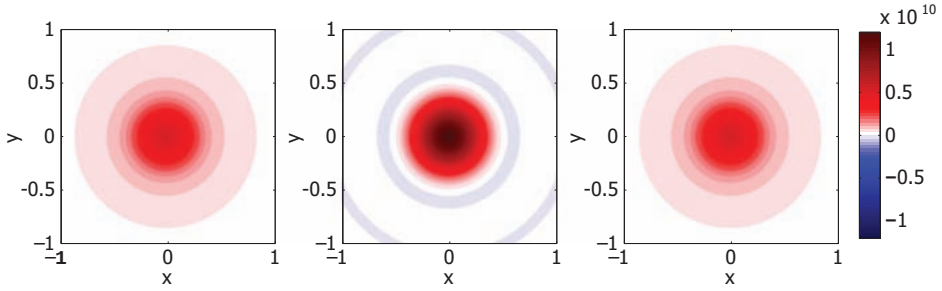

Figure 5.8: *The z-component of the Poynting vector represented by means of color shading for three through-focus planes ($f = \pi, 0, -\pi$). The incident state of polarization is linear (x-direction), the numerical aperture of the focused beam is 0.95, and the system is aberration-free.*

If we take a closer look at the z-component of the Poynting vector at best focus (see middle graph of Figure 5.8), we see that the circular symmetry of the z-component of the Poynting vector is conserved at high NA. Also, if we compute the same quantity with an y-polarized incident beam, the distribution of the z-component in focus is the same and we can thus conclude that the z-component of the Poynting vector is independent of the state of polarization of the incident beam. Furthermore, we observe that in certain annular regions in the nominal focal plane the z-component of the Poynting vector becomes negative. This indicates the presence of strongly curved streamlines and, in the extreme case, vortices in the energy flow pattern. In Figure 5.9 we have plotted some energy flux lines in the neighborhood close to the zeros of the z-component of the Poynting vector.

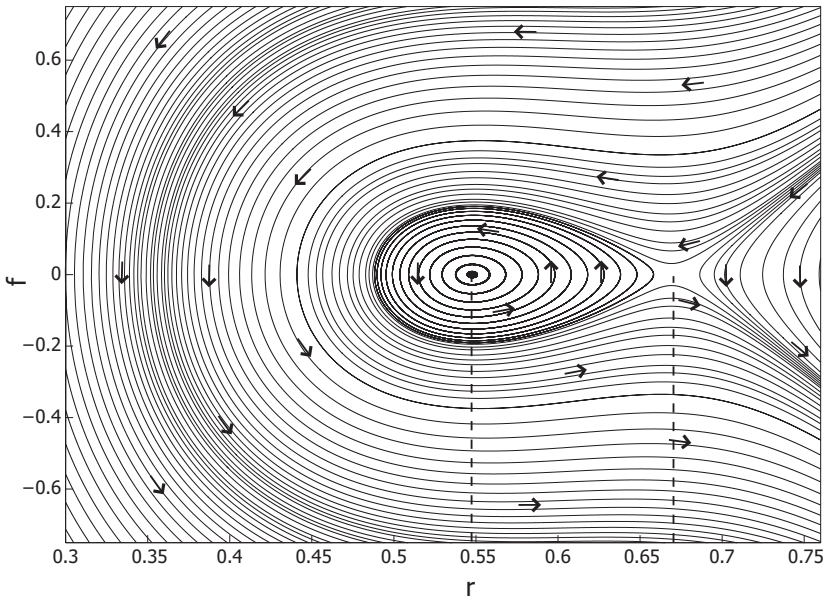

Figure 5.9: *Flow lines of the Poynting vector close to the first zeros in the nominal focal plane. The state of polarization is arbitrary. The average propagation direction of the flow through focus is downward in the figure. Particular patterns in the energy flow pattern can be found, for instance, at lateral positions* $r = 0.55$ *(vortex) and* $r = 0.68$ *(saddle) in the nominal focal plane (*$f = 0.0$*).*

The resulting flow pattern of the Poynting vector shows symmetry with respect to the optical axis (vertical in the figure) and there is a particular flow pattern around singular points, two of which have been represented in the figure, a vortex at $(r, f) \approx (0.55, 0)$ and a saddle point structure at $(r, f) \approx (0.68, 0)$.

5.2.2 Diverted energy flow due to aberrations

In Section 3.7, we have already depicted the through-focus energy transfer of a high-NA aberration-free optical system for several polarization states of the incident beam. Now, if we introduce aberrations to the optical system this will, of course, alter the flow of energy in the focal region. Because of the efficient way in which aberrations are represented in the ENZ formalism, together with its energy flow visualization capabilities, it is well suited to study these diverted flows of energy. As an example, we consider the Poynting vector for an optical system influenced by astigmatism.

In Figure 5.10, the state of polarization is linearly x-polarized, $[p_x, p_y] = [1, 0]$, and the beam is affected by astigmatism with a set of Zernike aberration coefficients β_n^m that correspond to an aberration $\Phi = \sum \alpha_n^m R_n^m(\rho) \exp(im\theta)$ in the phase part of the pupil function $\exp\{i\Phi(\rho, \theta)\}$ with coefficients $\alpha_2^2 = \alpha_2^{-2} = \pi/4$ and all others equal to zero. The resulting β-coefficients were obtained using

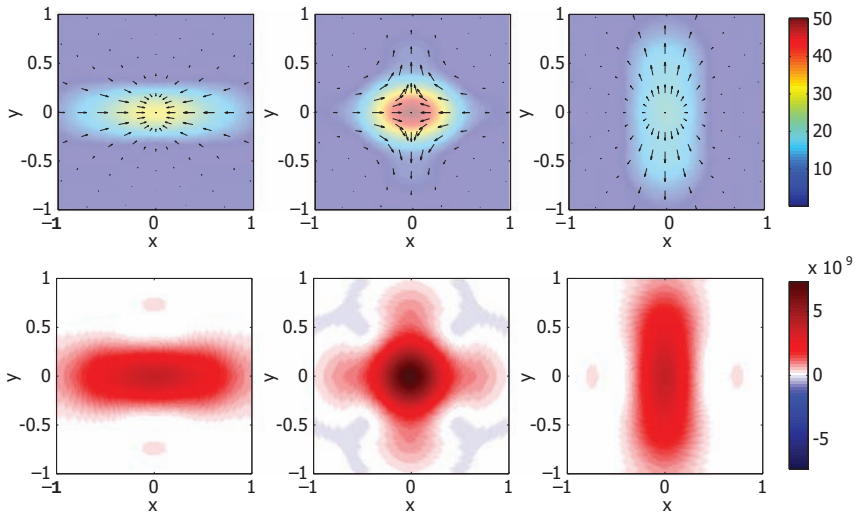

Figure 5.10: *Cross-sections of the energy density (upper row, color-shading, units* Jm^{-3}*) in three image plane settings (two focal depths in front of the nominal focal plane (*$f = \pi$*), in focus (*$f = 0$*), and two focal depths beyond the nominal focal plane (*$f = -\pi$*)). In the same graphs, the* (x, y)*-components of the Poynting vector have been represented by arrows. The length of the arrows has been normalized to the largest transverse component in the picture. In the lower row, the z-component of the Poynting vector has been represented by means of color shading (units* Wm^{-2}*). The incident state of polarization is linear (x-direction), the numerical aperture of the focused beam is* 0.95*, and the system is influenced by a certain amount of astigmatic aberration.*

a third-order development of the exponential function according to $\exp(i\Phi) = 1 + i\Phi - \Phi^2/2 - i\Phi^3/6$. In focus, the electric energy density function has adopted the characteristic cross-like shape, while out-of-focus, the characteristic focal lines become visible. The polarization influence causes a disparity between the two focal lines. The transverse energy flow pattern shows the inward and outward direction in the out-of-focus planes; in focus, the flow pattern corresponding to a saddle-point is observed. The z-component of the Poynting vector shows the 4ϕ-dependence in focus, while out-of-focus the 2ϕ-dependence dominates.

Then, if we also plot the linear and angular momentum flux components (Figure 5.11), we can observe another interesting effect. Examining the M_{zz} component we find that, although the total integrated z-angular momentum flux is zero over the focal plane, it is possible to spatially select diagonal portions of the beam that carry specific z-angular momentum. The splitting in plus and minus z-angular momentum in the focal plane becomes more important when the astigmatic aberration is increased. In this way, it is possible to create selective angular momentum that propagates in the z-direction; the disadvantage is the loss-in-resolution that is accompanied by the increase in wavefront aberration.

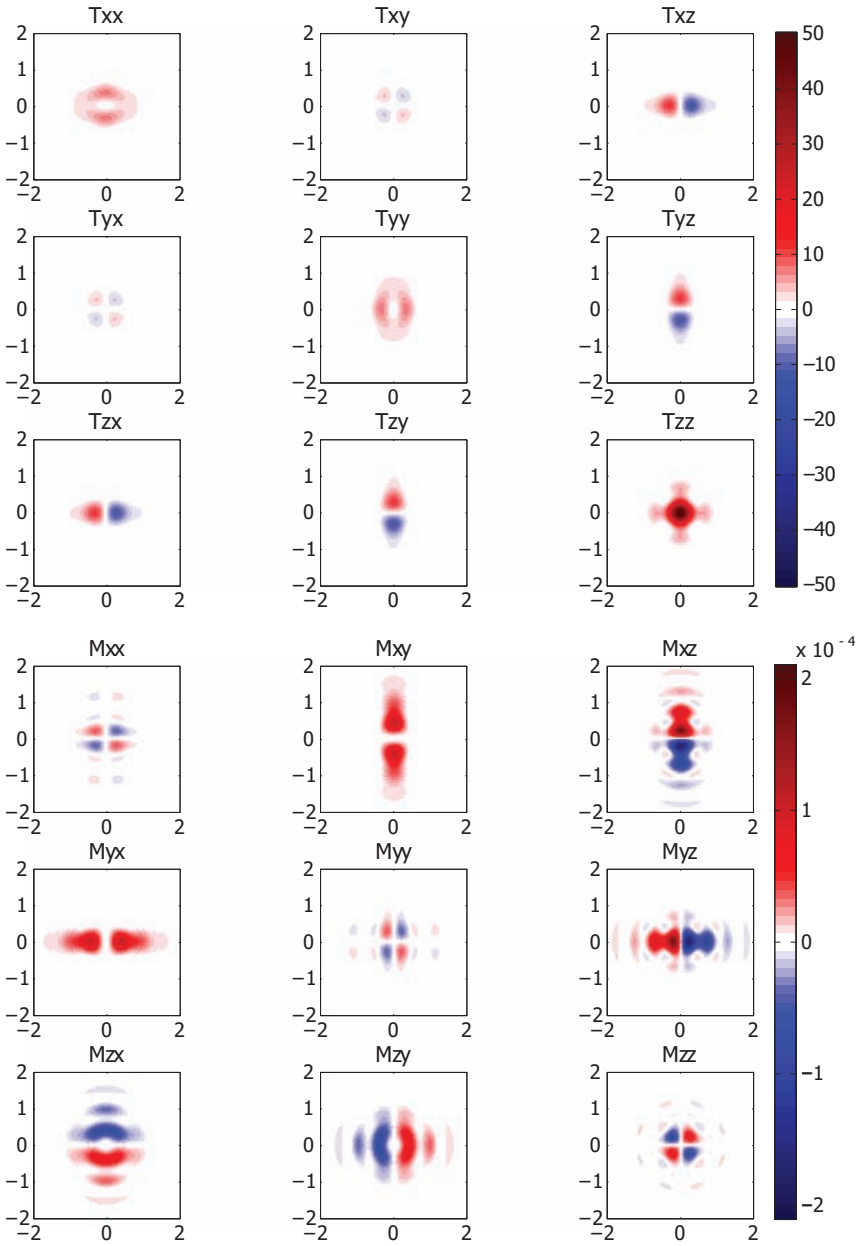

Figure 5.11: *Row one to three: graphs of the linear momentum flux components T_{ij} in the nominal focal plane. Row four to six: the M_{ij}-flux components in the same plane. The incident state of polarization is linear (x-direction), the numerical aperture of the focused beam is* 0.95*, and the system is influenced by a certain amount of astigmatic aberration.*

5.2.3 A helical phase beam

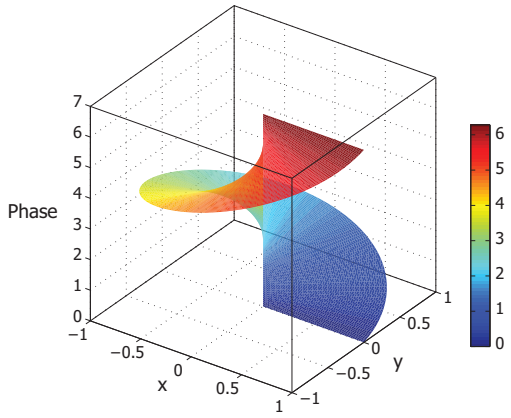

Figure 5.12: *Schematic representation of a helical phase beam. The phase is distributed in such a way that, when you go round the pupil at an equal distance from the center, the phase linearly varies between zero and* 2π*. Consequently there is a singularity in the center of the pupil and also a line at which a phase jump of* 2π *occurs.*

The final example we discuss in this section applies to a helical phase beam (see Figure 5.12). Normally, these beams are described by Gauss-Laguerre modes as solutions of the paraxial wave equation. Here, we use the Zernike wavefront aberration representation in complex form and achieve a helical wavefront shape by putting β_1^1=1, $\beta_0^0 = \beta_1^{-1}$=0. This yields a pupil function proportional to $\rho \exp(i\theta)$ that fits on a circular pupil with a sharp edge. In this sense, it is a more realistic pupil function realization than an infinitely extending Gauss-Laguerre mode. Figure 5.13 clearly shows the doughnut-cross-section and the spiral phase of the x-component of the electric field. The component E_z out-of-focus, normally composed of two lobes along the x-axis in phase opposition, is now transformed into an S-shaped profile with a maximum on the axis. This is due to the fact that the cancellation of the z-field component by geometrically opposite vector contributions is now turned into a constructive superposition because of the helical phase function. The absence of lateral components and the sole presence of a z-oriented electric field component in the beam center results in a donut-like flow pattern of the axial component of the Poynting vector. In Figure 5.14, row one to three, we show the T-flux components, that have a close resemblance with the T-components in Figure 3.13, both introducing a helical flow pattern of momentum in the beam. The main difference is found in the T_{zz}-component that has a doughnut-shape in the case of the helical phase aberration. Inspection of the M-flux components for both cases (left-handed circular polarization, see Figure 3.13, and helical phase according to an $\exp(+i\theta)$-function, Figure 5.14, row four to six), shows a very close resemblance; it can also be concluded that the sign of the angular momentum is identical in both cases.

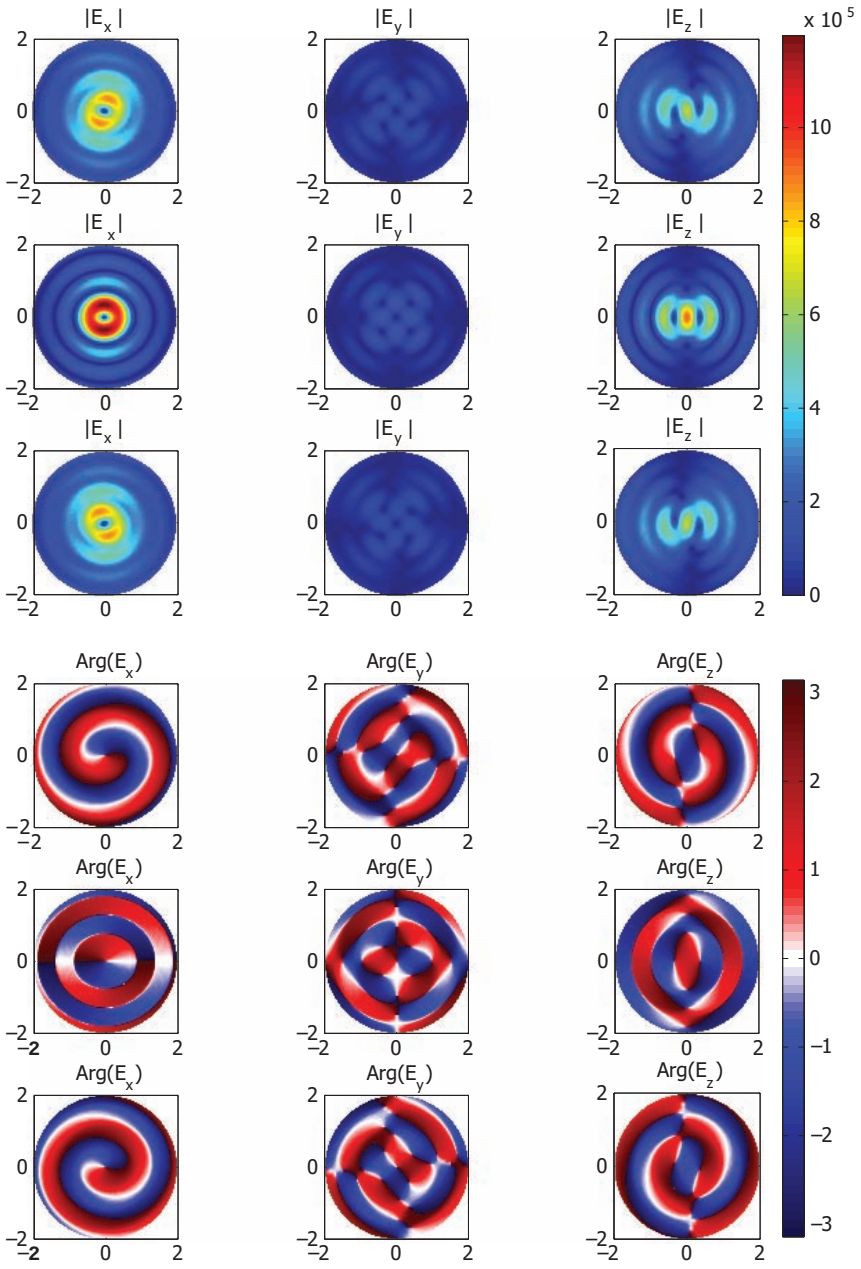

Figure 5.13: *The moduli (row one to three) of the electric field components and their phases (row four to six) in three image plane settings* ($f = -\pi,\ 0, +\pi$, *columns one to three, respectively) for a helical phase linearly polarized beam,* $[p_x, p_y] = [1, 0]$, *with the single Zernike coefficient* β_1^1=*1,* NA-*value* $s_0 = 0.95$.

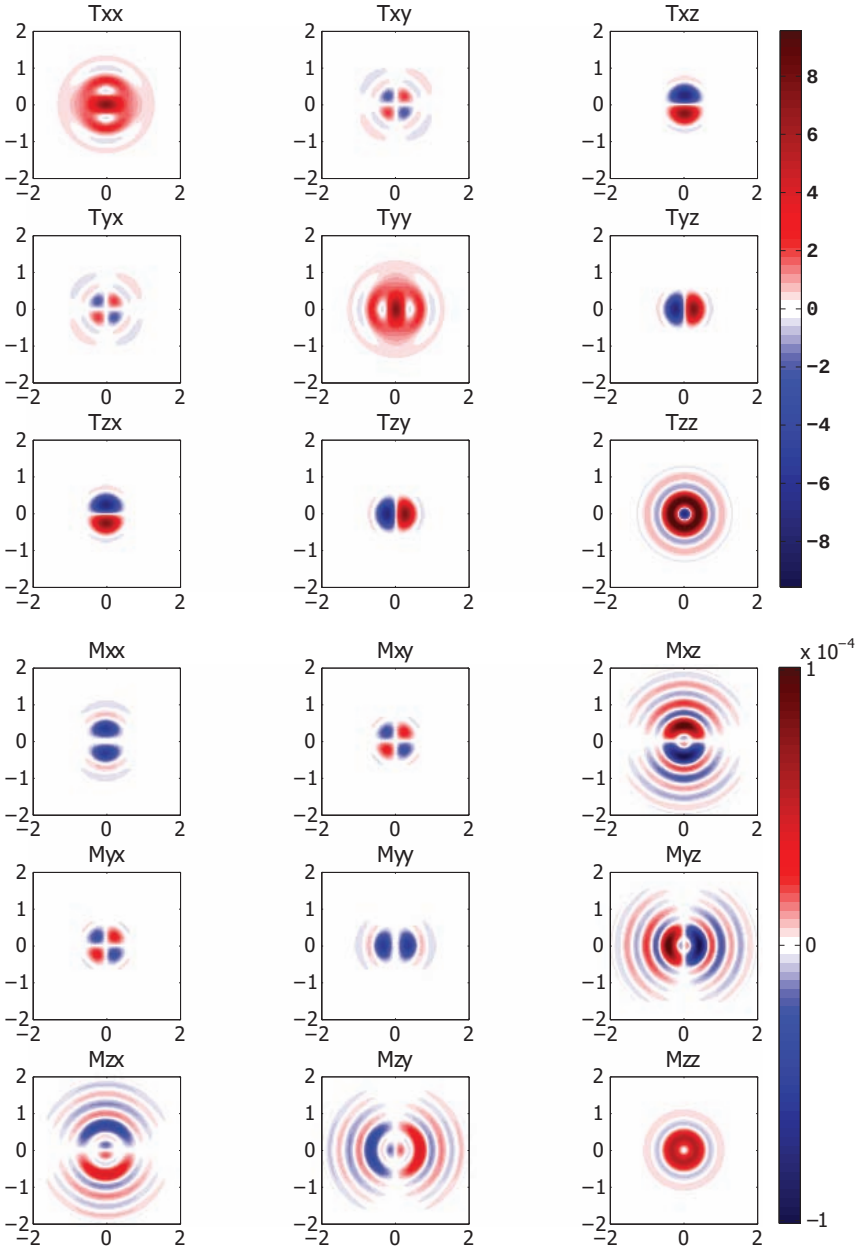

Figure 5.14: *Row one to three: graphs of the linear momentum flux components T_{ij} in the nominal focal plane and the M_{ij}-flux components in the same plane (row four to six). Same numerical aperture, state of polarization and value of helical phase term as in Figure 5.13.*

5.3 ENZ-based imaging of extended objects

The applications discussed so far all involved a theoretical point-object located at infinity. In this section, we consider the image generation for more realistic objects located at a finite distance from the optical system based on the results presented in Section 3.4 (see also [45,67]). The main complications that arise, for objects other than a point-source at infinity, are that the entrance pupil is no longer a flat surface and that the distribution in this pupil will not be uniform. Implementation of a non-flat entrance pupil into the ENZ imaging model has been carried out in Section 2.2. This has resulted in an expression for the electromagnetic field components in the focal region that is very similar to the point-source at infinity case. The second complication, namely the non-uniform entrance pupil distribution, does not require any fundamental changes of the standard ENZ formalism. It will only generate some extra non-uniformity in the exit pupil distribution and this can be treated in a completely analogous way as with image computations of highly aberrated PSF's. We simply have to include the relevant field components in the entrance pupil, together with the optical system transmission function, into the Zernike expansions of Eq.(3.25) and apply the resulting β-coefficients to Eq.(3.29). Of course, this approach requires accurate knowledge of the actual field in the entrance pupil generated by the interaction between the object and the incident illumination. In our work, we have used for this purpose an FDTD-based electromagnetic solver in conjunction with an implementation of the Stratton-Chu formalism. However, a detailed discussion and evaluation of these methods, to efficiently obtain the field in the entrance pupil, is outside the scope of this thesis and for more information on these two specific methods we refer to [45,68]. In the remainder of this section we therefore assume that the field components in the entrance pupil are known.

5.3.1 The aerial-image of an isolated mask-object

As an example we will now compute the through-focus image for the mask object depicted in the top row of Figure 5.15. This so-called double hammerhead object is an often used test object in lithographic simulations because it closely resembles one of the critical features on the chip, namely the interconnects between different chip layers. To compute the $4\times$ reduced aerial image that is produced from this mask object by the lithographic system, we proceed as follows. We use a x-polarized beam at normal incidence to illuminate the object and apply FDTD simulations to generate the resulting near-field. Subsequently, the Stratton-Chu formalism is applied to propagate the radiating field components towards the entrance pupil. The resulting $E_{0,x}$ and $E_{0,y}$ components are shown in the second row of Figure 5.15. Inserting $E_{0,x}$ and $E_{0,y}$ into Eq.(3.25) and assuming the optical system to be free of transmission defects and aberrations ($T_I(\rho,\theta) = 1$), we get two sets of β-coefficients that fully define the imaging problem at hand. Inserting these coefficients into Eq.(3.29), we obtain the electric vector field in the focal region from which we can easily deduce the through-focus electric energy density that is shown in the last row of Figure 5.15. This example clearly shows that the image is a rather blurred representation of the true object and this is, of course,

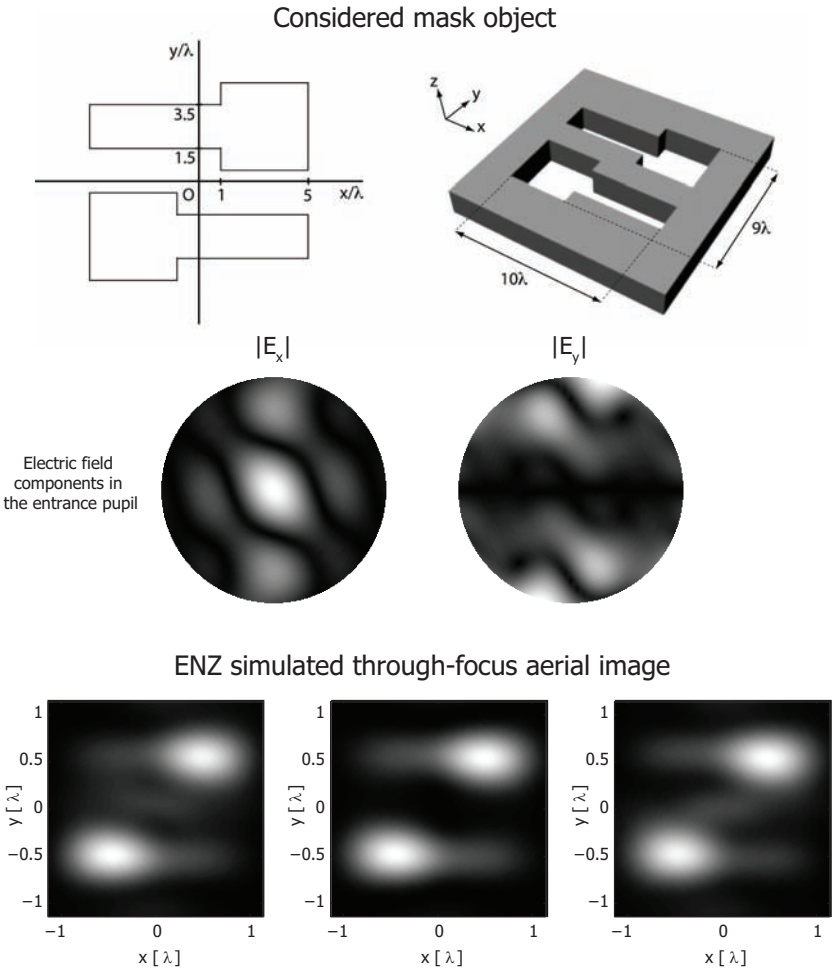

Figure 5.15: *This figure illustrates ENZ-based imaging. In the top row, we show the object, being in this case two hammerhead-shaped holes in a* 1λ *thick layer of chromium. Note that the indicated object dimension are given at the mask-scale. The second row shows the resulting* $E_{0,x}$ *and* $E_{0,y}$ *components in the entrance pupil when the object is illuminated with an* x*-polarized beam at normal incidence. In the third row, the ENZ-simulated through-focus aerial image is shown generated by an optical system having a numerical aperture of* 0.95 *and a magnification of* 0.25.

due to the fact that we are imaging in the sub-wavelength regime. In practice, the image is commonly improved by applying so-called optical proximity corrections (OPC) [108]. These corrections consist of additional non-printing features added to the mask object to improve the actual pattern printed on the mask. One can understand that it is essential for this to have highly advanced and accurate imaging techniques that correctly incorporate the subtle effects introduced by the OPC features. Please note that the simulation presented in Figure 5.15 pertains to illumination of the object by a single coherent plane wave generated by a given point of the sampled incoherent light-source (for details see Section 2.3). To obtain the total intensity distribution generated by a lithographic system, we should repeat the above described coherent simulation for all sampled points of the source and add their contributions incoherently.

5.3.2 Illustrating the advantage of a non-periodic imaging method

One of the main differences between conventional and ENZ-based image simulation methods is the fact that the first is periodic and the latter is non-periodic (see also [67]). Studying the printability of a specific structure or object is in many cases an isolated imaging problem. The way in which such structures are dealt with in the periodic methods involves a large increase of the period by means of zero-padding around the region of interest. Of course a large period is undesired as it will increase the computational burden. In Figure 5.16, we compare the image performance of both periodic and non-periodic imaging in the case of an isolated object. For this purpose, we have computed the image produced by a mask with a 180 nm contact hole that is illuminated by 193 nm x-polarized light at normal incidence. In this simulation we have used the following settings for the lithographic process; immersion fluid $n = 2.32$, NA $= 2.2$, $|M| = 0.25$. Note that these settings by no means reflect the current state-of-the-art, but were chosen to clearly visualize the periodicity effect under study.

In the top-left corner of Figure 5.16, we show the resulting image for the isolated structure computed with the non-periodic ENZ algorithm. The top-right picture shows a simulation of the same contact hole, except that the object is quasi-periodic with a unit cell of 360x360 nm. (Note that we speak of quasi-periodicity as we consider a mask with a 3x3 formation of the unit cell, instead of a real periodic object which can not be treated directly by our simulation tool.) It is clear from this image that the period should be increased to obtain an accurate prediction for the image for a single hole. In the bottom-left picture the exercise has been repeated for the same contact hole, but now with a doubled period (unit cell is 720x720 nm). Finally, the bottom-right picture shows the image for a unit cell of 900x900 nm. Although the bottom-left image is far better than the top-right image, there are still distinct differences with the isolated case (top-left image). One should consider a unit cell as large as 900x900 nm to closely resemble the isolated case. This effectively means that for an equally accurate periodic treatment of this contact hole, we have to consider a computational domain that is at least 4 times larger than what it should be for an ENZ-based computation.

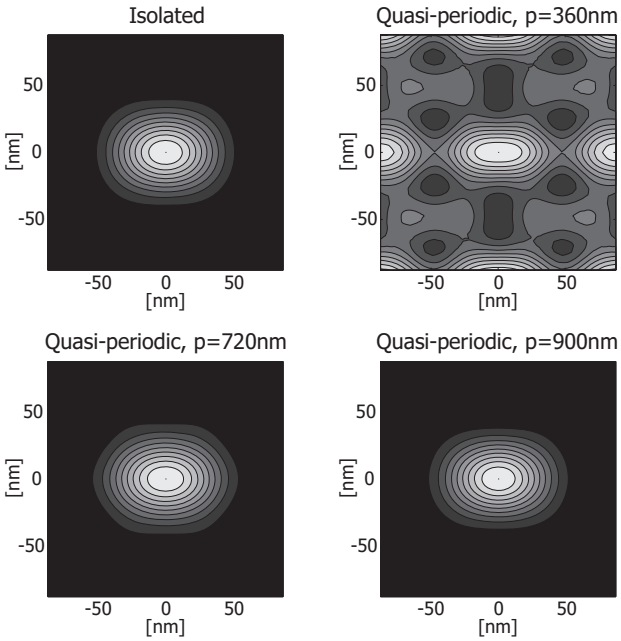

Figure 5.16: *This figure illustrates the difference between periodic and non-periodic mask imaging of a* 180 nm *contact hole* (*Note that again all measures are given at the mask-scale*). *A period* $p = 360\,\mathrm{nm}$ *is clearly insufficient to produce a good image. Doubling the period to* $p = 720\,\mathrm{nm}$ *helps, resulting in a residual root-mean-square* (RMS) *error of* 2%. *However, a period up to* $p = 900\,\mathrm{nm}$ *is required to obtain an accurate* ($\mathrm{RMS} \approx 1\%$) *quasi-isolated image using a periodic method* (*imaged by a lithographic immersion system;* $\lambda = 193\,\mathrm{nm}$, *immersion fluid* $n = 2.32$, $\mathrm{NA} = 2.2$, *reduction* $4x$. *Note that these settings do not pertain to a realistic lithographic system but they were chosen to clearly visualize the effects under study*).

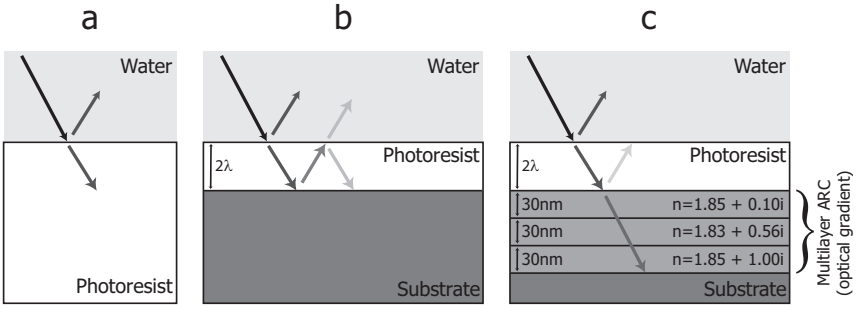

Figure 5.17: *Three stack configurations in image space that occur in optical lithographic imaging.*

This exercise has shown that the ENZ-based algorithm requires a far smaller mask area to be considered in order to obtain accurate images of isolated structures and that if a periodic method is used, great care should be taken in defining a large enough unit cell in order to achieve realistic results.

5.4 ENZ-based image formation in a stratified image space

In Section 3.5 of this thesis, we have presented Eqs.(3.47)-(3.48) which can be used to calculate the forward and backward propagating electromagnetic field components in a given layer of a multilayer stack in the image region of an optical system. In the present section, we apply these expressions to some optical systems in which layered configurations in image space play an important role and we will verify our results by comparing them with an existing method based on a numerical evaluation of the Richards and Wolf diffraction integral [59, 109].

5.4.1 Multilayer effects in lithographic resist images

Our first example illustrates the importance of multilayer modeling in deep UV high-numerical-aperture optical lithography, i.e. $\lambda = 193\,\text{nm}$ and NA $= 1.368$ (water immersion). In Figure 5.17, three different possible models for the wafer stack configuration are shown. In configuration a, it is assumed that the light has to cross a single material interface before image formation takes place in a half space of photoresist with index of refraction $n = 1.76$. In configuration b, a more realistic wafer stack is considered in which the effect of a highly reflective silicon substrate, with index of refraction $n = 0.78 + 2.46i$, is taken into account. Configuration c shows a more advanced stack in which an anti-reflective coating (ARC) is included [110]. This ARC acts as an optical gradient to minimize the light reflections coming from the substrate.

For all three configurations, we have computed the through-focus point-spread function (PSF) that is formed in the resist layer. The geometric best-focus position was set one wavelength inside the layer of resist ($z = 0$ in Figure 5.18), meaning that focal shifts introduced by the layer transitions were not corrected for. The results are shown in Figure 5.18, where the first column contains data obtained with the ENZ method presented in this paper and, for comparison, the second column contains data for the same configurations, this time obtained by means of numerical integration of the diffraction integrals. As can be seen from these figures, there is a very good agreement (10^{-3} or better in amplitude) between the ENZ method and its numerical integration counterpart. This is as expected as the used numerical integration method typically has an accuracy of 10^{-3} in amplitude.

Comparing the results at different rows in Figure 5.18, we see that the simplified representation of the wafer stack given by configuration a accurately predicts the focal shift, relative to the geometrical best focus position, introduced by the medium transition. However, by comparing rows one and two, we see that neglecting the influence of the substrate is not allowed. As a matter of fact, the standing

wave pattern observed for configuration b is unacceptable from a lithographer's point of view and therefore, in practice, one often applies an anti-reflective coating (ARC). An ARC has been included in configuration c and it can be seen that it effectively reduces the standing wave non-uniformity down to an acceptable value.

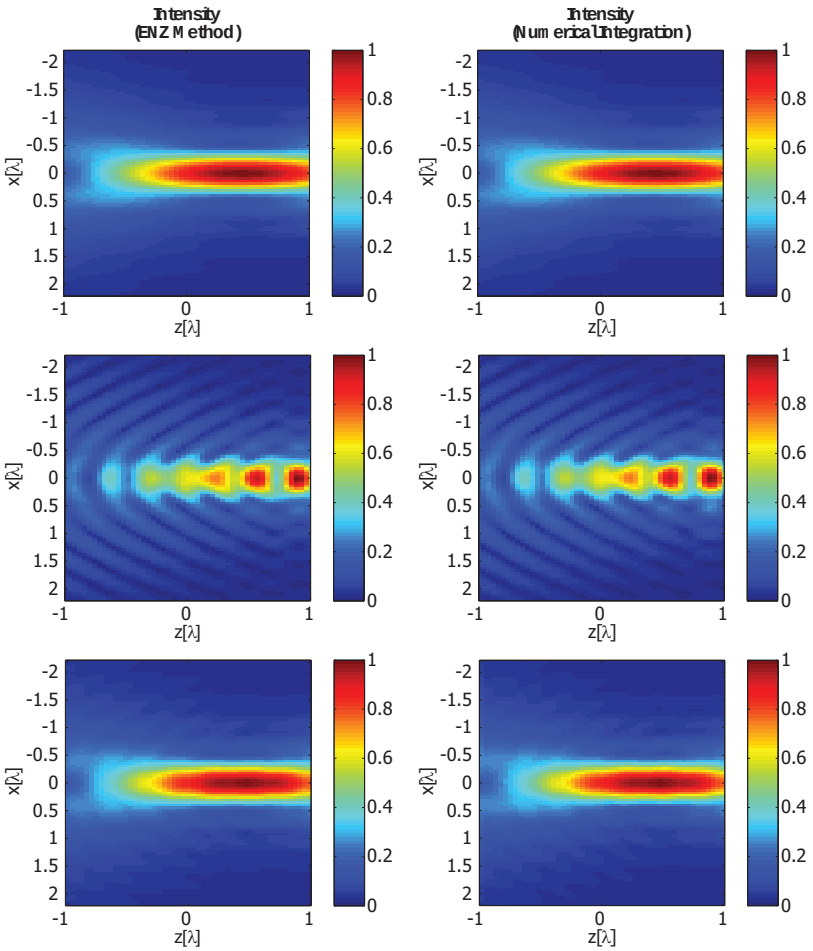

Figure 5.18: *Comparison between the ENZ method (left column) and a fully numerical integration method (right column). The graphs show, from top to bottom, the intensity of the x-polarized point-spread distribution in the resist layer for the configurations a, b and c, presented in Figure 5.17. The geometric best focus position in water immersion without any layer would be located at the axial position $z = 0$.*

5.4.2 Air-gap effects when imaging with a solid immersion lens

The second example of this section involves a proposed next-generation optical disk read-out system. In this system, a high refractive index 'solid' immersion lens is placed very closely to the disk in order to improve the read-out resolution by optical tunneling of high spatial frequencies corresponding to evanescent plane waves. The thin layer of air between the lens and the spinning disk should be as small as possible for resolution purposes but large enough to avoid the risk of mechanical contact during play-back of a disk. The width of the air gap strongly influences the performance of the system. In Figure 5.19 we have plotted the through-focus intensity profile of the point-spread function that, in this example, serves as the read-out spot. Various effects introduced by the air-gap can be observed. A focal shift is present which should be accounted for in the actual design of the system. For large air-gaps, the average intensity of the light spot goes down and the full width at half maximum of the scanning light spot gradually increases. This means that there is an maximum air-gap width for which the read-out beam still has a sufficiently small size whilst the spot intensity is adequate for read-out with a good signal-to-noise ratio. Figure 5.19 applies to a solid immersion lens with a numerical aperture of 1.45. It is seen that the full width at half maximum of

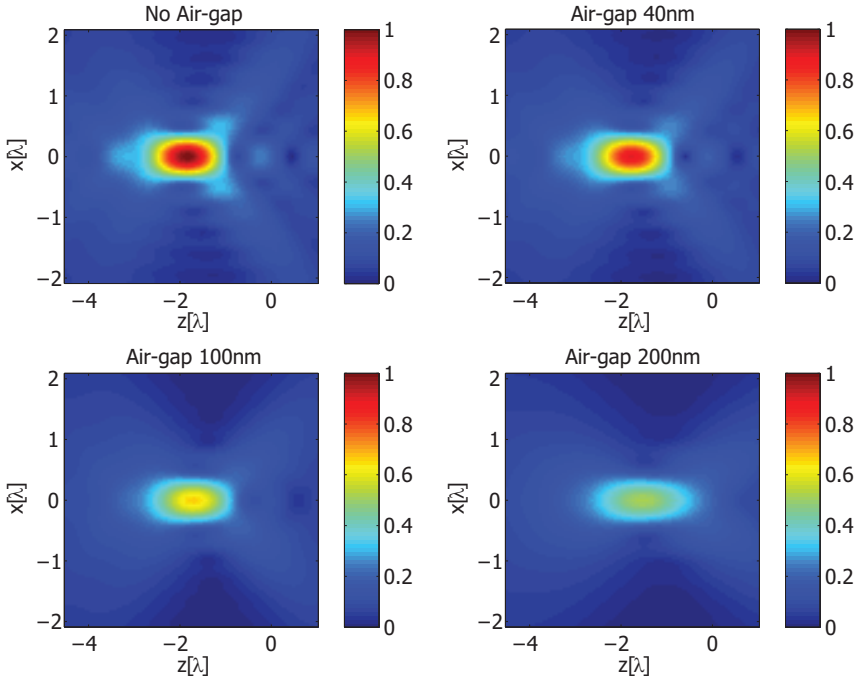

Figure 5.19: *Point-spread formation in a layer of polycarbonate* ($n = 1,62$) *using a solid immersion lens* ($n = 2.086$) *for various values of the air-gap thickness* (NA $= 1.45$, $\lambda = 405\,\mathrm{nm}$).

the lateral intensity profile starts to increase substantially once the air gap width exceeds 40 nm. A practical compromise between disk storage capacity, optical transmission through the gap and mechanical robustness of the system was found to be a gap width of typically 25 nm [111].

5.5 ENZ-based optical system characterization

The ENZ theory has been originally developed to enable the characterization of optical systems [12–14, 64, 91–95]. In other words, it was meant to reconstruct the optical transmission function from which one could then deduce the aberrations influencing the system. In Chapter 4, the necessary tools to perform ENZ-based system characterization were introduced and this resulted in a recipe to construct a linear system of equations that, upon solving, yields the desired Zernike coefficients describing the aberrational state of the optical system. To construct this linear system, we require the same basic functions V_n^m and $V_{n,j}^m$ that occur in the computation of the optical PSF and, in addition, a measurement of the through-focus PSF of the optical system under consideration. In this section, we present an aberration retrieval exercise showing the reconstruction of the transmission function for a strongly aberrated optical system. Due to the unavailability of suitable experimental data, this experiment is fully performed in simulation, where we have tried to approach experimental conditions by artificially adding noise to our simulations. In addition, this example will show the large added value of the predictor-corrector procedure that strongly enhances the performance and applicability of ENZ retrieval. Furthermore, we will treat two advanced situations in which the basic ideas behind the ENZ retrieval formalism can be used. The first advanced example involves the reconstruction of an annular pupil following the recipe described in Subsection 4.2.3. The final example of this section discusses the characterization of microlenses. Because these lenses are generally not well described using the Debye integral (see Section 4.5), we can also not directly apply the ENZ retrieval procedure. Nevertheless, it was shown in Section 4.5 that ENZ theory, with some minor adjustments, can be adapted to also produce accurate results for optical systems used outside the Debye regime and thus this adjustment will also enable retrieval for this class of optical systems.

5.5.1 Reconstruction of the aberration function under simulated experimental conditions

A through-focus intensity distribution, belonging to the exit-pupil field defined in Table 5.1, is simulated (top row Figure 5.20). In order to approach experimental conditions, we have added noise to this distribution in the second row of Figure 5.20. Subsequently, this noisy distribution serves as the intensity input of the ENZ retrieval process and the results of the basic ENZ retrieval operation are shown in the third row of Figure 5.20. Note that the retrieval operation generates estimates for the true β-coefficients and these estimates were used to generate the distribution in the third row. Although, the correspondence is rather good, differences between the true and retrieved PSF's remain (see also Table 5.1). These

retrieval errors are caused by the linearization applied in the construction of the retrieval process in Section 4.2. Fortunately, we have seen in Section 4.3 that these errors can be largely removed using the so-called predictor-corrector procedure. Applying this procedure we obtain the far better retrieval result shown in the bottom row of Figure 5.20. Also comparing the right-most column of Table 5.1 with the input coefficients we see that the reconstruction of the β-coefficients is now very good even for the significantly aberrated optical system considered in this example (RMS wavefront deviation in the pupil of approximately $80\,\mathrm{m}\lambda$).

		$SNR = \infty$		$SNR = 10$	
Input coeff.		Lin. retr.	Pr.-Corr.	Lin. retr.	Pr.-Corr.
β_0^0	1.0	1.1294	1.0000	1.1291	1.0004
β_1^{-1}	0.0	0.1002	0.0000	0.0934	0.0050
	$+i0.5$	$+i0.4278$	$+i0.5000$	$+i0.4277$	$+i0.4933$
β_1^1	0.0	0.0997	0.0000	0.0973	-0.0124
	$+i0.5$	$+i0.4576$	$+i0.5000$	$+i0.4598$	$+i0.5068$
β_3^{-1}	0.5	0.4545	0.5000	0.4401	0.4688
	$+i0.0$	$+i0.0028$	$+i0.0000$	$+i0.0144$	$+i0.0099$
β_3^1	-0.5	-0.4330	-0.5000	-0.4339	-0.5041
	$+i0.0$	$-i0.0008$	$+i0.0000$	$-i0.0174$	$-i0.0385$
β_2^0	0.0	0.0382	0.0000	0.0220	-0.0264
	$+i0.0$	$+i0.0000$	$+i0.0000$	$-i0.0176$	$-i0.0270$
β_2^{-2}	0.0	0.1138	0.0000	0.1276	0.0112
	$+i0.5$	$+i0.5813$	$+i0.5000$	$+i0.5306$	$+i0.4327$
β_2^2	0.0	0.1113	0.0000	0.1122	0.0060
	$+i0.5$	$+i0.3039$	$+i0.5000$	$+i0.3095$	$+i0.5137$
β_3^{-3}	-0.5	-0.3269	-0.5000	-0.3821	-0.5468
	$+i0.0$	$-i0.0843$	$+i0.0000$	$-i0.0641$	$+i0.0253$
β_3^3	0.5	0.5534	0.5000	0.5631	0.5139
	$+i0.0$	$+i0.0869$	$+i0.0000$	$+i0.0535$	$-i0.0296$

Table 5.1: *Sets of β-coefficients describing the field in the exit pupil of an optical system* (NA $= 0.95$). *The first column contains the input coefficients that were used to generate the PSF shown in the top row of Figure 5.20. The second and third column contain estimates of the input coefficients that were obtained using the standard and iterative versions of the ENZ retrieval formalism, respectively. The fourth and fifth column pertain to estimates obtained in the same manner, but with white noise added to the input data having a Signal-to-Noise-Ratio* (SNR) *of* 10.

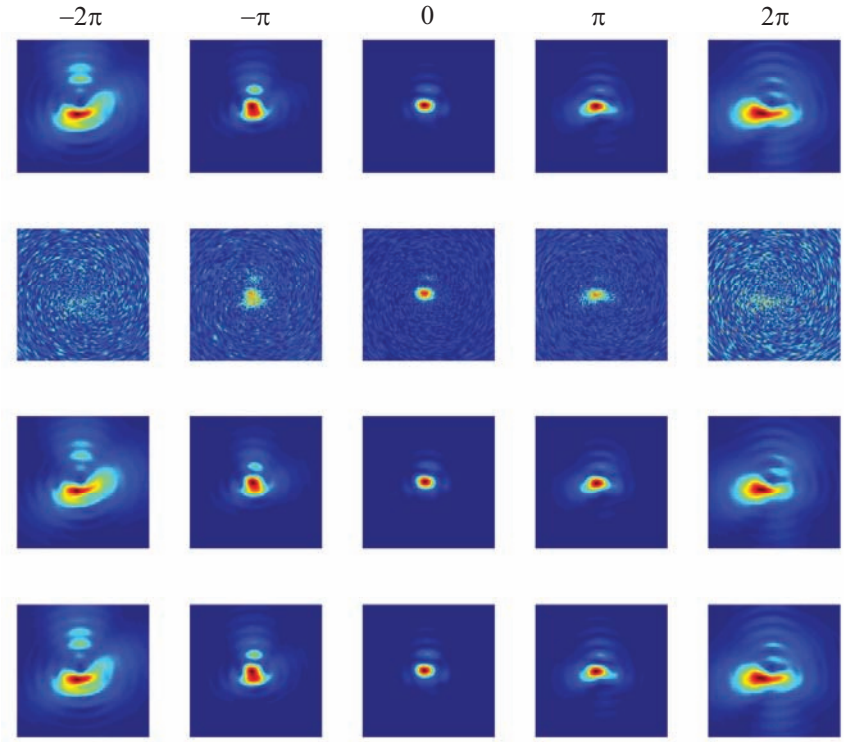

Figure 5.20: *The through-focus intensity distribution for the system* (NA = 0.95*, x-polarization*) *defined in Table. 5.1. The upper row is the actual distribution, the second row is what results after adding noise with a SNR of* 10*, the third row is the distribution defined by the* β*-estimates obtained with the standard ENZ retrieval and the last row is the distribution resulting after the predictor-corrector procedure is applied. Note that all images have been scaled according to their maximum value in order to show maximum detail. The SNR-value of 10 applies to the in-focus distribution; from the pictures in the second row it is clear that the SNR-value is much lower for the out-of-focus intensity distributions.*

5.5.2 ENZ retrieval of an annular shaped pupil

Using the results of Section 3.6 it is also possible to reconstruct the aberration function of an annular pupil. To illustrate this feature of the ENZ formalism we consider the retrieval of a Gaussian, comatic pupil function (with $s_0 = 0.95$)

$$P(\rho,\theta) = \exp\left[-\gamma\rho^2 + i\,\alpha\,R_3^1(\rho)\cos\theta\right]\,, \qquad 0 \le \rho \le 1\,,\;\; 0 \le \theta \le 2\pi\,, \tag{5.2}$$

which is obstructed in the disk $0 \le \rho < \varepsilon = \frac{1}{2}$ and we take $\alpha = \gamma = 0.1$. For this we apply the ENZ retrieval procedure as given in Sections 4.2 and 4.3 in which the $V_{n,j}^m$ are to be replaced throughout by the $W_{n,j}^m$ of Eq.(3.65). Since this example can at the present stage only be considered in a simulation environment, we have generated the "recorded" intensity in the focal region in simulation. This we do as follows. Based on the explicit results given in Appendix A of [64], the Zernike expansion P on the full disk $0 \le \rho \le 1$ can be written as

$$P(\rho,\theta) = \sum_{m,n} \beta_{|m|+2p}^m\, Z_{|m|+2p}^m(\rho,\theta)\,, \qquad 0 \le \rho \le 1\,,\;\; 0 \le \theta \le 2\pi\,. \tag{5.3}$$

The β's occurring above can be found by inserting the coefficients explicitly given in Eq.(A19) of [64] into Eq.(4.3). The representation Eq.(5.3) holds naturally also on the annular set $\varepsilon \le \rho \le 1$, $0 \le \theta \le 2\pi$, and thus the PSF computation scheme of Section 3.3, using this representation of P and with $W_{n,j}^m$ instead of $V_{n,j}^m$ as described earlier, can be applied. In theory, when infinite series in Eq.(5.3) are used, the coefficients retrieved with this procedure are not identical to the β's used in Eq.(5.3); see [75], Appendix B for more details. However, in the experiment we input and retrieve only β's with $0 \le |m|, n \le 10$, and thereby avoid this non-uniqueness problem. For this finite set of aberration coefficients, we use the iterative version (predictor-corrector approach) of the ENZ retrieval method as described in Section 4.3. In Figure 5.21a we show modulus and phase of $P_{analytic} - P_{beta}$ where $P_{analytic}$ is the pupil function $P(\rho,\theta)$ of Eq.(5.2) and P_{beta} is the pupil functions $P(\rho,\theta)$ of Eq.(5.3) in which the summations have been restricted to the terms m, p with $0 \le |m|, |m| + 2p \le 10$. In Figure 5.21b we show modulus and phase of $P_{beta} - P_{retrieved}$. Here P_{beta} is the same as in Figure 5.21a, and $P_{retrieved}$ is the pupil function resulting from taking the same linear combination of Zernike terms that constitute P_{beta} but now with β's that are obtained by applying 60 iterations of the predictor-corrector procedure using $|U_{beta}|^2$ as "recorded" intensity in the focal region. Note that the error levels in Figure 5.21b are well below those in Figure 5.21a, hence a Figure 5.21c, showing the modulus and phase of $P_{analytic} - P_{retrieved}$, would practically coincide with Figure 5.21a and is therefore omitted.

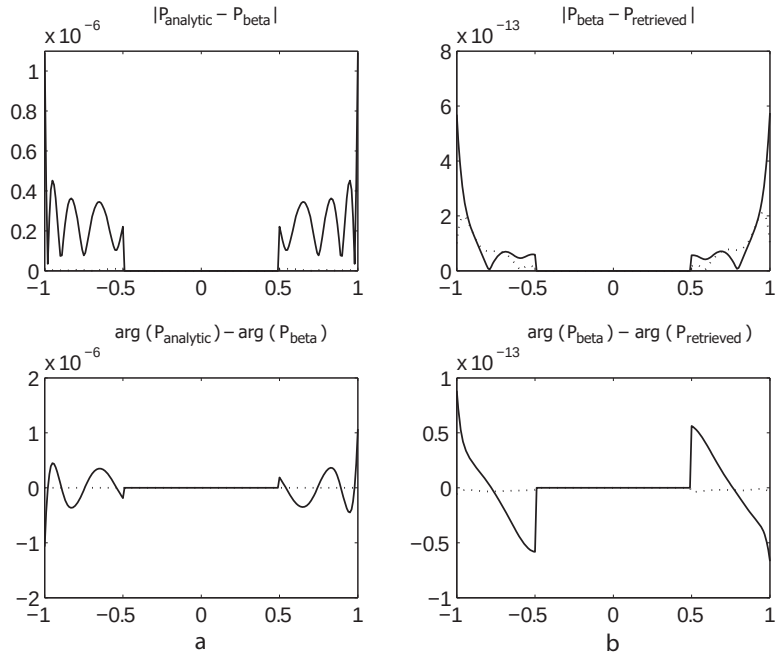

Figure 5.21: *Cross-sections of the modulus and phase of (a) $P_{analytic} - P_{beta}$ and (b) $P_{beta} - P_{retrieved}$ defined on the annular set $\varepsilon = \frac{1}{2} \leq \rho \leq 1$. Here $P_{analytic}$ is given in Eq.(5.2) with $\alpha = \gamma = 0.1$ and P_{beta} is given by Eq.(5.3) in which the summations are restricted to m, p with $0 \leq |m|$, $|m|+2p \leq 10$. Finally, $P_{retrieved}$ is reconstructed from the β-coefficients obtained using 60 iterations of the high-NA ($s_0 = 0.95$) predictor-corrector procedure of the ENZ retrieval method.*

5.5.3 Characterization of a microlens

Although a microlens is nothing else than a very small lens, its characterization based on through-focus intensity measurements is much more complicated than that of a regular size lens. The complications arise from the fact that focusing by a microlens is not accurately described by the Debye diffraction integral. This is largely due to the limited size of the aperture of a microlens, which is typically smaller than a few hundred wavelengths. As a direct consequence, the ENZ retrieval formalism, which depends on the analytic solutions of this integral, also does not yield accurate results for microlenses. This issue was already discussed in Section 4.5 and there it was also shown that, with some relatively simple scaling operations, the validity of the Debye representation can be extended into the microlens regime.

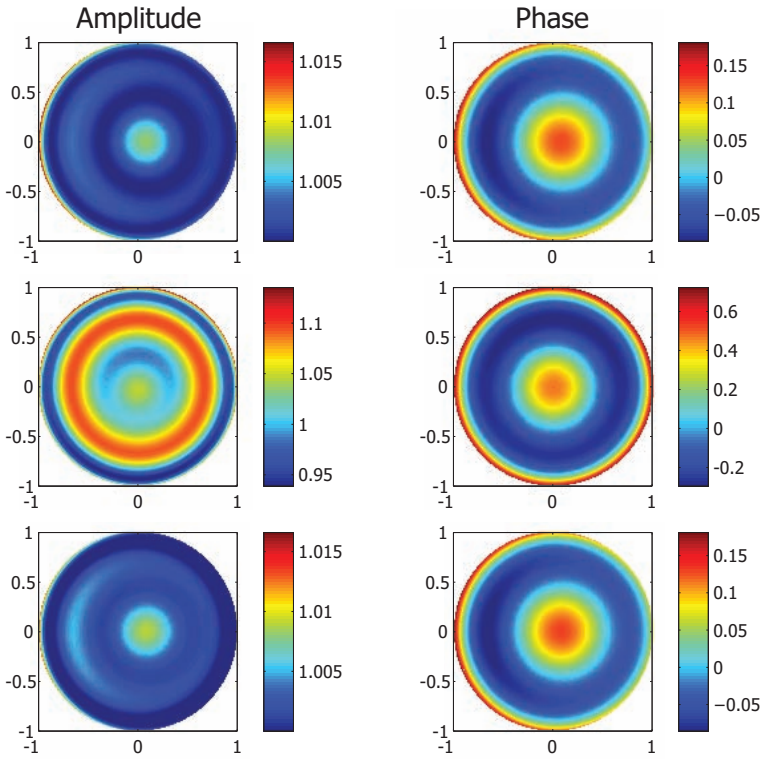

Figure 5.22: *Retrieval applied to a microlens* (*Diameter* $= 40\,\mu$m, NA $= 0.01$ *and* $\lambda = 400$ nm). *In the top row the actual pupil distribution is shown. The second row shows the retrieval result when no additional measures are taken to correct for the effects introduced by the validity issue of the Debye integral. In the bottom row the correction of the Debye integral is applied resulting in far better retrieval results.*

To illustrate that the corrected Debye integral yields accurate results for microlenses, we will now present an ENZ-based aberration retrieval exercise performed on a microlens having a diameter of $40\,\mu$m. As we have no experimental through-focus intensity data of a microlens available, a simulated through-focus distribution, obtained by numerical evaluation of the Rayleigh diffraction integral, serves as the input intensity data. The pupil or aberration function applied in this example is shown on the first row of Figure 5.22. The focal intensity distribution that is generated from this will subsequently serve as the input data of the ENZ retrieval procedure. The difference with standard ENZ retrieval is that the ENZ basic functions, that serve to construct the inversion matrix, are in this case generated using the scaled versions of the variables r and f given in Eqs.(4.28) and (4.29). As we have seen in Section 4.6 there are no further corrections to the ENZ inversion scheme required thus allowing us to proceed precisely as described

in Sections 4.2 and 4.3. In the bottom row of Figure 5.22 we have shown the pupil function that is retrieved using the corrected ENZ basic functions. For comparison we have also included in the middle row of Figure 5.22 the pupil function that results when this correction is not applied. Comparing both retrieved pupil functions, we see that uncorrected retrieval of microlens data clearly yields incorrect results, while by applying our corrections introduced in Section 4.5, we can hugely improve the retrieval accuracy.

5.5.4 ENZ retrieval as a means to determine unknown system parameters

It was already shown in [92] that the accuracy achieved by the ENZ retrieval algorithm strongly depends on the correctness of the applied system parameters such as the numerical aperture and the state of polarization of the incident light. In fact, it is generally true for well-corrected optical systems that if wrong parameter values are applied, the reconstructed aberration will be larger than the actual one [92]. This relation gives us the opportunity to actually determine the exact value of these system parameters in the case that they are not exactly known, by minimizing the total aberration size as a function of the system parameters. To illustrate this approach we have shown in Figure 5.23 the error in the retrieved β-coefficients versus the value of the NA for the optical system defined in Table 5.2. It is clearly seen that all β-coefficients sharply converge to their exact value when the actual value of the NA $= 0.95$ is approached. The same exercise is also performed for the case that the incident state of polarization is not exactly known and the results are shown in Figure 5.24. Again the β-coefficients sharply converge when the exact polarization state is approached indicating that accurate determination of the polarization state using the ENZ formalism is feasible.

	Input value
β_0^0	1.0000
β_2^0	$0.0200i$
β_3^{-1}	$0.0500i$
β_3^1	$0.0500i$
β_2^{-2}	$0.0100i$
β_2^2	$0.0100i$

Table 5.2: *Set of β-coefficients describing the field in the exit pupil of the optical system ($NA = 0.95$) under consideration.*

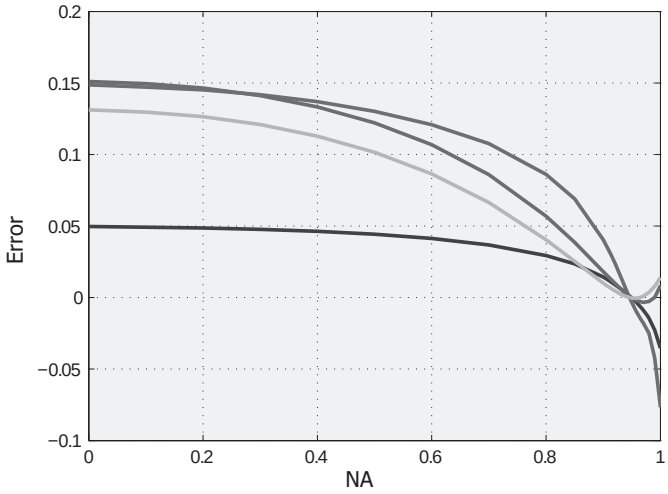

Figure 5.23: *The error present in some relevant β-coefficients when retrieving the system defined in Table 5.2 while assuming different values for the NA. The different lines pertain to typical aberration coefficients; the residual errors for all aberrations are smallest at the correct* NA *value.*

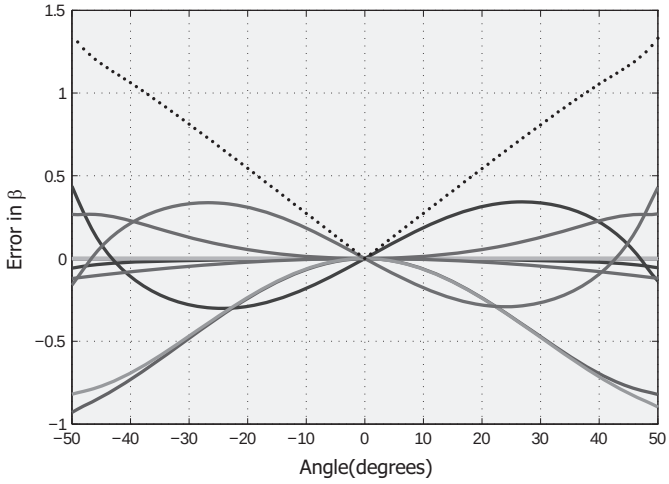

Figure 5.24: *The error present in some selected retrieved β-coefficients (solid-lines) for different angles of deviation relative to the actual linear state of polarization of the system under consideration (in this case pure x-polarization). In addition a measure for the total error, defined here as $\left(\sum \left(\beta_{error}\right)^2\right)^{\frac{1}{2}}$, is plotted (dotted line).*

5.6 Summary and discussion

In this chapter we have presented a selection of possible applications of the ENZ diffraction theory. This selection is by no means complete and many other examples could be thought of. However, we do hope that these examples have given the reader some feeling on the capabilities and restrictions of the ENZ theory.

In Section 5.1, some examples on the computation of PSF's for general optical systems are presented. This is the most direct application of the ENZ theory and the various applications nicely illustrate the large versatility of the method. Basically all optical systems having a circular symmetry can be treated even if they are influenced by large aberrations or when the field distribution far from focus is required. In Section 5.2, we emphasize another feature of the ENZ method, namely the fact that, without much extra effort, we obtain with this method both the electric and magnetic field distributions in focus. As a result we also have easy access to the other electromagnetic quantities in focus. As is shown by the examples presented in this section, this feature is especially convenient to visualize the transport of energy and momentum through focus. Together with the efficient representation of special types of pupil distributions, such as the helical phase, in terms of Zernike functions and the possibility to express their contributions analytically, this approach provides the scientific community with additional physical insight regarding the optical phenomena occurring in the focal region.

In the applications presented in Section 5.3 the ENZ formalism is used as a tool to generate highly accurate images of complicated objects in an efficient manner. There we make use of the appealing feature of the ENZ theory that it can basically image any pupil distribution as long as it can be accurately represented by a finite number of Zernike coefficients. This application provides a non-periodic alternative to other imaging methods and is in that sense well suited to be applied in benchmarking exercises. More examples in which the ENZ formalism is applied in general imaging are presented in Section 5.4. There we have shown that the often occurring case of a stratified image space is also no problem for the ENZ imaging algorithm. As it is shown this has its applications in the simulation of resist patterns generated by a lithographic mask and the study of the air-gap effect in a solid-immersion disk read-out system.

Finally in Section 5.5, some applications of the ENZ inversion scheme are given. In fact the ENZ theory was originally developed to enable the reconstruction of the transmission function of an optical system from through-focus intensity data alone. However, ENZ system characterization has been further explored in a way that it is now feasible for a large range of optical systems including those operating at high NA or having an annular aperture. It has even been shown that ENZ retrieval can be applied to optical systems that operate outside the Debye regime, which is somewhat surprising for a method that is based on an analytic solution of this Debye integral. Another application of ENZ inversion treated in this section is that it can be used to determine a system parameter, such as the NA or polarization state of an optical system, by minimizing the total retrieved aberration as a function of these parameters.

Chapter 6

Concluding remarks

In this thesis, we have dealt with the model based description of advanced optical systems in order to be able to accurately and efficiently simulate the image they produce from a given object. To this extent, we have introduced a novel imaging model, in which we have applied as few approximations as possible, to obtain a method that yields accurate simulation results for even the most demanding optical systems. The resulting imaging method requires an algorithm that can accurately compute the field distribution in the focal region of an optical system based on the field distribution in the exit pupil. This relation between the pupil and the image is governed by the Debye diffraction integral and can generally only be evaluated numerically for a general pupil. This is problematic when extremely accurate simulation results are required because the numerical evaluation of the Debye integral can quickly become too computationally involved or does not reach the desired accuracy at all. In this thesis, we have overcome this problem by applying the Extended Nijboer-Zernike (ENZ) theory of diffraction as a means to efficiently image general objects with an accuracy down to machine precision.

6.1 ENZ diffraction theory

The ENZ theory of diffraction, of which a detailed derivation is included in Chapter 3, is a generalization of the diffraction theory formulated in the first half of the 20 th century by Zernike and Nijboer. It basically provides a semi-analytic solution to the Debye diffraction integral for a pupil distribution given in terms of Zernike circle polynomials. This, together with the fact that the Zernike circle polynomials constitute a complete orthogonal set on the unit disk, result in a method that can in principle be used to solve the Debye integral for general field distributions in the exit pupil. This feature has been used repeatedly throughout this thesis to construct semi-analytic expressions for the field in the focal region for a variety optical systems. Although standard ENZ theory describes imaging in the scalar regime, it has been shown that also an equivalent vectorial version of the ENZ theory can be devised. Applying the ENZ theory in this vector diffraction case results in somewhat more complicated expressions, that nonetheless have the same

structure and application possibilities as the scalar results.

Compared to other methods that provide analytical results for the diffraction problem, the ENZ theory has the advantage that it can very well cope with the circular hard diaphragm encountered in many optical problems. This is because the Zernike expansion naturally includes the sharply bounded circular configuration of the pupil, and thus requires a relatively modest amount of coefficients to describe it accurately. Other solutions based on special functions (see Subsection 2.1.5 for an enumeration) lack this efficient representation of a sharply bound pupil and are therefore considered to be less appropriate. In addition, the Zernike functions used to describe the pupil are directly related to image contributions by specific aberrations and this makes that the study of aberration effects on the produced image becomes a relatively simple and well structured task.

Altogether, the main features of the ENZ theory can be summarized as follows. The semi-analytic nature of the solution provided by the ENZ theory assures that the Debye integral can be evaluated down to machine precision. The use of Zernike functions to represent the pupil make the method well fitted to treat optical systems with a circular diaphragm and the direct relation of the Zernike polynomials with respect to aberrations is beneficial in the study of aberrational influences. On the other hand, the application of the ENZ theory is less appropriate when there is no circular diaphragm, as, in this case, large numbers of Zernike coefficients are required to represent the pupil and the method consequently becomes inefficient.

6.2 ENZ-based imaging of a point source

In Chapter 3, we have applied the main results of the ENZ theory to all kinds of optical problems related to imaging. A straightforward implementation of the basic ENZ results enabled the efficient computation of PSF's for both low- and high-NA optical imaging systems. The general advantages of the ENZ theory, already quoted above, are preserved for this application, thus providing an extremely accurate and versatile computation method for aberrated PSF's. Another advantage of the ENZ formalism, that has become apparent in this thesis, is that every Zernike term used in the expansion of the pupil has a fixed contribution to the image that is independent of the pupil distribution itself. As a result, stored values of the ENZ basic functions can be used repeatedly to enhance the efficiency of this approach when multiple pupils are to evaluated. Also in the case of NA-reduced, annularly shaped and multi-ringed pupils, it was shown that the analysis according to the ENZ theory is beneficial in terms of efficiency. In the vectorial case, there is another advantage of the ENZ approach, namely that, with a limited amount of extra effort, one can obtain analytic expressions for both the electric and magnetic fields in the focal region. As it was shown, this makes it very straightforward to compute and assess all the electromagnetic quantities in the focal region.

In comparison to other methods that are used to compute the PSF, for example the commonly used Fourier-based methods, we have seen that the ENZ formalism has several advantages. The pupil representation in terms of Zernike functions is more efficient than the rectangular grid used in the Fourier approach, the ENZ method can evaluate a single arbitrary image point at a time and the

ENZ method can use tabulated data to improve its performance. On the other hand, the downside of the ENZ method is that it is a less established method for which no easy-to-use software package exists yet. As a result, the application of the ENZ method requires a relatively large amount of preliminary work and, consequently, until a user-friendly software package becomes available, it may be too involved for the average user in need of a PSF-computation.

6.3 ENZ-based general imaging

Apart from point sources, the results of the ENZ theory can be equally well applied to compute the image of more general objects. This is possible because we can relate a general field in the entrance pupil to the resulting field in the focal region using Debye-like integrals and the ENZ theory also yields a solution to these integrals. To compute the image of an extended object using the ENZ approach, we thus require the electric field in the entrance pupil to be known. Although we have applied FDTD-simulations, in conjunction with a Stratton-Chu based near-to-far-field transformation to obtain the entrance pupil distribution, it is, in principle, irrelevant which method is used for this part of the computation. It was shown that, although this imaging approach is only allowed when the object is illuminated coherently, also more general kinds of illumination can be evaluated, for example, illumination using a finite incoherent source. This is done by sampling the source and solving the imaging problem separately for all resulting coherent source-points. In this so-called Abbe-approach, the final image is obtained by incoherent summation of all source-point image contributions. The main limitation of the ENZ method is that the object under study should be small compared to the distance between object and entrance pupil. For most of the applications quoted in this thesis, this condition is of minor importance as the objects are generally small. Note that this condition is imposed by the imaging model and does not represent a limitation of the ENZ theory. Moreover, we expect that future development of the imaging model can largely remove this limitation.

By combining ENZ imaging with multilayer theory, we could also devise an ENZ-based imaging method capable of producing images within a stratified image space. In order for an imaging method to be useful, this extension is indispensable as in most advanced imaging applications some sort of layered configuration is present in image space. For example, in lithography, an image is formed in a thin layer of photoresist deposited on top of a complicated layered wafer-stack. An additional advantage of the ENZ method in the multilayer case again originates from its decomposition in terms of pre-computable basic functions. This allows for a very efficient optimization of the field in a given layer of a multilayer. Changing or adding any layers outside the layer of interest can strongly change the field distribution in this layer, but does not influence the basic functions used to describe this field. Only the coefficients pertaining to this field, depending on the Fresnel coefficients, will change, but their computation is generally only a small fraction of the overall computational burden. It should be noted that, when the layer of interest itself changes, the ENZ basic functions should be recomputed. For the time being, ENZ multilayer image computations are restricted to layers that can

be approximated to be free of absorption. This limitation only applies for the layer in which the field should be computed, all other layers in the multilayer can be absorbing. Again this limitation is not fundamental and we expect to be able to remove it through further research on the subject.

Also in the extended imaging and multilayer case, the ENZ formalism provides both the electric and magnetic fields in image space. This could possibly be beneficial to the optical community to compute more accurately the interaction between the light constructing the image and the optically active materials such as resist or the optically active layer in optical data-storage.

6.4 ENZ-based system characterization

The application that initiated the development of the ENZ theory is that of optical system characterization or aberration retrieval. We have shown that it is possible to reconstruct the exit pupil from through-focus intensity PSF data using an inversion scheme based on the ENZ theory. Having the exit pupil distribution available, one can derive from this the transmission function or Zernike aberration coefficients describing the optical quality of the imaging system. In a sense, this is a remarkable result as we determine both amplitude and phase deviations in an optical system by analyzing intensity data in which all phase information is lost. The poor dimensionality of this problem is relieved by the use of data from several through-focus planes and this also has a beneficial effect on the noise-sensitivity of the method. ENZ inversion is possible for both low- and high-NA optical systems and even for optical systems having a non-standard pupil shape, like an annulus. We have even given an approach to determine possible birefringence present in an optical system based on ENZ inversion. This does however require several consecutive measurements of the through-focus PSF for different polarization settings.

In its basic form, ENZ inversion only applies to well corrected optical systems. This is because a linearization is applied that introduces errors when the aberrations of the system under investigation become too large. Nevertheless, we have shown that our so-called predictor-corrector approach can largely remove this error, making the method applicable to aberration sizes as large as 0.3λ RMS. We have also seen that the common measurement approach to obtain the PSF data forces the analysis of the problem outside the Debye regime by effectively reducing the NA to a value below 0.01 (Section 4.5). This is a problem as ENZ inversion only yields accurate results inside this regime. Fortunately, we could overcome this problem by introducing scaled variables that basically make the Debye integral approach the Rayleigh integral, which is valid at a far larger range of NA-values, thus extending the applicability of ENZ inversion. Additionally, this correction also makes it possible to analyze other optical systems outside the Debye regime that are well-described using the Rayleigh integral, such as microlenses having an aperture just a few hundred wavelengths in diameter.

In this thesis, we have also dealt with the Strehl ratio. This very simple and well-established quality measure is an important quantity in the discussion of the performance of low-NA optical systems, but it was shown to be problematic when high-NA optical systems are considered. Through an ENZ-based analysis of the

Strehl ratio at high-NA, we have shown that, in contradiction to what is generally assumed, the amplitude distribution in the pupil does have an influence on both the position and strength of the maximum intensity in image space. As a result, it is not possible to devise a simple expression that can predict the Strehl ratio on the basis of Zernike coefficients and it is even possible for the Strehl ratio to become slightly larger when a certain aberration is increased. It is thus important that optical engineers recognize that the Strehl ratio at high-NA has characteristics that are in conflict with the behavior of the Strehl ratio at low-NA.

6.5 Outlook and recommendations for further research

In this thesis, we have reported on the major developments of the ENZ theory in recent years. Although the progress has been large, some loose ends still remain that deserve further research effort in the near future. Not discussed in this thesis, but certainly something of large potential, is the possibility to derive the derivatives of the Zernike basic functions analytically. This would make it, for example, possible to predict the effect of enlarging a specific aberration on the image. On the other hand, the derivatives with respect to the polar coordinates in image space would allow the incorporation of diffusion effects into the image computation. Also, the application of the ENZ theory slightly outside the Debye regime, as briefly discussed in Section 4.5, is a topic that deserves further research to be fully understood and exploited.

With respect to the ENZ imaging model some further developments are possible and even desirable. First of all, it would be interesting to remove the requirement that the object is small compared to its distance to the pupil. Secondly, the multilayer version of the ENZ imaging model should be further generalized to also allow the computation of the field in an image space layer that is absorptive or that contains evanescent fields.

Regarding ENZ characterization, the focus of further developments is twofold. First of all the realization of an object that closely resembles a real point object is often cumbersome. The actual objects used in ENZ characterization are pinholes of a finite size. Although a first order correction of this finiteness is already available through an adapted defocus parameter, this correction might be insufficient, especially at high-NA. This possible issue should be studied further, and if the effects turn out to be significant, it will be necessary to account for them in order to enable widespread use of accurate ENZ system characterization. The second front at which more work is absolutely necessary is that of the experiment itself. Although some experimental work has been performed over the years mainly by Dirksen [12–14, 95, 106, 107], the availability of experimental data to verify the new extensions of the ENZ theory has been minimal. This is mainly caused by the limited availability of data from advanced optical systems that are described by the ENZ theory. Other experiments that could be performed in our own labs are not yet completed. Preliminary experimental results showed that there are issues related to the validity of the Debye integral with respect to our set-up. Present

work is in progress to fully understand this issue and to demonstrate that, using a correction of the type presented in Section 4.5, ENZ optical system characterization is possible using our experimental set-up operating slightly outside the Debye regime.

Appendix A

Series representations for the ENZ diffraction integrals

In this appendix, we present series expansions to efficiently compute the various diffraction integrals that occur in the ENZ-theory. Almost all the mathematical derivations have been previously published in journal papers and are exclusively due to A.J.E.M. Janssen [9, 45, 48, 64, 65, 112].

A.1 The V_n^m-function (limited defocus))

In Eqs.(3.13)-(3.15) a series representation was given for the scalar ENZ diffraction integral given by

$$V_n^m = \int_0^1 \rho \exp(if\rho^2) R_n^{|m|}(\rho) J_m(2\pi\rho r) d\rho. \tag{A.1}$$

Alternatively, the same integral can also be represented as

$$V_n^m = \varepsilon_m \exp(if) \sum_{l=0}^{\infty} \left(\frac{-2if}{v}\right)^l \sum_{j=0}^{p} u_{lj} \frac{J_{|m|+l+2j+1}(v)}{v} \tag{A.2}$$

with $\varepsilon_m = -1$ for odd $m < 0$ and $\varepsilon_m = 1$ otherwise. The coefficients u_{lj} are given by

$$u_{lj} = (-1)^p \frac{(|m|+l+2j+1)}{(q+l+j+1)} \binom{|m|+j+l}{l} \binom{j+l}{l} \binom{l}{p-j} \Big/ \binom{q+l+j}{l} \ , \tag{A.3}$$

with $l = 1, 2, \ldots, j = 0, \ldots, p$ and where we have again set

$$v = 2\pi r \ , \qquad p = \frac{n-|m|}{2} \ , \qquad q = \frac{n+|m|}{2} \ . \tag{A.4}$$

A.2 The V_n^m-function (large defocus)

Starting from Bauer's identity

$$\exp(if\rho^2) = \exp(\tfrac{1}{2}if)\sum_{k=0}^{\infty}(2k+1)\,i^k\,j_k(\tfrac{1}{2}f)\,R_{2k}^0(\rho)\ , \tag{A.5}$$

(see [113], formula 10.1.47 on p. 440 with $R_{2k}^0(\rho) = P_k(2\rho^2-1)$), V_n^m can be written as

$$V_n^m(r,f) = \exp(\tfrac{1}{2}if)\sum_{k=0}^{\infty}(2k+1)\,i^k\,j_k(\tfrac{1}{2}f)\int_0^1 R_{2k}^0(\rho)\,R_n^m(\rho)\,J_m(2\pi\rho r)\,\rho\,d\rho\ , \tag{A.6}$$

with

$$j_k(z) = \left(\frac{\pi}{2z}\right)^{1/2} J_{k+\frac{1}{2}}(z)\ , \quad k = 0,\ 1, ..., \tag{A.7}$$

the spherical Bessel functions of the first kind, see [113], Chapter 10. Then by writing the polynomial product in the integrand of Eq.(A.6) as

$$R_{2k}^0(\rho)\,R_{m+2p}^m(\rho) = \sum_l w_{kl}\,R_{m+2l}^m(\rho)\ , \tag{A.8}$$

and using the basic result given in Eq.(3.6), we obtain the following series representation for the V_n^m-function that is valid for large values of f

$$V_n^m(r,f) = \varepsilon_m\exp(\tfrac{1}{2}if)\sum_{k=0}^{\infty}(2k+1)i^k j_k(\tfrac{1}{2}f)\sum_{l=\max(0,k-q,p-k)}^{k+p}(-1)^l\,w_{kl}\,\frac{J_{m+2l+1}(2\pi r)}{2\pi r}. \tag{A.9}$$

It was shown in [65] that the coefficients w_{kl} occurring in the expression above can be represented by a double series involving the product of three other coefficients according to

$$w_{kl} = \sum_{s=0}^{p}\sum_{t=0}^{\min(k,s)} f_{ps}^m\,g_{k+s-2t,\,l}^m\,b_{kst}\ , \tag{A.10}$$

with the coefficients f, g and b given by

$$f_{ps}^m = (-1)^{p-s}\,\frac{2s+1}{p+s+1}\,\frac{\binom{m+p-s-1}{m-1}\binom{m+p+s}{s}}{\binom{p+s}{s}}\ , \qquad s = 0, ..., p\ , \tag{A.11}$$

$$g_{ul}^m = \frac{m+2l+1}{m+u+l+1}\,\frac{\binom{m}{u-l}\binom{u+l}{l}}{\binom{m+l+u}{m+l}}\ , \qquad u = l, ..., l+m\ , \tag{A.12}$$

$$b_{s_1s_2t} = \frac{2s_1+2s_2-4t+1}{2s_1+2s_2-2t+1}\,\frac{A_{s_1-t}\,A_t\,A_{s_2-t}}{A_{s_1+s_2-t}}\ , \quad t = 0, ..., \min(s_1,s_2), \tag{A.13}$$

where $A_k = \binom{2k}{k}$. For $m = 0$ we should read Eqs.(A.11-A.12) as

$$f_{ps}^0 = \delta_{ps}, \quad g_{ul}^0 = \delta_{ul}, \tag{A.14}$$

with δ being Kronecker's delta.

A.3 The T_n^m-function (large defocus)

Here we give a series representation for the T_n^m-function of Eq.(3.16) that is valid for arbitrary defocus values f. Writing $n = m + 2p$ and using the result given in [65], Eq.(36) we have

$$T_{m+2k,m} = \sum_{p=0}^{k} h_{kp}^m V_{m+2p,m} \ , \tag{A.15}$$

where

$$h_{kp}^m = \frac{m+2p+1}{m+p+k+1} \frac{\binom{k}{p}}{\binom{m+k+p}{p}}, \quad p = 0, 1, ..., j \ . \tag{A.16}$$

This is in principle enough to evaluate T_n^m at large f as we have available an expression for V_n^m that is valid at large f in Eq.(A.9). However, many terms in the various summations to compute T_n^m become zero and therefore the series representation for T_n^m is most conveniently written as

$$T_n^m(r,f) = \varepsilon_m \exp(\tfrac{1}{2}if) \sum_{k=0}^{\infty} (2k+1) i^k j_k(\tfrac{1}{2}f) \sum_{l=\max(0,k-m-p)}^{k+p} (-1)^l \, u_{kl}(m,p) \, \frac{J_{m+2l+1}(2\pi r)}{2\pi r}, \tag{A.17}$$

where

$$u_{kl}(m,p) = \sum_{s=0}^{p} \sum_{t=0}^{\min(k,s)} h_{ps}^0 \, b_{kst} \, g_{k+s-2t,\,l}^m \ , \tag{A.18}$$

with the coefficients given by Eqs.(A.12), (A.13) and (A.16), respectively.

A.4 The $V_{n,j}^m$-function (object at infinity)

We now present a series expansion for the integrals $V_{n,j}^m(r,f)$ given by

$$\begin{aligned} V_{n,j}^m(r,f) \quad = \quad & \int_0^1 \rho^{|j|} \frac{\left(1+\sqrt{1-s_0^2\rho^2}\right)^{-|j|+1}}{(1-s_0^2\rho^2)^{1/4}} \exp\left[\frac{if}{u_0}\left(1-\sqrt{1-s_0^2\rho^2}\right)\right] \times \\ & R_n^{|m|}(\rho) J_{m+j}(2\pi r\rho) \rho d\rho \ , \end{aligned} \tag{A.19}$$

with m, n, j integers, $|j| \leq 2$ and $n - |m| \geq 0$ and even.

Although diffraction integrals of the type given in Eq.(A.19) can be evaluated using the V_n^m-functions (see for example [9]), we will present here an expansion that makes use of the T_n^m basic integrals of Eq.(3.16). This is because an expansion according to the T_n^m-functions is more orderly and allows a better monitoring of the convergence of the solution. This expansion has already been given in [48], Appendix D.2, but is reproduced below with some minor corrections.

We write

$$R_n^{|m|}(\rho) = \rho^{|m|} \sum_{s=0}^{p} C_s \rho^{2s} \ , \ \ C_s = (-1)^{p-s} \binom{q+s}{p} \binom{p}{s} \ , \tag{A.20}$$

and

$$\frac{\left(1+\sqrt{1-s_0^2\rho^2}\right)^{-|j|+1}}{(1-s_0^2\rho^2)^{1/4}}\ \exp\left[\frac{if}{u_0}\left(1-\sqrt{1-s_0^2\rho^2}\right)\right] = \exp\{g'+if'\rho^2\}\sum_{t=0}^{\infty}B_t\rho^{2t}. \tag{A.21}$$

where again $p=(n-|m|)/2$, $q=(n+|m|)/2$. Then

$$V_{n,j}^m(r,f)=\exp(g')\sum_{s=0}^{p}\sum_{t=0}^{\infty}C_sB_tT_{|j|+|m|+2s+2t}^{m+j}(r,f')\ , \tag{A.22}$$

where for integer k, l with $l-|k|$ even and ≥ 0

$$T_l^k(r,f')=\int_0^1\rho^l\exp\{if'\rho^2\}J_k(2\pi r\rho)\rho d\rho\ . \tag{A.23}$$

These T_l^k have been computed in Eq.(3.17) or when large values of f are present using the recipe presented in Appendix A.3.

What remains is the computation of the coefficients B_t, g' and f' occurring at the right-hand side of Eq.(A.21). As a first step, we bring the fraction on the left-hand side of Eq.(A.21) into the exponential function and split off the optimal quadratic part $g'+if'\rho^2$. The Taylor expansion of the remaining part in the exponential is written as $\sum_{t'=0}^{\infty}A_{t'}\rho^{2t'}$. The coefficients B_t are defined by

$$\sum_{t=0}^{\infty}B_t\rho^{2t}=\exp\left(\sum_{t'=0}^{\infty}A_{t'}\rho^{2t'}\right). \tag{A.24}$$

Using $u_0=\sqrt{1-s_0^2}$ and $d_0=(u_0/s_0)^2$ as auxiliary quantities, the detailed scheme now looks as follows (see also [48], Appendix D.2),

$$\begin{cases} a_0=\frac{1}{2}-\frac{1}{6}d_0, & b_0=\frac{1}{2}d_0+\ln\left(\frac{u_0}{d_0}\right), & c_0=-\left\{1+\frac{1-s_0^2}{s_0^2}\ln(1-s_0^2)\right\},\\ a_1=\frac{1}{2}\left(1-\frac{1}{5}d_0^2\right), & b_1=-\frac{1}{4}d_0\left(2-d_0\right), & c_1=-3\sum_{r=1}^{\infty}\frac{s_0^{2r}}{(r+1)(r+2)}, \end{cases} \tag{A.25}$$

$$\begin{cases} g'=-\frac{1}{4}(c_0-c_1)+(-|j|+1)(b_0-b_1)+if(a_0-a_1),\\ f'=\frac{1}{2}ic_1+2fa_1-2i(-|j|+1)b_1, \end{cases} \tag{A.26}$$

$$\begin{cases} A_0=(-|j|+1)\ln 2-g', & A_1=\frac{1}{4}s_0^2\left(|j|+\frac{2if}{u_0}\right)-if',\\ A_{t'}=\left\{(|j|-1)\binom{-\frac{1}{2}}{t'}(-1)^{t'}+\frac{1}{2}-\frac{if}{u_0}\binom{-\frac{1}{2}}{t'-1}(-1)^{t'}\right\}\frac{s_0^{2t'}}{2t'}, & t'=2,3,.... \end{cases} \tag{A.27}$$

where the binomial coefficients having non-integer input values, occurring in the expression for $A_{t'}$, can be evaluated using the binomial definition in terms of gamma-functions

$$\binom{x}{y}=\frac{\Gamma(x+1)}{\Gamma(y+1)\Gamma(x-y+1)}\ . \tag{A.28}$$

The values of the B-coefficients in Eq.(A.22) are then given by

$$B_0 = \exp(A_0) \ , \qquad B_{t+1} = \sum_{j=0}^{t} \frac{t+1-j}{t+1} \, A_{t+1-j} \, B_j \ , \qquad t = 0, 1, ... \ . \quad \text{(A.29)}$$

The number of coefficients to be used can be judged from the convergence of the series expansion for $V_{n,j}^m(r, f)$. Even for numerical aperture values s_0 as high as 0.95, a limited number of coefficients is generally needed to attain an accuracy of, say 10^{-4}, in complex amplitude, or, equivalently, 10^{-8} in intensity. Such an accuracy is largely sufficient in practical applications where the measured intensity data, to be used in a retrieval process, are affected by noise at a much higher level.

A.5 The $V_{n,j}^m$-function (object at a finite distance)

Here we present a method for obtaining a series expansion for the integral $V_{n,j}^m(r, f)$ given by

$$\begin{aligned} V_{n,j}^m(r,f) &= \int_0^1 \rho^{|j|} \frac{\left\{ \left(1 - {s_0}^2\rho^2\right)^{\frac{1}{2}} + \left(1 - s_{0,M}^2\rho^2\right)^{\frac{1}{2}} \right\}^{-|j|+1}}{\left(1 - {s_0}^2\rho^2\right)^{\frac{1}{4}} \left(1 - s_{0,M}^2\rho^2\right)^{\frac{3}{4}}} \times \\ &\quad \exp\left[\frac{if}{u_0}\left(1 - \sqrt{1 - s_0^2\rho^2}\right)\right] R_n^{|m|}(\rho) J_{m+j}(2\pi r\rho)\rho d\rho, \quad \text{(A.30)} \end{aligned}$$

that occurs when an object, located at a finite distance from the entrance pupil, is imaged (see also [45], Appendix A). We follow a similar approach as in Appendix A.4 to transform the integral in Eq.(A.30) into a tractable form. In this case we write

$$\begin{aligned} &\exp\left[\frac{if}{u_0}\left(1 - \sqrt{1 - s_0^2\rho^2}\right)\right] \frac{\left\{ \left(1 - {s_0}^2\rho^2\right)^{\frac{1}{2}} + \left(1 - s_{0,M}^2\rho^2\right)^{\frac{1}{2}} \right\}^{-|j|+1}}{\left(1 - {s_0}^2\rho^2\right)^{\frac{1}{4}} \left(1 - s_{0,M}^2\rho^2\right)^{\frac{3}{4}}} \\ &\qquad = \exp\left\{g' + if'\rho^2\right\} \sum_{t=0}^{\infty} B_t \rho^{2t} \ , \quad \text{(A.31)} \end{aligned}$$

so that we can directly apply the same approach as in Appendix A.3 and we are left to determine the new coefficients B_t, g' and f'. The coefficients g' and f' are again defined by requiring the best fit for the constant and the quadratic term in ρ in the logarithm of the function Eq.(A.31). So let

$$\begin{aligned} F(\rho) &= \frac{if}{u_0}\left(1 - \sqrt{1 - s_0^2\rho^2}\right) \\ &\quad + (-|j| + 1) \ln\left[\left(1 - {s_0}^2\rho^2\right)^{\frac{1}{2}} + \left(1 - s_{0,M}^2\rho^2\right)^{\frac{1}{2}}\right] \\ &\quad - \frac{1}{4}\ln\left(1 - {s_0}^2\rho^2\right) - \frac{3}{4}\ln\left(1 - s_{0,M}^2\rho^2\right) \ , \quad \text{(A.32)} \end{aligned}$$

and define

$$A(\rho) = 1-\sqrt{1-s_0^2\rho^2} = \sum_{n=0}^{\infty} a_n\rho^{2n} \ , \tag{A.33}$$

$$B(\rho) = \ln\left[\left(1-{s_0}^2\rho^2\right)^{\frac{1}{2}}+\left(1-s_{0,M}^2\rho^2\right)^{\frac{1}{2}}\right] = \sum_{n=0}^{\infty} b_n\rho^{2n} \ , \tag{A.34}$$

$$C(\rho) = \ln\left(1-{s_0}^2\rho^2\right)+3\ln\left(1-s_{0,M}^2\rho^2\right) = \sum_{n=0}^{\infty} c_n\rho^{2n} \ , \tag{A.35}$$

so that

$$F(\rho) = \frac{if}{u_0}A(\rho)+(-|j|+1)\,B(\rho)-\frac{1}{4}C(\rho) = \sum_{n=0}^{\infty} f_n\rho^{2n} \ , \tag{A.36}$$

$$f_n = \frac{if}{u_0}a_n+(-|j|+1)\,b_n-\frac{1}{4}c_n \ , \ \ n=0,1,... \ . \tag{A.37}$$

We shall determine a_n, b_n and c_n.

$\mathbf{a_n}$: We have by Taylor expansion

$$a_0=0 \ ; \ \ a_n=-\binom{\frac{1}{2}}{n}(-1)^n s_0^{2n} \ , \ \ n=1,2,... \ . \tag{A.38}$$

$\mathbf{b_n}$: Consider the function

$$f(x)=\ln\left[(1-x)^{\frac{1}{2}}+(1-ax)^{\frac{1}{2}}\right] \ . \tag{A.39}$$

Then

$$\begin{aligned} f'(x) &= \frac{1}{2}\frac{1}{(1-x)^{\frac{1}{2}}+(1-ax)^{\frac{1}{2}}}\left(\frac{-1}{(1-x)^{\frac{1}{2}}}+\frac{-a}{(1-ax)^{\frac{1}{2}}}\right) \\ &= -\frac{1}{2}\frac{(1-x)^{\frac{1}{2}}-(1-ax)^{\frac{1}{2}}}{(1-x)-(1-ax)}\frac{(1-ax)^{\frac{1}{2}}+a(1-x)^{\frac{1}{2}}}{(1-x)^{\frac{1}{2}}(1-ax)^{\frac{1}{2}}} \\ &= \frac{1}{2x}\left(1-(1-ax)^{-\frac{1}{2}}(1-x)^{-\frac{1}{2}}\right) \\ &= -\frac{1}{2}\sum_{t=1}^{\infty}\left[(-1)^t\sum_{r=0}^{t}\binom{-\frac{1}{2}}{r}\binom{-\frac{1}{2}}{t-r}a^r\right]x^{t-1} \ , \end{aligned} \tag{A.40}$$

where the third identity is obtained by working out the numerator and denominator and simplifying, and the fourth identity is obtained by multiplying the Taylor expansions of $(1-ax)^{-1/2}$ and of $(1-x)^{-1/2}$. Therefore, by integrating from 0 to x,

$$f(x) = \ln 2-\sum_{t=1}^{\infty}\left[\frac{(-1)^t}{2t}\sum_{r=0}^{t}\binom{-\frac{1}{2}}{r}\binom{-\frac{1}{2}}{t-r}a^r\right]x^t \ . \tag{A.41}$$

Using (A.41) with $a = \frac{s_{0,M}^2}{s_0^2}$ and $x = s_0^2\rho^2$, we see that

$$b_0 = \ln 2 \ ; \ b_n = -\frac{(-1)^n}{2n} \sum_{r=0}^{n} \binom{-\frac{1}{2}}{r} \binom{-\frac{1}{2}}{n-r} s_0^{2(n-r)} s_{0,M}^{2r} \ , \ n = 1, 2, \dots . \tag{A.42}$$

c_n: We have by Taylor expansion

$$c_0 = 0 \ ; \ c_n = -\frac{(s_0)^{2n} + 3(s_{0,M})^{2n})}{n} \ , \ n = 1, 2, \dots . \tag{A.43}$$

Thus, with a_n, b_n, c_n from Eqs.(A.38), (A.42) and (A.43), we can compute the f_n of $F(\rho) = \sum_{n=0}^{\infty} f_n \rho^{2n}$ according to Eq.(A.37).

Next, we proceed by writing

$$F(\rho) = g' + if'\rho^2 + \sum_{n=0}^{\infty} A_n \rho^{2n} \ , \tag{A.44}$$

where $g' + if'\rho^2$ is the best quadratic approximation of $F(\rho)$ using $\rho d\rho$ on $[0, 1]$ as weight function. To this end, we convert the Taylor expansion $\sum_{n=0}^{\infty} f_n \rho^{2n}$ of $F(\rho)$ into a Zernike expansion $\sum_{k=0}^{\infty} \beta_{2k}^0 R_{2k}^0$ according to the formula

$$\beta_{2k}^0 = \sum_{n=k}^{\infty} \frac{2k+1}{k+1} \frac{\binom{n}{k}}{\binom{n+k+1}{n}} f_n \ , \ k = 0, 1, \dots , \tag{A.45}$$

see [7], Eq. (10). Now

$$\beta_0^0 R_0^0(\rho) + \beta_2^0 R_2^0(\rho) = (\beta_0^0 - \beta_2^0) + 2\beta_2^0 \rho^2 \tag{A.46}$$

is the desired best approximation of $F(\rho)$. Hence

$$g' = \beta_0^0 - \beta_2^0 \ , \ f' = \frac{2}{i}\beta_2^0 \ , \tag{A.47}$$

and

$$A_0 = f_0 - g' \ , \ A_1 = f_1 - if' \ ; \ A_n = f_n \ , \ n = 2, 3, \dots . \tag{A.48}$$

The final step in achieving Eq.(A.31) consists of again applying Eqs.(A.24) and (A.29). Using these results we can compute the $V_{n,j}^m$ of Eq.(A.30) again according to Eq.(A.22), with the B_t-coefficients this time given by the recipe described above.

A.6 The $V_{n,j,t_\pm/r_\pm}^m$-function (multilayer case)

In this appendix, we present a method for obtaining a series expansion for the integral $V_{n,j,t_\pm}^m(r, f)$ given by

$$V_{n,j,t_\pm}^m(r, f) = \int_0^1 \rho^{|j|} \frac{\left\{ \left(1 - {s_{0,h}}^2\rho^2\right)^{\frac{1}{2}} \pm \left(1 - s_{0,M}^2\rho^2\right)^{\frac{1}{2}} \right\}^{-|j|+1}}{\left(1 - {s_0}^2\rho^2\right)^{\frac{1}{4}} \left(1 - s_{0,M}^2\rho^2\right)^{\frac{3}{4}}} \times$$
$$\exp\left[\frac{if}{u_{0,h}} \left(1 - \sqrt{1 - s_{0,h}^2\rho^2} \right) \right] R_n^{|m|}(\rho) J_{m+j}(2\pi r\rho) \rho d\rho. \tag{A.49}$$

We use the identity

$$\begin{aligned}\left(1-{s_{0,h}}^2\rho^2\right)^{\frac{1}{2}}\pm\left(1-s_{0,M}^2\rho^2\right)^{\frac{1}{2}} &= \\ &= \begin{cases} \left(1-{s_{0,h}}^2\rho^2\right)^{\frac{1}{2}}+\left(1-s_{0,M}^2\rho^2\right)^{\frac{1}{2}}\ , \text{ + case} \\ \frac{\left(s_{0,M}^2-s_{0,h}^2\right)\rho^2}{\left(1-{s_{0,h}}^2\rho^2\right)^{\frac{1}{2}}+\left(1-s_{0,M}^2\rho^2\right)^{\frac{1}{2}}}\ , \text{ − case} \end{cases} \\ &= \left[\left(1-{s_{0,h}}^2\rho^2\right)^{\frac{1}{2}}+\left(1-s_{0,M}^2\rho^2\right)^{\frac{1}{2}}\right]^{\sigma}\left[\left(s_{0,M}^2-s_{0,h}^2\right)\rho^2\right]^{\frac{1-\sigma}{2}} \qquad \text{(A.50)}\end{aligned}$$

where $\sigma=\pm1$ indicates both sign possibilities, to write Eq.(A.50) in the form

$$\begin{aligned}V^m_{n,j,t_\pm}(r,f) &= \left(s_{0,M}^2-s_{0,h}^2\right)^{\frac{1}{2}(1-\sigma)(-|j|+1)}\times \\ &\int_0^1 \rho^{1-\sigma+\sigma|j|}\frac{\left\{\left(1-{s_{0,h}}^2\rho^2\right)^{\frac{1}{2}}+\left(1-s_{0,M}^2\rho^2\right)^{\frac{1}{2}}\right\}^{\sigma(-|j|+1)}}{\left(1-{s_0}^2\rho^2\right)^{\frac{1}{4}}\left(1-s_{0,M}^2\rho^2\right)^{\frac{3}{4}}}\times \\ &\exp\left[\frac{if}{u_{0,h}}\left(1-\sqrt{1-s_{0,h}^2\rho^2}\right)\right]R_n^{|m|}(\rho)J_{m+j}(2\pi r\rho)\rho d\rho. \qquad \text{(A.51)}\end{aligned}$$

This expression can be evaluated in completely the same manner as the integral discussed in Appendix A.5. We write (see also [112])

$$\begin{aligned}&\exp\left[\frac{if}{u_{0,h}}\left(1-\sqrt{1-s_{0,h}^2\rho^2}\right)\right]\frac{\left\{\left(1-{s_{0,h}}^2\rho^2\right)^{\frac{1}{2}}+\left(1-s_{0,M}^2\rho^2\right)^{\frac{1}{2}}\right\}^{\sigma(-|j|+1)}}{\left(1-{s_0}^2\rho^2\right)^{\frac{1}{4}}\left(1-s_{0,M}^2\rho^2\right)^{\frac{3}{4}}} \\ &\qquad = \exp\left\{g'+if'\rho^2\right\}\sum_{t=0}^{\infty}B_t\rho^{2t}\ . \qquad \text{(A.52)}\end{aligned}$$

so that we are again left to determine the coefficients g', f' and B_t, as well as C_s. The determination of these coefficients can be performed as in Appendix A.5. The resulting series expansion for $V^m_{n,j,t_\pm}$ then becomes

$$\begin{aligned}V^m_{n,j,t_\pm}(r,f) &= \left(s_{0,M}^2-s_{0,h}^2\right)^{\frac{1}{2}(1-\sigma)(-|j|+1)}\times \\ &\exp\{g'\}\sum_{s=0}^{p}\sum_{t=0}^{\infty}C_sB_tT^{m+j}_{1-\sigma+\sigma|j|+|m|+2s+2t}(r,f')\ . \qquad \text{(A.53)}\end{aligned}$$

The T_l^k occurring in Eq.(A.53) are again the same as those defined in Eq.(3.17). However, the series expansion of Eq.(A.17) that can be used to evaluate it, is only valid for $l-|k|\geq 0$, while in Eq.(A.53) values $l-|k|<0$ can also occur. We therefore derive here another computation scheme for T_l^k, that is valid for general integer values of l and k.

We have Bauer's formula

$$\exp\left(if'\rho^2\right)=\exp\left(\tfrac{i}{2}f'\right)\sum_{q=0}^{\infty}\left(2q+1\right)i^q j_q(\tfrac{1}{2}f')R^0_{2q}(\rho)\ , \qquad \text{(A.54)}$$

so that

$$T_l^k(r,f') = \exp\left(\tfrac{i}{2}f'\right)\sum_{q=0}^{\infty}(2q+1)\,i^q j_q(\tfrac{1}{2}f')\int_0^1 \rho^l R_{2q}^0(\rho)J_k(2\pi r\rho)\rho d\rho \ . \quad \text{(A.55)}$$

The series in Eq.(A.55) has excellent convergence properties, with no loss of digits, and taking the terms with $q \le \frac{3}{4}|f'|+5$ yields in all cases sufficient accuracy.

Next, we consider the integrals $\int_0^1 \rho^l R_{2q}^0(\rho)J_k(2\pi r\rho)\rho d\rho$. There is the expansion of $J_k(x)$ based on the Zernike polynomials according to

$$J_k(2\pi r\rho) = \sum_{t=0}^{\infty} 2(k+2t+1)(-1)^t \frac{J_{k+2t+1}(2\pi r)}{2\pi r} R_{k+2t}^k(\rho) \ , \quad \text{(A.56)}$$

and this Zernike expansion is also excellent convergent. It is sufficient to include all terms with $l \le \max\{0, \frac{3}{2}|\pi r|+4-\frac{1}{2}k\}$ to get sufficient convergence. Therefore,

$$T_l^k(r,f') = 2\exp\left(\tfrac{i}{2}f'\right)\times$$
$$\sum_{q,t=0}^{\infty}(2q+1)\,(k+2t+1)\,i^q(-1)^t j_q(\tfrac{1}{2}f')\frac{J_{k+2t+1}(2\pi r)}{2\pi r}E_{lkqt} \ , \quad \text{(A.57)}$$

in which

$$E_{lkqt} = \int_0^1 \rho^l R_{2q}^0(\rho)R_{k+2t}^k(\rho)\rho d\rho \ . \quad \text{(A.58)}$$

These E_{lkqt} can be computed as follows. We write $k = l+2r$, where r is integer and can be positive, zero or negative, but in all cases $l+r \ge 0$ and $r \le k$. Then we write

$$E_{lkqt} = \int_0^1 \rho^{l+r} R_{2q}^0(\rho)\rho^{-r}R_{k+2t}^{l+2r}(\rho)\rho d\rho \ . \quad \text{(A.59)}$$

Now for integer N, M, K with N, $M \ge 0$ and $N-M$ even and ≥ 0 and $K = -M, -M+1, \cdots$, we show below that ($P=(N-M)/2$, $Q=(N+M)/2$)

$$\rho^K R_N^M(\rho) = \sum_{j=0}^{P} C_j(N,M,K)R_{N+K-2j}^{M+K}(\rho) \ , \quad \text{(A.60)}$$

where, using Pochhammer's symbol $(x)_j = 1$ $(j=0)$, $= x(x+1)\cdots(x+j-1)$, $j = 1,2,\cdots$,

$$C_j(N,M,K) = \frac{N+K-2j+1}{N+K-j+1}\binom{P}{j}\frac{(Q+K-j)!(N-j)!}{Q!(N+K-j)!}(K-j+1)_j \ . \quad \text{(A.61)}$$

Using Eq.(A.60) with $K = l+r$, $M=0$, $N=2q$ and $K=-r$, $M=l+2r$,

$N = k + 2t$, respectively, in Eq.(A.59), we get

$$E_{lkqt} = \int_0^1 \sum_{j_1=0}^{q} C_{j_1}(2q, 0, l+r) R^{l+r}_{l+r+2q-2j_1}(\rho) \times \sum_{j_2=0}^{t} C_{j_2}(k+2t, l+2r, -r) R^{l+r}_{l+r+2t-2j_2}(\rho)\rho d\rho \tag{A.62}$$

$$= \sum_{j=\max(0,q-t)}^{\min(q,l+r)} \frac{C_j(2q, 0, l+r) C_{j+t-q}(k+2t, l+2r, -r)}{2(l+r+2q-2j+1)} \ .$$

Here it has also been used that (orthogonality)

$$\int_0^1 R^{l+r}_{l+r+2s}(\rho) R^{l+r}_{l+r+2t}(\rho)\rho d\rho = \frac{\delta_{st}}{2(l+r+2s+1)} \ , \ s, t = 0, 1, \cdots \ . \tag{A.63}$$

For a proof of Eqs.(A.60)-(A.61) one can consult [112], Appendix A.

Appendix B

Analytic results for various Zernike expansion coefficients

In this Appendix, we present the various Zernike expansions of the amplitude and phase functions that are required for the analysis of the Strehl ratio at high NA (Section 4.6). Again the expressions presented in this appendix are largely the work of one of our collaborators, A.J.E.M. Janssen, who can be considered a true expert on polynomial expansions in general and Zernike expansions in particular. Only the results are given; the intricate derivations that were regularly encountered have been omitted (see also [63]).

We first present some basic quantities, related to high-NA imaging and then produce the expressions for the Zernike coefficients of the relevant aperture functions. At the end of the Appendix, numerical values of coefficients are listed pertaining to a NA-value of 0.95. These numerical values are useful in evaluating the relative importance of terms contributing to the Strehl intensity and they support the reasoning why some of these terms have been deleted from the analysis.

- Definition of some constants

$$c_0 = (1 - s_0^2)^{1/2}, \qquad d_0 = \left(\frac{1 - c_0}{s_0}\right)^2 \tag{B.1}$$

- Expansion coefficients of $(1 - s_0^2\rho^2)^\alpha$

$$(1 - s_0^2\rho^2)^\alpha = \sum_{n=0}^{\infty} D_{2n}^0(\alpha) R_{2n}^0(\rho) \ , \quad n = 0, 1, ... \tag{B.2}$$

$$D_{2n}^0(\alpha) = \frac{2n+1}{n+1} \sum_{k=n}^{\infty} \frac{(-1)^k \binom{\alpha}{k} \binom{k}{n}}{\binom{n+k+1}{k}} \, s_0^{2k} \ , \quad n = 0, 1, ... \tag{B.3}$$

- Expansion coefficients of $1-(1-s_0^2\rho^2)^\alpha$

$$1-(1-s_0^2\rho^2)^\alpha = \sum_{n=1}^{\infty} G_{2n}^2(\alpha) R_{2n}^2(\rho)\ , n=1,2,... \tag{B.4}$$

$$G_{2n}^2(\alpha) = -\frac{2n+1}{n}\sum_{k=n}^{\infty} \frac{(-1)^k\binom{\alpha}{k}\binom{k-1}{n-1}}{\binom{n+k+1}{k+1}}\, s_0^{2k}\ , \quad n=1,2,... \tag{B.5}$$

- Expansion coefficients of $\Delta(\rho)$

$$\Delta(\rho) = \frac{1-\sqrt{1-s_0^2\rho^2}}{1-c_0} = \sum_{n=0}^{\infty} \gamma_{2n}^0 R_{2n}^0(\rho)\ ; \qquad \Delta_1(\rho) = \Delta(\rho) - \gamma_0^0 \tag{B.6}$$

$$\gamma_0^0 = \frac{1+2c_0}{3(1+c_0)}, \qquad \gamma_{2n}^0 = \frac{1}{2}\left(\frac{d_0^{n-1}}{2n-1} - \frac{d_0^{n+1}}{2n+3}\right), \quad n=1,2,... \tag{B.7}$$

- Expansion coefficients of $A^0(\rho)$

$$A^0(\rho) = \frac{1+\sqrt{1-s_0^2\rho^2}}{2(1-s_0^2\rho^2)^{1/4}} = \sum_{n=0}^{\infty} a_{2n}^0 R_{2n}^0(\rho)\ ; \tag{B.8}$$

$$a_{2n}^0 = \frac{1}{2}\left(D_{2n}^0(-1/4) + D_{2n}^0(1/4)\right), \quad n=0,1,... \tag{B.9}$$

- Expansion coefficients of $A^2(\rho)$

$$A^2(\rho) = \frac{1-\sqrt{1-s_0^2\rho^2}}{2(1-s_0^2\rho^2)^{1/4}} = \sum_{n=0}^{\infty} a_{2n}^2 R_{2n}^2(\rho)\ ; \tag{B.10}$$

$$a_{2n}^2 = \frac{1}{2}\left(G_{2n}^2(1/4) - G_{2n}^2(-1/4)\right), \quad n=1,2,... \tag{B.11}$$

- Expansion coefficients of $A^0(\rho)\Delta_1(\rho)$

$$A^0(\rho)\Delta_1(\rho) = \frac{1+\sqrt{1-s_0^2\rho^2}}{2(1-s_0^2\rho^2)^{1/4}}\left[\frac{1-\sqrt{1-s_0^2\rho^2}}{1-c_0} - \gamma_0^0\right] = \sum_{n=0}^{\infty} C_{2n}^0 R_{2n}^0(\rho)\ ; \tag{B.12}$$

$$\begin{aligned} C_{2n}^0 \quad = \quad & \frac{1}{2(1-c_0)}\left[\{1-\gamma_0^0(1-c_0)\}D_{2n}^0(-1/4)\right. \\ & \left. -\gamma_0^0(1-c_0)D_{2n}^0(1/4) - D_{2n}^0(3/4)\right], \quad n=0,1,... \end{aligned} \tag{B.13}$$

- Expansion coefficients of $A^2(\rho)\Delta_1(\rho)$

$$A^2(\rho)\Delta_1(\rho) = \frac{1-\sqrt{1-s_0^2\rho^2}}{2(1-s_0^2\rho^2)^{1/4}}\left[\frac{1-\sqrt{1-s_0^2\rho^2}}{1-c_0} - \gamma_0^0\right] = \sum_{n=1}^{\infty} E_{2n}^2 R_{2n}^2(\rho)\ ; \tag{B.14}$$

$$E_{2n}^2 = \frac{-1}{2(1-c_0)}\left[\{1-\gamma_0^0(1-c_0)\}G_{2n}^2(-1/4) - \{2-\gamma_0^0(1-c_0)\}G_{2n}^2(1/4)+G_{2n}^2(3/4)\right], \quad n=1,2,... \text{ (B.15)}$$

To conclude this Appendix, we give the numerical values of the most important coefficients that are encountered in the Strehl ratio analysis ($s_0 = 0.95$).

	n=0	n=1	n=2	n=3	n=4	n=5
$c_0 =$	0.312250					
$d_0 =$	0.524100					
$a_{2n}^0 =$	1.028866	0.056333	0.042380	0.022633	0.011679	0.005987
$\gamma_{2n}^0 =$	0.412650	0.472532	0.077067	0.023276	0.008485	0.003395
$C_{2n}^0 =$	0.009615	0.496726	0.103650	0.042274	0.019268	0.009182
$a_{2n}^2 =$		0.413719	0.115181	0.046428	0.020838	0.009813
$E_{2n}^2 =$		0.121137	0.135165	0.056529	0.025408	0.011910

Bibliography

[1] Wikipedia, "Nimrud lens," http://en.wikipedia.org/wiki/Nimrud_lens.

[2] CBC News, "Scientists team up with b.c. firm to build biggest-ever optical telescope," http://www.cbc.ca/technology/story/2009/04/07/tech-090407-thirty-metre-telescope.html.

[3] Nikon Instruments Inc., "Nikon's New FN1 Upright Focusing Nosepiece Microscope Delivers Outstanding Image Results," http://www.nikoninstruments.com/News/US-News/Nikon-s-New-FN1-Upright-Focusing-Nosepiece-Microscope-Delivers-Outstanding-Image-Results.

[4] ASML, "ASML Image Library," https://asml.picturepark.com/Website/Publisher.aspx?Page=ASML.

[5] B. Arnett, "The world's largest optical telescopes," http://astro.nineplanets.org/bigeyes.html.

[6] P. Debye, "Das Verhalten von Lichtwellen in der Nahe eines Brennpunktes oder einer Brennlinie," Ann. Phys. **335**, 755–776 (1909).

[7] A. J. E. M. Janssen, "Extended Nijboer-Zernike approach for the computation of optical point-spread functions," J. Opt. Soc. Am. A **19**, 849–857 (2002).

[8] J. Braat, P. Dirksen, and A. J. E. M. Janssen, "Assessment of an extended Nijboer-Zernike approach for the computation of optical point-spread functions," J. Opt. Soc. Am. A **19**, 858–870 (2002).

[9] J. J. M. Braat, P. Dirksen, A. J. E. M. Janssen, and A. S. van de Nes, "Extended Nijboer-Zernike representation of the vector field in the focal region of an aberrated high-aperture optical system," J. Opt. Soc. Am. A **20**, 2281–2292 (2003).

[10] S. J. Heyes, "Fundamental aspects of solids & sphere packing," http://www.chem.ox.ac.uk/icl/heyes/structure_of_solids/lecture1/Lec1.html.

[11] Koninklijke Bibliotheek, "Frits Zernike (1888-1966)," `http://www.kb.nl/hkc/nobel/zernike/zernike.html`.

[12] P. Dirksen, J. J. Braat, P. De Bisschop, G. C. Janssen, C. A. Juffermans, and A. M. Williams, "Characterization of a projection lens using the extended Nijboer-Zernike approach," Proc. SPIE **4691**, 1392–1399 (2002).

[13] P. Dirksen, J. J. M. Braat, A. J. E. M. Janssen, C. A. H. Juffermans, and A. Leeuwestein, "Experimental determination of lens aberrations from the intensity point-spread function in the focal region," Proc. SPIE **5040**, 1–10 (2003).

[14] P. Dirksen, J. J. M. Braat, A. J. E. M. Janssen, and C. Juffermans, "Aberration retrieval using the extended Nijboer-Zernike approach," J. Microlith., Microfabr., Microsyst. **2**, 61 (2003).

[15] L. Seidel, "Über die Entwicklung der Glieder 3ter Ordnung welche den Weg eines ausserhalb der Ebene der Axe gelegene Lichtstrahles durch ein System brechender Medien bestimmen," Astr. Nach. **43**, 289–304 (1856).

[16] E. Abbe, "Beiträge zur Theorie des Mikroskops und der mikroskopischen Wahrnehmung," Arch. mikrosk. Anat. **9**, 413–468 (1873).

[17] H. Köhler, "On Abbe's theory of image formation in the microscope," J. Mod. Opt. **28**, 1691–1701 (1981).

[18] P. M. Duffieux, *L'intégrale de Fourier et ses applications à l'optique* (privately published, 1946). Second edition: (Masson, Paris, 1970) and English translation: (Wiley, New York and Chichester, 1983).

[19] A. Maréchal, "Study of the combined effects of diffraction and geometrical aberrations on the image of a luminous point," Rev. Opt. **26**, 257–277 (1947).

[20] H. H. Hopkins, "On the diffraction theory of optical images," Proc. R. Soc. London Ser. A **217**, 408–432 (1953).

[21] H. H. Hopkins, "The frequency response of a defocused optical system," Proc. R. Soc. London Ser. A **231**, 91–103 (1955).

[22] J. W. Goodman, *Introduction to Fourier optics* (Roberts & Co. Publishers, 2004).

[23] M. Born and E. Wolf, *Principles of optics* (Cambridge University Press, Cambridge, 1999), 7th ed.

[24] G. Airy, "Diffraction of an object glass," Trans. phil. Soc. Camb. **5**, 283 (1835).

[25] E. Lommel, "Die Beugungserscheinungen einer kreisrunden Oeffnung und eines kreisrunden Schirmchens," Abh. Bayer. Akad. Math. Naturwiss. Kl. **15**, 233–328 (1885).

[26] K. Strehl, *Theorie des Fernrohrs. Auf Grund der Beugung des Lichts. 1 Teil.* (J.A. Barth, Leipzig, 1894).

[27] A. E. Conrady, "The five aberrations of lens-systems," Mon. Not. R. Astr. Soc. **79** (1918).

[28] A. E. Conrady, "Star discs," Mon. Not. R. Astr. Soc. **79**, 575 (1919).

[29] J. Picht, "Über den Schwingungsvorgang, der einem beliebigen (astigmatischen) Strahlenbündel entspricht," Ann. Phys. **382**, 785–882 (1925).

[30] J. Picht, "Die Intensitätsverteilung in einem astigmatischen Strahlenbündel in Abhängigkeit von dem Brennlinienabstand und der Öffnung auf Grund der Wellentheorie des Lichtes," Ann. Phys. **385**, 491–508 (1926).

[31] F. Zernike, "Beugungstheorie des Schneidenverfahrens und seiner verbesserten Form, der Phasenkontrastmethode," Physica **1**, 689–704 (1934).

[32] B. Nijboer, "The diffraction theory of aberrations," Ph.D. thesis, University of Groningen (1942). Downloadable from: www.nijboerzernike.nl.

[33] D. G. Flagello, T. Milster, and A. E. Rosenbluth, "Theory of high-NA imaging in homogeneous thin films," J. Opt. Soc. Am. A **13**, 53–64 (1996).

[34] C. J. R. Sheppard and H. J. Matthews, "Imaging in high aperture optical systems," J.Opt. Soc. Am. A **4**, 1354–1360 (1987).

[35] K. Yamazoe, "Computation theory of partially coherent imaging by stacked pupil shift matrix," J. Opt. Soc. Am. A **25**, 3111–3119 (2008).

[36] V. S. Ignatowsky, "Diffraction of a lens of arbitrary aperture," Trans. Opt. Inst. **1**, 1–36 (1919).

[37] H. H. Hopkins, "The Airy disc formula for systems of high relative aperture," Proc. Phys. Soc. **55**, 116–128 (1943).

[38] E. Wolf, "Electromagnetic diffraction in optical systems. I. An integral representation of the image field," Proc. Roy. Soc. London A **253**, 349–357 (1959).

[39] B. Richards and E. Wolf, "Electromagnetic diffraction in optical systems. II. Structure of the image field in an aplanatic system," Proc. Roy. Soc. London A **253**, 358–379 (1959).

[40] P. Török and P. Munro, "The use of Gauss-Laguerre vector beams in STED microscopy," Opt. Expr. **12**, 36053617 (2004).

[41] C. J. R. Sheppard and P. Török, "Efficient calculation of electromagnetic diffraction in optical systems using a multipole expansion," J. Mod. Opt. **44**, 803818 (1997).

[42] S. S. Sherif and P. Török, "Eigenfunction representation of the integrals of the Debye-Wolf diffraction formula," J. Mod. Opt. **52**, 857–876 (2005).

[43] C. J. R. Sheppard, "Aberrations in high-aperture conventional and confocal imaging systems," Appl. Opt. **27**, 47824786 (1988).

[44] C. Colautti, B. Ruiz, E. E. Sicre, and M. Garavaglia, "Walsh functions: Analysis of their properties under Fresnel diffraction," J. Mod. Opt. **34**, 13851391 (1987).

[45] S. van Haver, J. J. M. Braat, A. J. E. M. Janssen, O. T. A. Janssen, and S. F. Pereira, "Vectorial aerial-image computations of three-dimensional objects based on the Extended Nijboer-Zernike theory," J. Opt. Soc. Am. A **26**, 1221–1234 (2009).

[46] J. A. Stratton and L. J. Chu, "Diffraction theory of electromagnetic waves," Phys. Rev. **56**, 99–107 (1939).

[47] E. Wolf and Y. Li, "Conditions for the validity of the Debye integral representation of focused fields," Opt. Commun. **39**, 205–210 (1981).

[48] J. J. M. Braat, S. van Haver, A. J. E. M. Janssen, and P. Dirksen, "Assessment of optical systems by means of point-spread functions," in "Progress in Optics," vol. **51**, E. Wolf, ed. (Elsevier B.V., Amsterdam, 2008), chap. 6, pp. 349-468 .

[49] R. M. Aarts, J. J. M. Braat, P. Dirksen, S. van Haver, C. van Heesch, and A. J. E. M. Janssen, "Analytic expressions and approximations for the on-axis, aberration-free Rayleigh and Debye integral in the case of focusing fields on a circular aperture," J. Europ. Opt. Soc. Rap. Public. **3** (2008).

[50] H. Ling and S. Lee, "Focusing of electromagnetic waves through a dielectric interface," J. Opt. Soc. Am. A **1**, 965–973 (1984).

[51] P. Török, P. Varga, Z. Laczik, and G. R. Booker, "Electromagnetic diffraction of light focused through a planar interface between materials of mismatched refractive indices: an integral representation," J. Opt. Soc. Am. A **12**, 325–332 (1995).

[52] A. Egner and S. W. Hell, "Equivalence of the Huygens-Fresnel and Debye approach for the calculation of high aperture point-spread functions in the presence of refractive index mismatch," J. Microsc. **193**, 244–249 (1999).

[53] C. Sheppard and C. Cogswell, "Effects of aberrating layers and tube length on confocal imaging properties," Optik **87**, 34–38 (1991).

[54] S. Hell, G. Reiner, C. Cremer, and E. H. K. Stelzer, "Aberrations in confocal fluorescence microscopy induced by mismatches in refractive index," J. Microsc. **169**, 391–405 (1993).

[55] D. G. Flagello and T. D. Milster, "Three-dimensional modeling of high-numerical-aperture imaging in thin films," Proc. SPIE **1625**, 246–261 (1992).

[56] A. K. Wong, *Optical Imaging in Projection Microlithography* (SPIE Press, Bellingham, 2005).

[57] M. Mansuripur, "Analysis of multilayer thin-film structures containing magneto-optic and anisotropic media at oblique incidence using 2 x 2 matrices," J. Appl. Phys. **67**, 6466–6475 (1990).

[58] M. Mansuripur, "Effects of high-numerical-aperture focusing on the state of polarization in optical and magneto-optical data storage systems," Appl. Opt. **30**, 3154–3162 (1991).

[59] A. S. van de Nes, L. Billy, S. F. Pereira, and J. J. M. Braat, "Calculation of the vectorial field distribution in a stratified focal region of a high-numerical-aperture imaging system," Opt. Exp. **12**, 1281–1293 (2004).

[60] J. M. A. van den Eerenbeemd, D. M. Bruls, C. A. Verschuren, B. Yin, and F. Zijp, "Towards a multi-layer near-field recording system: Dual-layer recording results," Jpn. J. Appl. Phys. **46**, 3894–3897 (2007).

[61] C. J. R. Sheppard, T. J. Connolly, J. Lee, and C. J. Cogswell, "Confocal imaging of a stratified medium," Appl. Opt. **33**, 631–640 (1994).

[62] V. N. Mahajan, "Strehl ratio for primary aberrations: some analytical results for circular and annular pupils," J. Opt. Soc. Am. **72**, 1258–1266 (1982).

[63] A. J. E. M. Janssen, S. van Haver, J. J. M. Braat, and P. Dirksen, "Strehl ratio and optimum focus of high-numerical-aperture beams," J. Europ. Opt. Soc. Rap. Public. **2**, 07008 (2007).

[64] C. van der Avoort, J. J. M. Braat, P. Dirksen, and A. J. E. M. Janssen, "Aberration retrieval from the intensity point-spread function in the focal region using the extended Nijboer-Zernike approach," J. Mod. Opt. **52**, 1695–1728 (2005).

[65] A. J. E. M. Janssen, J. J. M. Braat, and P. Dirksen, "On the computation of the Nijboer-Zernike aberration integrals at arbitrary defocus," J. Mod. Opt. **51**, 687–703 (2004).

[66] S. Stallinga, "Axial birefringence in high-numerical-aperture optical systems and the light distribution close to focus," J. Opt. Soc. Am. A **18**, 2846–2859 (2001).

[67] S. van Haver, O. T. A. Janssen, J. J. M. Braat, A. J. E. M. Janssen, H. P. Urbach, and S. F. Pereira, "General imaging of advanced 3D mask objects based on the fully-vectorial extended Nijboer-Zernike (ENZ) theory," Proc. SPIE **6924**, 69240U (2008).

[68] O. T. A. Janssen, S. van Haver, A. J. E. M. Janssen, J. J. M. Braat, H. P. Urbach, and S. F. Pereira, "Extended Nijboer-Zernike (ENZ) based mask imaging: efficient coupling of electromagnetic field solvers and the ENZ imaging algorithm," Proc. SPIE **6924**, 692410 (2008).

[69] A. Erdmann, C. K. Kalus, T. Schmoeller, Y. Klyonova, T. Sato, A. Endo, T. Shibata, and Y. Kobayashi, "Rigorous simulation of exposure over non-planar wafers," Proc. SPIE **5040**, 101–111 (2003).

[70] C. Mack, "Reducing proximity effects in optical lithography," Jpn. J. Appl. Phys. **35**, 6379–6385 (1996).

[71] B. Tatian, "Aberration balancing in rotationally symmetric lenses," J. Opt. Soc. Am. **64**, 1083–1091 (1974).

[72] V. N. Mahajan, "Zernike annular polynomials for imaging systems with annular pupils," J. Opt. Soc. Am. A **1**, 685–685 (1984).

[73] V. N. Mahajan, "Zernike annular polynomials and optical aberrations of systems with annular pupils," Applied Optics **33**, 8125–8127 (1994).

[74] A. J. E. M. Janssen and P. Dirksen, "Concise formula for the Zernike coefficients of scaled pupils," J. Microlithogr. Microfabr. Microsyst. **5**, 030501 (2006).

[75] A. J. E. M. Janssen, S. van Haver, P. Dirksen, and J. J. M. Braat, "Zernike representation and Strehl ratio of optical systems with variable numerical aperture," J. Mod. Opt. **55**, 1127–1157 (2008).

[76] J. J. M. Braat, S. van Haver, A. J. E. M. Janssen, and P. Dirksen, "Energy and momentum flux in a high-numerical-aperture beam using the extended Nijboer-Zernike diffraction formalism," J. Europ. Opt. Soc. Rap. Public. **2** (2007).

[77] J. D. Jackson, *Classical Electrodynamics* (John Wiley & Sons, New York, 1999).

[78] A. Boivin, J. Dow, and E. Wolf, "Energy flow in the neighborhood of the focus of a coherent beam," J. Opt. Soc. Am **57**, 1171–1175 (1967).

[79] A. J. E. M. Janssen and P. Dirksen, "Computing Zernike polynomials of arbitrary degree using the discrete Fourier transform," J. Europ. Opt. Soc. Rap. Public. **2**, 07012 (2007).

[80] The MathWorks, Inc., "Mathworks matlab, version 7.5.0.342 (r2007b)," `www.mathworks.com`.

[81] R. W. Gerchberg and W. O. Saxton, "Phase determination for image and diffraction plane pictures in the electron microscope," Optik **34**, 275–284 (1971).

[82] R. W. Gerchberg and W. O. Saxton, "A practical algorithm for the determination of phase from image and diffraction plane images," Optik **35**, 225–246 (1972).

[83] B. R. Frieden, "Restoring with maximum likelihood and maximum entropy," J. Opt. Soc. Am **62**, 511–518 (1972).

[84] R. A. Gonsalves, "Phase retrieval and diversity in adaptive optics," Opt. Eng. **21**, 829–832 (1982).

[85] D. Van Dyck and W. Coene, "A new procedure for wave function restoration in high resolution electron microscopy," Optik **77**, 125–128 (1987).

[86] J. R. Fienup, "Phase retrieval algorithms: a comparison," Appl. Opt. **21**, 2758–2769 (1982).

[87] R. Barakat and B. H. Sandler, "Determination of the wave-front aberration function from measured values of the point-spread function: a two-dimensional phase retrieval problem," J. Opt. Soc. Am. A **9**, 1715–1723 (1992).

[88] J. R. Fienup, J. C. Marron, T. J. Schulz, and J. H. Seldin, "Hubble Space Telescope characterized by using phase-retrieval algorithms," Appl. Opt. **32**, 1747–1767 (1993).

[89] I. Iglesias, "Parametric wave-aberration retrieval from point-spread function data by use of a pyramidal recursive algorithm," Appl. opt. **37**, 5427–5430 (1998).

[90] J. R. Fienup, "Phase retrieval for undersampled broadband images," J. Opt. Soc. Am. A **16**, 1831–1837 (1999).

[91] J. J. M. Braat, P. Dirksen, A. J. E. M. Janssen, S. van Haver, and A. S. van de Nes, "Extended Nijboer-Zernike approach to aberration and birefringence retrieval in a high-numerical-aperture optical system," J. Opt. Soc. Am. A **22**, 2635–2650 (2005).

[92] S. van Haver, J. J. M. Braat, P. Dirksen, and A. J. E. M. Janssen, "High-NA aberration retrieval with the extended Nijboer-Zernike vector diffraction theory," J. Europ. Opt. Soc. Rap. Public. **1**, 06004 (2006).

[93] S. van Haver, J. J. M. Braat, P. Dirksen, and A. J. E. M. Janssen, "High-NA aberration retrieval with the extended Nijboer-Zernike vector diffraction theory - Erratum," J. Europ. Opt. Soc. Rap. Public. **2**, 07011e (2007).

[94] P. Dirksen, J. J. Braat, A. J. Janssen, and A. Leeuwestein, "Aberration retrieval for high-NA optical systems using the extended Nijboer-Zernike theory," Proc. SPIE **5754**, 262–273 (2005).

[95] P. Dirksen, J. J. M. Braat, A. J. E. M. Janssen, A. Leeuwestein, T. Matsuyama, and T. Noda, "Aerial image based lens metrology for wafer steppers," Proc. SPIE **6154**, 61540X (2006).

[96] S. van Haver, A. J. E. M. Janssen, P. Dirksen, and J. J. M. Braat, "Extended Nijboer-Zernike (ENZ) based evaluation of amplitude and phase aberrations on scaled and annular pupils," in "EOS topical meeting on Advanced Imaging Techniques (2007) meeting digest," (2007).

[97] R. S. Longhurst, *Geometrical and Physical Optics* (McGraw-Hill, New York, 1974), 3rd ed.

[98] J. McGuire and R. Chipman, "Diffraction image formation in optical systems with polarization aberrations. I: Formulation and example," J. Opt. Soc. Am. A **7**, 1614–1626 (1990).

[99] S. Y. Lu and R. Chipman, "Homogeneous and inhomogeneous Jones matrices," J. Opt. Soc. Am. A **11**, 766–773 (1994).

[100] G. D. VanWiggeren and R. Roy, "Transmission of linearly polarized light through a single-mode fiber with random fluctuations of birefringence," Appl. opt. **38**, 3888–3892 (1999).

[101] S. Stallinga, "Light distribution close to focus in biaxially birefringent media," J. Opt. Soc. Am. A **21**, 1785–1798 (2004).

[102] S. Stallinga, "Strehl ratio for focusing into biaxially birefringent media," J. Opt. Soc. Am. A **21**, 2406–2413 (2004).

[103] C. J. R. Sheppard and P. Török, "Focal shift and the axial optical coordinate for high-aperture systems of finite Fresnel number," J. Opt. Soc. Am. A **20**, 2156–2162 (2003).

[104] J. J. M. Braat, S. van Haver, and A. J. E. M. Janssen, "Correction factor for the Debye integral in the small numerical aperture case," Manuscript in preparation.

[105] P. Ettl and K. Creath, "Comparison of phase-unwrapping algorithms by using gradient of first failure," Appl. Opt. **35**, 5108–5114 (1996).

[106] P. Dirksen, J. Braat, A. J. E. M. Janssen, A. Leeuwestein, H. Kwinten, and D. Van Steenwinckel, "Determination of resist parameters using the extended Nijboer-Zernike theory," Proc. SPIE **5377**, 150–159 (2004).

[107] P. Dirksen, J. J. M. Braat, and A. J. Janssen, "Estimating resist parameters in optical lithography using the extended Nijboer-Zernike theory," J. Microlith., Microfabr., Microsyst. **5**, 1–11 (2006).

[108] A. K. Wong, *Resolution enhancement techniques in optical lithography* (SPIE Press, Bellingham, 2001).

[109] A. S. van de Nes, "Rigorous electromagnetic field calculations for advanced optical systems," Ph.D. thesis, Delft university of technology (2005).

[110] H. L. Chen, W. H. Lee, W. Fan, S. Y. Chuang, Y. H. Lai, and C. C. Lee, "Reduction of polarization and swing effects in a high numerical aperture exposure system by utilizing resist antireflective coatings," Microelectr. Eng. **86**, 83–87 (2009).

[111] J. Lee, M. van der Aa, C. Verschuren, F. Zijp, and M. van der Mark, "Development of an air gap servo system for high data transfer rate near-field optical recording," Jpn. J. Appl. Phys. **44**, 3423–3426 (2005).

[112] J. J. M. Braat, S. van Haver, A. J. E. M. Janssen, and S. F. Pereira, "Image formation in a multilayer using the Extended Nijboer-Zernike theory," J. Europ. Opt. Soc. Rap. Public. **4**, 09048 (2009).

[113] M. Abramowitz and I. A. Stegun, *Handbook of Mathematical Functions* (Dover Publications Inc., New York, 1972), 9th ed.

Nawoord

Vier jaar lang wist ik dat dit moment ging komen. Vier jaar lang heb ik de tijd gehad om mezelf er op voor te bereiden. Maar dan toch, nu het moment daar is, voelt het nog onverwachts. Mijn tijd als promovendus zit er helaas op. In mijn ogen een zeer fijne tijd die werkelijk voorbij is gevlogen. De afgelopen jaren heb ik in grote vrijheid kunnen werken aan uitdagende optische vraagstukken, heb ik voor conferenties vele uithoeken van de wereld bezocht en heb ik vele interessante mensen ontmoet. Als je het mij vraagt een heerlijk leven en het is voor mij dan ook een raadsel waarom niet meer jonge Nederlandse afgestudeerden kiezen voor een promotietraject.

Nu we zijn aangekomen op één van de laatste bladzijden van mijn proefschrift, ben ik eindelijk in de gelegenheid de personen te bedanken die direct en indirect een belangrijke bijdrage hebben geleverd aan de totstandkoming van dit proefschrift. Hiervoor richt ik mij in de eerste plaats natuurlijk tot mijn eerste promotor, professor Braat. Beste Joseph, vanaf het moment dat u zich mengde in mijn universitaire carrière, als mentor professor in het eerste jaar van mijn studie Technische Natuurkunde, heeft u een onuitwisbare indruk achtergelaten. Uw oneindig lijkend geduld, ongelooflijke hoeveelheid parate kennis, warme persoonlijkheid en, volgens "de doctor", zo spreekwoordelijke beleefdheid bewonder ik zeer en zullen voor mij altijd als voorbeeld blijven dienen. Ook mijn tweede promotor, professor Urbach, die schijnbaar zonder moeite het stokje van professor Braat overnam toen deze met emiraat ging en copromotor, dr. Pereira, die vooral op experimenteel vlak een belangrijke bijdrage heeft geleverd, kan ik niet genoeg bedanken voor hun steun en inzet.

De meeste mathematische resultaten gepresenteerd in mijn proefschrift dienen grotendeels te worden toegeschreven aan dr. Janssen, oftewel "de doctor", zonder wiens mathematisch vernuft de ENZ theory niet mogelijk zou zijn geweest. Beste Guido, bedankt voor het wijzen van de weg door de wondere wereld van de analytische wiskunde en voor de onvergetelijke vergaderingen in uw kamer op de High Tech Campus in Eindhoven, die zonder uitzondering de autorit van anderhalf uur vanuit Delft meer dan waard waren. Hierbij dien ik ook gelijk dr. Dirksen te bedanken die, samen met prof. Braat en dr. Janssen, behoort tot de "founding fathers" van de ENZ theory. Zijn pionierswerk op experimenteel gebied en de door hem gegenereerde naamsbekendheid van de ENZ theorie zijn voor mij van zeer grote waarde geweest.

Op het gebied van simulaties en de daarvoor benodigde software-ontwikkeling gaat mijn dank vooral uit naar Olaf Janssen, Eric Schuitema, Arthur van de Nes en Roland Horsten. Hun hulp was essentieel bij het zetten van de eerste moeilijke stappen in het schrijven van een eigen softwaretool en zij hebben mij menigmaal weten te bevrijden uit oneindige "for-loops" en onbegrijpelijke "allocation errors". In de omgang met een ander crash-gevoelig systeem, namelijk het bureaucratisch apparaat van de Technische Universiteit Delft, ben ik veel dank verschuldigd aan Yvonne en Lucia. Het mag wel een keer gezegd worden dat zonder hun inzet en organisatorische kwaliteiten de Optica onderzoeksgroep als geheel al lang was verzand in de ondoorzichtige procedures van de universiteit. Dames bedankt hiervoor!

Naast hulp en assistentie op inhoudelijk en organisatorisch vlak is er nog iets essentieel in het succesvol volbrengen van een promotie, namelijk de mensen om je heen. Zij houden je met beide benen op de grond, zorgen ervoor dat je niet totaal vervreemd van de echte wereld en, het meest belangrijke, dat je er plezier in houdt. Wat dat betreft heb ik het uitermate getroffen met mijn promotieplaats binnen de Optica onderzoeksgroep van de Technische Universiteit Delft. Alle (ex)-collega's heel erg bedankt voor de fijne tijd en vooral ook voor de mooie herinneringen aan de Optica Uitjes, de Optica Kerstdiners, onze deelname aan de sportdagen, de OMOC avonden (met iets te cultureelverantwoorde films), de sociale activiteiten en culinaire hoogstandjes tijdens conferenties, de strandbezoekjes, de dubieus slechte films op het Rotterdam filmfestival, de barbecues in het park en het geroddel tijdens de koffiepauzes onder het genot van een stukje taart. Ik heb in elk geval geweldig genoten. In het bijzonder wil ik nog even mijn kamergenoten noemen die het door de jaren heen toch maar met me hebben uitgehouden. Arthur, Janne, Olaf, Maarten, Richard, Thijs en Erwan bedankt, "may the theoretical room rule for ever". Ook een speciaal dankwoord voor mijn paranimfen Olaf en Pascal. Ik ben jullie echt als vrienden gaan beschouwen. Bedankt dat jullie mij willen bijstaan tijdens de promotie en hopelijk zullen ook jullie (ja, ook jij Pascal) gladjes promoveren in de nabije toekomst.

Ter afsluiting richt ik mijn dank tot diegenen die het dichtst bij me staan en die mij gevormd hebben tot wie ik nu ben. Paps en mams, ondanks dat ik jullie lang niet altijd in begrijpelijk taal kon uitleggen waar ik nu in hemelsnaam mee bezig was, heb ik toch altijd van jullie onvoorwaardelijke steun en vertrouwen kunnen genieten. Bedankt dat jullie mij in zo'n grote mate hebben vrijgelaten in het maken van mijn eigen keuzes en dat ik mij zodoende heb kunnen ontwikkelen in die gebieden waarin ik werkelijk geïnteresseerd ben. En tenslotte, mijn allerliefste Janneke, jou hoop ik nog vele en vele jaren dagelijks te kunnen bedanken voor al het moois dat we samen al hebben en nog zullen krijgen.

Sven van Haver, Delft, 7 december 2009.

About the author

Sven van Haver

born in Leidschendam on
September 18, 1981.

Sven obtained his VWO-diploma cum laude in 1999 from the Dalton scholengemeenschap in Voorburg. Afterwards, he initiated a study of Applied Physics at the Delft University of Technology where he obtained his 'propedeuse' within one year. To conclude the following 'kandidaats' phase of the Applied Physics program, which is comparable to the Bachelor level, he performed an experimental project on the analysis of wavefronts using the Foucault test. This research has been performed at TNO in Delft under the supervision of H. de Man.

In the academic year 2003-2004, Sven initiated an Applied Physics research Master at the Delft University of Technology. As part of this two-year Master, he did an internship at Philips Research in Eindhoven under the supervision of dr. W. IJzerman. This internship involved the design of lenticulars to be applied in 3D display applications. The last year of his master, Sven joined the Optics Research Group to do research on the Extended Nijboer-Zernike (ENZ) diffraction theory and its application in aberration retrieval of high-numerical-aperture optical systems. His supervisor during the research project was prof.dr.ir. J.J.M. Braat and based on his work in this subject he obtained his Master degree in Applied Physics in December 2005. Apart from his strong interest in science, Sven is a passionate basketball player. During his study he played basketball for the Haaglanden Cobra's team participating in the top basketball league of the Netherlands.

After his graduation, Sven was offered a Ph.D. position by prof.dr.ir. J.J.M. Braat to continue his research on the applications of the ENZ theory. Between January 2006 and December 2009 he has been employed as a research assistant in the Optics Research Group at the Delft University of Technology on a project studying the effects of reflective surfaces in EUV-lithography. This project, being part of the large NanoNed program funded by the Dutch ministry of economic affairs, allowed Sven to further develop the ENZ theory to be applied in general

imaging applications such as lithography. During this time, daily supervision was provided by dr. S.F. Pereira and prof.dr.ir. J.J.M. Braat to whom prof.dr. H.P. Urbach was added in 2007 after prof. Braat retired as group leader.

In the four years of his Ph.D. Sven made many contributions to the development of the ENZ diffraction theory and in particular to its use in the simulation of images produced by advanced lithographic systems. This thesis provides a complete overview, and most of his work has also been published in scientific journals and is presented at several international conferences related to optics (see comprehensive listing below). Apart from his theoretical contributions, Sven also delivered a simulation tool that accurately describes image formation by a large variety of optical systems. Next to his research related work, Sven has also been involved in the supervision of students from the TU Delft as well as exchange students from France and he acted as a teaching assistant during the master course 'Computational Physics'. In addition, he also continued to invest in his personal development through a number of courses. He attended the graduate course 'Interaction of light and matter' organized by the Casimir Research School at Leiden University in 2006. In that same year he also took part in a two-week summerschool on optical modeling in Santiago de Compostela, Spain. In 2007, a computer science related course on .Net, C# and ASP.NET. organised by Twice IT in Driebergen was fulfilled succesfully. In May 2008, he participated in the 4th Fraunhofer IISB Lithography Simulation Course in Erlangen, Germany and in September of that same year he gave a lecture on Extended Nijboer-Zernike based lithographic imaging at the 6th Fraunhofer IISB Lithography Simulation Workshop in Athens, Greece. Finally, in February 2009, he followed another computer science course on 'Object Oriented Analysis and Design using UML' in Eindhoven, again being organised by Twice IT.

As of January 2010, Sven started a one year postdoctoral research project in the Optics Research Group, funded by an industrial partner, to incorporate the ENZ aberration retrieval functionality into their highly advanced optical equipment.

List of Publications

Refereed journal publications

[1] J. J. M. Braat, P. Dirksen, A. J. E. M. Janssen, S. van Haver, and A. S. van de Nes, "Extended Nijboer-Zernike approach to aberration and birefringence retrieval in a high-numerical-aperture optical system," J. Opt. Soc. Am. A **22**, 2635–2650 (2005).

[2] S. van Haver, J. J. M. Braat, P. Dirksen, and A. J. E. M. Janssen, "High-NA aberration retrieval with the extended Nijboer-Zernike vector diffraction theory," J. Europ. Opt. Soc. Rap. Public. **1**, 06004 (2006).

[3] A. J. E. M. Janssen, S. van Haver, J. J. M. Braat, and P. Dirksen, "Strehl ratio and optimum focus of high-numerical-aperture beams," J. Europ. Opt. Soc. Rap. Public. **2**, 07008 (2007).

[4] S. van Haver, J. J. M. Braat, P. Dirksen, and A. J. E. M. Janssen, "High-NA aberration retrieval with the extended Nijboer-Zernike vector diffraction theory - Erratum," J. Europ. Opt. Soc. Rap. Public. **2**, 07011e (2007).

[5] J. J. M. Braat, S. van Haver, A. J. E. M. Janssen, and P. Dirksen, "Energy and momentum flux in a high-numerical-aperture beam using the extended Nijboer-Zernike diffraction formalism," J. Europ. Opt. Soc. Rap. Public. **2** (2007).

[6] P. Lalanne, M. Besbes, J. P. Hugonin, S. van Haver, O. T. A. Janssen, A. M. Nugrowati, M. Xu, S. F. Pereira, H. P. Urbach, A. S. van de Nes, P. Bienstman, G. Granet, A. Moreau, S. Helfert, M. Sukharev, T. Seideman, F. Baida, B. Guizal, and D. van Labeke, "Numerical analysis of a slit-groove diffraction problem," J. Europ. Opt. Soc. Rap. Public. **2** (2007).

[7] A. J. E. M. Janssen, S. van Haver, P. Dirksen, and J. J. M. Braat, "Zernike representation and Strehl ratio of optical systems with variable numerical aperture," J. Mod. Opt. **55**, 1127–1157 (2008).

[8] R. M. Aarts, J. J. M. Braat, P. Dirksen, S. van Haver, C. van Heesch, and A. J. E. M. Janssen, "Analytic expressions and approximations for the on-axis, aberration-free Rayleigh and Debye integral in the case of focusing fields on a circular aperture," J. Europ. Opt. Soc. Rap. Public. **3** (2008).

[9] S. van Haver, J. J. M. Braat, A. J. E. M. Janssen, O. T. A. Janssen, and S. F. Pereira, "Vectorial aerial-image computations of three-dimensional objects based on the Extended Nijboer-Zernike theory," J. Opt. Soc. Am. A **26**, 1221–1234 (2009).

[10] J. J. M. Braat, S. van Haver, A. J. E. M. Janssen, and S. F. Pereira, "Image formation in a multilayer using the Extended Nijboer-Zernike theory," J. Europ. Opt. Soc. Rap. Public. **4**, 09048 (2009).

[11] J. J. M. Braat, S. van Haver, and A. J. E. M. Janssen, "Correction factor for the Debye integral in the small numerical aperture case," Manuscript in preparation.

Conference proceedings

[1] S. van Haver, A. J. E. M. Janssen, P. Dirksen, and J. J. M. Braat, "Extended Nijboer-Zernike (ENZ) based evaluation of amplitude and phase aberrations on scaled and annular pupils," in "EOS topical meeting on Advanced Imaging Techniques (2007) meeting digest," (2007).

[2] O. T. A. Janssen, S. van Haver, A. J. E. M. Janssen, J. J. M. Braat, H. P. Urbach, and S. F. Pereira, "Extended Nijboer-Zernike (ENZ) based mask imaging: efficient coupling of electromagnetic field solvers and the ENZ imaging algorithm," Proc. SPIE **6924**, 692410 (2008).

[3] S. van Haver, O. T. A. Janssen, J. J. M. Braat, A. J. E. M. Janssen, H. P. Urbach, and S. F. Pereira, "General imaging of advanced 3D mask objects based on the fully-vectorial extended Nijboer-Zernike (ENZ) theory," Proc. SPIE **6924**, 69240U (2008).

Bookchapter

[1] J. J. M. Braat, S. van Haver, A. J. E. M. Janssen, and P. Dirksen, "Assessment of optical systems by means of point-spread functions," in "Progress in Optics," vol. **51**, E. Wolf, ed. (Elsevier B.V., Amsterdam, 2008), chap. 6, pp. 349-468 .

Master's thesis

[1] S. van Haver, "Extended Nijboer-Zernike diffraction and aberration retrieval theory for high-numerical-aperture optical imaging systems," Master's thesis, Delft University of Technology (2005).

Technical report

[1] S. van Haver, "On the optical design of 3D displays," Tech. Rep. TN-2005/00134, Philips Research (2005).

Presentations at scientific meetings

[1] S. van Haver, J. J. M. Braat, P. Dirksen, and A. J. E. M. Janssen, "High-NA lens characterization by through-focus intensity measurements," presentation at European Optical Society (EOS) Annual Meeting, Paris (2006).

[2] S. van Haver, J. J. M. Braat, and S. F. Pereira, "Rigorous mask-imaging using the Extended Nijboer-Zernike diffraction theory," poster presented at NanoNed symposium, Eindhoven (2006).

[3] S. van Haver, O. T. A. Janssen, A. M. Nugrowati, M. Xu, S. F. Pereira, H. P. Urbach, and A. S. van de Nes, "Comparison of numerical methods in solving a slit-groove diffraction problem," poster presented at Network of Excellence on Micro-Optics (NEMO) meeting, Florence (2007).

[4] S. van Haver, J. J. M. Braat, and S. F. Pereira, "Extended Nijboer-Zernike (ENZ) based characterization of micro-lenses," poster presented at Network of Excellence on Micro-Optics (NEMO) meeting, Florence (2007).

[5] S. van Haver, A. J. E. M. Janssen, P. Dirksen, and J. J. M. Braat, "Extended Nijboer-Zernike (ENZ) based evaluation of amplitude and phase aberrations on scaled and annular pupils," poster presented at European Optical Society topical meeting on Advanced Imaging Techniques (EOS-AIT), Lille (2007).

[6] S. van Haver, A. J. E. M. Janssen, P. Dirksen, and J. J. M. Braat, "Imaging based on the Extended Nijboer-Zernike (ENZ) formalism," presentation at European Optical Society topical meeting on Advanced Imaging Techniques (EOS-AIT), Lille (2007).

[7] S. van Haver, O. T. A. Janssen, A. M. Nugrowati, J. J. M. Braat, and S. F. Pereira, "Novel approach to mask imaging based on the Extended Nijboer-Zernike (ENZ) diffraction theory," poster presented at Micro & Nano Engineering (MNE) conference, Copenhagen (2007). Received 1st. prize in best poster award.

[8] S. van Haver, O. T. A. Janssen, A. M. Nugrowati, J. J. M. Braat, and S. F. Pereira, "Novel approach to mask imaging based on the Extended Nijboer-Zernike (ENZ) diffraction theory," poster presented at NanoNed symposium, Nijmegen (2007).

[9] O. T. A. Janssen, S. van Haver, A. J. E. M. Janssen, J. J. M. Braat, H. P. Urbach, and S. F. Pereira, "Extended Nijboer-Zernike (ENZ) based mask imaging: efficient coupling of electromagnetic field solvers and the ENZ imaging algorithm," presentation at SPIE Microlithography conference, San Jose (2008).

[10] S. van Haver, O. T. A. Janssen, A. J. E. M. Janssen, J. J. M. Braat, H. P. Urbach, and S. F. Pereira, "General imaging of advanced 3D mask objects based on the fully-vectorial extended Nijboer-Zernike (ENZ) theory," presentation at SPIE Microlithography conference, San Jose (2008).

[11] S. van Haver, O. T. A. Janssen, A. M. Nugrowati, J. J. M. Braat, and S. F. Pereira, "Combining various optical simulation tools to enable complex optical system simulations," poster presented at Network of Excellence on Micro-Optics (NEMO) meeting, Santiago de Compostela (2008).

[12] S. van Haver, O. T. A. Janssen, A. J. E. M. Janssen, J. J. M. Braat, S. F. Pereira, and P. Evanschitzky, "Characterization of a novel mask imaging algorithm based on the Extended Nijboer-Zernike (ENZ) formalism," poster presented at Micro & Nano Engineering (MNE) conference, Athens (2008).

[13] S. van Haver, O. T. A. Janssen, J. J. M. Braat, and S. F. Pereira, "An alternative method for advanced lithographic imaging: the Extended Nijboer-Zernike formalism," lecture given at 6th Fraunhofer IISB Lithography Simulation Workshop, Athens (2008).

[14] S. van Haver, O. T. A. Janssen, J. J. M. Braat, and S. F. Pereira, "Image simulations of extended objects using an algorithm based on the Extended Nijboer-Zernike (ENZ) formalism," poster presented at European Optical Society (EOS) Annual Meeting, Paris (2008). Received 1st. prize in best poster award.

[15] S. van Haver, A. J. E. M. Janssen, J. J. M. Braat, and S. F. Pereira, "Imaging based on the Extended Nijboer-Zernike (ENZ) formalism," poster presented at Optical Society of America conference on Frontiers in Optics (ASO-FiO), Rochester (2008).

[16] S. van Haver, O. T. A. Janssen, J. J. M. Braat, and S. F. Pereira, "Characterization of a novel mask imaging algorithm based on the Extended Nijboer-Zernike (ENZ) formalism," poster presented at MicroNano conference, Wageningen (2008).

[17] S. van Haver, "Simulations of a complex lithographic system," invited talk at Fotonica Evenement, Nieuwegein (2009).

[18] S. van Haver, A. J. E. M. Janssen, P. Dirksen, and J. J. M. Braat, "Extended Nijboer-Zernike (ENZ) based imaging into an image region containing a layered configuration," presentation at European Optical Society topical meeting on Advanced Imaging Techniques (EOS-AIT), Jena (2009).

[19] J. J. M. Braat, S. van Haver, and S. F. Pereira, "Microlens quality assessment using the Extended Nijboer-Zernike diffraction theory," presentation at European Optical Society topical meeting on Optical Microsystems, Capri (2009).

[20] S. van Haver, J. J. M. Braat, and S. F. Pereira, "Accurate and efficient simulation of resist images generated by advanced lithographic system using the Extended Nijboer-Zernike (ENZ) diffraction theory," invited talk at MicroNano conference, Delft (2009).

Stellingen

behorende bij het proefschrift:

De Extended Nijboer-Zernike diffractietheorie en haar toepassingen

te verdedigen op vrijdag 5 februari 2010 om 12:30 te Delft door ir. Sven van Haver.

1. Complexe Zernikecoëfficiënten zijn een logische uitbreiding van de gebruikelijke reële coëfficiënten wanneer men naast fase-aberraties ook geïnteresseerd is in amplitude-afwijkingen. *- Hoofdstuk 3 van dit proefschrift*

2. In tegenstelling tot wat algemeen wordt aangenomen hangt bij een geaberreerd optisch systeem de axiale positie van het afbeeldingsvlak met maximale Strehlverhouding ook af van de amplitude verdeling in de pupil. *- Hoofdstuk 4 van dit proefschrift*

3. Voor afbeeldingssimulaties is de vaak gehoorde uitspraak “een hogere simulatienauwkeurigheid vereist enkel meer geheugen en rekenkracht” onjuist.

4. Wanneer men nu, vanuit het niets, een model zou moeten construeren om afbeelding door geavanceerde optische systemen te beschrijven, zou dit niet op de Hopkins methode worden gebaseerd.

5. Het feit dat een geopperd nieuw model of methode mathematisch eleganter is dan bestaande alternatieven is op zichzelf genoeg reden voor het verder uitwerken en testen ervan.

6. Het huidig gevoerd wetenschappelijk beleid in Nederland zal er op den duur toe leiden dat er meer emigratie dan immigratie van kenniswerkers plaatsvindt.

7. Voor het bereiken van wetenschappelijke vooruitgang is creativiteit even belangrijk als intelligentie en kennis.

8. Een team onderzoekers is in grote mate te vergelijken met een basketbalteam; als men ervoor zorgt dat de specifieke kwaliteiten van de individuen onderling complementair zijn, zal het team als geheel beter presteren.

9. Het negeren van informatie verbetert het geheugen.

10. Een strikte tijdregistratie met bijbehorende 8-urige werkdag is funest voor het wetenschappelijk proces.

Deze stellingen worden opponeerbaar en verdedigbaar geacht
en zijn als zodanig goedgekeurd door de promotoren
Prof.dr.ir. J.J.M. Braat en Prof.dr. H.P. Urbach.

Propositions

accompanying the Ph.D. thesis:

The Extended Nijboer-Zernike diffraction theory and its applications

To be defended on Friday February 5th 2010 at 12:30 in Delft by ir. Sven van Haver

1. Complex Zernike coefficients are a logical extension of the usual real ones when, apart from phase aberrations, also amplitude defects are considered.

   - Chapter 3 of this thesis

2. For an aberrated optical system, the axial position of the image plane in which the Strehl-ratio is maximal depends on the amplitude distribution in the pupil, this in contrast to what is generally assumed.

   - Chapter 4 of this thesis

3. For image simulations, the common claim that a higher simulation accuracy only requires more memory capacity and computational power, is false.

4. If today, one would have to construct a new model from scratch to describe image formation by advanced optical imaging systems, then this model would not be based on the Hopkins approach.

5. The fact that a newly proposed model or method is mathematically more elegant than existing alternatives should, by itself, be enough reason to justify its development and testing.

6. The currently applied scientific policy in the Netherlands will eventually lead to a surplus of knowledge emigrants instead of immigrants.

7. To make significant scientific progress, creativity is as important as intelligence and knowledge.

8. A team of researchers is very similar to a team of basketball players; if one makes sure that the individual team members have specific qualities that are mutually complementary, then the team as a whole will obtain better results.

9. Neglect of information improves memory.

10. A strict working-hours-registration-system together with an 8-hour workday is disastrous for the scientific process.

These propositions are considered to be opposable and defendable
and as such have been approved by the promoters
Prof.dr.ir. J.J.M. Braat and Prof.dr. H.P. Urbach.

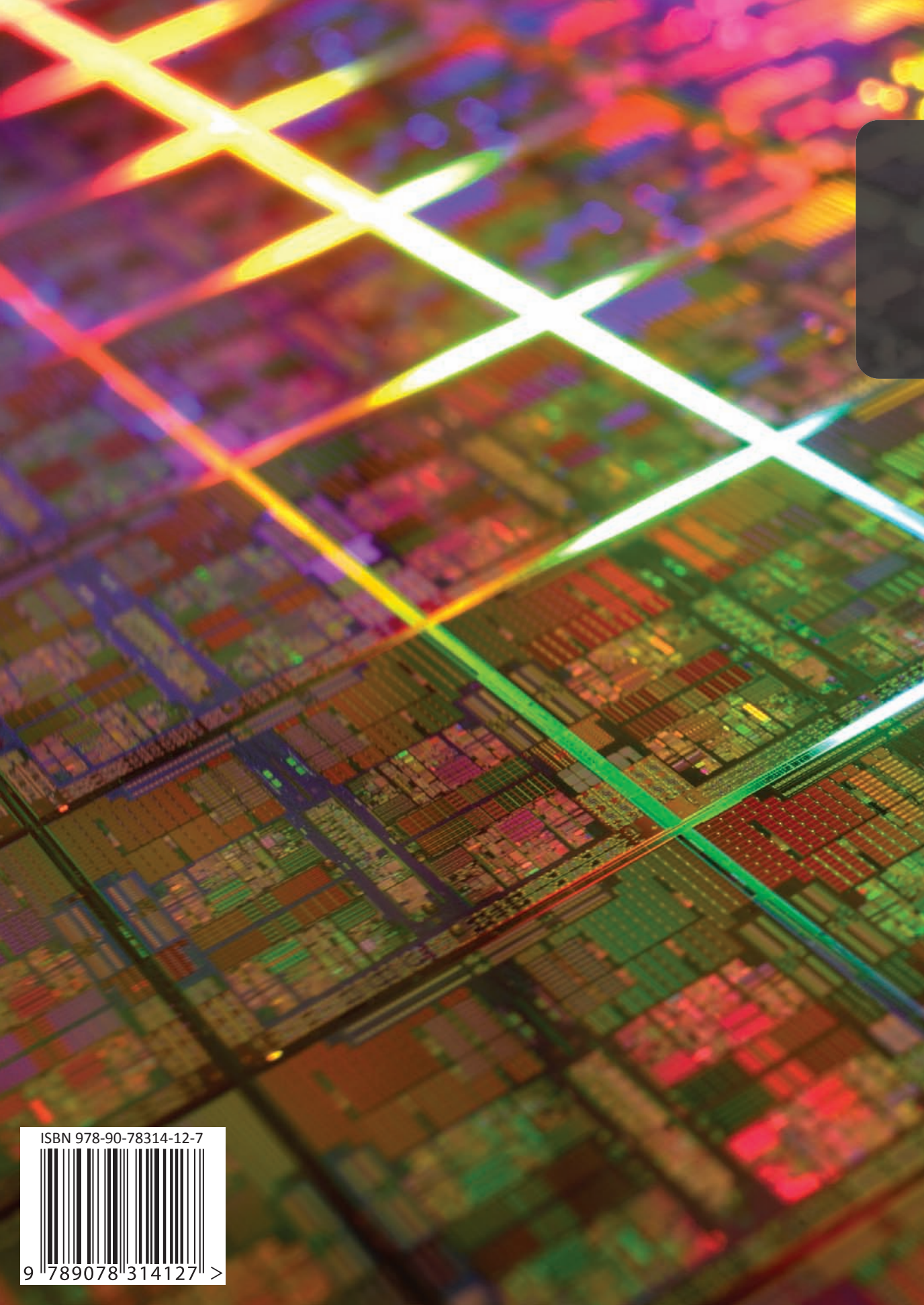

ISBN 978-90-78314-12-7